Sheffield Hallam University

Computer simulation of confined and flexoelectric liquid crystalline systems.

BARMES, F.

Available from the Sheffield Hallam University Research Archive (SHURA) at:

http://shura.shu.ac.uk/19318/

A Sheffield Hallam University thesis

This thesis is protected by copyright which belongs to the author.

The content must not be changed in any way or sold commercially in any format or medium without the formal permission of the author.

When referring to this work, full bibliographic details including the author, title, awarding institution and date of the thesis must be given.

Please visit http://shura.shu.ac.uk/19318/ and http://shura.shu.ac.uk/information.html for further details about copyright and re-use permissions.

CITY CAMPUS, HOWARD STREET
SHEFFIELD S1 1WB

101 715 899 1

REFERENCE

ProQuest Number: 10694199

All rights reserved

INFORMATION TO ALL USERS
The quality of this reproduction is dependent upon the quality of the copy submitted.

In the unlikely event that the author did not send a complete manuscript
and there are missing pages, these will be noted. Also, if material had to be removed,
a note will indicate the deletion.

ProQuest 10694199

Published by ProQuest LLC (2017). Copyright of the Dissertation is held by the Author.

All rights reserved.
This work is protected against unauthorized copying under Title 17, United States Code
Microform Edition © ProQuest LLC.

ProQuest LLC.
789 East Eisenhower Parkway
P.O. Box 1346
Ann Arbor, MI 48106 – 1346

Computer simulation of confined and flexoelectric liquid crystalline systems

F. Barmes

June 2003

A thesis submitted in partial fulfillment of the requirements of Sheffield Hallam University for the degree of Doctor of Philosophy


SHEFFIELD HALLAM UNIVERSITY
TH
ADSETTS CENTRE

Abstract

In this Thesis, systems of confined and flexoelectric liquid crystal systems have been studied using molecular computer simulations. The aim of this work was to provide a molecular model of a bistable display cell in which switching is induced through the application of directional electric field pulses.

In the first part of this Thesis, the study of confined systems of liquid crystalline particles has been addressed. Computation of the anchoring phase diagrams for three different surface interaction models showed that the hard needle wall and rod-surface potentials induce both planar and homeotropic alignment separated by a bistability region, this being stronger and wider for the rod-surface varant. The results obtained using the rod-sphere surface model, in contrast, showed that tilted surface arrangements can be induced by surface absorption mechanisms. Equivalent studies of hybrid anchored systems showed that a bend director structure can be obtained in a slab with monostable homeotropic anchoring at the top surface and bistable anchoring at the bottom, provided that the slab height is sufficiently large and the top homeotropic anchoring is not too strong.

In the second part of the Thesis, the development of models for tapered (pear-shaped) mesogens has been addressed. The first model considered, the truncated Stone expansion model, proved to be unsuccessful in that it did not display liquid crystalline phases. This drawback was then overcome using the alternative parametric hard Gaussian overlap model which was found to display a much richer phase behaviour. With a molecular elongation $k = 5$, both nematic and interdigitated smectic A_2 phases were obtained.

In the final part of this Thesis, the knowledge acquired from the two previous studies was united in an attempt to model a bistable display cell. Switching between the hybrid aligned nematic and vertical states of the cell was successfully performed using pear shaped particles with both dielectric and dipolar couplings to an applied field. Also, a parameter window was identified, for values of the electric field, dielectric susceptibility and dipole moment, for which directional switching is achievable between the bistable states.

Acknowledgments

Over the past three years, I have met and spent time with many people who directly or indirectly made their contribution to this Thesis and who I am indebted to.

First of all, I would like to thank my supervisors in Sheffield, Dr. Douglas J. Cleaver and Pr. Christopher M. Care for giving me the opportunity of taking this PhD and for their guidance and help throughout this project. A big *gracie* also to my third supervisor, Pr. Claudio Zannoni for offering me the opportunity of conducting part of my research in his group in Bologna. Also, my work during the past three years would not have been that enjoyable without the presence of my many colleagues in Sheffield, Mike, David, Dmytro, Fatima, Vicktor, Richard, Rachael, Kev, Lee, Sergei, Lloyd, Gavin, Balaczs, Tim and those in Bologna, Matteo, Davide, Luca, Silvia, Bebo, Alberto, Corrado, Tim and Alberto. Thanks also to Kevin Blake for his expertise as a system administrator and all his guidance which helped me so much in my battle with Linux and Unix systems. I must also mention the valuable help from Dmytro in deriving the results shown in Appendix A.

Also, I can not forget all those people who helped me in having a life out of the lab. Especially a big thank you to Steve and Serena who made my induction to this country so easy and enjoyable. I have spent a brilliant time living at their place. Thanks also to the 'corps' at the Hallamshire aikido club, Lou, Will, Ben, Mark, Adam, Steve, Gavin, Simon and Chris who make the standard of aikido in Sheffield something to be reckoned with. Thanks also to Dmytro, Ben and Mike for being such fine housemates.

Last but by far not least, I wish to acknowledge my family, especially my parents, my sister and Audrey for their love and support.

... A Audrey

"L'éxperience, c'est comme une lanterne accrochée dans le dos qui n'éclaire que le chemin parcouru."

D'après le Dr. E. Sexe

Advanced studies

- September 2000 : Complex fluids 2000, Sheffield Hallam University.
- December 2000 : British Liquid Crystal Society (BLCS) Winter Workshop. University of Hull.
- July 2001 : Collaborative Computational Project 5 (CCP5) summer school, methods in molecular simulations. UMIST. Poster presentation *"A computer simulation study of modified surface interactions in liquid crystalline systems"*
- July 2001 : presentation *"A computer simulation study of modified surface interactions in liquid crystalline systems"*. Materials Research Institute, Sheffield Hallam University.
- September 2001 : Poster presentation *"A computer simulation study of modified surface interactions in liquid crystalline systems"*. CCP5 annual meeting, "Liquids and Liquid Interfaces", Warwick university.
- May 2002 : presentation *"Surface induced structural changes in confined liquid crystalline systems: a computer simulation study"*. Univeristá di Bologna.
- September 2003 : presentation *"Towards modeling surface induced switching in bistable devices"*. CCP5 annual meeting, "Advances in simulations of molecules and materials", Durham university.
- February 2003 : presentation *"Towards modeling surface induced switching in bistable devices"*. Materials Research Institute, Sheffield Hallam University.
- July 2003 : presentation *"Flexoelectricity induced switching in bistable LCD cells"*. University of Strathclyde.

Contents

Introduction

Overview

The liquid crystalline phases which were discovered in 1888, represent a state of matter which shares properties of both its neighbouring isotropic liquid and crystal solid phases. As a result of this, liquid crystals have found many industrial applications in fields as different as biology, rheology, laser optics or tribology. However the greatest application of liquid crystals is, without any doubt, in the field of electro-optic displays.

In the most common liquid crystal display cells, the so called super-twisted nematic displays, surface interactions play a significant role in device operation; switching between the 'on' and 'off' states is achieved by changing the molecular orientations from a field aligned to a surface aligned arrangement. The surface treatment of the cell surfaces, therefore, plays a significant role in the cell performance characteristics such as switching speed, viewing angle and contrast. Surprisingly, the surface treatments used industrially are often applied following empirical rules and a full understanding at a molecular scale of the surface-induced structural changes near the surfaces is still lacking. The reasons for this lie in the very complexity of liquid crystalline phases which renders a full theoretical treatment extremely difficult while most experimental approaches are unable to achieve the much needed molecular resolution. Consequently, the behaviour of liquid crystals at interfaces has become a particular focus for numerical simulations in which the study of generic models, based on statistical mechanics, can be used to gain

an in-depth insight into molecular behaviour.

The latest developments in liquid crystal display technology have lead to bistable displays which are thought to rely on the properties of flexoelectric mesogen molecules for their operation. The advantage of these displays lies in their reduced power consumption, leading to a battery lives about one thousand times longer than those super-twisted nematic displays. Again, bistable devices rely crucially on surface effects for their successful operation, hence the importance of a sound knowledge of the interfacial region properties. Also, the use of flexoelectric particles requires a good understanding of this particular class of liquid crystal.

Aims

The work presented in this Thesis addresses the study of confined and flexoelectric liquid crystalline systems by means of molecular simulations. The final aim is the development of a model for a display cell represented by an hybrid anchored slab with homeotropic anchoring at the top surface and bistable homeotropic-planar anchoring on the bottom surface. In such a cell, switching between the two stable states, the so called HAN and vertical states, is thought to be induced by the flexoelectric characteristic of the molecules and application of an appropriate electric pulse [1]. In order to successfully model such a system requires three key aspects to be investigated.

First the study of confined liquid crystalline systems is addressed. The aim here is to perform a thorough investigation of surface-induced structural changes on a system of confined ellipsoidal-shaped hard particles in a slab geometry using a range of different surface potentials. In this study both symmetric and hybrid anchoring conditions are used. The main goals here are the localization and characterization of the planar-homeotropic anchoring transition and the identification of possible regions of bistability between the two surface arrangements. Hybrid

anchored systems are also investigated so as to determine the parameterisation necessary to maintain continuous director profiles in simulations of HAN arrangement.
Results corresponding to this first part of the Thesis are presented in Chapter 4 and 5.

The second aim of this Thesis is the development of molecular model of hard pear-shaped particles which are thought to exhibit flexoelectric behaviour. A key target from this study is a model for pear shaped particles which displays liquid crystalline phases, most specifically a stable nematic phase which forms spontaneously upon compression. Results corresponding to this second part of the Thesis are presented in Chapter 6.

In the last part of this Thesis, the results obtained from the two previous studies are brought together towards the final aim of this Thesis, and the simulation of confined systems of pear shaped particles is addressed. Here, modeling is performed of a display cell having hybrid anchoring conditions with homeotropic arrangement on the top surface and homeotropic-planar bistable anchoring on the bottom surface. Switching between the two stable states of this cell, the so called HAN and vertical states, is attempted through application of an alternatively positive or negative electric pulse. The aim here is to determine some of the molecular mechanism relevant to this recent development in LCD technology. Results corresponding to this last part of the Thesis are presented in Chapter 7.

Organisation of the Thesis

Chapter 1 provides some background information about liquid crystals. Specifically the characterization of the different bulk liquid crystalline phases is discussed and the class of flexoelectric particles and their properties is considered. This Chapter then follows on the description of the two main theories of liquid crystals

as well as the experimental techniques most commonly used. As a conclusion the different applications of liquid crystals are presented.

Chapter 2 reviews the techniques and models relevant to the molecular simulation of liquid crystals as well as the properties of confined liquid crystalline systems and their anchoring transitions. The simulation techniques and models relevant to liquid crystals are reviewed first, followed by a survey of the modeling of flexoelectric particles. The last part of this Chapter concentrates on the simulation of confined systems and of their anchoring transitions.

Chapter 3 combines review and results and focuses specifically on the simulation of hard Gaussian overlap (HGO) particles. The literature concerning this specific molecular model is reviewed and the techniques used for the computation of observables are presented. Some preliminary results for the bulk behaviour of the HGO models are then given, considering both calamitic and discotic particles.

Chapter 4 presents the results corresponding to the first part of the study of confined systems. Here the surface induced effects on systems of HGO particles confined in a slab geometry are studied. Using a simple surface potential, namely the hard needle wall potential (HNW), these effects are characterized and their regions of stability compared with analytical results. From this, the anchoring transition between the two stable surface arrangements (planar and homeotropic) is located as a function of density and anchoring conditions. Here, regions of bistability between the two surface arrangements are identified.

In Chapter 5, more advanced confined configurations are studied. In the first part, the surface induced effects obtained using two more realistic surface potentials, namely the rod-sphere (RSP) and the rod-surface (RSUP) potentials, are investigated and the results compared with an analytical treatment. In the second part of this Chapter, the case of hybrid systems is investigated using the HNW poten-

tial. Systems of HGO particles are considered confined in a slab geometry with different anchoring conditions on each surface. The effects of hybrid anchoring on the bistability regions are investigated and the structural transition between the homeotropic and planar surface arrangements is investigated. Finally the possibility of obtaining a continuous transition between these two is considered.

Chapter 6 related to a different line of work. Here models for the description of hard pear-shaped particles are developed. For this, two models are considered. The first model is the so called Stone expansion model, a steric version of a potential used previously by the Bologna group [2] while the second model is the parametric hard Gaussian overlap (PHGO) which was developed within this project to resolve some difficulties experienced with the former model. The bulk phase diagrams and structural observables of the phases obtained using these models are presented and their applicability for the modeling of pear shaped liquid crystal molecules is discussed.

Chapter 7 is the last substantial Chapter of this thesis. Here, the knowledge acquired from the preceding studies of confined ellipsoidal particles and the bulk behaviour of pear shaped models is brought together in a study of confined systems of flexoelectric particles. The aim here is to achieve directional field induced switching between the two stable states of a hybrid anchored display cell model. In order to achieve this, a modified version of the RSUP model is implemented, and the resulting surface induced structural changes studied. Specifically a region of bistability between the planar and homeotropic anchoring states is sought. This region of bistability is then used to investigate the mechanisms of easy and hard switching between the HAN and vertical states of the cell; the relevance of the model to the operation of bistable cell is then discussed.

Finally, the main results and conclusions of the Thesis are brought together, and suitable areas for future work are listed.

Chapter 1

The liquid crystalline phases

Introduction

Up to the end of the 19^{th} century, the three known states of matter were gas, liquid and solid. According to dictionary definitions [3, 4] a substance is gaseous if it expands to fill its container homogeneously, regardless of its volume, displays a high compressibility and shows no positional correlations on length scales greater than the molecular size. At the other extreme, a solid retains its shape, can support shear and its atoms are restricted in space, oscillating about a fixed position. Two type of solids can be distinguished; in crystalline solids, the atoms are regularly spaced on a 3 dimensional lattice, whereas in amorphous or glassy solids, the atoms are disordered on a large scale but ordered in the range of a few molecular lengths.

Liquid is a state of matter which exists between the two preceeding phases. A liquid substance only fills part of its container and its localisation is largely controlled by the gravitational force. Actually a liquid is only one component of a two phase system as every liquid is always searching to be in equilibrium with its own saturated vapor. A liquid has no rigidity, gives no resistance to shear under static conditions and has a small volume compressibility. On a microscopic scale, the positions of the constituent molecules are randomly distributed and no long range order can be found. Molecules in a liquid are subject to Brownian diffusion.

However, this picture changed somewhat in the late eighteen eighties. Slightly before then a number of scientist noticed some uncommon crystallization behaviour in certain substances which were found to transform from isotropic liquid to a non-crystalline form before undergoing full crystallization. At the time, this was attributed to the presence of impurities in the samples. The actual discovery of liquid crystals is attributed to Friedrich Reinitzer [5] who, in 1888, was studying a compound related to cholesterol (cholesteryl benzoate). Reinitzer observed what he referred to as 'two melting points' and identified the new phase; this was later termed liquid crystal by his friend and colleague Otto Lehmann [6] who performed the first polarised optical microscopic measurements on liquid crystals.
Although not much studied at first because of the lack of the direct applications, interest in liquid crystals increased dramatically during the 20^{th} century, mostly because of Liquid Crystal Display (LCD) applications; a wide understanding of these phases and the molecules that form them has now been built up.

1.1 Characterization of liquid crystals.

1.1.1 The liquid crystalline phases

The liquid crystalline phases refer to states of matter that exist between the isotropic liquid and crystalline solid. A liquid crystal phase is formed by mesogenic particles, hence the term mesogen used to refer to a molecule that forms a mesophase or liquid crystalline phase. A mesophase shares properties with both the liquid phase (flow, zero resistance to shear) and the crystalline phase (long range positional and/or orientational order, anisotropic optical properties). The term liquid crystal actually encompasses several different phases, the most common of which are smectic and nematic [7, 8, 9].
A necessary but not sufficient requirement for a molecule to form a liquid crystalline phase (or mesophase) is a strong anisotropy in shape; mesogens are either calamitic (rod shaped) or discotic (disc like). Their phase transitions can be tem-

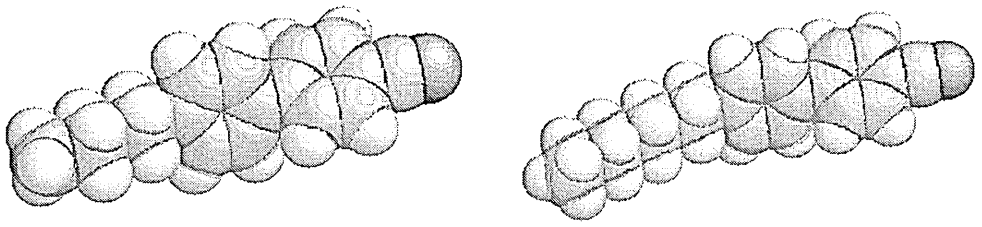

(a) 5CB (b) 8CB

Figure 1.1 : 4-pentyl-4'-cyanobiphenyl (5CB) and 4-octyl-4'-cyanobiphenyl (8CB) molecules

perature driven (thermotropic mesogens) or density driven (lyotropic mesogens).

Calamitic mesogens

Typically a calamitic mesogen contains an aromatic rigid core, formed from 1,4-phenyl groups, to which one or more flexible alkyl chains are attached [10]. Short alkyl chains are typical of nematogens (mesogens that form nematic phases) while longer alkyl chains are related to smectogens (mesogens that form smectic phases). Liquid crystalline phases can be enhanced by increasing the length and polarisability of the molecule as well as the addition of a terminal cyano group which induces polar interactions between pairs of molecules. Lateral substituents (usually attached at the side of molecules in aromatic cores) can influence molecular packing. For instance, adding a fluoro group enhances polarisability but disrupts molecular packing leading to a shift in the isotropic-nematic transition. Creating a lateral dipole can promote formation of a tilted smectic C and, in the case of chiral phases, gives rise to ferroelectricity. Further details regarding the effects of specific functions on liquid crystalline phase behaviour can be found in [11].
The classic example of mesogenic substances are the nCB family shown on Figure 1.1. Here the aromatic core is made of a meta biphenyl; on one end of this core is the flexible tail, an alkyl chain of n carbons ($C_nH_{2n+1},$) and on the other end the head, composed by a cyano group. The influence of the alkyl chain length

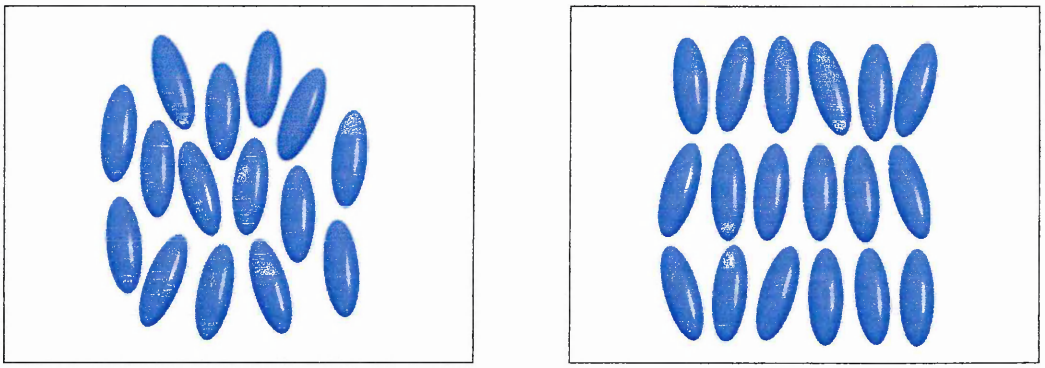

(a) (b)

Figure 1.2 : The nematic (a) and smectic (b) phases.

is readily observable by comparing the phase sequences of the 5CB and 8CB.

5CB : Crystal $^{23°C}$ → Nematic $^{35°C}$ → Isotropic

8CB : Crystal $^{21°C}$ → Smectic A $^{32.5°C}$ → Nematic $^{40°C}$ → isotropic

The two main liquid crystalline phases available to calamitic mesogens are nematic and smectic.

The nematic phase is the simplest liquid crystalline phase and can be formed by calamitic and discotic mesogens alike. This phase is characterized by :

- no long range translational order
- long range orientational order.

In the nematic phase (Figure 1.2(a)) the molecular positions are randomly distributed across the sample but their long axes all point, on average, towards the same direction, the director $\hat{\mathbf{n}}$. Also in the case of a nematic phase with a zero polar moment, the symmetry properties of the phase remain unchanged upon inversion of the director's direction. If chiral molecules are used, a cholesteric or chiral nematic phase can be obtained. The difference between this and the standard nematic phase is that in the former, the director twists as a function of position.

The smectic phase is characterized by :

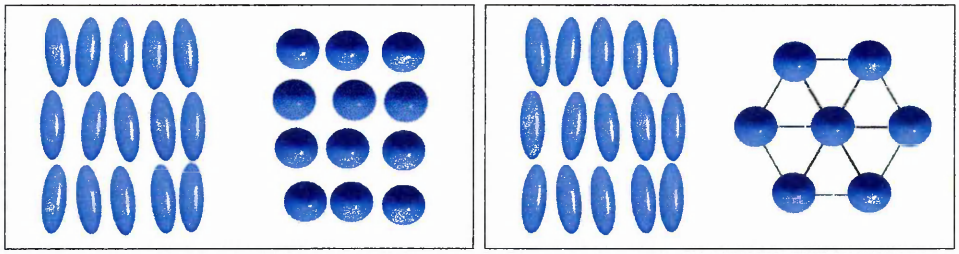

(a) Smectic A

(b) Smectic B

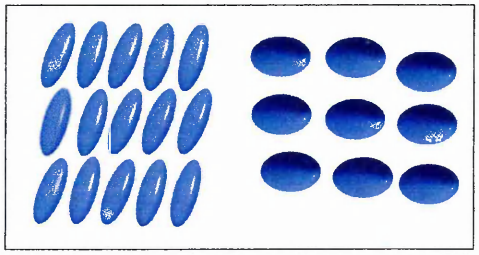

(c) Smectic C

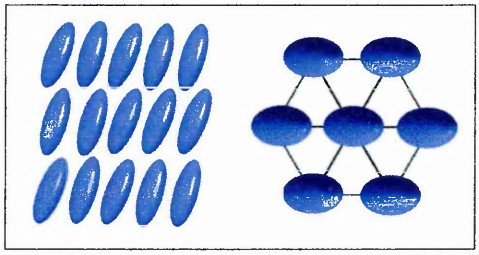

(d) Smectic I

Figure 1.3 : Different types of smectic phases. Each Subfigure shows a front view on the left and a top view on the right. All these phases lack long range positional order.

- long range translational order (*i.e.* one or two dimensions)
- long range orientational order.

In smectic phases (Figure 1.2(b),) as well as pointing along a common direction, the molecules are organized in layers. According to the angle between the director and the layer normal as well as any in plane positional ordering, several different smectic phases can be identified as shown on Figure 1.3.

Discotic mesogens

Discotic molecules typically have a core composed of aromatic rings connected in an approximately circular arrangement from which alkyl chains extend radially (see Figure 1.4). Discotic mesogens form discotic nematic and columnar phases. Several types of the latter exist (see Figure 1.5,) namely disordered (d), ordered (o) and tilted (t) and for each of these there can be three column arrangements

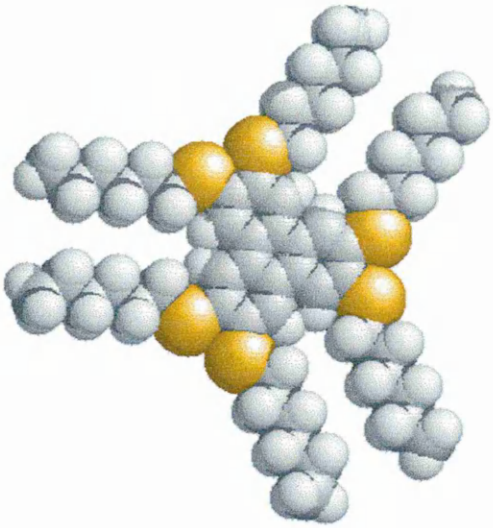

Figure 1.4 : Molecular representation of the HHTT molecule (2,3,6,7,11-hexahexylthiotriphenylene).

(a) Disordered (d) (b) Ordered (o) (c) Tilted (t)

Figure 1.5 : The different discotic columnar phases.

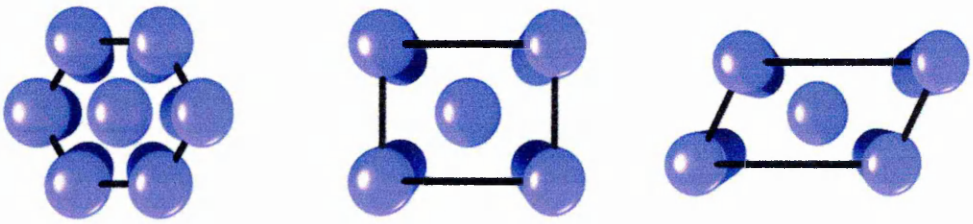

(a) Hexagonal (h) (b) Rectangular (r) (c) Oblique (ob)

Figure 1.6 : The different discotic columnar phases.

namely hexagonal (h), rectangular (r) and oblique (ob). For instance a hexagonal disordered columnar phase is referred to as $\mathrm{Col}_{\mathrm{hd}}$ and an oblique ordered columnar phase as $\mathrm{Col}_{\mathrm{ob,o}}$.

1.2 Flexoelectric liquid crystals.

1.2.1 The flexoelectric effect.

When a liquid crystal is subjected to a splay or bend strain, a net electrical polarization can be created. This effect was first explained in 1969 by R.B. Meyer [12]. Reciprocally, flexoelectric mesogens will splay or bend upon application of an electric field according to the reverse flexoelectric effect.

Originally the flexoelectric effect was explained to arise for particles with a strong shape anisotropy (*i.e.* pear or banana shaped particles) and a strong permanent dipole [12]. According to Meyer, a splay distortion would arise for wedge or pear shaped particles while a bend distortion is associated with banana shaped particles. The relation between the electrical polarization $\mathbf{P}$ and the flexoelectric splay and bend coefficients e_{1z} and e_{3x} is given by [13]:

$$\mathbf{P} = e_{1z}\left(\hat{\mathbf{n}}(\nabla \cdot \hat{\mathbf{n}})\right) + e_{3x}\left(\nabla \times \hat{\mathbf{n}}\right) \times \hat{\mathbf{n}} \tag{1.1}$$

Means for the calculation of the flexoelectric coefficients were later devised by Derzhanski and Petrov [14, 14] and Helfrich [15]. The latter author also extended Meyer's theory to polarizable molecules [16]

Eight years after Meyer's original theory, another mechanism for flexoelectricity in liquid crystals was proposed by Prost and Marcerou [17]. In this work, the electrostatics of uniaxial phases were examined to recognize the link between polarization and strain. A two term expression for the flexoelectric tensor was derived (see Equation 2.9 of [17]) where the first term corresponds to a dipolar effect equivalent to that proposed by Meyer, while the second relates to a non zero quadrupole moment that pertains even with non pear or banana shaped molecule (*i.e.* ellipsoids). The authors also showed that both mechanisms contributed to

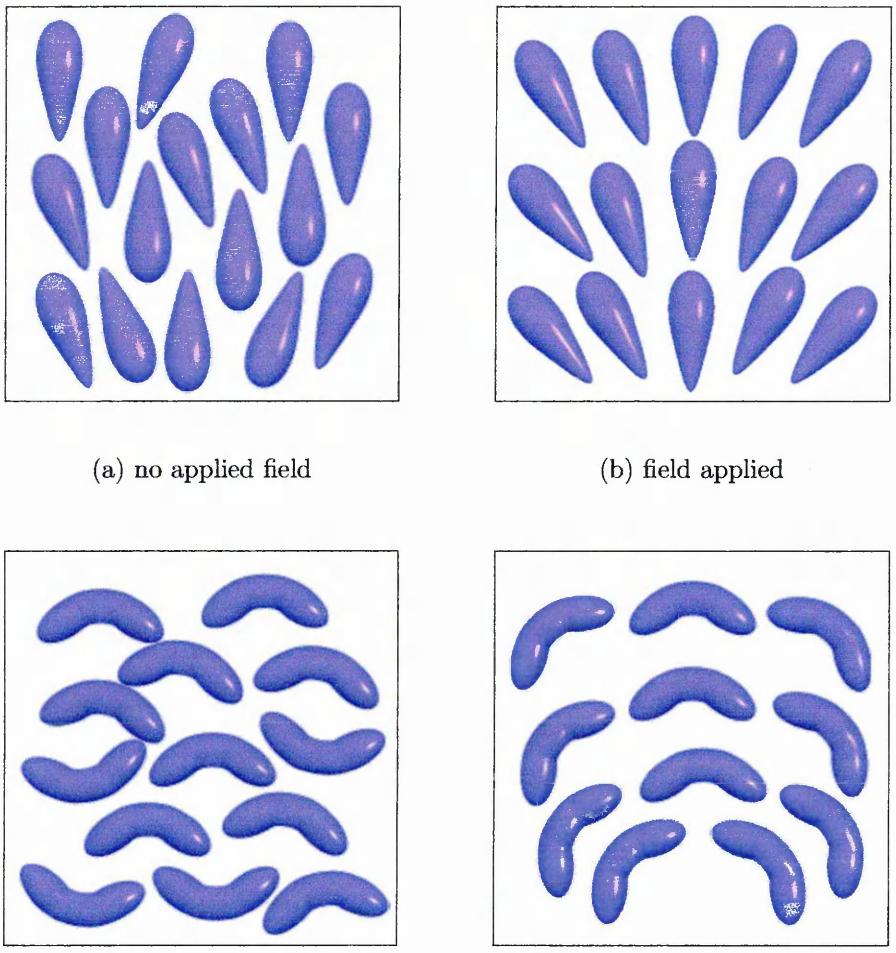

(a) no applied field

(b) field applied

(c) no applied field

(d) field applied

Figure 1.7 : Representation of the polarisation induced distortions in flexoelectric systems. Pear shaped particles (top) have a splay distortion while banana shaped particles (bottom) display a bend distortion. The distorted phases correspond to a situation with an electric field $\mathbf{E}$ *applied vertically and pointing towards to the top of the page.*

the total flexoelectric coefficient $f = e_{1z} + e_{3x}$ with similar orders of magnitude. The implication of this result is that flexoelectricity is an intrinsic property of liquid crystals as most mesogens have non zero quadrupole moments. Also, this effect should be observable not only in the nematic phase as proposed by Meyer, but also in the isotropic phase (see [18] for the first experimental verification of this) as well as the smectic phase [19].

1.2.2 The flexoelectric coefficients.

Due to the comparability of the contributions from the dipolar and quadrupolar mechanisms to the flexoelectric coefficients, identification of which contribution is the largest is not a trivial exercise. Resolving this question requires a means of separating the two effects. One such method is the study of the thermal dependence of the flexoelectric coefficient f. From the study of Prost and Marcerou [17, 20] the expression for f is :

$$f = e_{1z} + e_{3x} \qquad \text{(in Meyer's notation)} \tag{1.2}$$

$$f = f^M + f^Q \tag{1.3}$$

$$f = K_{11}\frac{\epsilon_{\parallel}^0 - \epsilon_{\parallel}^1}{4\pi\mu_{\parallel}} + K_{33}\frac{\epsilon_{\perp}^0 - \epsilon_{\perp}^1}{4\pi\mu_{\perp}} - \frac{2}{3}N\theta_a S \tag{1.4}$$

In the first two terms representing f^M, K_{11} and K_{33} are respectively the splay and bend Frank Oseen elastic constant [13], $\epsilon_{\parallel}^0$ and $\epsilon_{\perp}^0$ are the dielectric constant taken respectively parallel and perpendicular to the director $\hat{\mathbf{n}}$ and μ^{-1} measures the degree of asymmetry of the compound under interest. In the last term representing f^Q, N is the number of particles per unit volume, θ_a is the quadrupole tensor as defined in [17] and S is the order parameter as defined in [13].

From Equation 1.4, it is readily observable that f depends linearly on K_{11} and K_{33} that is linearly with S^2 if Meyer's contribution is of more significance. If the quadrupolar contribution is the larger, then f is a linear function of S.

Although several methods are available for the measurement of the flexoelectric coefficients [13, 7, 21, 22], the best seems to be the "interdigital electrodes technique" (see [19] and [23] for a detailed description) as used by Marcerou and Prost. This setup involves the use of a spatially periodic electric field (created by the interdigitated electrodes) which induces a periodic distortion of the liquid crystal. This distortion corresponds to a grating which scatters light. Measurements of the flexoelectric coefficients are thus performed through the measurement of the scattered light intensity.

Measurements of the thermal dependence of f has been performed by Marcerou and Prost [23] for four different mesogens ranging from symmetric to strongly dipolar. Although the expectation from this study was that the quadrupolar contribution would prove stronger for the most symmetrical mesogens, with Meyer's contribution being stronger for the dipolar particles, the results showed that the quadrupole contribution was actually stronger for virtually all compounds. The only case where Meyer's contribution was more significant was that of a molecule with strong steric constraints as already suggested a previous study [20]. This last finding was later confirmed in [24] in a study of cyanobiphenyl components using a different measurement technique. In parallel with this, using the Onsager-like theory of Straley [25], Osipov [26] showed that the dipole flexoelectricity is significant only for molecules with large transverse dipoles; this condition is met by the mesogens mentioned above which showed Meyer's flexoelectricity.
Some subsequent theoretical work from the same author [27], using a Landau-de Gennes formalism contradicted the general results from this series of experiments, as it predicted a S^2-like variation. This discrepancy is likely explained by the lack of conformational freedom in the theoretical treatment, however.
Using density functional theory, Singh and Singh [28] showed that, given increased knowledge of the molecular parameters of a system, the flexoelectric coefficients (taking into account both mechanisms) can be accurately calculated. The main drawback of this treatment is its restriction to rigid particles. This restriction was

subsequently lifted by Ferrarini [29] who applied mean-field treatment to MBBA which took into account the structure of the molecule's transformers.
Model for flexoelectric pear-shaped molecules have been designed for use in computer simulations [30, 31]. These have found non zero splay and near to zero bend flexoelectric coefficients in accordance with Meyer's theory. These models were subsequently refined so as to become monosite as opposed to multisite [2], leading to phases with net polar order. More details on these studies are given in Chapter 2.

The interest in flexoelectric particles is not only of academic interest as the phenomenon finds some very important applications in bistable liquid crystal display devices [1, 32] which could lead to the development of the next generation of displays.

1.3 Theoretical approach to liquid crystals.

As interest in liquid crystal grows, the number of theories used to describe their complicated phase behaviour increases similarly. Here the focus is brought on to bear on to molecular theories that, using statistical mechanics, take the intermolecular potential as a starting point from which to deduce the macroscopic phase behaviour.
Theoretical studies of simple atomic fluids [33] show that the liquid phase can be described effectively using intermolecular potentials of the Lennard-Jones form, *i.e.* containing both long range attractive and short range repulsive component. Mesogens can be represented with a similar class of potentials, though account has to be taken of the inherent in their elongated shape. One significant question considered by these theories is which of the repulsive and attractive components of the interaction are of greater importance in mesophase formation. As a result, theories have been developed which consider both of these contributions to the anisotropic potentials and thus quantify their respective influences. The two main

and complementary approaches are described in the following Sections, namely Onsager and Maier-Saupe theories.

1.3.1 Density functional theory

The phase structure of simple atomistic fluids can be described successfully using hard spheres as models, that is considering only the repulsive part of their pair potential [34]. The extension of this principle to the mesoscale was first achieved by Lars Onsager in 1949 [35] in a study of colloidal particles (tobacco virus). The main idea underlying this seminal work is that the mechanism for spontaneous ordering in a system of hard molecules is based on competition between the orientational entropy that destroys nematic order and the positional entropy that favors it [13].

Onsager theory is derived from the cluster approach [11] and is a density functional theory in which the free energy $\mathcal{F}$ is expressed as a density virial expansion [36].

$$\mathcal{F} = \mathcal{F}^{id} + \mathcal{F}^{ex} \tag{1.5}$$

$$\mathcal{F}^{id} = N(\log\rho - 1) + N\int f(\hat{\mathbf{u}})\log\left(4\pi f(\hat{\mathbf{u}})\right)d\hat{\mathbf{u}} \tag{1.6}$$

$$\mathcal{F}^{ex} = \rho\mathcal{B}_2\left(f(\hat{\mathbf{u}})\right) + \frac{1}{2}\rho^2\mathcal{B}_3\left(f(\hat{\mathbf{u}})\right) + \frac{1}{3}\rho^3\mathcal{B}_4\left(f(\hat{\mathbf{u}})\right) + \ldots \tag{1.7}$$

Where $\mathcal{F}^{id}$ and $\mathcal{F}^{ex}$ are the ideal and excess parts of $\mathcal{F}$ and $f(\hat{\mathbf{u}})$ is the orientational distribution function that depends on the particle orientation vector $\hat{\mathbf{u}}$. Each $\mathcal{B}_i$ represents the excluded volume in a cluster of i particles.
Onsager made the following assumptions :

- The molecules (spherocylinders of length L and diameter D) interact only through steric repulsion (no interpenetration).
- The volume fraction is much smaller than 1.
- The rods are very long ($L \gg D$).

Within these assumptions, Onsager showed that the virial expansion can be truncated after the second coefficient; he showed that the third one vanishes and assumed the same for the the following coefficients. This makes his approach the simplest form of density functional theory.

The implication of his results is that, in the limits considered, the N-I transition can be explained exclusively using short range repulsive forces. However, the approximations made in this theory worsen considerably as the particle elongation is reduced because the density of the transition is not vanishing. Therefore this theory can not be applied to mesogens with a standard elongation of 3 to 5. Early computer simulations of hard prolate particles by Vieillard-Baron [37] and later Frenkel *et al.* [38, 39] showed qualitative but not quantitative agreement with Onsager's theory

This does not imply that density functional theory can not be applied to liquid crystalline behaviours, only that, for the accurate description of mesogens, more virial coefficients are needed. The most obvious approach, then is to calculate higher order coefficients, as been done in [40, 41], but the difficulty of the task increases significantly with the order of the coefficients. A better approach is the use of resummation techniques such as the y-expansion [42, 43] that allow the indirect inclusion of high order coefficients. Some other resummation methods have been used successfully on single component [44, 45] and mixture systems [46, 47] leading, recently, to considerable improvements in the description of anisotropic fluids [48].

1.3.2 Maier Saupe theory.

In the early 20^{th} Century, Born showed that the anisotropic component of the pair potential was responsible for the order-disorder transitions in nematic phases [11]. This was later expanded by Maier and Saupe to give rise to the so called Maier Saupe (MS) theory [49, 50, 51].

The configurational partition function of a fluid is expressed as :

$$Q_N = \frac{1}{N!} \int e^{-\beta U(\mathbf{X}^N)} d\mathbf{X}^N \tag{1.8}$$

where $\mathbf{X}^N$ represents the full set of positional and orientational coordinates for the N particles of the fluid. In the case of a perfect gas, as every particle's behaviour can be taken to be independent of all others [4], the partition function can be transformed into the product of N single particle partition functions, each of which is easily solvable. However, in the case of a fluid phase, and even more so a mesophase, the relatively high density implies that each particle's energy is dependent on several other particles' coordinates so that the previous simplification is no longer valid.

MS theory aims to resolve this difficulty using the so called molecular field approximation. This approximation removes the need for the consideration of each individual pair potential; rather each particle is taken to reside in a field which mimics the presence of all the other particles. Effectively each particle is assumed to be was moving in an energy continuum. As a result $U(\mathbf{X}^N)$ can be written as the sum of N energies, each of which is a function of the coordinates of a single particle :

$$U(\mathbf{X}^N) = \sum_{i=1}^{N} U(\mathbf{X}_i) \tag{1.9}$$

The problem, then, is to find an expression for the mean-potential experienced by the particles. Several approaches have been used for this. The most intuitive approach is to average the anisotropic pair potential over the coordinates of one particle [52] while one of the most simple and rigorous is to start from the singlet distribution function and solve the Bogoliubov-Born-Green-Kirkwood-Yvon hierarchy of equations as described in [11]. In a translationally invariant situation, the general form of the final mean potential depends only on β, the angle between the particle under consideration and the director $\hat{\mathbf{n}}$, so:

$$U(\beta) = -\epsilon \overline{P_2} P_2(cos^2\beta) \tag{1.10}$$

where $\overline{P_2}$ is the nematic order parameter, $P_2(x)$ is the second order Legendre

polynomial of x and ϵ is a scaling constant which is given by :

$$\epsilon = -V\left(\frac{\partial \epsilon}{\partial V}\right)_T \tag{1.11}$$

Another form for ϵ is given in [9] by the identification :

$$\epsilon = \frac{A}{V^2} \tag{1.12}$$

where the value of A is determined by the interaction properties of the molecules. In any case the general approach for the implementation of Maier Saupe theory is as follows :

- Choose the anisotropic term of the pair potential
- Implement the mean field approximation
- Determine the mean potential
- Deduce the singlet distribution function
- Use this function to calculate the entropy, Helmholtz free energy and order parameters.

The two major elements of the theory that influence its accuracy are the mean field approximation and the form of the mean potential.

Maier Saupe theory can be tested using both computer simulation and real experiment, though the former has an advantage since it can test the validity of the mean field approximation as the mean-potential can be specified in the 'computer experiment'. The theory is reasonably successful in describing, qualitatively, the behaviour of mesogens, showing a first order IN transition. The temperature dependence of the order parameters is also well described qualitatively. The limits of the Maier Saupe theory become apparent in the quantitative predictions, errors being attributed, in part, to the use of the mean field approximation (although some improvement can be made by improving the form of the potential.) A more fundamental weakness of the mean field approximation is that it neglects spacial

and orientational correlations between molecules.

The main conclusion that can be drawn from this is that while MS theory is most effective at long range it can successfully describe liquid crystalline behaviour. This implies that short-range repulsive forces have little role to play, whereas short range potentials have been shown to be responsible for both the ordering of nematics and the structure of normal liquids. This apparent discrepancy can be resolved by appreciating that the long range attractive part of the potential used in MS theory can be regarded as describing the interactions between clusters of highly ordered particles.

1.4 Experimental study of liquid crystals.

1.4.1 Optical polarising microscopy.

Optical polarising microscopy is the main technique used for liquid crystalline phase characterization [9]. Historically it was also the first technique used by Lehmann when he studied the liquid crystalline samples provided by Reinitzer.
The technique consists of observing, under a microscope, a sample sandwiched between crossed polarizers. An isotropically liquid phase does not affect the light and, therefore, no light can cross the analyzer. In the case of a liquid crystalline phase, however, the birefringent property of the material induces refraction of the light according to the director orientation. Since only the component of the refracted light parallel to the analyzer polarization direction is transmitted, the intensity of the transmitted light varies from white if $(\hat{\mathbf{n}} \cdot \hat{\mathbf{p}}) = 0$ to black if $(\hat{\mathbf{n}} \cdot \hat{\mathbf{p}}) = 1$ where $\hat{\mathbf{p}}$ is the polarisation direction direction of the analyser. Moreover, because of defects in the structure and disclination lines, the orientation of $\hat{\mathbf{n}}$ typically varies with position and, therefore, so does the intensity of transmitted light. Distinct patterns can be observed for different mesophases. Examples of these patterns can be found in [8].
Nematic phases induce the so called Schlieren textures where black threads mark-

ing the disclination lines can be observed. These threads lead to the name 'nematic' being used for this phase. Smectic A liquid crystals have a 'fan-like' pattern when viewed through crossed polarizers and smectic C a combination of both. The smectic B phase induces an altogether different pattern of 'mosaic' or broken fan textures. However not every phase can be distinguished clearly. For example, smectic I and smectic F phases induce patterns very similar to that of the smectic C phase which makes the task of identification very difficult if this is the only technique to be used.

1.4.2 Differential scanning calorimetry.

Differential scanning calorimetry (DSC) is a technique used to complement optical polarising microscopy in the phase characterization of liquid crystals [9]. This technique measures enthalpy changes (ΔH) at phase transitions. The phase type of the sample is not examined using this technique, but the value of the enthalpy gives some information about the degree of molecular order in a mesophase.
With this technique, two independently heated furnaces are used. One is empty or contains a reference sample (usually gold) and the second contains the sample under study. Both furnaces are linked to control loops which insure that they are kept at the same temperature as each other. Upon cooling or heating, the heat absorbed by or released from the sample in order to keep the furnaces at the same temperature is measured. Differences between the heat measurement for the two furnaces indicate phase transitions. With this technique, temperatures ranging from $-180°C$ to $600°C$ can be accessed.

Thermodynamics state that there are two types of phase transition discontinuous (1^{st} order) and continuous (2^{nd} order) corresponding to discontinuities in,

respectively, the first and second derivatives of the Gibbs free energy G :

$$G = H - TS \tag{1.13}$$

$$\left(\frac{\partial G}{\partial T}\right) = -S \tag{1.14}$$

$$\left(\frac{\partial^2 G}{\partial T^2}\right) = -\frac{C_p}{T} \tag{1.15}$$

Thus, a first order transition induces a discontinuity in the entropy and a peak of the DSC baseline can be observed, whereas a second order transition is indicated by inflexion of the baseline.

Thus a DSC trace can reveal phase transitions that would be missed by optical polarising microscopy because of the smallness of changes in the optical properties. Conversely phase transitions with small enthalpy changes but rather different optical properties can be missed with the DSC but are easily detected with optical polarising microscopy.

1.4.3 X-ray and neutron diffraction.

X-ray diffraction is one of the most effective techniques for liquid crystalline phase characterization [10, 11]. Here the mesophase is characterised by analysis of the diffraction pattern of an X-ray beam incident upon a sample in which the molecules are aligned with the beam. According to Bragg's law, diffraction is obtained at an angle θ when $\lambda = 2d\sin\theta$ where λ is the light wavelength and d the intermolecular spacing.

Liquid crystal diffraction patterns are characterized by two lateral vertical clear areas that account for the vertical alignment of the molecules. In the case of a nematic, horizontal clear areas, corresponding to diffuse low intensity peaks, can be observed above and below the centre of the pattern. In the case of a smectic, the latter are replaced by points corresponding to sharp high intensity peaks induced by the smectic layering. In the case of a smectic A, those points are located on the vertical axis whereas they lie at an angle in the case of a tilted smectic such as a monodomain smectic C.

1.5 Applications

1.5.1 Liquid Crystal Displays

Since the discovery of electro-optical effects in liquid crystals in about 1968, their main applications have been in the display technology [53]. The first device that could be used industrially is the Twisted Nematic device (see Figure 1.8).

This device uses a liquid crystal sandwiched between two electrically conductive glass plates rubbed so as to induce a planar surface arrangement. This cell is placed between crossed polarizers. The direction of rubbing on the glass plates is made parallel to the local polarizing direction, thus inducing a twist of 90° from the top to the bottom of the cell. Due to the optical anisotropy of the liquid crystal, the direction of polarization of the light in the cell is twisted (following the director,) as a result of which the light is transmitted through the analyzer. This correspond to a light cell.

Upon application of an electric field **E** between the glass plates, the molecules reorient to be approximately parallel to **E**; in this state, the polarization of the light is left unchanged by the liquid crystal molecules and therefore no light can be transmitted. This corresponds to the dark state.

The TN cell is mostly used in the wrist-watch type of display [54] and can employ different types of compound [55, 56], the most simple of which is the 5CB. In order to meet the requirements for more sophisticated displays, such as those used in cellular phones or laptop computers, more advanced display cell have been designed. The first such improvement is the Supertwisted Nematic Cell (STN). This is a direct refinement of the TN cell but with more advanced mesogens allowing a twist of 270° instead of 90°. This results in a sharper and faster transition between the light and dark states.

Further refinements have been achieved by improving the addressing of the display's individual pixels. This lead to the development of the active matrix TFT display which are, to date, the most used screens for laptop computers.

The current trend is towards the development of bistable displays [57, 58, 1] where,

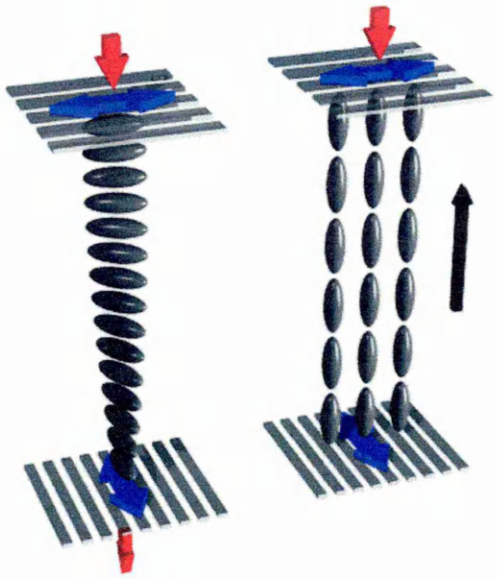

Figure 1.8 : Schematic representation of the Twisted Nematic display cell. The 'on' state without applied field is shown on the left and the 'off' state with applied electric field represented by the black arrow is shown on the right.

by having two stable arrangements corresponding to the light and dark states of the cell, the electric field no longer needs to be applied to maintain the dark state. Rather an electric pulse is used to switch the cell. The main advantages of such display are their much reduced power consumption, which is of crucial importance in portable devices. Additionally, such displays can be used as optical storage devices. Further developments in this area include tristable nematics displays, which, have the potential to yield extremely versatile functionality [59].

1.5.2 Other applications.

There are numerous applications for liquid crystals other than display. In laser optics, for instance, a laser can produce grid patterns in a nematic phase which, in turn, can be used as switches for another laser. Polymer dispersed liquid crystal (PDLC) sheet can be formed into big panels which, upon application of an electric field, can be made opaque or transparent. A rather versatile bathroom window can be produced that way, as shown in [9].

Liquid crystals have also been proposed for applications in engineering [60, 61, 62] that exploit the variation of the viscosity coefficients of mesogens in different phases. This may lead to the development of very efficient lubricants or bearings which can act as breaks if their temperature exceeds some threshold.

Finally, one possibly surprising area for the application of liquid crystal science is the human body itself, but many living cells and viruses display and utilise liquid crystalline prospectives [63].

Chapter 2

Computer simulations of liquid crystals

Introduction

Computer simulations act as a link between theory and experiment. Experimental analysis is limited in that, usually, only bulk averaged properties are measurable meanwhile, the complicated nature of mesogens and their interaction potentials prevents the possibility of a full theoretical treatment capable of predicting the phase behaviour of real mesogens. These limitations can be resolved using computer simulations, where, by using a model interaction in an appropriately designed 'computer experiment', full molecular insight into the system can be gained. Using the results of statistical mechanics, macroscopic properties can be computed which, in turn, can be used to test the theories from which the model originated. The validity of the model can, thus, be checked against experimental results. Computer simulations can also act as predictive tools in the design of novel compounds or for the study of systems under conditions that can only be attained in the laboratory with great difficulty and cost.

The first part of this Chapter contains a description of the two main methods used in the simulations of liquid crystals at a molecular scale, namely the Monte Carlo method and Molecular dynamics. Following this, previous work on the computer

simulation of liquid crystals is reviewed. Here attention is concentrated on generic hard particles and Gay-Berne models, and their extension to treat flexoelectric behaviour. The Chapter then concludes with a review of progress on the simulation of confined liquid crystalline systems and their anchoring properties.

2.1 Molecular modeling techniques.

2.1.1 The Monte Carlo Method

The Monte Carlo (MC) method is used to find the solution of mathematical problems using a probabilistic approach and is currently applied to a wide variety of different problems. According to Hammersley and Handscomb, " Monte Carlo methods comprise of that branch of experimental mathematics which is concerned with experiments on random numbers" [64]. In the molecular physics of liquid crystals, the term Monte Carlo usually refers to the specific sampling method as proposed by Metropolis *et al.* [65].

The Metropolis solution.

Considering a system of N particles in the canonical (constant NVT) ensemble and assuming pairwise interactions between the particles ; the total potential $\mathcal{V}$ is given by [11] :

$$\mathcal{V} = \sum_{i \neq j}^{N} U(\mathbf{X}(i), \mathbf{X}(j)) \quad i, j \in [1 \ldots N] \tag{2.1}$$

where $\mathbf{X}$ is the complete set of positions, orientations and momenta of the system. In this canonical ensemble, a time independent configurational property can be obtained from :

$$\langle \mathcal{A} \rangle_{\text{real}} = \int \rho_{\text{NVT}}(\mathbf{X}) \mathcal{A}(\mathbf{X}) d\mathbf{X}^N \tag{2.2}$$

with :

$$\rho_{\text{NVT}} = \frac{e^{-\beta \mathcal{V}}}{Q_{\text{NVT}}} \tag{2.3}$$

Q_{NVT}, being the partition function for the canonical ensemble. If the system is ergotic, $\langle \mathcal{A} \rangle_{\mathrm{real}}$ can be obtained by averaging its instantaneous values over a sufficient number of uncorrelated state points, $\mathbf{\Gamma}_i$, provided that they appear with a probability proportional to the probability density of the considered ensemble. Therefore :

$$< \mathcal{A} >_{\mathrm{real}} = \frac{1}{M} \sum_{i=1}^{M} \mathcal{A}_i \tag{2.4}$$

Metropolis *et al.* designed a stochastic process for creating such a sequence of state points in the canonical ensemble where each configuration $\mathbf{\Gamma}_i$ appears with a probability $e^{-\beta \mathcal{V}}$. This sequence corresponds to a discrete Markov chain, that is a stochastic sequence of states within each step of which memory extends only to the preceeding state [66].

The theory of discrete Markov chains [33] shows that the probability, ρ_b, that the system evolves from state a to state b is given by :

$$\rho_b = \rho_a \pi_{ab}, \tag{2.5}$$

where π_{ab} is the transition matrix. Intuitively the properties of π_{ab} read :

$$\pi_{ab} \geq 0 \tag{2.6}$$

$$\sum_b \pi_{ab} = 1. \tag{2.7}$$

Also the condition of microscopic reversibility requires that the probability of going from state b to a is equal to that of the reverse transition and, therefore :

$$\rho_a \pi_{ab} = \rho_b \pi_{ba}. \tag{2.8}$$

The transition matrix for the system under consideration is not directly available, however the limiting distribution ρ_∞ is known to be the probability density of the canonical ensemble (ρ_{NVT}), that is :

$$\rho_\infty = \rho_{\mathrm{NVT}}(\mathbf{\Gamma}_\infty) \tag{2.9}$$

$$= \frac{1}{Q_{\mathrm{NVT}}} e^{-\beta \mathcal{V}(\mathbf{\Gamma})}. \tag{2.10}$$

The scheme introduced by Metropolis *et al.* allows the construction of an appropriate phase space trajectory which obeys Equations 2.7 and 2.8.

In its most basic form, the Metropolis method considers a two dimensional system of N atoms (with straightforward extension to three dimensions.) Phase space is sampled by choosing one particle i at random and assigning it a new random position within a square of arbitrary size centered on the particle's old position. The move is accepted if it is downhill in energy ($\delta\mathcal{V}_{ab} = \mathcal{V}_b - \mathcal{V}_a \leq 0$). If, however, the move is uphill in energy ($\delta\mathcal{V}_{ab} > 0$), then the move is accepted with a probability $e^{-\beta\delta\mathcal{V}_{ab}}$. This is performed by generating a random number $\xi \in [0:1]$. The move is accepted if $\xi \leq e^{-\beta\delta\mathcal{V}_{ab}}$ and rejected otherwise. This sequence of particle choosing-moving is then repeated until a sufficient number of uncorrelated moves are achieved.

The method can be extended to three dimensional systems of non spherical and even non rigid molecules where new states are created by changing the positions and the orientations of the molecules [66]. A summary of the Monte Carlo algorithm in the canonical ensemble is given on Figure 2.1.
According to the nature of the system studied, other moves have been used such as reptation moves [67] or flip moves [2]. Similarly Monte Carlo simulation of flexible molecules can be achieved by moving sub-molecular segments independently. As a result for more advanced systems, one Monte Carlo move is composed of several different type of molecular moves (change in orientation, position, flip, reptation etc.). If at any Monte Carlo step, different combination of molecular moves are performed, the use of a given move type should be probabilistic so as to keep the Markov chain stochastic [66].

1. Choose a particle i at random

2. Assign a new random position and orientation

3. **if** $(\delta\mathcal{V}_{ab} \leq 0)$ **OR** $(\xi \leq e^{-\beta\delta\mathcal{V}_{ab}})$

   Accept move

   else

   Reject move

4. Store instantaneous observable.

5. Return to step 1 until n_{step} performed.

6. Compute observable average .

Figure 2.1 : The Monte Carlo algorithm in the canonical ensemble

Extension to the isothermal-isobaric ensemble.

The Metropolis solution was first applied in the canonical ensemble, but it can readily be extended to other ensembles such as the isothermal-isobaric as proposed by Wood [68]. The extension of the MC method into another ensemble requires knowledge of its probability density ρ_{ens}. For the isothermal-isobaric ensemble, this is :

$$\rho_{\text{NPT}} = \frac{1}{Q_{\text{NPT}}} e^{-\beta(\mathcal{V}(\Gamma)+PV)} \tag{2.11}$$

where P represents the pressure and V the volume. The implementation of the MC method in this alternative ensemble requires the generation of a Markov chain with a state probability proportional to $e^{-\beta(\mathcal{V}(\Gamma)+PV)}$. This is achieved using a similar algorithm to that for the canonical ensemble, the difference being that volume changes are performed in order to keep the pressure constant. Because of the computational overhead associated with volume changes, they are typically attempted with a frequency of once every n sweeps (*i.e.* n attempted move per particle) where n is typically $\in [1 : 10]$. Volume changes are assessed by testing

the variation in enthalpy δH [66] given by :

$$\delta H_{ab} = \delta \mathcal{V}_{ab} + P(V_b - V_a) - \frac{N}{\beta} \ln \left(\frac{V_b}{V_a} \right). \tag{2.12}$$

A given volume change move is accepted if $\delta H_{ab} \leq 0$ or $\xi \leq e^{-\beta \delta H_{ab}}$ and rejected otherwise.

Several methods can be used to generate the volume changes. One of these involves generating a random change in volume (δV,) computing the corresponding changes in box lengths and rescaling the particle coordinates accordingly. However this imposes the constraint that the simulation box remain cubic and involves changing, simultaneously, the lengths of all three box sides. Another scheme is to change every box length independently by choosing a box dimension randomly and assigning it a new length using a random variation. This method allows the box shape to change and, if necessary, adapt to the nature of the phase of the system under study.

2.1.2 Generating random orientations

The generation of new random orientations is not a trivial exercise as can be the generation of new random positions. Here two methods for the generation of random orientations are described, namely the Barker-Watts method and the so called Local Frame method.

The problem

The aim is to generate a new orientation $\hat{\mathbf{u}}_n$ given an initial orientation $\hat{\mathbf{u}}_o$ so that the distribution of possible trial orientations is uniform in a portion of the unit sphere delimited by a chosen boundary.

The orientation vectors $\hat{\mathbf{u}}$ are defined according to θ and ϕ, respectively, the zenithal and azimuthal Euler angles :

$$\hat{\mathbf{u}} = \begin{pmatrix} u_x \\ u_y \\ u_z \end{pmatrix} = \begin{pmatrix} \cos\phi \sin\theta \\ \sin\phi \sin\theta \\ \cos\theta \end{pmatrix} \tag{2.13}$$

with :

$$\begin{aligned} \theta &\in [0 : \pi] \\ \phi &\in [-\pi : \pi] \end{aligned}$$

The generation of $\hat{\mathbf{u}}_n$ is performed so that :

$$\theta_n = \theta_o + \delta\theta \tag{2.14}$$

$$\phi_n = \phi_o + \delta\phi \tag{2.15}$$

Where $\delta\theta$ and $\delta\phi$ are random angular displacement defined by the limiting conditions :

$$\begin{aligned} \delta\theta &\in [0 : \theta_{\max}] \\ \delta\phi &\in [-\pi : \pi] \end{aligned}$$

It can be shown that the direct generation of $\delta\theta$ as :

$$\theta_n = \theta_o + (2\xi_\theta - 1)\delta\theta_{\max}$$

leads to non-uniform distribution of $\delta\theta$, in conflict with the MC move acceptance criterion [66]. Rather, random $\cos\theta$ should be generated as :

$$\cos\theta_n = \cos\theta_o + (2\xi_\theta - 1)\delta(\cos\theta_{\max})$$

The Barker Watts method

The so called Barker Watts method [69] has been proposed as a fast method for generating random orientation. In Monte Carlo codes, orientation vectors are best represented by unit vectors rather than by explicitely stating the Euler angles. The Barker-Watts method allows the generation of random orientations without the

computational overhead associated with the use of trigonometric functions. With this method a new orientation is generated as :

$$\hat{\mathbf{u}}_n = \mathbf{A}_\alpha \hat{\mathbf{u}}_o \tag{2.16}$$

where $\mathbf{A}_\alpha$ is one of the rotation matrices $\mathbf{A}_x, \mathbf{A}_y, \mathbf{A}_z$, chosen at random :

$$\mathbf{A}_x = \begin{pmatrix} 1 & 0 & 0 \\ 0 & \cos\theta^R & \sin\theta^R \\ 0 & -\sin\theta^R & \cos\theta^R \end{pmatrix} \tag{2.17}$$

$$\mathbf{A}_y = \begin{pmatrix} \cos\theta^R & 0 & -\sin\theta^R \\ 0 & 1 & 0 \\ \sin\theta^R & 0 & \cos\theta^R \end{pmatrix} \tag{2.18}$$

$$\mathbf{A}_z = \begin{pmatrix} \cos\theta^R & \sin\theta^R & 0 \\ -\sin\theta^R & \cos\theta^R & 0 \\ 0 & 0 & 1 \end{pmatrix} \tag{2.19}$$

and θ^R is a random angle so that $\theta^R \in [0 : \theta_{\max}]$.

This method has the advantage of being very fast, but also presents some possible drawbacks. If $\delta\theta_{\max} = \pi$, the generation of 2.10^6 $\hat{\mathbf{u}}_n$ with $\hat{\mathbf{u}}_o = \hat{\mathbf{z}}$ shows that only a small portion of the unit sphere is available (see Figure 2.2(a).) This does not usually prevent good phase space sampling in the Monte Carlo sequence as the particles follow Brownian motion and, thus, $\hat{\mathbf{u}}_o$ is not constant. Therefore if $\hat{\mathbf{u}}_n$ at step $t+1$ is created using $\hat{\mathbf{u}}_n$ from step t, the full unit sphere is available (see Figure 2.2(b).) This behaviour can, however, raise some problems in simulations with very low acceptance rates or where the director is aligned to a fixed direction by, *e.g.*, a surface interaction or applied field.

The Local Frame method

The Local Frame method has been designed in order to provide a method which samples the full unit sphere at every step if $\delta\theta_{max} = \pi$. The principle here is to generate a random orientation $\hat{\mathbf{u}}_n^{f'}$ in the molecular frame f' which is transformed

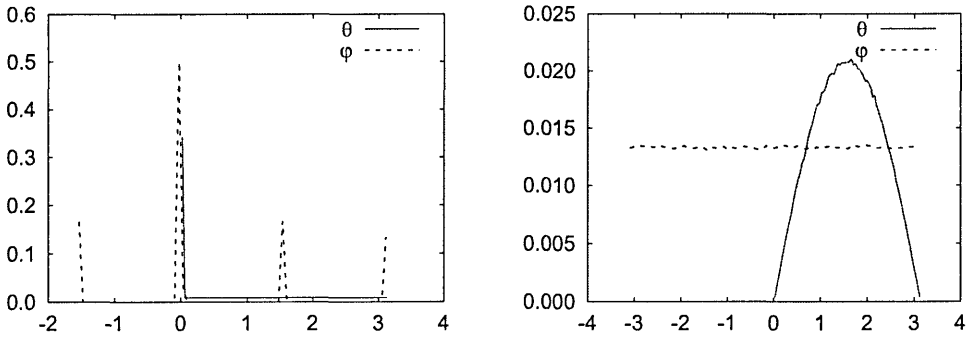

(a) $\hat{\mathbf{u}}_o^{(t)} = (0,0,1)$ (b) $\hat{\mathbf{u}}_o^{(t)} = \hat{\mathbf{u}}_n^{(t-1)}$

Figure 2.2 : Distribution of the Euler angles for generated random configuration using the Barker-Watts method. The Figure on the left corresponds to a generation with constant $\hat{\mathbf{u}}_o$ and the Figure on the right to a distribution using changing input orientations.

into $\hat{\mathbf{u}}_n^f$ in the laboratory frame f using an appropriate rotation matrix.
$\hat{\mathbf{u}}_n^{f'}$ is given by :

$$\hat{\mathbf{u}}_n^{f'} = \begin{pmatrix} \cos\phi_R \sin\theta_R \\ \sin\phi_R \sin\theta_R \\ \cos\theta_R \end{pmatrix} \tag{2.20}$$

with :

$$\cos\theta_R = 1 - \xi_\theta(1 - (\cos\theta_{\max})) \tag{2.21}$$

$$\phi_R = (2\xi_\phi - 1)\pi \tag{2.22}$$

and where ξ_θ and ξ_ϕ are random numbers in $[0 : 1]$. The transformation of $\hat{\mathbf{u}}_n^{f'}$ into $\hat{\mathbf{u}}_n^f$ is given by :

$$\hat{\mathbf{u}}_n^f = \mathbf{R}_T^{-1}\hat{\mathbf{u}}_n^{f'} \tag{2.23}$$

where $\mathbf{R}_T$ is the rotation matrix that transforms a vector $\hat{\mathbf{u}}$ from $\mathbf{u} = (\cos\phi\sin\theta$,-$\sin\phi\sin\theta, \cos\theta)$ in f to $\hat{\mathbf{u}} = (0,0,1)$ in f'. In a right handed coordinate system, this transformation is a rotation of ϕ about $\hat{\mathbf{z}}$ followed by a rotation of θ about $\hat{\mathbf{y}}$

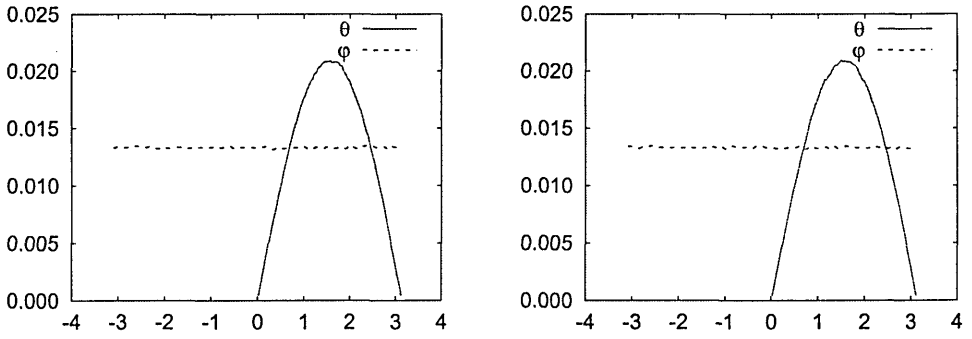

(a) $\hat{\mathbf{u}}_o^{(t)} = (0, 0, 1)$ (b) $\hat{\mathbf{u}}_o^{(t)} = \hat{\mathbf{u}}_n^{(t-1)}$

Figure 2.3 : Distribution of the Euler angles for generated random configuration using the Local-Frame method. The Figure on the left corresponds to a generation with constant $\hat{\mathbf{u}}_o$ and the Figure on the right to a distribution using changing input orientations.

thus :

$$\mathbf{R}_T = \mathbf{R}_{\theta,\mathrm{y}}\mathbf{R}_{\phi,\mathrm{z}} \tag{2.24}$$

$$\mathbf{R}_T = \begin{pmatrix} \cos\theta & 0 & -\sin\theta \\ 0 & 1 & 0 \\ \sin\theta & 0 & \cos\theta \end{pmatrix} \cdot \begin{pmatrix} \cos\phi & \sin\phi & 0 \\ -\sin\phi & \cos\phi & 0 \\ 0 & 0 & 1 \end{pmatrix} \tag{2.25}$$

$$\mathbf{R}_T = \begin{pmatrix} \cos\theta\cos\phi & \cos\theta\sin\phi & -\sin\theta \\ -\sin\phi & \cos\phi & 0 \\ \sin\theta\cos\phi & \sin\theta\sin\phi & \cos\theta \end{pmatrix} \tag{2.26}$$

and therefore :

$$\mathbf{R}_T^{-1} = \begin{pmatrix} \cos\phi\cos\theta & -\sin\phi & \cos\phi\sin\theta \\ \sin\phi\cos\theta & \cos\phi & \sin\phi\sin\theta \\ -\sin\theta & 0 & \cos\theta \end{pmatrix} \tag{2.27}$$

If $\theta_{\max} = \pi$, this method allows one to sample from the full unit sphere at every random generation (see Figure 2.3) ; however it presents the drawback of being slower than the Barker-Watts method. As a result the latter is still preferentially

used for Monte Carlo simulations with s sufficiently high acceptance rate. The Local Frame method, on the other hand, shows its strength in the generation of random initial configurations or for simulations where acceptable phase space sampling requires the use of simulation parameters inducing a low acceptance rate.

2.1.3 Molecular Dynamics

The Molecular Dynamics (MD) method was introduced by Alder and Wainwright in 1959 [70] in an attempt to describe the time evolution of fluids at a molecular level ; at the time only the Monte Carlo method was available for the task. The technique involves solving the simultaneous Newtonian (spherical molecules) or the combined Newtonian-Euler (non-spherical molecules) equations of motion for all particles in the system over a finite (and usually short) time. The method is based on the statistical mechanics result that an ensemble average of a given property $\mathcal{A}_{\text{real}}$ of an ergotic system can be obtained from the time average of its instantaneous values as :

$$\begin{aligned} \mathcal{A}_{\text{real}} &= \langle \mathcal{A}(\mathbf{X}(t)) \rangle_{\text{time}} \\ &= \frac{1}{t_{obs}} \int_0^{t_{obs}} \mathcal{A}(\mathbf{X}(t))\, dt \end{aligned} \tag{2.28}$$

where $\mathbf{X}(t)$ describes the set of positional and orientational coordinates of the N particles system at a time t. The general algorithm of the Molecular Dynamics method is described on Figure 2.4.

With this process, the method used to calculate the force field is of critical importance as it governs the equilibrium behaviour of the model. Solving the equations of motion is also the most time consuming part of the whole algorithm. Several algorithms have been developed for the optimization of this task, the most common of which are the original Verlet algorithm [71], the so called 'leap-frog' algorithm [72] and the velocity-Verlet algorithm [73]. The success of these lies in their time efficiency and ease of implementation.

1. Create an initial configuration.
2. Calculate the forces on each particle.
3. Update the particles positions and velocities to the current time step.
4. Calculate the instantaneous properties.
5. Return to step 2 until n time steps performed.
6. Compute the time average properties.

Figure 2.4 : The Molecular Dynamics algorithm.

The advantage of the MD technique is that it allows the study of transport properties of particles and, therefore, renders possible the study of relaxation phenomena, which cannot be addressed using the Monte Carlo method.

One difficulty that arises with Molecular Dynamics is that when faced with systems having both short and long time scale oscillations, the time step employed must be small enough to capture the high frequency behaviour ; nevertheless, the total run length is required to be sufficient to allow the system to exhibit long time scales phenomena. This problem is very common in the study of polymers, and biological systems.

Also it should be noted that Molecular Dynamics requires the use of a differentiable model, as the forces and torques are derived from gradient of the intermolecular potential [66]. This said, discontinuous potentials, such as the square well potential [70, 74] have been used in MD simulations. In these case, the whole algorithm needs to be re-cast so as to consider binary collisions rather than fixed time steps. With more complicated non-differentiable models, however, the MD method cannot be used.

2.2 Molecular models of Liquid Crystals

At a molecular scale, a first approximation of the shape of liquid crystals molecules would be a rod or a disc for, respectively, calamitic and discotic mesogens. Using such objects, interacting through appropriate intermolecular potentials, provides an excellent testbed for theories on the origins of liquid crystals phases. Two types of particles are commonly used. Hard particles models have their basis in Onsager theory, which shows that short range repulsive interactions alone can lead to the formation of liquid crystal phases such as the nematic phase. A refinement of these models is to incorporate the attractive forces which are responsible for the more sophisticated mesophases. Section 2.2.1 discuss the first type of models while the effects of attractive forces for the most popular soft model, namely the Gay-Berne model, are presented in Section 2.2.2.

2.2.1 Hard particle models.

Hard ellipsoids of revolution

The structure of simple atomic fluids can be described efficiently and surprisingly accurately using hard sphere models. The most obvious extension of this result that incorporate the anisotropy of mesogens is to represent the particles by hard ellipsoids of revolution (HER) with semi axes $a = b \neq c$. For this model, the length to width ratio k is defined by $k = \frac{a}{c}$. Also both discotic and calamitic particles can be modeled according to the value of k. Although spherocylinders were used in Onsager's treatment, the HER can be expected to follow the Onsager solution as it can be shown that for both shapes, the expression for the excluded volume of a pair of particles as a function of their relative orientation α takes the form $V_{\text{excl}} \sim \sin\alpha\ \alpha$ [39].

The main drawback of the HER model is that the contact distance between two ellipsoids can not be expressed in a closed form. The first Monte Carlo simulation of this model was performed on a two dimensional system by Vieillard-Baron in the early 1970's [37]. This work gave the first algorithm for the contact distance

between two ellipses and showed that excluded volume effects play an important role in mesophase formation. However, limitations in computer power prevented Vieillard-Baron from establishing the behaviour of three dimensional systems. The contact distance computation algorithm was later refined by Perram *et al.* [75, 76] and a tentative phase diagram for three dimensional systems was proposed by Frenkel *et al.* [38]. This showed the existence of four different phases namely isotropic, nematic, plastic crystal and ordered crystal. A more thorough investigation by Frenkel and Mulder [39] established the range of stability of those phases; more specifically nematic phases were found for $k \geq 2.75$, the transition density reducing with increased molecular elongation. Comparison of those results with the y-expansion density functional theory where the free energy expansion was cut at the third term [42] showed good agreement for $\frac{1}{3} \leq k \leq 3$; a worsening of the theoretical predictions was found with more extreme k values, however.
Despite the argument from Zarragoicoecha *et al.* [77] that the stability of the nematic phase for $k = 3$ is an artifact of the limited system size employed by Frenkel *et al.* simulations, subsequent work by Allen and Mason [78] for several system sizes confirmed the validity of the phase diagram proposed by Frenkel *et al.* An extension of this phase diagram was later proposed by Camp *et al.* [79] who computed of the exact location of the isotropic-nematic phase transition using Gibbs-Duhem integration techniques.

Studies by Allen *et al.* [80, 81] of a biaxial version of the hard ellipsoid model ($a \neq b \neq c$) for $\frac{c}{a} = 10$ and $1 \leq \frac{b}{a} \leq 10$ showed the existence of isotropic, nematic, discotic nematic and biaxial phases. Again, the exact location of the isotropic-nematic and isotropic-discotic nematic phase transitions were computed using Gibbs-Duhem integration methods.
The extensive studies performed on this model have established a comprehensive and very precise phase diagram as a function of molecular elongation. The range of stability of the different phases can be summarized as :

- plastic solid : $k \in [\frac{1}{1.25} : 1.25]$

- ordered solid : $k \in [\frac{1}{2} : 2]$
- discotic nematic : $k \leq \frac{1}{2.75}$
- nematic : $k \geq \frac{1}{2.75}$

The major conclusion that can be drawn from these results is that Onsager's solution applied at the intermediate values $k \sim 3 - 5$ corresponding to the elongation of common mesogens.

Hard spherocylinders.

Another very popular model for calamitic liquid crystals is the hard spherocylinder (HSC). This is the model used by Onsager, that is a cylinder of length L and diameter D terminated by two hemispherical caps of diameter D. The elongation k of such an object is therefore $k = \frac{L+D}{D}$. The reasons for the use of this model are threefold. First it is the shape used in Onsager's theory and therefore the most obvious choice to make when testing this theory using computer simulations. Also for computational purposes, the model presents the advantage of having a tractable expression for the contact distance. Finally the spherocylinder shape resembles closely that of the liquid-crystal-phase-forming tobacco virus [82, 83]. There is, however, no obvious extension of this model to discotic particles ; equivalence could be considered using cut spheres [84] or sort cylindrical segments [85]

The first computer simulation on hard spherocylinders was performed by Vieillard-Baron [86] using elongations $k = 2$ and 3, but this study did not find any stable nematic phases. Limitations in computer power prevented the author from fully investigating a system with $k = 6$. In 1987, Frenkel [87, 88] performed the first simulations of three dimensional systems of hard spherocylinders with elongation $k \in [0 : 5]$ and free translation and rotation; the authors found the model to exhibit three phases, namely : isotropic liquid, nematic and smectic A. With the shorter elongation $k = 3$, Veerman and Frenkel [89] found the nematic and smectic phases to become respectively unstable and metastable. A more complete phase

diagram was later proposed by Mc Grother *et al.* [90] for different values of k in the range [3 : 5] and confirmed the results from Frenkel *et al.* The authors also showed that as k was increased, the smectic A phase was stable for $\frac{L}{D} \geq 3.2$ whereas the nematic phase required $\frac{L}{D} \sim 4$. Bolhuis and Frenkel [91] later refined and completed this phase diagram into the Onsager limit.

From these studies the phase diagram of the HSC can be summarized as :

- Nematic : $\frac{L}{D} \geq 3.7$.
- Smectic A : $\frac{L}{D} \geq 3.1$.

2.2.2 The Gay-Berne model.

Despite their simplicity and their success in modeling liquid crystalline phases, the steric models discussed above have limitations in that they can not be used to model every liquid crystalline phase (*e.g.* smectic B) and the effect of attractive interactions can not be studied.

The first mathematically tractable model for soft particles was developed in 1972 by Berne and Pechukas [92]. This model describes the interaction between soft ellipsoidal particles through a potential $\mathcal{V}^{BP}$ which is alternately repulsive and attractive at short and long ranges. This potential however presented unrealistic features such as having equal well depths for end to end and side by side parallel molecular arrangements. These deficiencies were resolved by Gay and Berne [93] who modified the functional form of the Berne-Pechukas potential so that it could give a reasonable fit to a linear arrangement of four Lennard-Jones sites. This resulted in the now widely used Gay-Berne model $\mathcal{V}^{GB}$ expressed as :

$$\begin{aligned} \mathcal{V}^{GB} &= 4\epsilon(\hat{\mathbf{u}}_i, \hat{\mathbf{u}}_j, \hat{\mathbf{r}}_{ij}) \left\{ R^{12} - R^6 \right\} \\ \text{with } R &= \frac{\sigma_0}{r - \sigma(\hat{\mathbf{u}}_i, \hat{\mathbf{u}}_j, \mathbf{r}_{ij}) + \sigma_0}. \end{aligned} \tag{2.29}$$

Where $\sigma(\hat{\mathbf{u}}_i, \hat{\mathbf{u}}_j, \mathbf{r}_{ij})$ is the shape function for two Gaussian ellipsoids, as deter-

mined originally by Berne and Pechukas [92],

$$\sigma(\hat{\mathbf{u}}_i, \hat{\mathbf{u}}_j, \mathbf{r}_{ij}) = \sigma_0 \left\{ 1 - \frac{1}{2}\chi \left[\frac{(\hat{\mathbf{r}}_{ij} \cdot \hat{\mathbf{u}}_i + \hat{\mathbf{r}}_{ij} \cdot \hat{\mathbf{u}}_j)^2}{1 + \chi(\hat{\mathbf{u}}_i \cdot \hat{\mathbf{u}}_j)} + \frac{(\hat{\mathbf{r}}_{ij} \cdot \hat{\mathbf{u}}_i - \hat{\mathbf{r}}_{ij} \cdot \hat{\mathbf{u}}_j)^2}{1 - \chi(\hat{\mathbf{u}}_i \cdot \hat{\mathbf{u}}_j)} \right] \right\}^{-\frac{1}{2}} \tag{2.30}$$

σ_0 defines the unit of distance and χ is the shape anisotropy parameter defined using k the length to breadth ratio as :

$$\chi = \frac{k^2 - 1}{k^2 + 1}. \tag{2.31}$$

The energy strength parameter is defined as :

$$\epsilon(\hat{\mathbf{u}}_i, \hat{\mathbf{u}}_j, \hat{\mathbf{r}}_{ij}) = \epsilon_0 \epsilon_1^{\nu}(\hat{\mathbf{u}}_i, \hat{\mathbf{u}}_j) \epsilon_2^{\mu}(\hat{\mathbf{u}}_j, \hat{\mathbf{u}}_j, \hat{\mathbf{r}}_{ij}) \tag{2.32}$$

with :

$$\epsilon_1(\hat{\mathbf{u}}_i, \hat{\mathbf{u}}_j) = \left[1 - \chi^2 (\hat{\mathbf{u}}_i \cdot \hat{\mathbf{u}}_j)^2 \right]^{-\frac{1}{2}} \tag{2.33}$$

and

$$\epsilon_2(\hat{\mathbf{u}}_i, \hat{\mathbf{u}}_j, \hat{\mathbf{r}}_{ij}) = 1 - \frac{1}{2}\chi' \left[\frac{(\hat{\mathbf{r}}_{ij} \cdot \hat{\mathbf{u}}_i + \hat{\mathbf{r}}_{ij} \cdot \hat{\mathbf{u}}_j)^2}{1 + \chi'(\hat{\mathbf{u}}_i \cdot \hat{\mathbf{u}}_j)} + \frac{(\hat{\mathbf{r}}_{ij} \cdot \hat{\mathbf{u}}_i - \hat{\mathbf{r}}_{ij} \cdot \hat{\mathbf{u}}_j)^2}{1 - \chi'(\hat{\mathbf{u}}_i \cdot \hat{\mathbf{u}}_j)} \right]. \tag{2.34}$$

Here χ' is the energy anisotropy parameter defined using k' the ratio of end to end and side by side well depth (ϵ_{ee} and ϵ_{ss} respectively) :

$$\begin{aligned} \chi' &= \frac{k'^{\mu^{-1}} - 1}{k'^{\mu^{-1}} + 1} \\ k' &= \frac{\epsilon_{ee}}{\epsilon_{ss}} \end{aligned} \tag{2.35}$$

The Gay-Berne model behaviour can be easily tuned through modification of the four parameters k, k', μ and ν.

Preliminary simulation results by Adam *et al.* [94], using the parameterisation $GB(k, k', \nu, \mu) = GB(3, 5, 1, 2)$, showed the Gay-Berne model to be suitable for liquid crystal modeling as both isotropic and nematic phases were observed. Subsequent work by Luckhurst and Stephens [95] using the slightly different parameterisation $GB(3, 5, 2, 1)$ found a much richer phase diagram containing isotropic, nematic, smectic A, smectic B and crystal phases. Thanks to a very thorough study by the Seville group [96, 97, 98], the full liquid crystalline phase diagram of

the model was then determined for $GB(3,5,1,2)$.

The parameterisation $GB(3,5,3,1)$ was used by other groups [99, 100]; while this gives the same isotropic, nematic and smectic phases as the previous parameterisation, the increased value of μ allows for a wider nematic region.

The substantially different parameterisation $GB(4.4, 39.6^{-1}, 0.74, 0.8)$ was used by Luckhurst and Simmonds [101] in an attempt to use a model better fitted to representing real mesogens. This parameterisation was obtained from fitting the Gay-Berne potential to a uniaxial version of a realistic potential of the p-terphenyl molecule. The authors found a phase behaviour compatible with their aim; the model displayed isotropic, nematic and smectic phases. Subsequently, Bates and Luckhurst [102] performed a thorough study using the parameterisation $GB(4.4, 20^{-1}, 1, 1)$ and found the model to exhibit isotropic, nematic, smectic A and smectic B phases in good agreement with the behaviour of the real mesogens this parameterisation was modeling. An investigation into the generic effects of the attractive part of the potential [103] showed that smectic order is favoured as k' is increased, thus showing the importance of attractive forces for the formation of smectic phases by ellipsoidal particles. A similar study into the effects of molecular elongation on the Gay-Berne phase diagram [104] showed significant changes notably in the location of the isotropic-nematic phase transition.

More recently, various extensions of the Gay-Berne model have been performed. Cleaver *et al.* [105] generalised the potential to give an interaction for particles with different elongations thus opening up the possibility of modeling LC mixtures. Zewdie [106, 107] developed a Corner-like potential where the range and energy strength parameters are expanded in terms of a complete orthogonal basis set, namely Stone [108] functions. The advantage of this method is that each term in the energy strength parameter can be associated with a given type of interaction thus allowing fine tuning of the model. Application of this approach to the modeling of discotic particles [106] lead to the formation of isotropic, discotic-nematic, columnar and crystal phases while the modeling of calamitic particles (using an

equivalent of $GB(3,5,1,2)$) showed isotropic, nematic, smectic A, smectic B and crystal phases in agreement with [94].

Biaxial particles have been studied by the Bologna group [109, 110] using a generalization of the Gay-Berne potential to the interaction between two arbitrary ellipsoidal particles presented in [111]. These studies have indicated that the answer to the much argued about question of the existence of biaxial phases is that, such phases can exist since both biaxial nematic and smectic phases have been observed.

The inclusion of dipole electrostatic moments into Gay-Berne particles has been studied by Houssa *et al.* [112, 113] and revealed that although the location of the phase transitions of the model are insensitive to the strength of the dipoles, the electrostatic forces were found to have a considerable effect on the nature of the observed phases. multipole electrostatic moments has also been considered. Specifically, Berardi *et al.* [114] included two outboard permanent dipoles at various angles from the axis and observed tilted smectic phases whose intra-layer arrangement was compatible with Smectic I and tetragonal smectic T. The inclusion of quadrupole moments into a $GB(4,5,2,1)$ system [115] proved to have strong effects upon the smectic regions of the phase diagrams such as the replacement of a smectic B by a Smectic I phase. These developments, along with the extended possibility of parameterisation, makes, the Gay-Berne model a very versatile one which can be applied to a wide number of different types of interactions.

2.3 Modeling of flexoelectric particles

Flexoelectricity is an important property to be considered in the design of materials for use in liquid crystal devices. It has been shown, theoretically, that flexoelectricity can be used as the driver for the switching in new generation LCDs [1]. Although thoroughly studied experimentally and theoretically (see Chapter 1), computer simulation studies of flexoelectric particles are relatively scarce, mainly due to the difficulty of modeling the shape anisotropy if Meyer's principle is to

be considered. Models showing ferroelectric behaviour, have, however been well studied [116, 117].

One attempt at modeling flexoelectric particles was performed by Neal *et al.* [118] in their study of molecules formed from rigid assemblies of three Gay-Berne sites. One of these models was a triangular arrangement of parallel particles whose overall shape resembled that of a pear. This system exhibited an isotropic to smectic ordering transition in which the particles adopted anti-parallel orientations in adjacent layers. A subsequent attempt at modeling pear shaped particles was performed by Stelzer *et al.* [30] using Gay-Berne sites to one end of each was connected a Lennard-Jones sphere. Isotropic, nematic and smectic phases were found for this model. The computation of the flexoelectric coefficients gave a non-zero splay coefficient and, within error estimates, a zero bend coefficient in accordance with Meyer's theory. Subsequent simulations by Billeter and Pelcovits [31], using a slightly different energy parameterisation and a different method for the computation of the flexoelectric coefficient showed results in agreement with [30].
Berardi *et al.* [2] subsequently developed a single-site potential for pear shaped particles using Zewdie's Stone expansion approach [106, 107]. This study was rather successful as this computationally efficient model showed isotropic, nematic and smectic phases, the latter two of which, upon application of an appropriate energy parameterisation, exhibited net polar order. Further details regarding this potential are provided in Chapter 6

2.4 Liquid crystals in confined geometries

The behaviour of nematic liquid crystals close to a confining substrate is of fundamental importance for liquid crystal display design [53]. This has lead to many experimentalist studies into the interfacial properties of confined liquid crystals [119, 120]. These types of systems have also been well studied theoretically

using a wealth of different techniques such as van der Waals theory [121], density functional theory [122, 123] and mean field approximation [124]. Comparatively, the number of molecular computer simulations of confined liquid crystal systems is rather small.

From the wealth of experimental data available, it is clear that the confinement of liquid crystals breaks the symmetry of the confined fluid by inducing two main effects [125] namely positional layering and orientational ordering through a mechanism called *anchoring.*

The first effect is a universal consequence of confinement and has been observed by Schoen [126, 127] through computer simulations of atomic (*i.e.* Lennard-Jones) fluids. On the other, hand surface-induced orientational order is specific to molecules with shape anisotropy such as mesogens. For these particles, several surface arrangements can be observed according to the particles' orientations with respect to the substrate as shown on Figure 2.5. These arrangement are homeotropic, planar and tilted with respectively $\theta = 0$, $\frac{\pi}{2}$ and $\in]0 : \frac{\pi}{2}[$, where θ is the angle between the surface normal and the mean particle orientation. Further details regarding variations on these three basic types of surface ordering (*i.e.* monostable, multistable and degenerate) are given in [125]. The surface energy, or anchoring energy f_S is commonly taken to be related to θ_S, the angle between the surface director and the natural anchoring angle, by $f_s = \frac{1}{2} W_0 \sin^2(\theta_S)$ [125, 128] where W_0 is the anchoring strength and measures the ease with which the director can deviate from the imposed anchoring direction.

Early computer simulation studies of confined liquid crystalline systems used the Lebwohl-Lasher lattice based models [129, 130] and were successful in describing the enhanced order found in interfacial regions and shifts in the location of the isotropic-nematic transition due to the confinement. However the very nature of such a lattice model introduces limitations, particularly its neglect of surface induced layering.

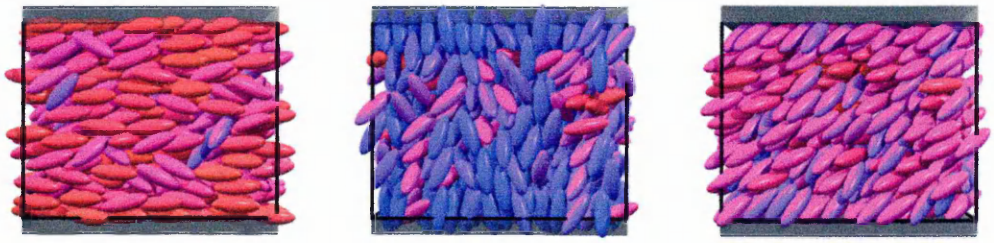

(a) Planar (b) Homeotropic (c) Tilted

Figure 2.5 : Illustration of the three main surface arrangements. The substrates are represented by the gray semi-transparent thick lines.

Subsequently, Chalam *et al.* [96] used the Monte Carlo technique on a system of confined Gay-Berne particles using a separable form for the particle-surface potential. This study confirmed the behaviour seen in lattice simulations, showing a shift of the isotropic-nematic transition to higher temperatures due to the stabilization of the liquid crystalline phases by the substrate. However the use of a surface potential which was separable into spacial and angular parts meant that the shape of the particles was not properly taken into account. This was remedied by Zhang *et al.* [131] who used the same molecular model with a separable substrate potential and observed tilted layers at the surface. Wall and Cleaver [132], using a modified surface potential, extended this study so as to include the effect of changing temperature and phase. Another modification of this surface potential, involving azimuthal coupling, was used by Latham and Cleaver [133] in systems of confined mixtures of Gay-Berne particles. In these studies the alterations to the surface potential were restricted to the well-depth anisotropy term, whereas the shape function of the potential was always that for the interaction between a Gaussian ellipsoid and a sphere.

Although it has been shown that, in a confined system, the bulk orientation is often determined by the orientational distribution of the surface particles [131], some

authors have found rather different behaviour. Gruhn and Schoen [134, 135, 136] studied very thin films of Gay-Berne particles in a slab geometry confined between surfaces of rigidly fixed atoms; upon changing the thickness of the film, the orientation of bulk region particles was found to change regularly from planar to homeotropic. Another example of this kind of behaviour is provided by the work of Palermo *et al.* [137] who observed abrupt changes in particle orientation when moving from the surface to the bulk regions in systems of Gay-Berne particles absorbed at graphite surfaces.

Simulations of confined hard particles have also been performed. Allen [128] used a system of hard ellipsoid with elongation $k = 15$ confined so that their centres of mass interacted sterically with smooth substrates. A homeotropic substrate arrangement was observed. Subsequently van Roij *et al.* [138, 139, 140] used hard spherocylinders confined between a hard smooth wall and an isotropic liquid crystal and observed surface induced wetting and planar ordering. These studies also showed that the planar arrangement is the natural state of hard-rod nematic phase in contact with a flat surface and when surface absorption is not made possible. Chrzanowska *et al.* and Cleaver *et al.* [141, 142] used the Hard Gaussian Overlap (HGO) model (*i.e.* a hard version of the Gay-Berne model) in symmetric and hybrid anchored films using the Hard Needle Wall (HNW) potential as a surface model. Simulations of symmetrically anchored systems showed that appropriate tuning of the HNW potential lead the preferred surface arrangement to switch between planar and homeotropic. Hybrid anchored systems exhibited a discontinuous transition from bent-director (or HAN) to uniform director arrangements as the anchoring coefficients of the surfaces were made sufficiently different. This result was consistent with experimental observations [143] of 5CB molecules spun cast onto silicon wafers which were subject to planar anchoring at the solid substrate and homeotropic anchoring at the free surface. Upon increasing the film thickness from a few molecular lengths to more than 20 nm, the molecules which first formed small islands proved able to form a stable film at increased thick-

nesses since they were then able to adopt a bent-director. A similar result was shown theoretically by Šarlah and Žumer [144] that is, very thin films with hybrid anchoring do not show a bent-director structure.

Realistic simulations of confined molecules have also been performed. Cleaver and Tildesley [145] have performed energy minimisations on systems of 8CB molecules, represented by an assembly of 22 spherical sites, absorbed on either a smooth or graphite planar substrates. They found that strips of 50 molecules formed structures almost fully compatible with scanning tunneling microscopy (STM) observations. Later, Yoneya and Iwakabe [146] performed molecular dynamics simulations on systems of 8 molecules of 8CB anchored on graphite and initially arranged in the structures shown by the STM experiment. However, due to the small system size used and the lack of periodic boundary conditions, these arrangements proved to be unstable. These limitations were later removed by Cleaver *et al.* [147] who studied periodic systems of monolayers of 8CB and 10CB molecules anchored on graphite using energy minimisation and molecular dynamics techniques. The findings of this study showed structures fully consistent with the STM observations. A more systematic series of simulations was conducted by Binger and Hanna [148, 149, 150] who performed realistic molecular dynamics and molecular mechanics simulations of various liquid crystals molecules (*e.g.* 5CB, 8CB, MBF). Systems ranging from single molecules up to two monolayers anchored on different polymeric substrates (*e.g.* PE, PVA, Nylon 6) were investigated. The authors found that for most substrates, the molecules adopt planar arrangements with specific favoured conformations. In the most recent of these studies [150] the atoms of the substrate were replaced by a pseudo potential which had the combined effects of saving computer power and making the substrate model more generic. The results from this last set of simulations proved to be very encouraging as they were fully consistent with previous results despite the increased simulation speed.

2.5 Anchoring Transitions

The study of confined liquid crystalline systems has shown that different particle-substrate interactions can lead to various types of surface anchoring. A number of experimental studies have reported that, upon changing some of the experimental conditions (*i.e.* temperature, structure of the aligning agent), transitions between two surface arrangements can be observed which leads to a change in the bulk alignment. Transitions which meet these requirements are called *anchoring transitions.* However, even in studies where the surface induced structural changes have been thoroughly studied, the mechanisms underlying these anchoring transitions remain relatively unexplained. From the many experimental studies reporting anchoring transitions, it can be deduced that a concensus about the origins of these transitions is still lacking since a number of different mechanisms have been proposed to explain the origins of anchoring transitions.

The first observed anchoring transitions were temperature driven [151, 152] ; other authors have shown that anchoring transitions can be obtained by a change in the conformation of the surface aligning agent [153, 154]. Light can also induce anchoring transitions by changing the structure of the substrate molecules (*e.g.* light induced cis-trans isomerization) and, therefore, the particle-substrate interaction [155]. This is a feature that can be exploited in optical storage devices. The absorption behaviour of a liquid crystal on the substrate [156, 157] or of volatile molecule on the liquid crystal substrate interface [119] can also lead to anchoring transitions if the amount of absorbed particles or the nature of the absorption is changed. One last mechanism is the memory effect whereby a multistable anchoring system can preferentially adopt one of its possible anchoring states due to the history of the sample [125, 158].

Although a number of mechanisms underlying anchoring transitions are in principle known (see [159] for a review) very few theoretical analyses have been performed. Teixeira and Sluckin [160, 161] used a Landau-de Gennes free energy

functional to study the planar to homeotropic anchoring transition in systems of liquid crystals confined by different substrates. They found a rich anchoring behaviour, despite a number of simplifications that had to be made, which helped in the identification of the possible mechanisms responsible for anchoring transition; in this case, the compositions of binary mixtures of liquid crystals and the amount of adsorption at the surface. Subsequently Teixeira *et al.* [162] used a Landau-de Gennes formalism to observe a temperature driven anchoring transition at the interface between a liquid crystal and smooth solid surface, thus confirming the experimental findings.

The effect of non-uniform substrates (*i.e.* microtextured) has been studied by Qian and Sheng [163, 164] using a Landau-de Gennes formalism. They show that the effect of the substrate is to induce temperature dependent tilt angles separated by phase transitions.

The literature on computer simulations of anchoring transition is extremely scarce. Cleaver and Teixeira [142] have studied systems of hard Gaussian overlap particles confined in a slab geometry and interacting with smooth substrates via the hard needle wall potential. There, adsorption phenomena induced an homeotropic to planar anchoring transition as the surface potential parameterisation was changed. More details into similar systems can be found in Chapter 4. Another simulation study of an anchoring transition was that of Lange and Schmid [165, 166, 167] who observed an anchoring transition between tilted and homeotropic arrangements in a system of ellipsoidal Gay-Berne confined by grafted polymer chains (made of Gay-Berne ellipsoids) as the grafting density was changed.

Chapter 3

Computer simulations of Hard Gaussian Overlaps

Introduction

In the previous Chapter it was shown that the Gay-Berne potential is one of the most versatile molecular models for liquid crystal simulations. Depending on the chosen shape and energy parameterisation, it can be used to model many liquid crystalline phases. However, when the nematic phase only is of interest, the use of hard particle models is a preferable option, being computationally easier and faster to implement than the soft models. Also hard particles have proven to be a very good test-bed for perturbation theories.

In this Chapter the computer simulation of such a model, the hard Gaussian overlap (HGO) model is discussed. First a literature review of the computer simulations and theoretical work performed on this model is provided. The techniques used for the computation of the most relevant observables in computer simulations are then presented. Finally, some preliminary results from bulk simulations of prolate and oblate HGO particles are presented. A comparison with existing results for calamitic molecules is also included.

3.1 The Hard Gaussian Overlap Model.

The HGO model is a steric model in which the contact distance is the shape parameter determined by Berne and Pechukas [92]. The HGO model can be seen as an equivalent of the Gay-Berne model stripped of its attractive interactions. The hard Gaussian overlap potential $\mathcal{V}^{\text{HGO}}$ between two particles i and j with respective orientations $\hat{\mathbf{u}}_i$ and uj and intermolecular vector $\mathbf{r}_{ij} = r_{ij}\hat{\mathbf{r}}_{ij}$ is defined as :

$$\mathcal{V}^{\text{HGO}} = \begin{cases} 0 & \text{if} \quad r_{ij} \geq \sigma(\hat{\mathbf{u}}_i, \hat{\mathbf{u}}_j, \mathbf{r}_{ij}) \\ \infty & \text{if} \quad r_{ij} < \sigma(\hat{\mathbf{u}}_i, \hat{\mathbf{u}}_j, \mathbf{r}_{ij}) \end{cases} \tag{3.1}$$

where $\sigma(\hat{\mathbf{u}}_i, \hat{\mathbf{u}}_j, \mathbf{r}_{ij})$ is the contact distance :

$$\sigma(\hat{\mathbf{u}}_i, \hat{\mathbf{u}}_j, \mathbf{r}_{ij}) = \sigma_0 \left\{ 1 - \frac{1}{2}\chi \left[\frac{(\hat{\mathbf{r}}_{ij} \cdot \hat{\mathbf{u}}_i + \hat{\mathbf{r}}_{ij} \cdot \hat{\mathbf{u}}_j)^2}{1 + \chi(\hat{\mathbf{u}}_i \cdot \hat{\mathbf{u}}_j)} + \frac{(\hat{\mathbf{r}}_{ij} \cdot \hat{\mathbf{u}}_i - \hat{\mathbf{r}}_{ij} \cdot \hat{\mathbf{u}}_j)^2}{1 - \chi(\hat{\mathbf{u}}_i \cdot \hat{\mathbf{u}}_j)} \right] \right\}^{-\frac{1}{2}}. \tag{3.2}$$

Here σ_0 is the unit of distance and χ is the shape anisotropy parameter defined using k the length to breadth ratio as :

$$\chi = \frac{k^2 - 1}{k^2 + 1} \tag{3.3}$$

Although this model was originally derived using geometrical considerations, the hard Gaussian overlap molecule can not be represented by a solid shape [168], rather it is a mathematical abstraction of an interaction surface between two non-spherical objects. The shape of an HGO molecule can, however, be taken to be very close to that of an ellipsoid of revolution. For example one can assume the contact distance of the interactions between two ellipsoids and two HGOs in the arrangements shown in Figure 3.1. The two models agree for end to end and side by side configurations. However, in the case of a T-geometry, the HGO contact distance is $\sigma = \frac{\sigma_0}{(1-\chi)^{\frac{1}{2}}}$ rather than $\frac{\sigma}{2} = \sigma_0(1+k)$ for the hard ellipsoid of revolution (HER) model. Due to this similarity, the volume of an HGO molecule is often taken to be that of the equivalent ellipsoid [168, 169], that is :

$$V_{\text{HGO}} = \frac{\pi}{6} k \sigma_0^3. \tag{3.4}$$

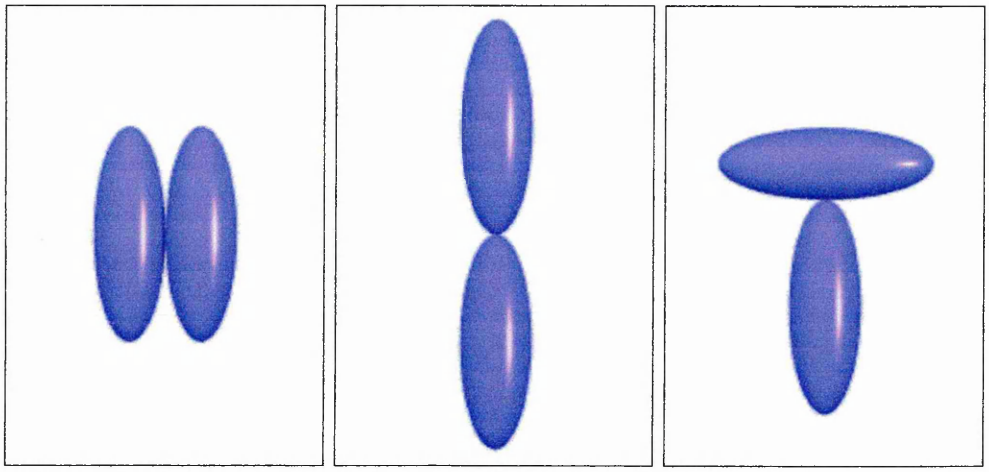

(a) $\sigma_{\mathrm{HGO}} = \sigma_{\mathrm{HER}} = \sigma_0$ (b) $\sigma_{\mathrm{HGO}} = \sigma_{\mathrm{HER}} = \sigma_0 k$ (c) $\sigma_{\mathrm{HGO}} = \frac{\sigma_0}{(1-\chi)^{\frac{1}{2}}}$ $\sigma_{\mathrm{HER}} = \frac{\sigma_0}{2}(1+k)$

Figure 3.1 : Comparison between the contact distances for the HGO and HER models.

A more comprehensive comparison between the HGO and HER models has been performed by Bhethanabotla and Steele [170] who computed the virial coefficients B_2 to B_5 for both models with $k \in [1.5 : 3.0]$. They found that the differences between equivalent coefficients of the two models are insignificant for this range of elongation. Since the HGO model is computationally cheaper than the HER would, and, due to the similarities just outlined, a similar phase diagram is to be expected for both models. This explains for the HGO model being increasingly used.

An extensive amount of theoretical work has been performed on the HGO fluid through which the model's virial coefficients [171, 170, 168] and equation of state [172, 173] have been obtained. The first molecular simulation of the HGO fluid were performed by Padilla and Velasco [36] on systems of $N = 256$ and 512 particles with elongation $k = 3$ and 5 using the Monte Carlo method in the isothermal-isobaric ensemble. Here the authors found both isotropic and nematic phases, the transition densities and pressures (ρ^*, P^*) being approximately $(0.295, 4.5)$ for $k = 3$ and $(0.116, 0.88)$ for $k = 5$. This work was later refined by

de Miguel and Martín del Río [169] who accurately located the isotropic-nematic transition regions for systems of $N = 500$ molecules with $k \in [3 : 10]$. Comparison of these results with the transition properties of the HER showed quantitative differences which have been explained to be a consequence of the larger excluded volume of a pair of HGO.

The latest study on the HGO fluid was performed by de Miguel and Martín del Río [174] where the equation of state of the model was computed and compared to several theoretical approaches ; the best agreement being found with the Parsons-Lee density functional theory.

3.2 Observables computation.

In this Section, the computational details are given for the calculation of the most important observables considered in this thesis. First, the observables used for the measurement of positional order are considered, followed by those related to orientational order. This section closes on the computation of observables profiles for the study of confined systems.

3.2.1 Positional order

The radial pair distribution function : $g(r)$

The pair distribution function $g(r)$ is of great importance in the molecular simulations of fluids as it provides detailed insight into the structure of the studied phase. $g(r)$ represents the probability of finding a pair of particles i and j with an intermolecular separation r_{ij}. As a result, quantitative insight into the the nature of the studied phase (gas-liquid-solid) and the positional correlations of the particles can be obtained using $g(r)$. This function can be expressed as [66] :

$$g(r) = \frac{V}{N^2} \left\langle \sum_i \sum_{j \neq i} \delta(r - r_{ij}) \right\rangle \tag{3.5}$$

Where $\delta(r - r_{ij})$ is a function which is non zero over a given interval, V is the volume and N the number of particles.

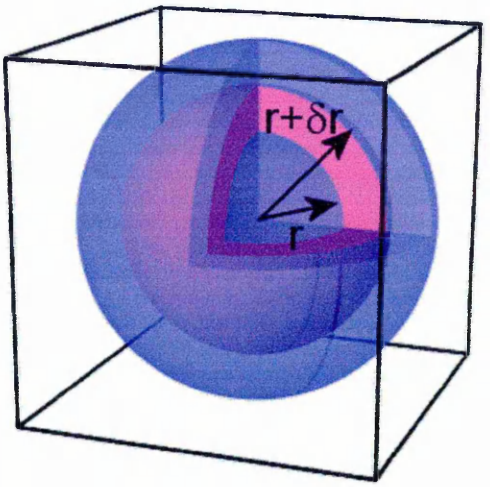

Figure 3.2 : Representation of the volume corresponding to a spherical shell between the distances r and $r + \delta r$ as used for the computation of $g(r)$. For clarity purposes, part of the volume has been excised.

Within the course of a simulation, $g(r)$ is constructed by computing an histogram of all pair separations $r_{ij} \in [r : r+\delta r]$ where $r \in [0 : \frac{L_{\min}}{2}]$ and $L_{\min}$ is the shortest simulation box length. The histogram bin heights represent the average particle occupancies in concentric spherical shells around any particle taken as the reference (see Figure 3.2). In order to obtain $g(r)$, the histogram must be normalized by the average expected occupancy of an ideal gas at the same density. This implies that the histogram bin corresponding to a distance r, must be normalized by $\rho^* V_{\text{shell}}(r)$ where ρ^* is the number density of the fluid and $V_{\text{shell}}(r)$ is the volume between two spheres of radius r and $r + \delta r$. The volume $V_{\text{shell}}(r)$ is shown on Figure 3.2 and is given by :

$$\begin{aligned} V_{\text{shell}} &= \frac{4}{3}\pi \left[(r+\delta r)^3 - r^3\right] \\ V_{\text{shell}} &= \frac{4}{3}\pi \left[(\delta r)^3 + 3r^2\delta r + 3r(\delta r)^2\right] \end{aligned} \tag{3.6}$$

To obtain of smooth functions requires the computation of an average $g(r)$ from several uncorrelated configurations. This in turns, implies that the histogram

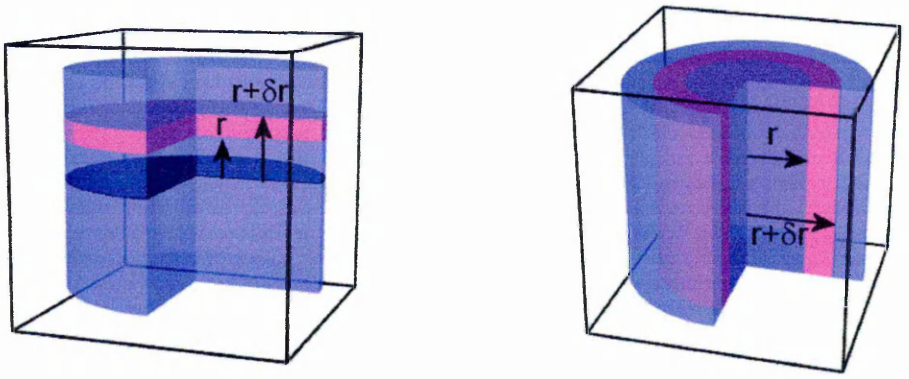

(a) $g_{\parallel}(r_{\parallel})$ (b) $g_{\perp}(r_{\perp})$

Figure 3.3 : Representation of the volumes corresponding to a cylindrical shell between the distances r and $r + \delta r$ as used for the computation of $g_{\parallel}(r_{\parallel})$(a) and $g_{\perp}(r_{\perp})$(b). For clarity purposes, part of the volume has been excised.

must also be normalized by N_{call}, the number of configurations used. Also the histogram must be normalized by N, the number of particles used so as to make it system-size independent. As a result the total normalization coefficient is given by :

$$\begin{aligned} f_{\text{norm}} &= (N N_{\text{call}} \rho^* V_{\text{shell}})^{-1} \\ f_{\text{norm}} &= (3V) \left\{ 4N^2 N_{\text{call}} \pi \left[(\delta r)^3 + 3r^2 \delta r + 3r(\delta r)^2 \right] \right\}^{-1} \end{aligned} \tag{3.7}$$

Projections of $g(r)$: $g_{\parallel}(r_{\parallel})$ and $g_{\perp}(r_{\perp})$

In the case of liquid crystalline phases, the anisotropic nature of the fluid can make it necessary to consider different distribution functions in different directions of space. For instance, the distributions functions resolved parallel and perpendicular to the director, namely $g_{\parallel}(r_{\parallel})$ and $g_{\perp}(r_{\perp})$, are of great utility in the study of smectic phases. The former measures the degree of layering in the sample while the latter measures the intra-layer positional order.

The approach used in the computation of $g_{\parallel}(r_{\parallel})$ and $g_{\perp}(r_{\perp})$ is very similar to

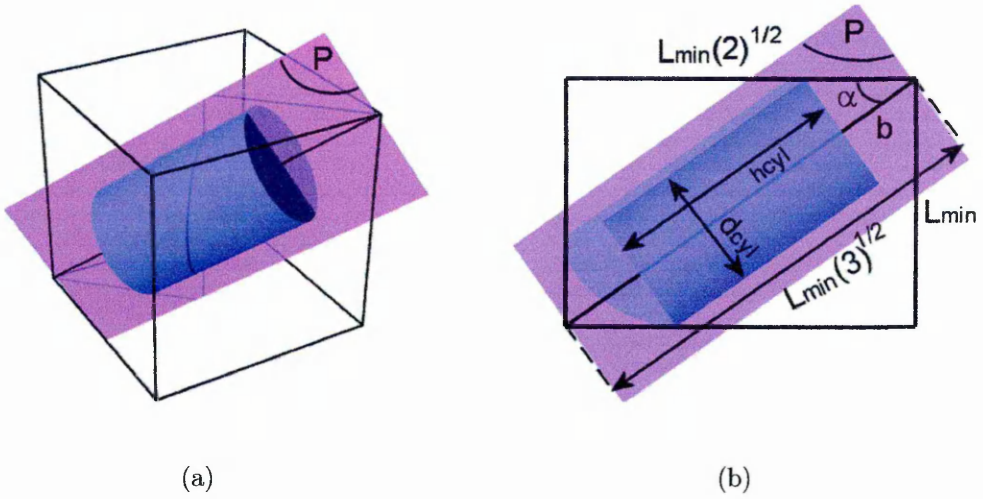

(a) (b)

Figure 3.4 : Representation of the geometry used for the calculation of the size of the cylinder used for the computation of $g_{\parallel}(r_{\parallel})$ and $g_{\perp}(r_{\perp})$. (a) shows a three dimensional view and (b) is the projection of (a) in the plane P taking $h_{\text{cyl}} = L_{\text{min}}$.

that used for $g(r)$. Here histograms of the projection of $\mathbf{r_{ij}}$ parallel ($r_{\parallel} = \hat{\mathbf{n}} \cdot \mathbf{r_{ij}}$) and perpendicular ($r_{\perp} = \sqrt{r_{ij}^2 - r_{\parallel}^2}$) to the director $\hat{\mathbf{n}}$ are considered. In order to simplify the normalization process, the histograms are computed within a cylindrical geometry as shown on Figure 3.3. Again, the histograms are normalized by $\rho^* V_{\text{shell}}$, the expected average occupancy of a shell of an ideal gas, N_{call} and N. However, because a cylinder is considered, the expression for V_{shell} is different. This is given for each of the functions as :

$$V_{\text{shell}} = \begin{cases} \pi r^2 \delta r & \text{for} \quad g_{\parallel}(r_{\parallel}) \\ h_{\text{cyl}} \pi \left[(\delta r)^2 + 2r\delta r \right] & \text{for} \quad g_{\perp}(r_{\perp}) \end{cases} \tag{3.8}$$

where h_{cyl} represents the height of the cylinder in which the computation is performed. The size of the cylinder must be chosen so as to be smaller than the simulation box but large enough to consider as wide a region as possible. The chosen method sets the cylinder height to $h_{\text{cyl}} = 0.8 L_{\text{min}}$. The cylinder radius r_{cyl} is then chosen so that the cylinder would just fit in a cubic box of size L_{min} if

$h_{\text{cyl}} = L_{\text{min}}$ (See Figure 3.4). Therefore the size of the cylinder is :

$$h_{\text{cyl}} = 0.8 L_{\text{min}} \tag{3.9}$$

$$r_{\text{cyl}} = b \tan \alpha \tag{3.10}$$

where b and α are shown on Figure 3.4 and are given by :

$$b = \frac{L_{\text{min}} \left(\sqrt{3} - 1\right)}{2}$$

$$\alpha = \arccos \sqrt{\frac{2}{3}}$$

Molecule-based projections of $g(r)$: $g_{\parallel}^{\text{mol}}(r_{\parallel})$ and $g_{\perp}^{\text{mol}}(r_{\perp})$

In ordered systems where the particles form layers which are not parallel with one another, taking the director $\hat{\mathbf{n}}$ as the reference for the computation of the pair correlation functions becomes irrelevant. Rather an alternative scheme which allows to 'follow' the layers is needed. This is obtained by the use of $g_{\parallel}^{\text{mol}}(r_{\parallel})$ and $g_{\perp}^{\text{mol}}(r_{\perp})$ which give the pair correlation functions parallel and perpendicular to the molecular orientation rather than $\hat{\mathbf{n}}$. In practice, these histograms are computed for every pair of particles i and j taking $\hat{\mathbf{u}}_i$ as the reference. $r_{\parallel}$ and $r_{\perp}$ are then defined as :

$$r_{\parallel} = \hat{\mathbf{u}}_i \cdot \mathbf{r}_{\mathbf{ij}} \tag{3.11}$$

$$r_{\perp} = \sqrt{r_{ij}^2 - r_{\parallel}^2} \tag{3.12}$$

The same cylinder geometry is used as for the computation of $g_{\parallel}^{\text{mol}}(r_{\parallel})$ and $g_{\perp}^{\text{mol}}(r_{\perp})$, the difference being that its orientation changes according to which particle i is being considered.

3.2.2 Orientational order

Nematic order parameter.

The liquid crystalline phase can be characterized partly through the long range orientational order of the molecules; this triggers the need for an appropriate order

parameter so as to quantify the degree of order in a given phase. Ideally this order parameter should have a value of zero for a phase with an isotropic distribution of molecular orientations and a value of one for a phase with perfect alignment.

Experimentally, an appropriate definition for this is the so called nematic order parameter P_2 [9] which is the average over all particles of the second order Legendre polynomial in $\cos\alpha$, where α is the angle between every molecule and the director $\hat{\mathbf{n}}$ [9].

$$P_2 = \langle P_2(\cos\alpha)\rangle_{\text{particles}} \tag{3.13}$$

$$P_2 = \left\langle \frac{3}{2}\cos^2\alpha - \frac{1}{2} \right\rangle_{\text{particles}} \tag{3.14}$$

Also, the nature of $P_2(\cos\alpha)$ involving $\cos^2\alpha$ implies that the nematic order parameter does not differentiate particles with orientations $\hat{\mathbf{u}}_i$ and $-\hat{\mathbf{u}}_i$.

Within the scope of computer simulations, the computation of P_2 and, thus, its run average $\langle P_2\rangle$is not trivial. However it can be shown [175, 176] that the problem can be reduced to the diagonalisation of the ordering matrix $Q_{\alpha\beta}$, a traceless second order tensor defined as :

$$Q_{\alpha\beta} = \frac{1}{2N}\sum_{i=1}^{N}\{3u_{i,\alpha}u_{i,\beta} - \delta_{\alpha\beta}\} \tag{3.15}$$

where $\delta_{\alpha\beta}$ is the Kroeneker function. The order parameter P_2 is defined by λ_+, the maximum Eigen value of $Q_{\alpha\beta}$ [175]. The director is, then, the Eigen vector associated with λ_+.
In a simulation, the nematic order parameter $\langle P_2\rangle$is obtained by averaging the values of P_2 obtained from a significant number of uncorrelated configurations.

Eppenga and Frenkel [175] showed that, while this method is very accurate for the description of well ordered phases, the case of the less ordered phases is more problematic, especially for small systems. Indeed, in the case of a phase with an isotropic distribution of orientations, P_2 should be zero whereas the value of the

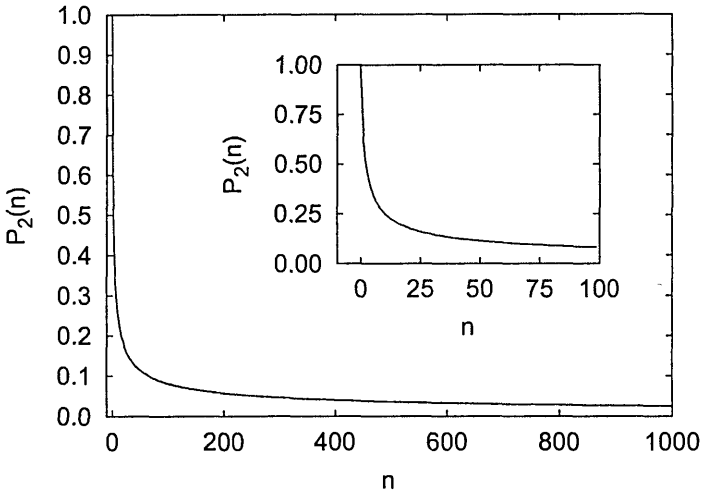

Figure 3.5 : Variation of the value of $\lambda_+(n)$ computed using the **Q** *matrix method for a system of n particles with an isotropic distribution of orientations.*

computed λ_+ decays to zero as the number of particles increases (Figure 3.5). The difference between the computed and expected values become negligible for a particle numbers $N \geq \mathcal{O}(10^3)$.

Polar order parameter.

In the case of molecules with permanent dipole moments, both the order in the system, and the direction of $\hat{\mathbf{n}}$ become important. The task of differentiating $\hat{\mathbf{u}}_i$ and $-\hat{\mathbf{u}}_i$ is achieved using the first order Legendre polynomial $P_1(\cos\alpha) = \cos\alpha$. The polar order parameter is therefore referred to as $\langle P_1 \rangle$.
The computation of $\langle P_1 \rangle$ requires the knowledge of the polar director $\hat{\mathbf{n}}_{P1} = \frac{\mathbf{n}_{P_1}}{|\mathbf{n}_{P_1}|}$ with :

$$\mathbf{n}_{P1} = \frac{1}{N}\sum_{i=1}^{N} \hat{\mathbf{u}}_i. \tag{3.16}$$

and the instantaneous value of P_1 is given by :

$$P_1 = |\mathbf{n}_{P_1}| \tag{3.17}$$

The simulation averaged polar order parameter $\langle P_1 \rangle$ is obtained by taking the average of the instantaneous P_1 values from a high enough number of uncorrelated configurations.

A low polar order parameter does not necessarily indicate a disordered phase as non-polar nematic phases usually have an equal proportion of particles with $\hat{\mathbf{u}}_i \sim \hat{\mathbf{n}}$ and $\hat{\mathbf{u}}_i \sim -\hat{\mathbf{n}}$; however a high value of P_1 does imply a high value of P_2.

3.2.3 Observables profiles

In confined systems, the presence of interfaces introduces structural changes which, for a given set of thermodynamic and surface parameters, are functions of the distance from the substrate. As a result, a great deal of insight into surface induced effects can be obtained through computation of observables profiles. Since it is common to consider the case of a slab geometry in the $\hat{\mathbf{z}}$ direction (such as that used in Chapter 4), such profiles are referred to as the z-profiles.

The computation of most profiles is very straightforward; the simulation box is divided into N_{slice} virtual slices, of width w_{slice} parallel to the substrates, in which the observables are computed independently. The computation of the profile $\mathcal{A}(z)$ of a property $\mathcal{A}$ requires the computation of $\mathcal{A}$ in each slice. $\mathcal{A}(z_0)$ is obtained by computing $\mathcal{A}$ considering only those particles whose z coordinates z_i are such that $z_i \in [z_0 - \frac{w_{\text{slice}}}{2} : z_0 + \frac{w_{\text{slice}}}{2}]$. In the course of a simulation, smooth profiles are obtained through averaging a significant number of instantaneous profiles (typically 500) obtained from uncorrelated configurations.

The most commonly computed profiles are $\rho^*_\ell(z)$ and $Q_{zz}(z)$. The former measures the variation of density across the simulation box. Its computation requires simple division of the number of particles in a given slice by the volume of that slice.

$Q_{zz}(z)$ represents the variation of the zz element of $Q_{\alpha\beta}$ across the slab. Q_{zz} measures the degree of order with respect to $\hat{\mathbf{z}}$, the surface normal. $Q_{zz} = -0.5$ for perfect order perpendicular to $\hat{\mathbf{z}}$ (planar arrangement) and $Q_{zz} = 1.0$ for perfect order parallel to $\hat{\mathbf{z}}$ (homeotropic arrangement.) Again the computation of $Q_{zz}(z)$ is straightforward as it can be performed by considering only those particles whose

centres of mass are located within the slice of interest.

In some cases however, the computation of the profiles is not straightforward. A good example is the computation of $P_2(z)$. Here, the reduced number of particles in each slice introduces a lack of accuracy of the computed profiles because of the n dependence of λ_+ as presented in Section 3.2.2. As a result, the value of P_2 in a given slice at position z_0 can not be computed simply by applying the $\mathbf{Q}$ matrix method to those particles whose centres of mass lie within the slice. Rather, $P_2(z_0)$ is computed using the approach proposed by Wall and Cleaver [132] and based on the original expression for λ_+ from [175] :

$$\lambda_+ - \frac{3\lambda_+}{4n}\left[1 + P_2^2(n-1)\right] - \frac{P_2^3}{4} - \frac{3}{4n}\left(P_2^2 - P_2^3\right) - \frac{1 - 3P_2^2 + 2P_2^3}{4n^2} \tag{3.18}$$

where λ_+ is the maximum Eigen value of $Q_{\alpha\beta}$ and P_2 denotes the true order parameter in the slice. This can be rearranged so as to give a polynomial in P_2 as :

$$aP_2^3 + bP_2^2 + cP_2 + d = 0 \tag{3.19}$$

with :

$$\begin{aligned} a &= -n^2 + 3n + 2 \\ b &= -3\lambda_+ n(n-1) - 3(n-1) \\ c &= 0 \\ d &= 4n^2\lambda_+^3 - 3n\lambda_+ - 1 \end{aligned}$$

$P_2(z_0)$ is then obtained by solving Equation 3.19 taking into account the n particles which belong to the slice centred at $z = z_0$. It should be noted that some special cases must be considered. The computation is skipped if $n = 0$ or 1 as this would lead, respectively, to a trivial solution or an incorrect value of $P_2 = 1$. In the case $n = 2$, Equation 3.19 reduces to a second order polynomial with roots $P_2 = \pm\sqrt{-\frac{d}{b}}$.

If the roots of Equation 3.19 are complex then an alternative scheme is used where $P_2 = P_2^{\text{recal}}$ with $P_2^{\text{recal}} = \lambda_+ - \langle\lambda^{\text{rd}}(n)\rangle$. Here $\langle\lambda^{\text{rd}}(n)\rangle$ is the average λ_+ obtained

from applying the $\mathbf{Q}$ matrix method to a high number (*e.g.* 10^5) of configuration of n particles with an isotropic distribution of orientations. If $P_2^{\text{recal}} < 0$ then the computation of P_2 for this slice is skipped.

3.3 Computer simulations

In this Section, results from Monte Carlo computer simulations of bulk systems of hard Gaussian overlap particles are presented. Although most of these simulations do not lead to new results (as the phase diagram of the model is already known,) they do provide a good test-bed for the simulation code used to produce the novel results given in Chapter 4 to 6.

Two sets of results are presented here. First the bulk simulation of calamitic particles is considered using two elongations $k = 3$ and 5. The phase diagrams from these simulations are compared with those extracted from the literature [36, 169] in order to validate the simulation code. Results from the simulation of discotic particles are then presented using the elongations $k = 1/3$ and $1/5$.

3.3.1 Calamitic particles

Calamitic mesogens have been simulated using the hard Gaussian overlap model in the canonical and isothermal-isobaric ensembles and in compression sequences. Systems of $N = 1000$ particles with elongation $k = 3$ and 5 were used. Typical runs consisted of 5.10^5 to 1.10^6 sweeps (*i.e.* attempted moves per particle) for both equilibration and production. The phase diagrams of the model were generated by computing $P^*(\rho^*)$ from the constant NPT runs and $\langle P_2 \rangle(\rho^*)$ from both sets of runs. Those are shown on Figure 3.6 respectively for $k = 3$ and 5.

For both elongations the $P^*(\rho^*)$ curves show a 'plateau' characteristic of a first order transition. These correspond on $\langle P_2 \rangle(\rho^*)$ to a sharp, 'S'-shaped increase in the nematic order parameter from values corresponding to an isotropic phase to those consistent with a nematic phase. Observation of the configuration snapshots

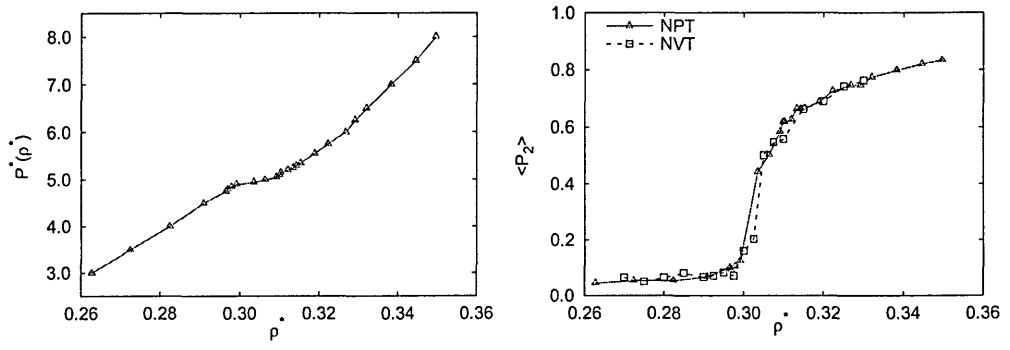

(a)

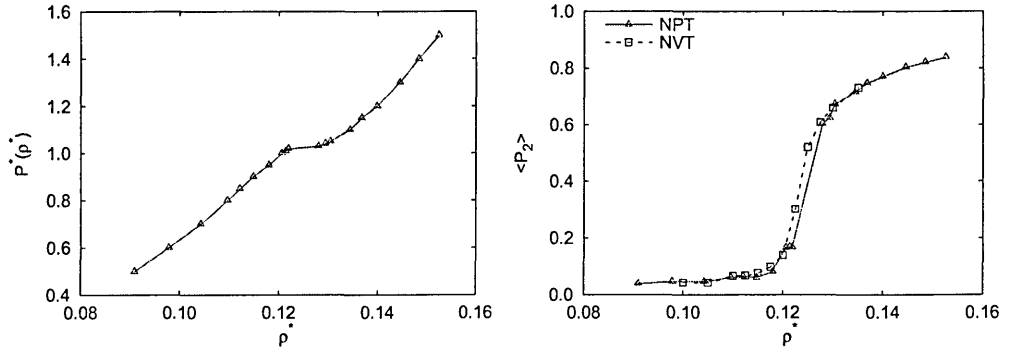

(b)

Figure 3.6 : Phase diagrams obtained from Monte Carlo simulations in the constant NPT and constant NVT ensembles of systems of $N = 1000$ hard Gaussian overlap particles with $k = 3$(a) and $k = 5$(b)

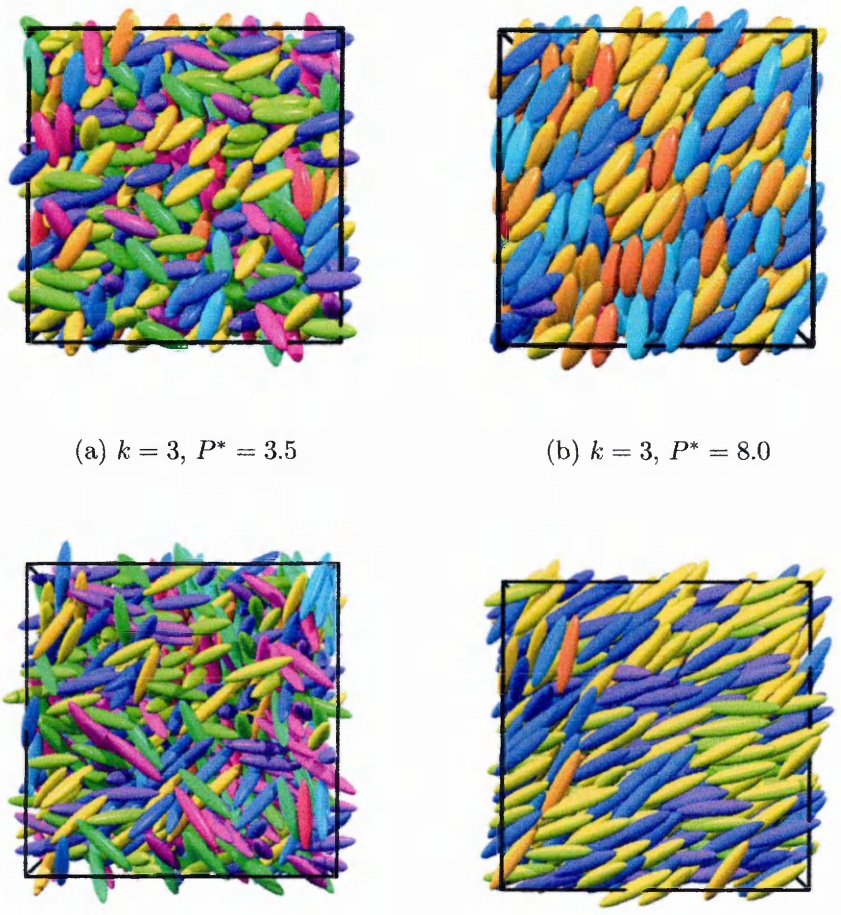

(a) $k = 3$, $P^* = 3.5$

(b) $k = 3$, $P^* = 8.0$

(c) $k = 5$, $P^* = 0.8$

(d) $k = 5$, $P^* = 1.5$

Figure 3.7 : Typical configuration snapshots obtained from constant pressure Monte Carlo simulation of systems of $N = 1000$ HGO particles with elongation $k = 3$(a,b) and 5(c,d).

Source	k	System size	P^*_{in}	ρ^*_i	ρ^*_n	$\frac{\rho^*_n - \rho^*_i}{\rho^*_i}$
[36]	3	256	4.50	0.290	0.299	0.031
[169]	3	500	4.92	0.299	0.304	0.019
this study	3	1000	4.975	0.299	0.309	0.033
[36]	5	256	0.880	0.113	0.120	0.062
[169]	5	500	0.996	0.119	0.127	0.067
this study	5	1000	1.025	0.122	0.127	0.040

Table 3.1 : Comparison of the isotropic-nematic transition data for the HGO model and $k = 3$ and 5 with existing results.

(*e.g.* Figure 3.7) confirms this. From these data P^*_{in}, the pressure at the isotropic-nematic coexistence and ρ^*_i and ρ^*_n respectively the density at coexistence of the isotropic and nematic phases can be estimated. Since the isotropic to nematic transition was not of specific interest in this thesis, those have not been determined with the great accuracy that techniques such as thermodynamic integration allow [79, 81]. Rather, ρ^*_i and ρ^*_n are taken to be the densities corresponding respectively to the beginning and end of the 'plateau' in $P^*(\rho^*)$. P^*_{in} is taken to be the average of the pressures corresponding to ρ^*_i and ρ^*_n. The coexistence data are shown in Table 3.1 along with the results from Padilla and Velasco [36] and de Miguel and Martín del Río [169] for comparison.

The comparison shows that the results obtained here are fully compatible with those obtained in [36] and [169]. The slight numerical differences can be attributed to the differences in system sizes. de Miguel [177] has already shown that the effect of increasing system sizes on the isotropic-nematic transition of system of Gay-Berne particles is to shift the transition to higher densities or lower temperatures. This shift can be observed through the shift of $\langle P_2 \rangle$and ρ^*_i and ρ^*_n to higher densities or lower temperature with increased system sizes. Another effect of system-size noticeable in de Miguel's results is a slight strengthening of the IN transition with bigger systems. The good agreement shown here validates the accuracy of the Monte Carlo simulation code used in this study.

3.3.2 Discotic particles

The Monte Carlo simulation code was subsequently applied to the modeling of discotic particles which have not been considered in the literature. These systems were simulated using methods adopted with the calamitic particles, that is using Monte Carlo simulations in the canonical and isothermal-isobaric ensembles. Systems of $N = 1000$ particles with elongations $k = 1/3$ and $1/5$ were simulated in compression sequences, using similar run lengths to those employed with the prolate elongaions. The phase diagrams obtained from these simulations are shown on Figure 3.8 for $k = 1/3$ and $k = 1/5$.

These results show a similar behaviour to that observed with the calamitic particles. Both $P^*(\rho^*)$ curves show a 'plateau' characteristic of a first order phase transition which corresponds to the typical sharp 'S'-shaped increase in $\langle P_2 \rangle(\rho^*)$ indicating an isotropic to discotic-nematic phase transition. This is further confirmed by observation of configuration snapshots, *e.g.* Figure 3.9. Despite the high pressures used here, no signs of a transition to a columnar phase have been observed. This is consistent with the lack of smectic phase for the hard Gaussian overlap model with $k > 1$.

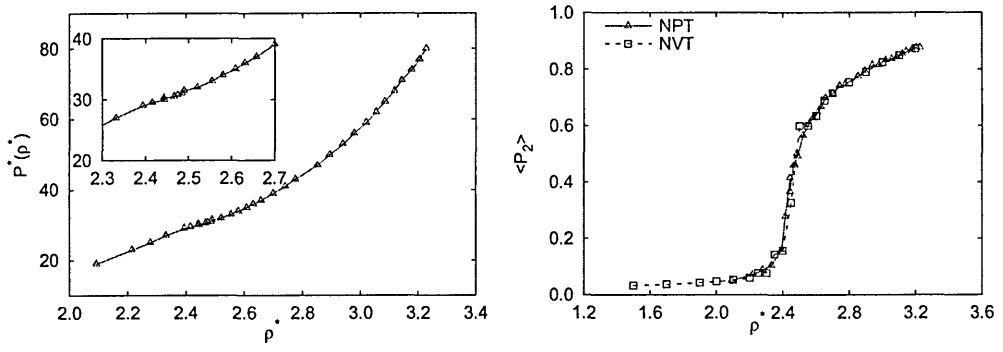

(a) $k = 1/3$

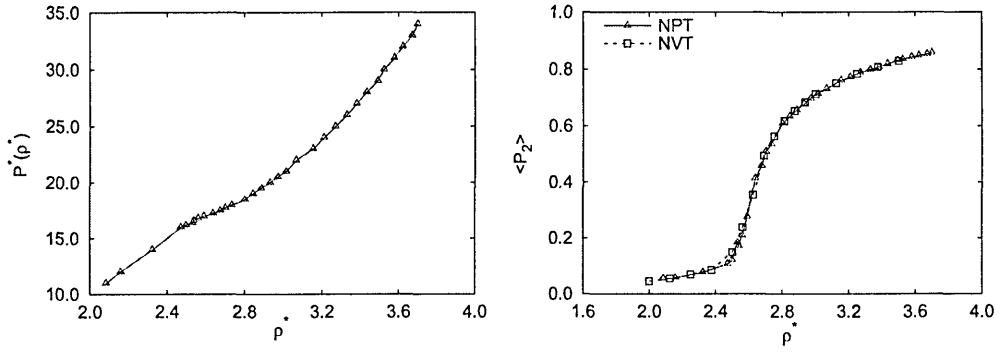

(b) $k = 1/5$

Figure 3.8 : Equation of states obtained from Monte Carlo simulations in the constant NPT and NVT ensembles of systems of $N = 1000$ hard Gaussian overlap particles with $k = 1/3$(a) and $k = 1/5$(b).

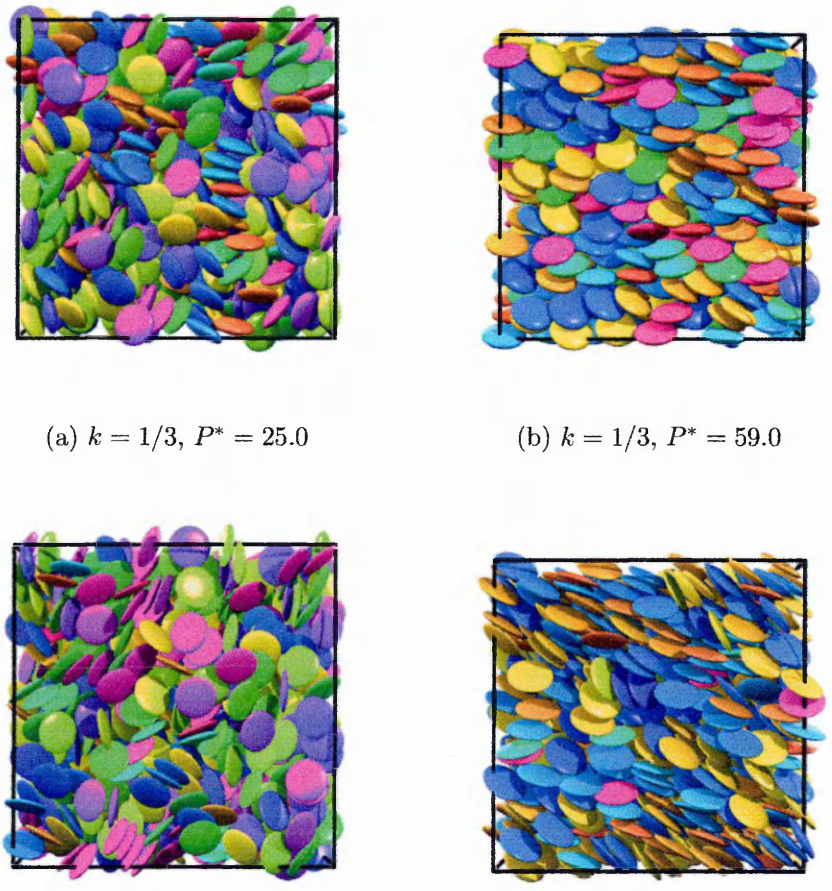

(a) $k = 1/3$, $P^* = 25.0$

(b) $k = 1/3$, $P^* = 59.0$

(c) $k = 1/5$, $P^* = 14.0$

(d) $k = 1/5$, $P^* = 30.0$

Figure 3.9 : Typical configuration snapshots obtained from constant pressure Monte Carlo simulations of systems of $N = 1000$ HGO particles with elongation $k = 1/3$(a,b) and $1/5$(c,d).

Chapter 4

Surface influence on liquid crystalline systems

Introduction

When a Liquid Crystal is placed in contact with another phase, a surface is created which breaks the symmetry of the system. There are two main effects to this symmetry breaking [125]. The first is to introduce molecular layering close to the interface while the second is to modify the surface orientational ordering in the interfacial region.

The purpose of this Chapter is twofold. First, the effects of confinement are studied on systems of ellipsoidal particles represented by the hard Gaussian overlap model and using a simple particle-surface potential, the so called Hard Needle Wall potential. The effects of varying density and particle-substrate interactions are studied.

The second aim of this Chapter is to study the anchoring transition from planar to homeotropic alignment. As very little simulation work has been performed on anchoring transitions, it is hoped that this study can shed some light on their origins. Finally, possible bistability regions in the anchoring behaviour of the models are examined.

4.1 A first surface potential

Here, surface induced structural changes are studied using ellipsoidal shaped particles interacting through the hard Gaussian overlap potential. In this Chapter all particle-surface interactions are performed using the Hard Needle Wall potential (HNW) [141] as this provides a simple and intuitive steric interaction which can be tuned so as to induce either homeotropic or planar arrangement. As a result surface induced structural changes can be studied using one model along with parameters values appropriate for both surface arrangements. Also, this potential allows the study of the transition from one arrangement to the other.

4.1.1 The Hard Needle Wall potential

With the Hard Needle Wall (HNW) potential, the particles do not interact directly with the surfaces, rather the surface interaction is achieved by a needle of length k_S placed at the centre of each particle (Figure 4.1). As a result, the HNW potential can be viewed as an extension of the potential used by Allen [128] where only the centre of mass interacts with the surface. The case considered in [128], thus, corresponds to the HNW potential with a zero needle length. The interaction potential between the needle and the surface is defined by $\mathcal{V}^{\mathrm{HNW}}$ as :

$$\mathcal{V}^{HNW} = \begin{cases} 0 & \text{if} \quad |z_i - z_0| \geq \sigma_w \\ \infty & \text{if} \quad |z_i - z_0| < \sigma_w \end{cases} \tag{4.1}$$

with :

$$\sigma_w = \frac{1}{2}\sigma_0 k_S \cos(\theta) \tag{4.2}$$

Here σ_0 defines the unit of distance, k_S is the dimensionless needle length and θ the angle between the surface normal and the particle's orientation vector, which and also corresponds to the Euler zenithal angle. The behaviour of $\sigma_w(\theta, k_S)$ is shown on Figure 4.2

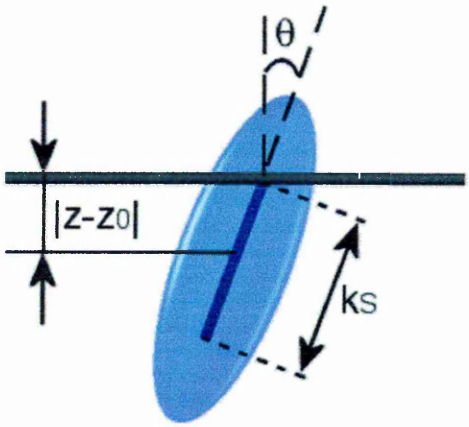

Figure 4.1 : The HNW configuration

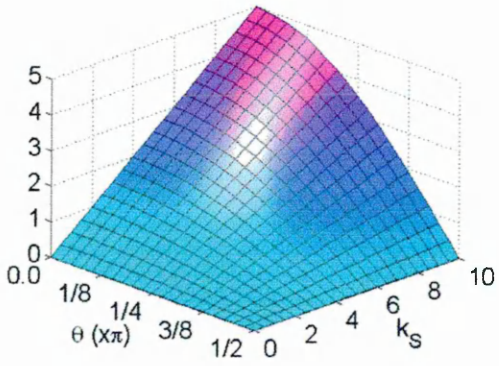

Figure 4.2 : Evolution of $\sigma_w(k_S, \cos\theta)$ for the HNW surface potential.

At high densities, this potential drives the preferred anchoring behaviour by dictating the volume of absorbed particles that can be subsumed into the surface. The only model parameter upon which the anchoring strength and angle are dependent is the needle length. According to this, there is a finite volume of any 'surface particle' that can be absorbed on the surface. The effect of this absorbed volume is to reduce the system's free energy due to the increased free volume (and, thus, entropy) it afford to rest of the system. The greater the volume absorbed, the lower the free energy. As a result the most stable surface arrangement, *i.e.* that which minimizes the free energy, is the one that maximizes the absorbed volume.

The surface behaviour of the HNW model has already been studied by Chrzanowska *et al.* [141] and Cleaver and Teixeira [142]. For small k_S, the homeotropic arrangement is most stable, whereas the planar arrangement is favored for long k_S. Some more quantitative insight into this can be obtained by studying the amount of volume that can be absorbed into the surface as a function of molecular orientation and needle length. Approximating the shape of a Gaussian ellipsoid to that of an ellipsoid of revolution [168], the volume V_e of a single particle of elongation k absorbed into the substrate as a function of k_S and θ can be obtained as described in Appendix A :

$$Ve = \frac{1}{3}\pi \left(\frac{1}{2} - \sqrt{\frac{\sigma_w^{\mathrm{HNW}}(k_S,\theta)}{k^2\cos^2\theta + \sin^2\theta}} \right)^2 \left(1 + \sqrt{\frac{\sigma_w^{HNW}(k_S,\cos\theta)}{k^2\cos^2\theta + \sin^2\theta}} \right) \tag{4.3}$$

On replacing $\sigma_w^{\mathrm{HNW}}(k_S,\theta)$ with the expression of Equation 4.2, V_e reads :

$$V_e = \frac{1}{8}\pi \left(-1 + \sqrt{\frac{k_S^2\cos^2\theta}{5+4\cos(2\theta)}} \right)^2 \left(2 + \sqrt{\frac{k_S^2\cos^2\theta}{5+4\cos(2\theta)}} \right) \tag{4.4}$$

A graphical representation of this function is given in Figure 4.3.
This shows that regardless the needle length, the absorbed volume of a single particle is maximal for $\theta = \pi/2$, suggesting that the planar arrangement should be most stable for every case. One exception is the case $k_S = 0$ where both

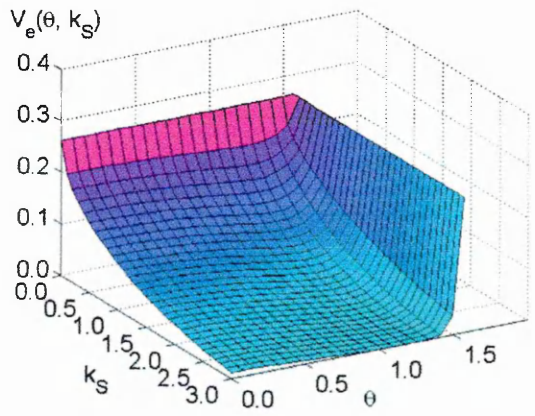

Figure 4.3 : Representation of the absorbed volume V_e of a single particle for the HNW potential as a function of k_S and θ.

planar and homeotropic arrangement allow the adsorption of an equal volume (half the ellipsoid volume.) Clearly this disagrees with the simulation results of [141, 142] where intermediate, short needle lengths also showed stable homeotropic alignment. This discrepancy can be resolved by also considering the packing behaviour of the two arrangements. This is described in the next Section.

4.1.2 Relative stability of anchoring orientations

We now consider the behaviour of a system of numerous hard Gaussian overlap molecules in a confined geometry, interacting with the surface through the HNW potential. The aim is to calculate the homeotropic to planar transition needle length for this system. Each particle close to the surface is approximated to be an ellipsoid of revolution with elongation $k = \frac{\sigma_\ell}{\sigma_0}$ and with semi axis $a = b = \frac{\sigma_0}{2}$ and $c = \frac{\sigma_\ell}{2}$. The following quantities are also defined :

- $Veps$: full volume of an ellipsoid.
- $V_P(k_S)$: volume absorbed by one ellipsoid with $\theta = \frac{\pi}{2}$
- S_P : area of the substrate occupied by one ellipsoid with $\theta = \frac{\pi}{2}$
- $V_H(k_S)$: volume absorbed by one ellipsoid with $\theta = 0$

- S_H : area of the substrate occupied by one ellipsoid with $\theta = 0$

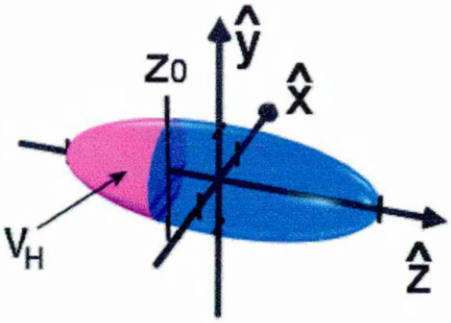

Figure 4.4 : Schematic representation of the geometry considered for the calculation of $V_H(k_S)$.

The homeotropic to planar transition can be understood by considering the ratio of the volume absorbed into the surface to the surface occupied by the particle on the substrate (*i.e.* the projection of the particle onto the substrate) for the two key arrangements. The free energy for these will be equal when the two ratios are equal. As a result, the problem of finding the anchoring transition needle length reduces to solving :

$$\frac{V_H(k_S)}{S_H} = \frac{V_P(k_S)}{S_P} \tag{4.5}$$

expression for $V_P(k_S)$ and S_P

The case of planar alignment is straightforward :

$$S_P = \frac{\pi\sigma_0\sigma_\ell}{4} \tag{4.6}$$

$$V_P = \frac{\pi\sigma_0^2\sigma_\ell}{12} \tag{4.7}$$

expression for S_H

In the case of Homeotropic arrangement, $\theta = 0 \forall k_S$. As a result, although the particle will be positioned at a different distances from the surface as a function

of k_S, the projection of the particle on to the surface is constant and thus :

$$S_H = \frac{\pi\sigma_0^2}{4} \tag{4.8}$$

expression for $V_H(k_S)$

The volume that can be absorbed if $\theta = 0$, is a function of k_S, but is not obtained trivially. The extreme cases are known :

$$\begin{aligned} V_H(0) &= \frac{Veps}{2} \\ V_H(k) &= 0 \end{aligned}$$

The set up shown in Figure 4.4 is considered where ultimately $V_H(k_S)$ corresponds to the solid volume. First an expression for V_F, the volume of a portion of an ellipsoid from the tip to a distance z_0 is required as a function of z_0. From this $V_H(k_S)$ can be identified. Starting from the equation of an ellipsoid :

$$\frac{x^2}{a^2} + \frac{y^2}{b^2} + \frac{z^2}{c^2} = 1 \tag{4.9}$$

V_F is given by ;

$$V_F = \int_{-c}^{z_0} \int_{y_{\min}}^{y_{\max}} \int_{x_{\min}}^{x_{\max}} dx.dy.dz \tag{4.10}$$

Using (4.9), the triple integral transforms to :

$$\begin{aligned} V_F &= \int_{-c}^{z_0} \int_{-\frac{b}{c}\sqrt{c^2-z_0^2}}^{\frac{b}{c}\sqrt{c^2-z_0^2}} \int_{-\frac{a}{b}\sqrt{b^2K-y^2}}^{\frac{a}{b}\sqrt{b^2K-y^2}} dx.dy.dz \qquad (4.11) \\ \text{with } K &= 1 - \frac{z^2}{c^2} \end{aligned}$$

and thus :

$$V_F = \pi ab \left[z_0 \left(1 - \frac{z_0^2}{3c^2} \right) + \frac{2c}{3} \right] \tag{4.12}$$

This expression can be checked, considering two known limits. If $z_0 = c$, $V_F = \frac{4}{3}\pi abc$ which is the full volume of an ellipsoid. If $z_0 = -c$, $V_F = 0$, again giving the expected result.

$V_H(k_S)$ can then be obtained by identification of the parameters a, b, c and z_o with the setup shown in Figure 4.4 using :

$$\begin{aligned} a &= b = \frac{\sigma_0}{2} \\ c &= \frac{\sigma_\ell}{2} \\ z_0 &= \frac{-k_S}{2} \end{aligned}$$

which leads to :

$$V_H = \frac{\pi\sigma_0^2}{4}\left[\frac{k_S}{2}\left(\frac{k_S^2}{3\sigma_\ell^2} - 1\right) + \frac{\sigma_\ell}{3}\right] \tag{4.13}$$

Transition needle length

Having obtained expressions for $V_H(k_S)$, S_H, $V_P(k_S)$ and S_P, Equation 4.5 can be solved.

$$\frac{V_H(k_S)}{S_H} = \frac{V_P(k_S)}{S_P} \tag{4.14}$$

$$\frac{1}{6k^2\sigma_0^2}k_S^3 - \frac{1}{2}k_S + \frac{\sigma_0}{3}(k-1) = 0 \tag{4.15}$$

Also, for clarity and generality purposes, the results are best expressed using the reduced needle length $k_S' = \frac{k_S}{k}$. This leads to :

$$\frac{k}{6\sigma_0^2}k_S'^3 - \frac{k}{2}k_S' + \frac{\sigma_0}{3}(k-1) = 0 \tag{4.16}$$

The transition needle length $k_S^{T\prime}$ is therefore given by the root of 4.16 satisfying $k_S^{T\prime} \in]0 : 1]$ The result is $k-$dependent, the variation of the transition $k_S^{T\prime}$ as a function of k is shown in Figure 4.5.

For the two elongations used in this study, that is $k = 3$ and 5, the transition needle length is :

$$\begin{aligned} k = 3 &: k_S^{T\prime} \sim 0.4817 \\ k = 5 &: k_S^{T\prime} \sim 0.6084 \end{aligned}$$

Thus with $k = 3$, the anchoring transition should occur for a reduced needle length of about 50% whereas with $k = 5$, the transition should occur for a reduced needle length of about 60%.

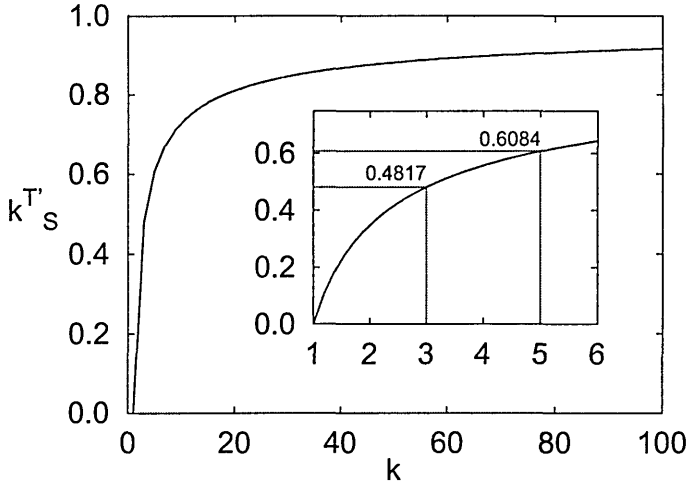

Figure 4.5 : Variation of $k_S^{T\prime}(k)$

4.2 Symmetric anchored systems

Here we present simulation results from a study of surface induced structural changes. Ellipsoidal shaped particles interacting through the hard Gaussian overlap model were considered while the HNW model was used for particle-substrate interactions. Monte Carlo simulations in the canonical ensemble of systems of $N = 1000$ particles confined in a slab geometry of height $L_z = 4\sigma_\ell$ were performed with the substrate being located on the top and bottom of the box ($z = -L_z/2$ and $z = L_z/2$); the system was periodic in the two other dimensions. The same anchoring conditions were applied on both substrates (symmetric anchoring). Using this combination of particle and surface potentials, the aims of this study were to model the main influences of confinement in liquid crystalline systems, namely surface induced layering and ordering, and to identify the influences of density and needle length on the preferred surface arrangements. In order to do so, a systematic approach has been undertaken; Figure 4.6(a) and (b) shows the state points at which the simulations have been performed as well as the direction of the simulation series. For each state points two simulations have been performed, first an equilibration simulation of $0.5.10^6$ sweeps has followed by a production run of another $0.5.10^6$ sweeps.

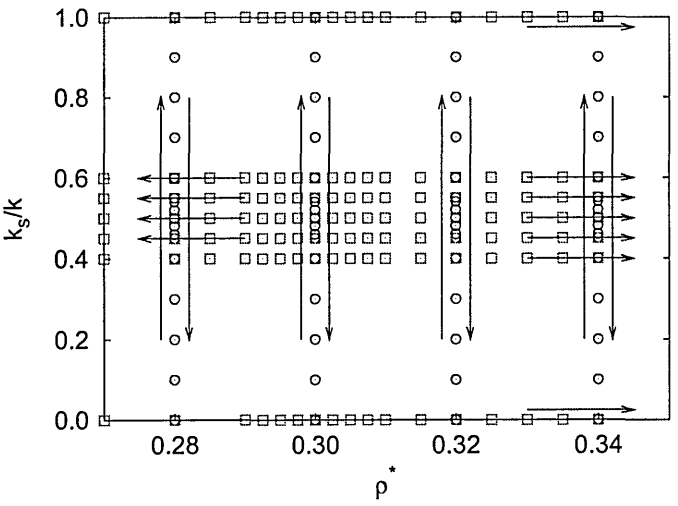

(a) $k = 3$

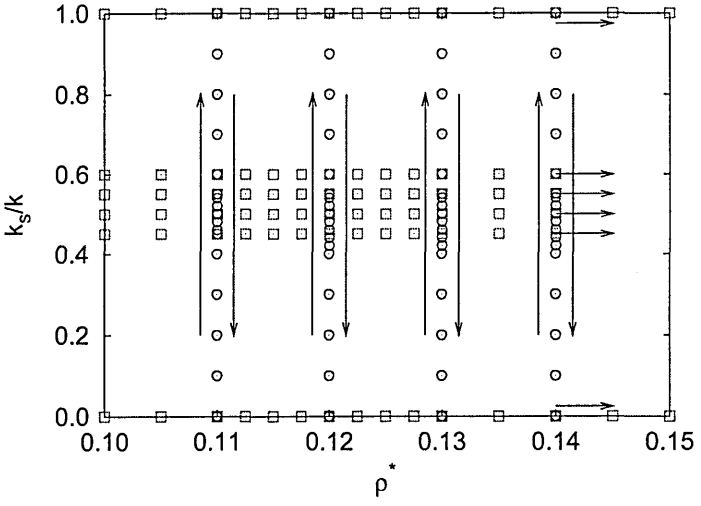

(b) $k = 5$

Figure 4.6 : Representation of the state points considered for the production of the data analysed in this Chapter.

4.2.1 Typical profiles

The first step is to understand surface induced structural changes for a set of needle lengths and densities. References [141, 142] provide some information through profiles from systems of particles with $k = 5$ and $k_S = 5$ [141] and $k_S = 2.75, 3.0$ [142]. Here a more exhaustive set of results are shown.

The study of the surface induced structural changes was performed through the computation of the z-profiles of three different observable. The density profile $\rho_\ell(z)$ provides information about the layering in the cell through the location number and height of its peaks. $Q_{zz}(z)$, provides information on the surface induced ordering with respect to the substrate normal. These two profiles can be used to characterize the type of surface anchoring adopted. $P_2(z)$ measures the degree of orientational order and, hence, the nature of the phase as a function of location in the slab.
In what follows typical profiles are presented for several needle lengths and system densities. These profiles were obtained from several series of simulations each performed with constant density and k_S either decreasing and increasing between the limits $[0 : k]$. Typical profiles are shown for densities corresponding to bulk isotropic and nematic phases. Needle lengths are chosen so as to correspond to homeotropic ($k_S < k_S^T$), competing ($k_S \sim k_S^T$), and planar arrangements ($k_S > k_S^T$).

Homeotropic anchoring

An homeotropic arrangement is observed when the orientation of the surface particles is such that $< \theta > \sim 0$, which for the HNW model occurs for short needle lengths ($k'_S \leq 0.25$). Typical profiles for this arrangement are showed on Figures 4.7 and 4.8 for, respectively, $k = 3$ and $k = 5$ using a reduced needle length $k'_S = 0.2$.

From these Figures, the surface induced structural changes associated with the

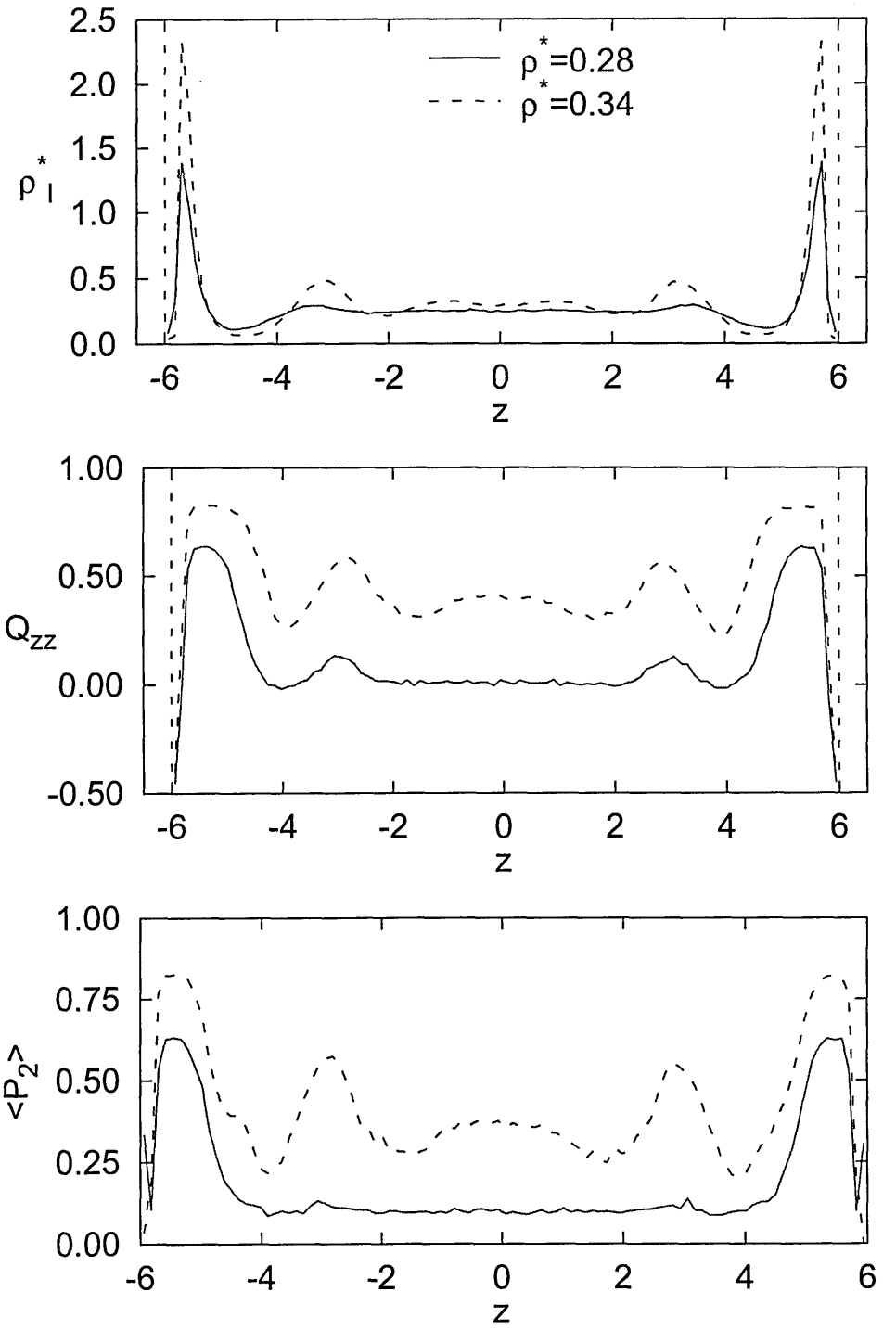

Figure 4.7 : Typical profiles corresponding to an homeotropic anchoring for $k = 3$ *and* $k'_S = 0.20$.

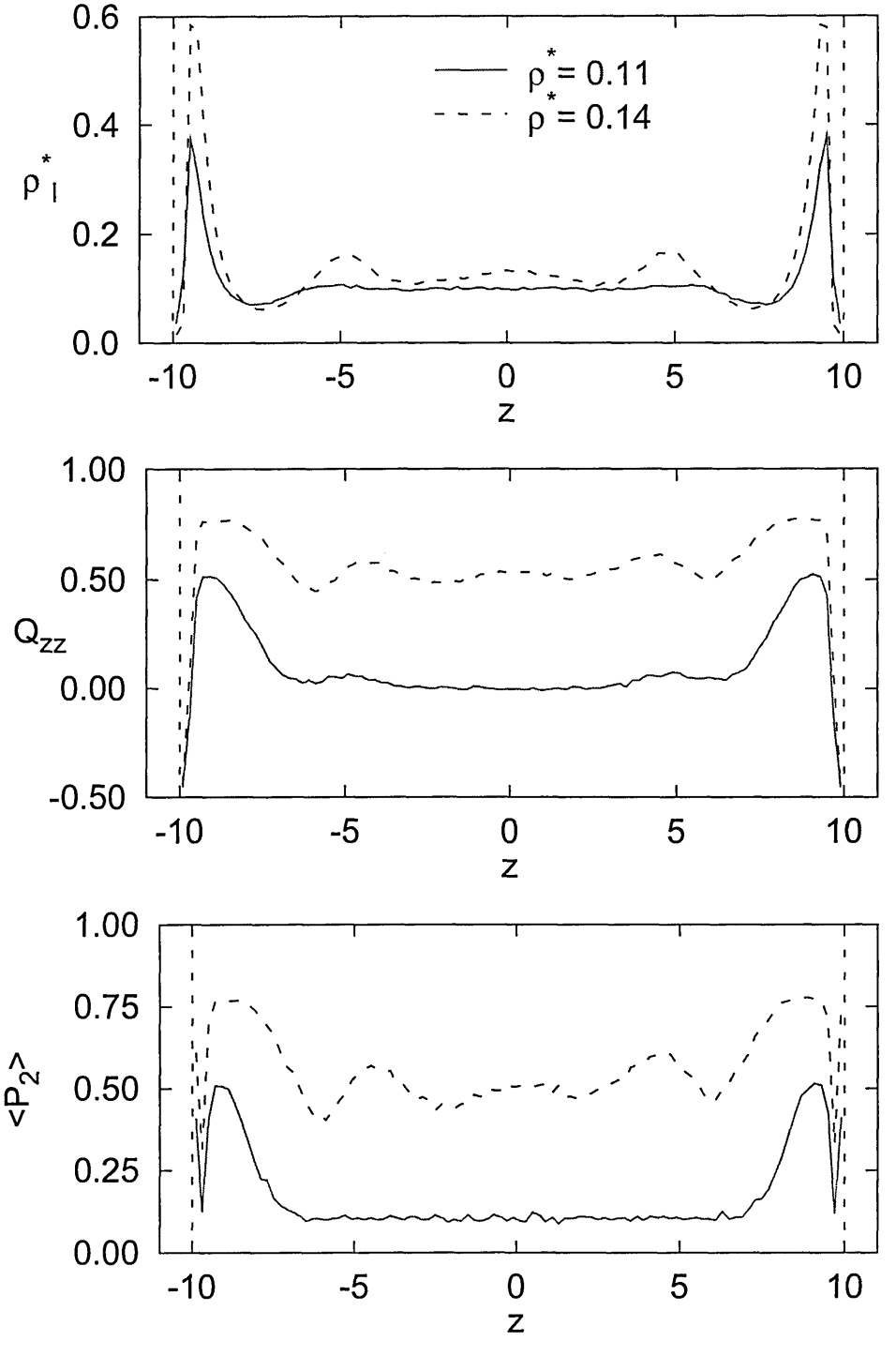

Figure 4.8 : Typical profiles corresponding to an homeotropic anchoring for $k = 5$ *and* $k'_S = 0.20$

homeotropic arrangement can be observed. $\rho_\ell^*(z)$ is an oscillatory function that displays its main peaks at $|z - z_0| \sim \frac{L_n}{2}$ which corresponds to the first layer of particles. Also, it should be noted that the periodicity of the peaks is very large (of the order of σ_ℓ), and no more than a total of five to six layers can be observed. This is compatible with the height of the simulation slabs of $L_z = 4\sigma_\ell$. The number of peaks in $\rho_\ell^*(z)$ clearly corresponds to a layered system with end to end alignment.

From the $Q_{zz}(z)$ profiles, the homeotropic arrangement can be determined from the regions of positive values. These correspond to regions of high $\rho_\ell^*(z)$, that is the interfacial regions for all densities and also the bulk region of the cell if the global number density is sufficient to support nematic order. $Q_{zz}(z)$ is also an oscillatory function whose maxima match those in $\rho_\ell^*(z)$; the higher the local density, the higher the order and, therefore, the better the ordering with respect to the wall.
It should be noted however, that regardless of the number density, $Q_{zz}(z)$ displays negative values very close to the surface ($|z - z_0| \leq \frac{L_n}{2}$) ; this is because there are always a few particles lying parallel to the walls in these regions. However, these planar particles correspond to regions of very low density, ρ_ℓ^*, and, therefore, their effect on the overall behaviour of the system is insignificant ; besides the higher the density, the less noticeable this effect.

$P_2(z)$ shows the orientational order as a function of position, a result that is not easily obtained experimentally. $P_2(z)$ also follows the oscillations of ρ_ℓ^*, for the same reasons as $Q_{zz}(z)$; regions of high local density induce regions of high local in-plane order.

Planar anchoring

A planar arrangement is observed when the average orientation in the interfacial region is parallel to the substrate, that is $< \theta > \sim \frac{\pi}{2}$. In the case of the HNW model, such an arrangement can be observed using long needle lengths ($k'_S \geq 0.75$). Typical profiles measuring the surface induced structural changes for this arrangement are shown on Figures 4.9 and 4.10, respectively, for $k = 3$ and $k = 5$.

The first difference to be noted when comparing these results with those obtained in the case of an homeotropic arrangement, is the difference in stratification. Because at the surface, $< \theta > \sim \frac{\pi}{2}$, the particles lie closer to the walls and as a result, the main peaks in ρ^*_ℓ are located at $|z - z_0| \sim 0$. The peak-peak separation of these functions are also much smaller than they were in the homeotropic case ($\sim \sigma_0$). The particles are, thus, now arranged in layers with a side by side alignment between one layer and the next.

$Q_{zz}(z)$ follows the same behaviour as $\rho^*_\ell(z)$ but adopts negative values in regions of high ρ^*_ℓ. Therefore maxima in ρ^*_ℓ, induce minima in $Q_{zz}(z)$ because high planar order is measured by negative values of $Q_{zz}(z)$. Comparison of the absolute value of $Q_{zz}(z)$ in the homeotropic and planar arrangements, suggests that for a given number density homeotropic ordering with respect to the surface is 'better' than the corresponding planar ordering. However since $Q_{zz} \in [-0.5 : 1]$, and an isotropic distribution of θ in a layer induces $Q_{zz} = 0$, a positive value of Q_{zz} should be compared to the double of a negative value. As a result a planar ordering with $Q_{zz} = -0.5$ is a 'good' as an homeotropic ordering with $Q_{zz} = 1$.

The form taken by $P_2(z)$ is very similar for homeotropic and planar arrangement as both follow the behaviour of the corresponding $\rho^*_\ell(z)$. The difference between the two arrangements lies in the peaks separation of $P_2(z)$.

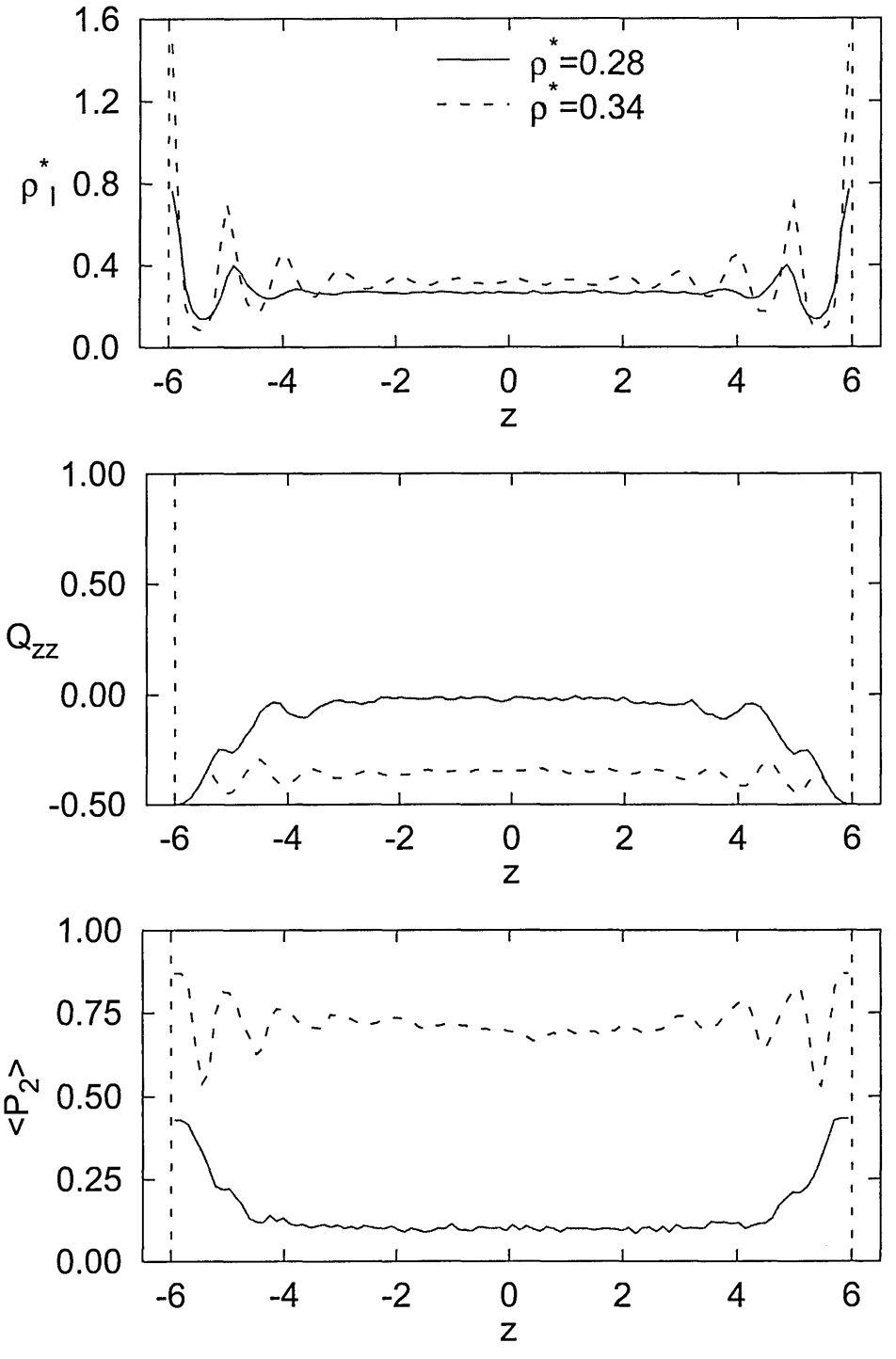

Figure 4.9 : Typical profiles corresponding to a planar arrangement with $k = 3$ *and* $k'_S = 0.80$.

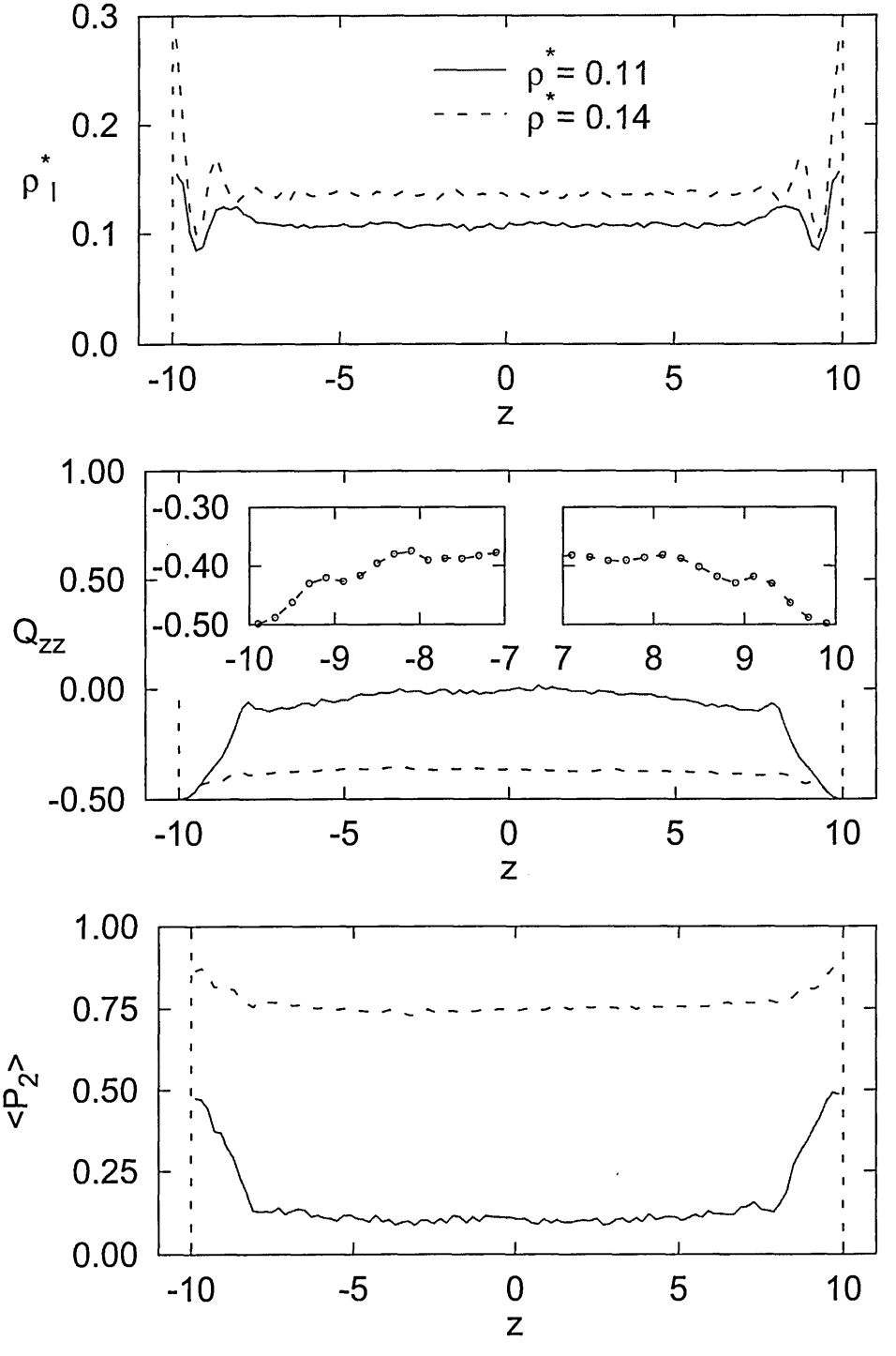

Figure 4.10 : Typical profiles corresponding to a planar arrangement and $k = 5$ *and* $k'_S = 0.80$.

Competing anchoring

The term competing anchoring refers to a situation where both planar and homeotropic arrangements are of comparable strength. In the case of the HNW model, this corresponds to a situation where $k'_S \sim k_S^{T\prime}$. Typical profiles corresponding to competing anchoring are shown on Figures 4.11 and 4.12 respectively for $k = 3$ and $k = 5$.

These results have been obtained for needle lengths very close but not equal to $k_S^{T\prime}$ as the values obtained by Equation 4.16 correspond to a very idealized case. It should be noted here that at high number densities, different profiles suggesting different surface arrangements were obtained depending on the history of the simulation sequence. Moreover, as in each case the profiles were obtained from fully equilibrated configurations, the presence of bistability is suggested here. Both sets of coexisting profiles are shown on the Figures.

In the case of **isotropic densities**, the surface induced layering shows features reminiscent with both planar and homeotropic influences. The interfacial region is characterized by two peaks of comparable height corresponding to particles with $\theta = 0$ and $\theta = \frac{\pi}{2}$. Since the particles in the interfacial region were equally distributed between those two regions, the heights of the two peaks are much smaller than those seen in the cases of strong planar or homeotropic anchoring. This double behaviour can also be observed on $Q_{zz}(z)$, as, in the interfacial region, both negative and positive values corresponding to high local densities can be observed. The $P_2(z)$ profile does not bring much more information as its behaviour follows that of $\rho_\ell^*(z)$.

In the case of **nematic densities**, the behaviour of the system is very different. Here, the increase in density had induced the particle to align and, therefore, choose one of the two possible surface arrangements. This prevented the system from simultaneously exhibiting both planar and homeotropic features. The profiles indicate that in the case of runs with decreasing k_S (*i.e.* coming from the

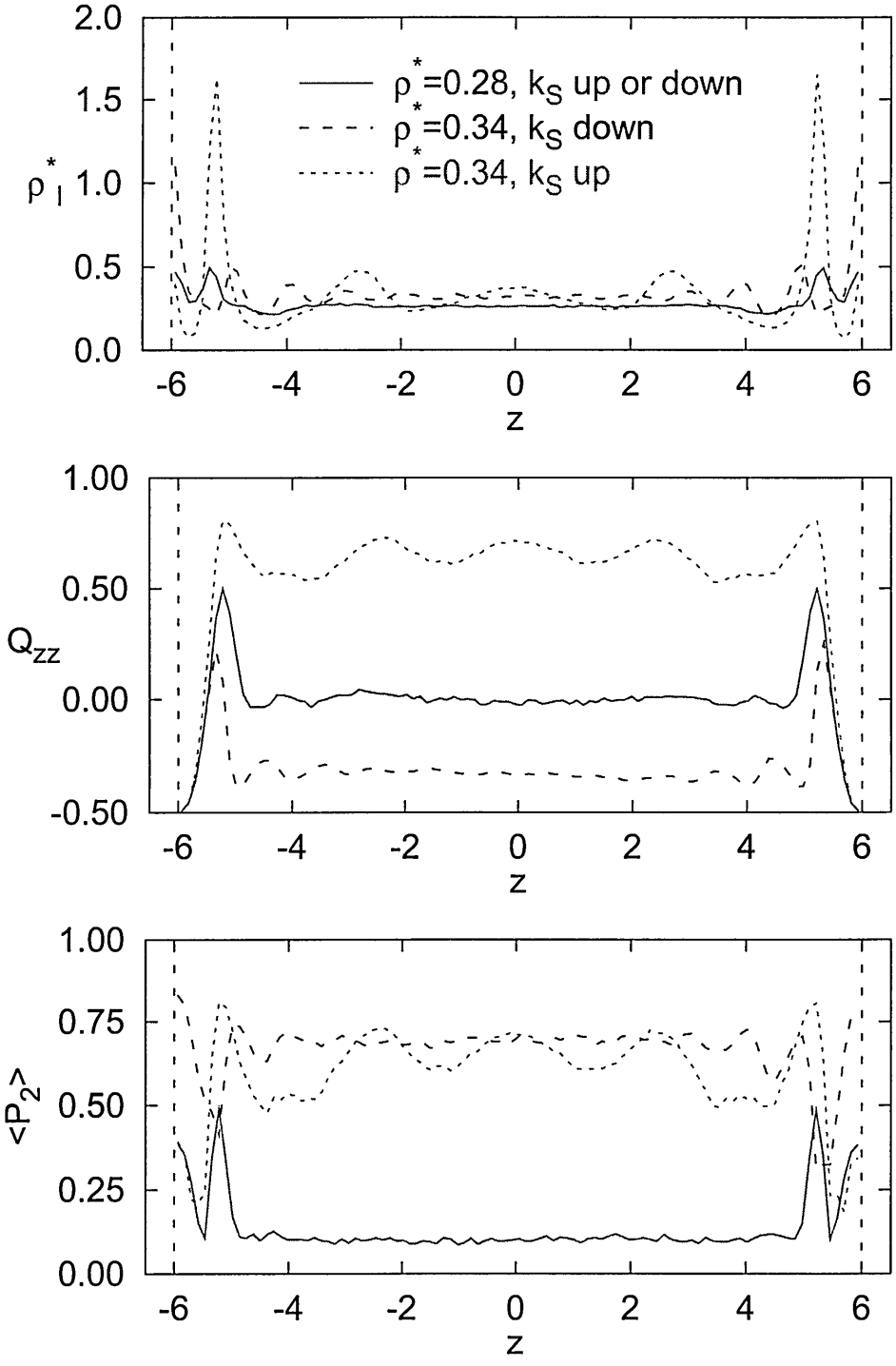

Figure 4.11 : Typical profiles for $k = 3$ and $L'_n = 0.48$

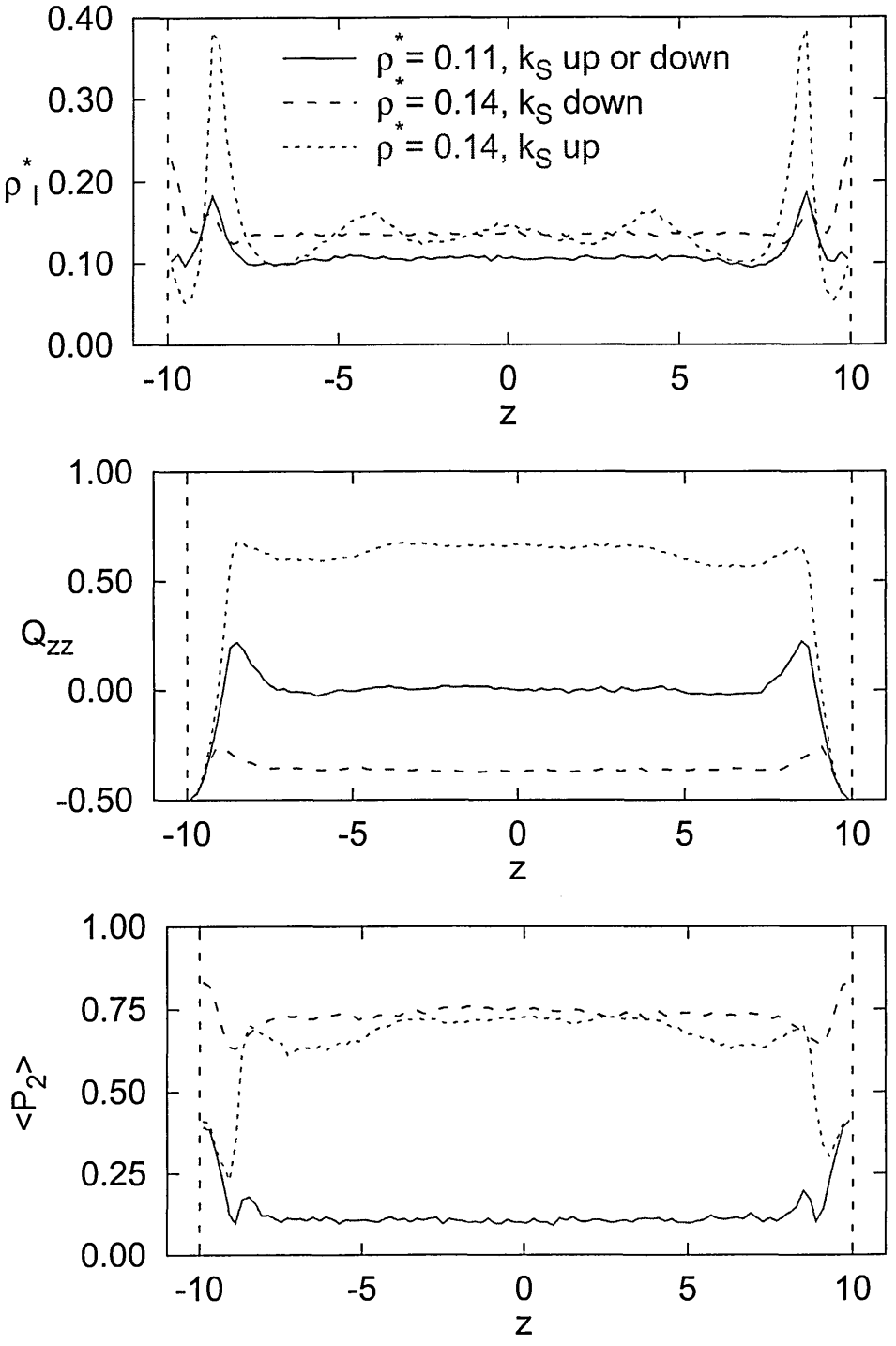

Figure 4.12 : Typical profiles for $k = 5$ and $L_n' = 0.54$

planar side), the cell displayed a planar arrangement whereas in the case of increasing needle lengths an homeotropic arrangement was found. This suggest that in the case of competing anchoring and high density, the surface arrangement was chosen according to the history of the system.

4.2.2 Influence of density

Observation of the profiles reveals that the density has a strong influence on the intensity of the surface induced effects; as stated earlier, the higher the number density the more intense the surface induced effects. In order to further study the influence of density on surface induced structural changes, Further simulations were carried out in series with constant k'_S and increasing and decreasing densities. From these, the $\rho^*_\ell(z,\rho^*)$, $Q_{zz}(z,\rho^*)$, and $P_2(z,\rho^*)$ surfaces have been computed. Results for the cases $k'_S = 0.0$ and $k'_S = 1.0$ are shown on Figures 4.13 and 4.14 for $k = 3$. The corresponding results for $k = 5$ are very similar and are, therfore, not shown here. Also, because hardly any hysteresis has been found between series with increasing and decreasing densities, only the results or series with increasing densities are shown.

Those measurements confirm the first observation using a smaller sample of densities (Section 4.2.1). At low densities, the surface induced effects are limited to the interfacial regions and the central region of the cell remains unaffected. On the $z-$profiles, this is characterized by short ranged surface features.

As the density is increased however, the surface influence extends further into the cell up to a density for which the full slab is uniformally aligned. The number of peaks on $\rho^*_\ell(z)$ increases steadily due to layering of the particles. As a result, the absolute values of the ordering observables increase as does the distance from the surface at which those functions start to decay. This translates to greater orientational ordering that extends further into the cell.

It is interesting to note that in the case of extreme homeotropic anchoring ($k'_S = 0.0$), regardless the density, the cell never displays uniform alignment since the bulk part of the cell never orders. This seems to contradict previous observations

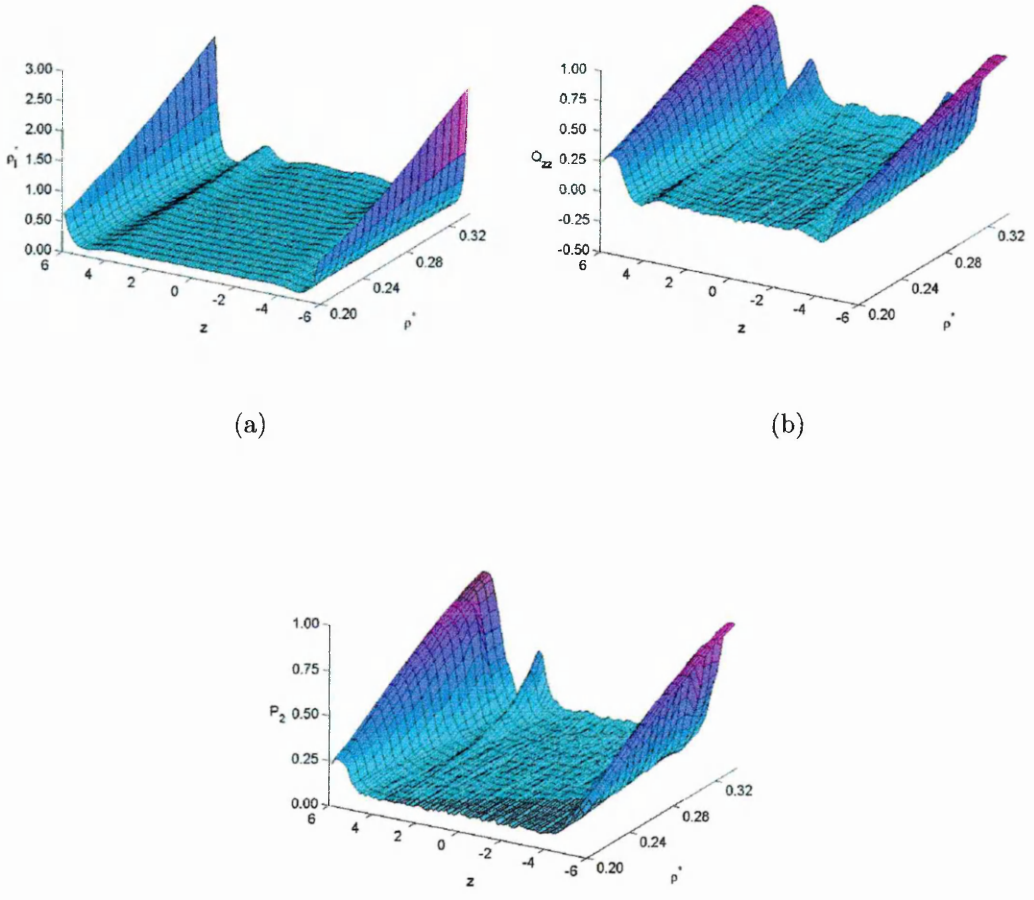

(a) (b)

(c)

Figure 4.13 : Influence of ρ^* on the z-profiles from series of simulation with increasing density of particles with $k = 3$ and $k'_S = 0.0$ (homeotropic anchoring).

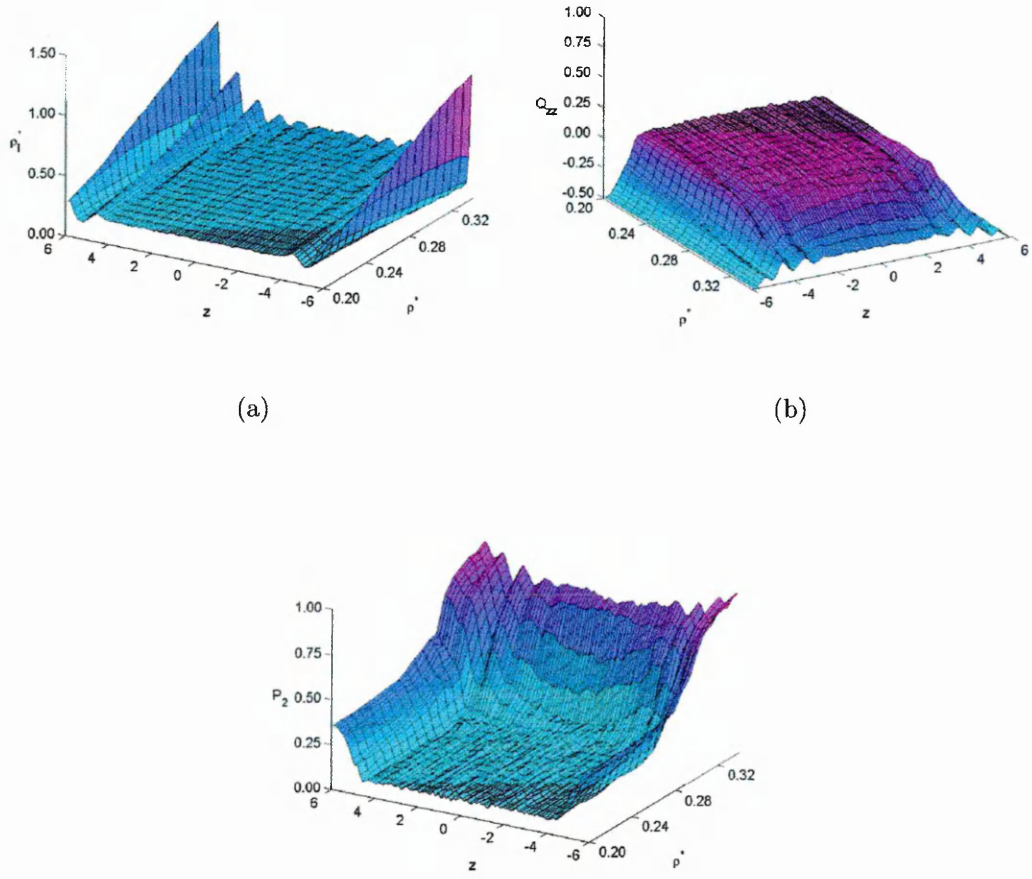

(a) (b)

(c)

Figure 4.14 : Influence of ρ^* on the z-profiles from series of simulation with increasing density of particles with $k = 3$ and $k'_S = 0.1$ (planar anchoring).

of systems of particles with elongation $k = 3$ under homeotropic anchoring (see Figure 4.7). However, due to the reduced needle lengths used here, the particle volume absorbed by the substrate leads to a lowering of the density in the bulk regions. This has the effect of shifting the I-N transition to densities out of the range considered here. This does not, however, question the existence of uniform alignment in the case $k'_S = 0.0$ as this has been observed with k=5.

Another effect that can be observed on Figures 4.13 and 4.14 is that the z gradients in $|Q_{zz}(z)|$ and $\rho^*_\ell(z)$ in the interfacial region increase when the bulk part of the cell becomes nematic. As a result of the bulk orientational order, interfacial regions come under the ordering influence of both the surfaces, through anchoring effects, and the bulk part of the cell, through elastic forces. This improves the quality of the layering and ordering in the interfacial regions.

4.2.3 Influence of k'_S

The influence of k'_S on the cell's behaviour is considerable, as this variable controls the type and strength of the surface anchoring. As the needle lengths is increased between from zero, the system undergoes a transition from homeotropic to planar anchoring. Section 4.1.2 gave the critical k'_S values for the this transition in the limit of close packing. In the simulations however, the local density at the interfaces is far from being that of close packing and is moreover a function of the global density. Therefore some shifts in $k_S^{T\prime}$ from the theoretical values are to be expected.

The purpose of this Section is to study, in greater detail, the effect of k'_S on the profiles and show the existence and nature of the homeotropic to planar anchoring transition. This has been achieved using simulations performed at constant densities in series of increasing and decreasing needle lengths. Two densities known to bulk isotropic and nematic phases have been considered. Results from the series with k'_S densities and $k = 3$ are shown in Figure 4.15 (isotropic density) and 4.16 (nematic density). The differences between the series with increasing and decreas-

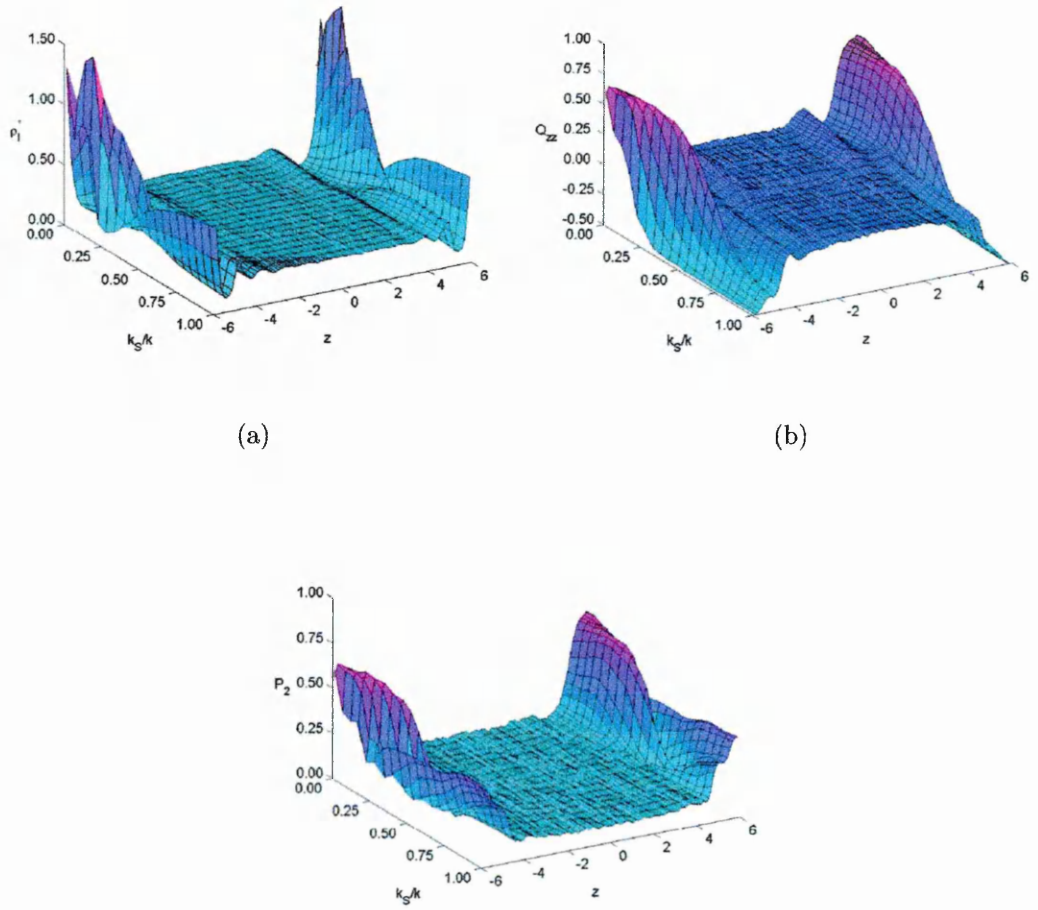

(a) (b)

(c)

Figure 4.15 : influence of k'_S on the z-profiles for $k = 3$ and $\rho^* = 0.28$.

ing k'_S are discussed in the next Section.

From Figures 4.15 and 4.16, typical features discussed previously corresponding to homeotropic and planar anchoring arrangements can be found by looking at curves corresponding to low and high values of k'_S, respectively. Here, rather, focus is brought to bear on the regions corresponding to competing anchoring, as these reveal the changes that take place during the anchoring transition.

As the transition region is approached (*e.g.* from the planar side), the height of the peaks in ρ_ℓ^* decrease rapidly, and at the transition, hardly any oscillations

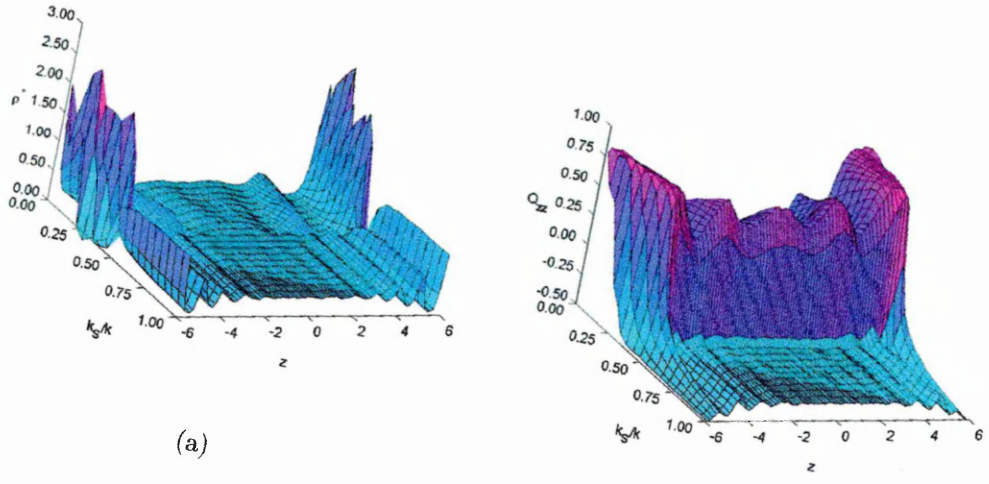

(a)

(b)

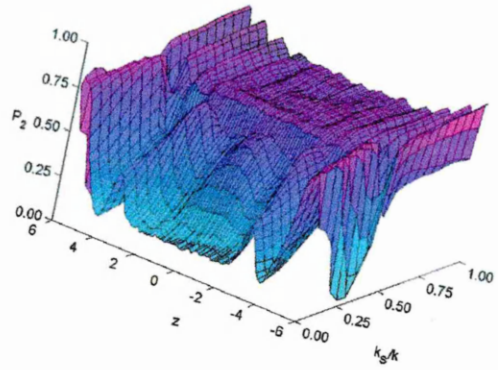

(c)

Figure 4.16 : influence of k'_S on the z-profiles for $k = 3$ and $\rho^* = 0.34$.

can be observed. This can be understood easily as at the transition, under equal influence from both type of anchoring, the particles diffuse almost homogeneously in bimodal surface layers which have features corresponding to both anchoring states; as a result, the density profile becomes relatively uniform. As the homeotropic anchoring becomes stronger, the system layers accordingly and a new oscillating pattern corresponding to homeotropic anchoring can be observed. It is interesting to note that the location maxima in $\rho_\ell^*(z)$ in the latter case coincide with those of the minima of the former.

As well as the changes in density, the centre of the slab undergoes an orientational disorder-order transition with k'_S as can be observed on $P_2(z, k'_S)$. The z-dependent oscillation pattern of this function also changes according to the state of the surface alignment.

$Q_{zz}(z, k'_S)$ shows the orientational reorganization that occurs during the transition. Upon approaching the transition region, this profile changes rapidly between the planar and homeotropic characteristics. The gradient of this change increases with the density but also with k; the transition is much sharper for $k = 5$ than for $k = 3$. Considering the needle length at which the change in the sign of Q_{zz} is observed, the theoretical predictions made in section 4.1.2 seem to be confirmed, particularly as the density is increased. A more detailed study of the homeotropic to planar transition region is presented in Section 4.3.

4.3 Surface influence on phase transitions.

4.3.1 The $\overline{Q}_{zz}$ and $\overline{P}_2$ observables.

To determine the location of the planar to homeotropic anchoring transition more precisely requires the ability to characterize quantitatively the nature of the arrangement displayed by a confined system. Section 4.2.1 has shown that simple observation of the profiles is not sufficient to determine the arrangement type as information from both $Q_{zz}(z)$ and $\rho_\ell^*(z)$ is required. Besides, quantitative in-

formation on the anchoring behaviour is hard to obtain solely by observation of profiles.

As the transition point is a function of both the global number density and needle length, a useful observable for characterising the surface arrangement would be a scalar able to distinguish both the type and strength of the anchoring for a given (ρ^*, k'_S) state point.

This need is fulfilled by the use of the novel observables $\overline{Q}_{zz}$ and $\overline{P}_2$. These are density-profile-weighted averages of, respectively, $Q_{zz}(z)$ and $P_2(z)$, taken over a given region of interest. In general $\overline{Q}_{zz}$ and $\overline{P}_2$ are defined as :

$$\overline{Q}_{zz} = \frac{\sum_{z_i} Q^n_{zz}(z_i)\rho^*_\ell(z_i)}{\sum_{z_i} \rho^*_\ell(z_i)} \tag{4.17}$$

$$\overline{P}_2 = \frac{\sum_{z_i} P_2(z_i)\rho^*_\ell(z_i)}{\sum_{z_i} \rho^*_\ell(z_i)} \tag{4.18}$$

where the z_i considered are restricted on the region of interest. Here $Q^n_{zz}(z)$ is a rescaled version of Q_{zz} such that $Q^n_{zz} \in [-1:1]$. Hence the definition of $Q^n_{zz}(z)$:

$$Q^n_{zz} = \begin{cases} Q_{zz} & \text{if } Q_{zz} \geq 0 \\ 2.Q_{zz} & \text{if } Q_{zz} < 0 \end{cases} \tag{4.19}$$

The computation of the $\overline{Q}_{zz}$ and $\overline{P}_2$ observables has been performed on regions of the cell corresponding to the interfacial and bulks domains. This has enabled the behaviour of the system to be studied in each region separately. The naming convention adopted for the observables corresponding to each region is described in Table 4.1.

It is now necessary to define an appropriate boundary between the interfacial and bulk regions. This boundary needs to be located at a point where the surface has no direct influence on the molecules; as a result the boundary z_i could be chosen such that $|z_i - z_0| = \frac{L_n}{2}$ since at $z = z_i$, the particles can rotate freely without direct interaction with the surface. This approach fails, however, in the limit of zero needle length, as it implies $|z_i - z_0| \sim 0$ whereas the z-profiles clearly show a non-zero interfacial regions for all needle lengths.

key	Description	Associated observables
Sb	Bottom interfacial region	$\overline{Q}_{zz}^{Sb}$, $\overline{P}_2^{Sb}$
Bu	Bulk region	$\overline{Q}_{zz}^{Bu}$, $\overline{P}_2^{Bu}$
St	Top interfacial region	$\overline{Q}_{zz}^{St}$, $\overline{P}_2^{St}$
Su	Both interfacial region	$\overline{Q}_{zz}^{Su}$, $\overline{P}_2^{Su}$

Table 4.1 : Naming convention for the simulation slab regions and associated observable.

A different approach was taken, therefore, in defining this boundary; the interfacial region width was made a function of the needle length and density by making the boundary z_i dependent on features of the density profiles. The scheme used is illustrated on Figure 4.17. If the anchoring was found to be planar (first local maximum of $\rho_\ell^*(z)$ at $|z_i - z_0| \sim 0$), the interfacial region was taken to extend from the surface to the distance corresponding to the second maximum in $\rho_\ell^*(z)$. If however, the anchoring was homeotropic (first local maximum of $\rho_\ell^*(z)$ at $|z_i - z_0| \sim \frac{L_n}{2}$) then the interfacial region was taken to extend from the surface to the first local minimum in $\rho_\ell^*(z)$. In those cases with ambiguous double peaked density profiles, the first scheme was adopted.

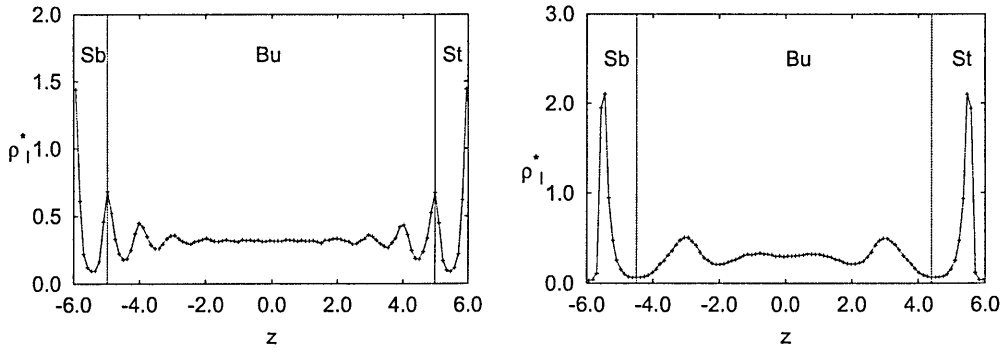

(a) planar case

(b) homeotropic case

Figure 4.17 : Definition of the slab interfacial and bulk regions.

4.3.2 Anchoring transitions.

Here, the planar to homeotropic anchoring transition is located from measurement of $\overline{Q}_{zz}$ as a function of ρ^* and k'_S which can be used to construct an anchoring phase diagram. Such diagrams have been determined for systems with elongations $k = 3$ and $k = 5$ using simulations performed at constant densities and increasing and decreasing needle lengths. Results for both series in the interfacial (Su) and bulk (Bu) regions are shown in Figures 4.18 and 4.19 for $k = 3$ and $k = 5$ respectively. The results obtained for the two elongations are very similar. In the **interfacial region**, the anchoring transitions occur at k_S/k values close to those predicted in section 4.1.2, as can be observed from the lines of constant $\overline{Q}_{zz}^{Su} = 0$. For higher densities, the agreement between the simulation and theoretical result can be seen to improve. Also the region around k'_S becomes sharper with increasing density indicating a possible discontinuous transition between planar and homeotropic anchoring states.

In the **bulk region**, little surface influence can be observed at low density, as the values of $\overline{Q}_{zz}^{Bu}$ remain close to zero due to the systems orientational isotropy. As the number density is increased, the local density in the bulk regions reaches values corresponding to bulk nematic densities. The surface influence then extends further into the cell and sharp anchoring transitions become apparent at needle lengths similar to those suggested by the interfacial region anchoring diagram. This, however, occurs for global number densities significantly greater than the isotropic to nematic transition densities of the equivalent bulk system (see Section 3.3.1). This indicates that the I-N transitions in the bulk regions were shifted to higher number densities due to the presence of the surfaces. this is further discussed in Section 4.3.4.

The anchoring phase diagrams are also found to be asymmetric in that bulk planar ordering develops at lower densities than its homeotropic counterpart. As stated earlier, this is due, in part, to the increased absorbed volume in the case of

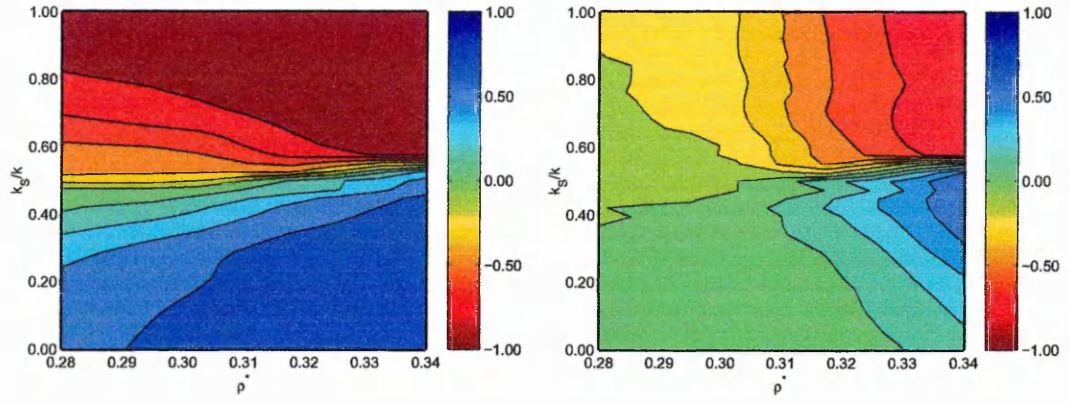

(a) Series with increasing k'_S.

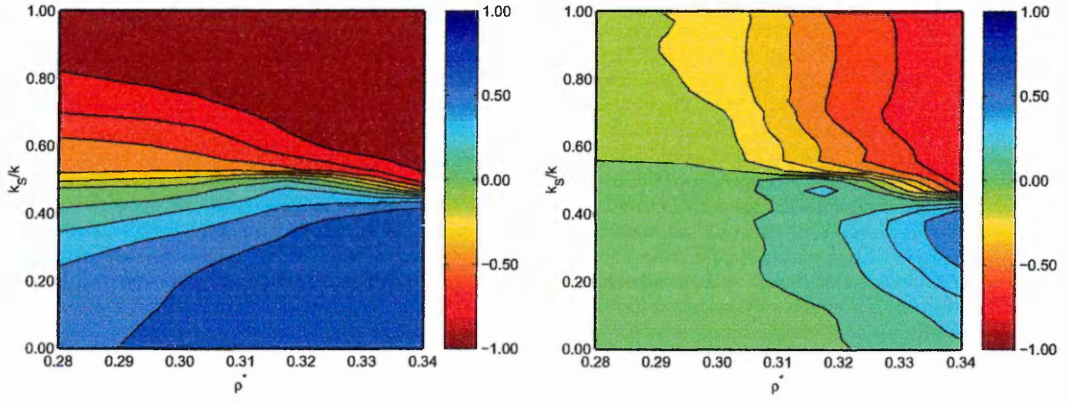

(b) Series with decreasing k'_S.

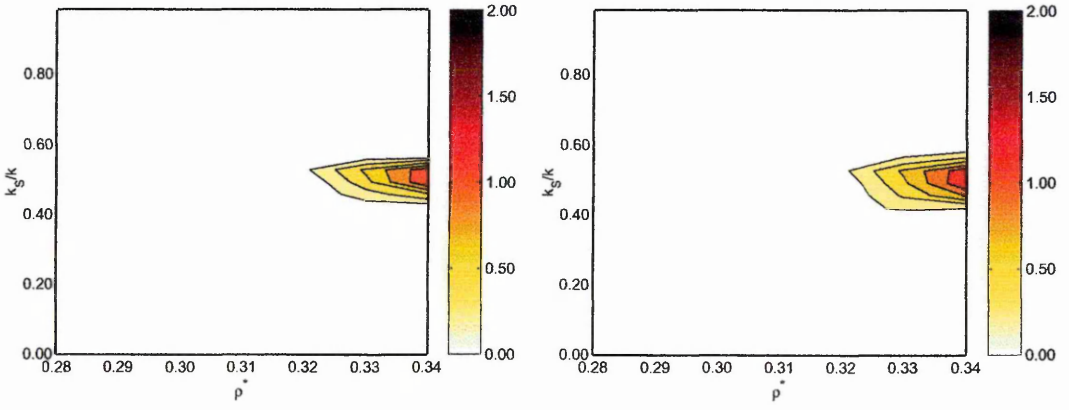

(c) Bistability phase diagram (*i.e.* difference between (a) and (b)).

Figure 4.18 : Anchoring phase diagrams of $\overline{Q}_{zz}$ for $k = 3$ for the surface (left) and bulk (right) regions of the cell.

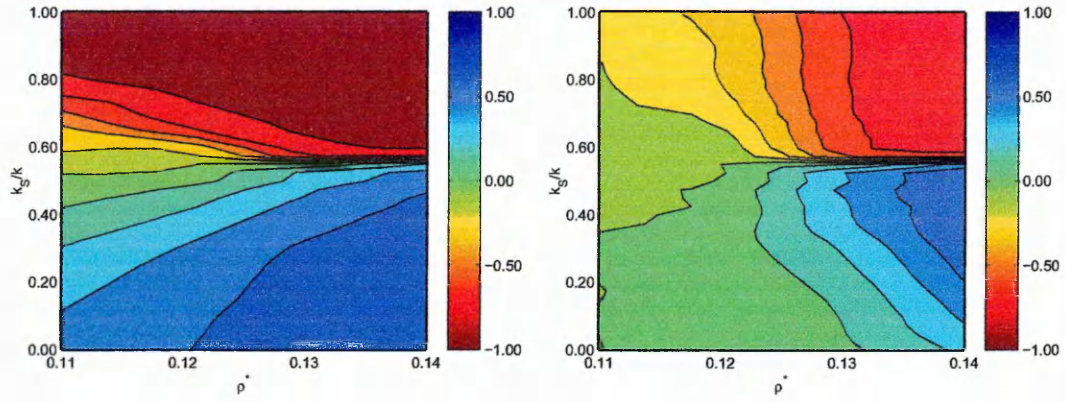

(a) Series with increasing k'_S.

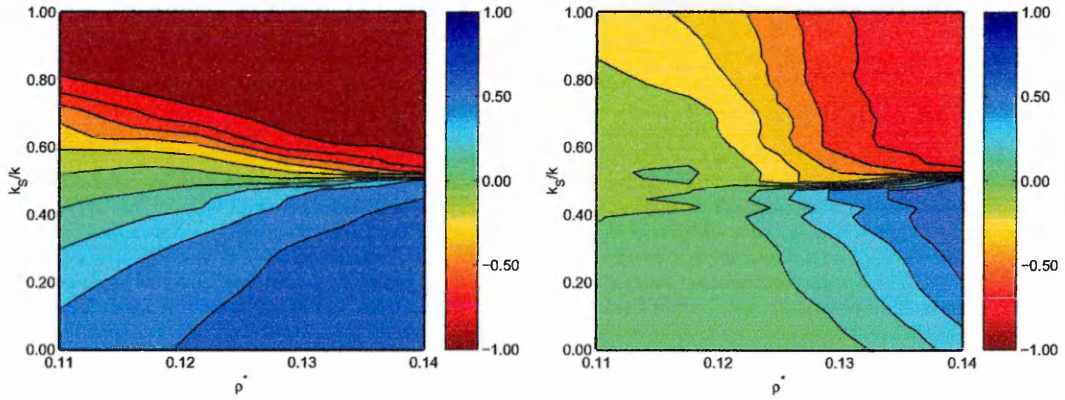

(b) Series with decreasing k'_S.

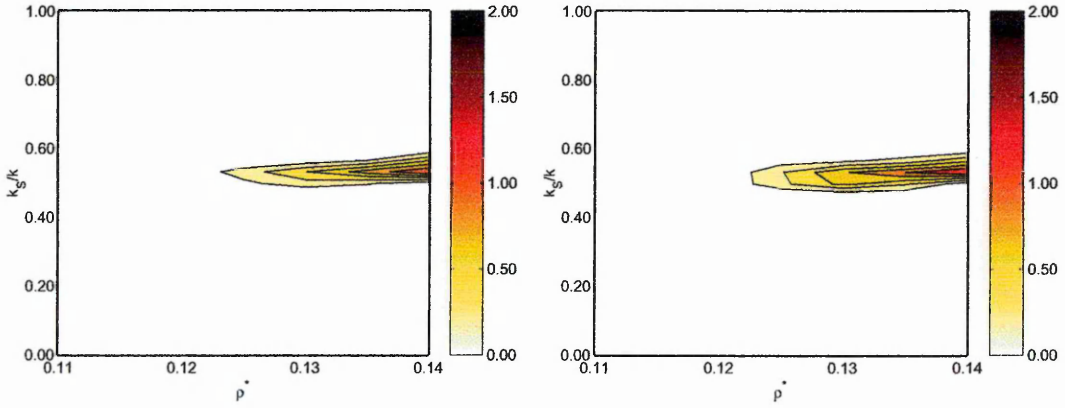

(c) Bistability phase diagram (*i.e.* difference between (a) and (b)).

Figure 4.19 : Anchoring phase diagrams of $\overline{Q}_{zz}$ for $k = 5$ for the surface (left) and bulk (right) regions of the cell.

homeotropic anchoring which is sufficient to prevent the observation of uniformly ordered slabs of homeotropic arrangement in the limit $k'_S = 0$ for the range of density considered here. That said, interpolation of the result determined here to higher densities suggests that homeotropically ordered phases should exist for $k'_S < k'^{T}_S$.

4.3.3 Anchoring bistability

Another interesting feature of Figures 4.18 and 4.19 comes from the comparison of the diagrams for increasing and decreasing needle lengths (*i.e.* diagrams (a) and (b)). As the density is increased, the hysteresis between the two set of results also increases. This confirms an earlier observation that in conditions corresponding to competing anchoring according the z-profiles observed can be dependent on sample's history (recall Figures 4.11 and 4.12).
Since all of the data used to construct those diagrams were obtained from equilibrated systems, these discrepancies suggest possible bistable behaviour for state points close to the anchoring transition. This bistability has been measured more precisely by computing the absolute value of the difference between results obtained with series of increasing and decreasing needle lengths. This difference equals 0 if the two diagram agree and 2 for full bistability. The results for both elongations in the interfacial and bulk regions of the slab, shown on Figures 4.18(c) and 4.19(c) indicate for both $k = 3$ and $k = 5$ distinct bistable regions at high densities.

In order to demonstrate the existence of this bistability, an attempt to switch the cell from planar to homeotropic and back has been carried out. For this, a previously equilibrated system of $N = 1000$ particles with $k = 3$, $\rho^* = 0.34$ and $k'_S = 0.5$ was taken. This configuration was extracted from a series performed with decreasing densities which showed planar anchoring at this state point. The switching was performed through the series of simulations R_1 to R_5 listed in Table 4.2, *i.e.* by applying and removing an electric field $\mathbf{E} = E\hat{\mathbf{z}}$ and taking the

Run	$\hat{\mathbf{E}}$	E	χ_e	run length
R_1	(0,0,0)	0.0	0.0	$0.25.10^6$
R_2	(0,0,1)	6.0	0.5	$0.25.10^6$
R_3	(0,0,0)	0.0	0.0	$1.00.10^6$
R_4	(0,0,1)	6.0	-0.5	$0.25.10^6$
R_5	(0,0,0)	0.0	0.0	$0.50.10^6$

Table 4.2 : Electric parameterisation in the switching between the planar and homeotropic states of the bistable system.

dielectric constant χ_e to be, alternately, positive and negative. The effect of the field is to align the particles parallel or perpendicular with $\mathbf{E}$ respectively for positive and negative values of χ_e, respectively.

While this setup is admittedly somewhat unrealistic, it can nevertheless be related to an experimental system in which the mesogens employed can display different dielectric constant according to the frequency of an applied AC field.

If the considered state points correspond to a bistable region, both planar and homeotropic phases should be obtained in the field-off runs provided the sample is prealigned suitably for each arrangement. The purpose of applying the field with each value of χ_e is, thus, to perform this pre-alignment operation.

The configuration snapshots corresponding to the initial and final states from each run are shown on Figure 4.20(a) to (f). The corresponding behaviour of $\overline{Q}_{zz}^{Su}$ and $\overline{Q}_{zz}^{Bu}$, as a function of Monte Carlo sweeps, are shown in Figures 4.21(a) and 4.21(b). Also, for comparison, the values of $\overline{Q}_{zz}$ at this state point and corresponding to the two different surface arrangements as obtained from the runs with increasing and decreasing k_S' are shown as horizontal lines.

The results confirm the existence of the bistable region. Run R_1 shows that the system remains stable in its initial planar arrangement; after reorientation of the particles along $\hat{\mathbf{z}}$ by the applied field (run R_2), the system equilibrates naturally to a homeotropic arrangement (run R_3) although the final value of $\overline{Q}_{zz}$ is higher

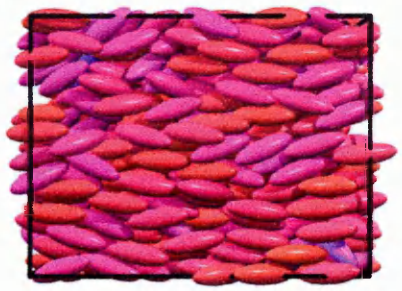

(a) start R_1

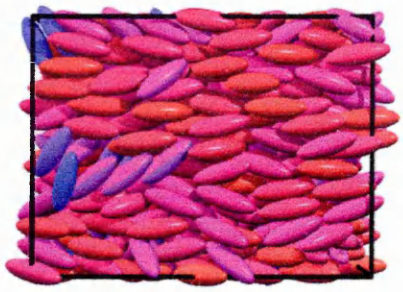

(b) end R_1

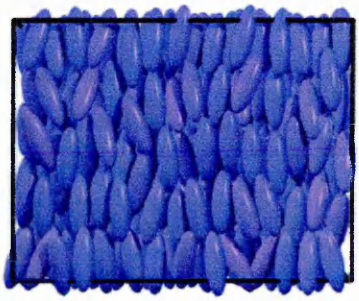

(c) end R_2

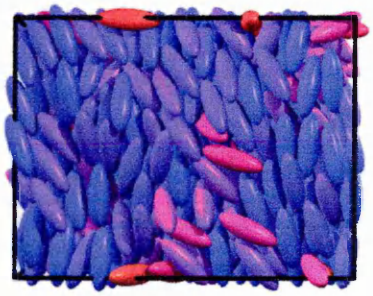

(d) end R_3

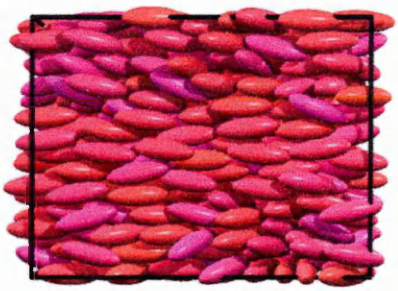

(e) end R_4

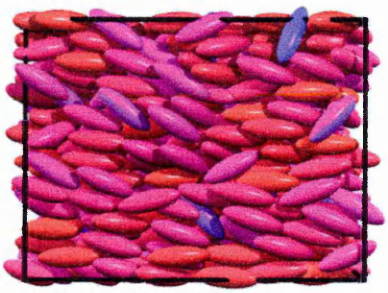

(f) end R_5

Figure 4.20 : Configuration snapshots corresponding to the initial (start) and final configurations of runs R_1 to R_5.

than that obtained from the previous runs performed in the computation of the anchoring phase diagrams. This discrepancy might be induced by the application of the strong value of the field which forced all interfacial particles to take an almost perfect homeotropic alignment. Upon removal of the field, the system equilibrated towards the stable homeotropic state, but due to packing constraints fewer particles were allowed to take a planar orientation close to the surface as in the case of previous simulations. This should not however question the equilibrium of the state obtained here. Upon changing the molecular dielectric susceptibility to $\chi_e < 0$, reapplication of the field (run R_4) recreates a planar arrangement which relaxes to the original stable state upon field removal (run R_5). In this case, the system equilibrated to the same value of $\overline{Q}_{zz}$ as that obtained previously as in the case of planar anchoring, there is no instance of homeotropic alignment in the interfacial region.

It should be noted also, that the 'response times' of the systems were different in the bulk and interfacial region; however the Monte Carlo technique was used and this does not follow the time evolution of the systems. An appropriate study of the dynamic behaviour of the system would have required the use of the Molecular Dynamics techniques, but this was not of prime interest here. The purpose of these simulations was to prove the existence of the bistability behaviour of the model, and within the simulation run lengths available here, this has been fulfilled.

4.3.4 The I-N transition.

Here, the influence of confinement on the liquid crystalline phase behaviour of the model is studied, specifically, the influence of confinement upon the location of the I-N transition is of interest. To some extend, this issue has already been addressed for similar systems studied very recently by Zhou *et al.* [178]. This work was based on simulations of hard Gaussian overlap particles of elongation $k \in [2:3]$ confined between plane structureless walls represented by a surface potential describing the interaction between an ellipsoid and a plane. The authors found that the effect of confinement was to shift the location of the I-N transition

towards lower number densities. Another effect was enhancement of orientational order in that particles whose shape anisotropy was not sufficient for the formation of liquid crystalline phases in the bulk (*i.e.* 3d) displayed ordered phases with an order parameter consistent with a nematic phase in confined systems.

The effect of confinement upon the phase behaviour of the model studied here was assessed by computing the variation of $\overline{P}_2$ and the average local density $\overline{\rho_\ell^*}$ in bulk and surface regions as a function of the overall number density ρ^* and reduced needle length k_S/k. Here the approach taken for the study of the anchoring transition was applied, using $P_2(z)$ as the main observable.
The order phase diagrams of the system as a function of ρ^* and k'_S have been computed from simulations with constant ρ^* performed in series of increasing and decreasing k'_S. The difference between this and the study of the anchoring transition is that now lines of constant k'_S on the diagram are of interest; the results shown here have been computed using series of simulations with constant density rather than constant needle lengths as more data were available for the former. However comparison of data obtained from series with constant density and varying needle length show that ultimately both series agree. For the sake of completeness, Figure 4.22 shows a sample of the results obtained for series of simulation with constant needle length and increasing densities. The order phase diagrams (obtained from the series with constant number density) for $k = 3$ in the interfacial and bulk regions are shown on Figure 4.23, and the evolution of $\overline{\rho_\ell^*}$ with ρ^* and k_S/k is shown on Figure 4.24. From these, the effects of confinement on the I-N transition can be assessed.

Observation of these results reveals the main effects of confinement mentioned in Chapter 2 and at the beginning of this Chapter. In the interfacial region, Figure 4.24 shows an enhanced density which, in turn, results in higher order as shown on Figure 4.23. As a result of this, the average local density in the bulk region is reduced, and so is the degree of ordering. Generally, therefore, the ef-

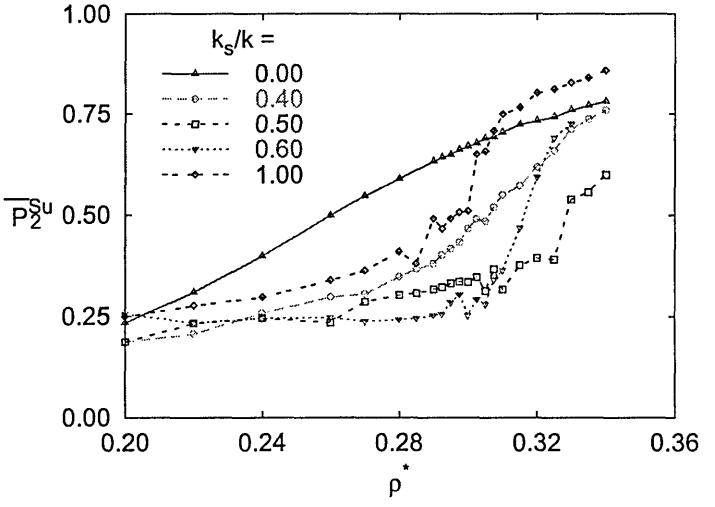

(a) interfacial region

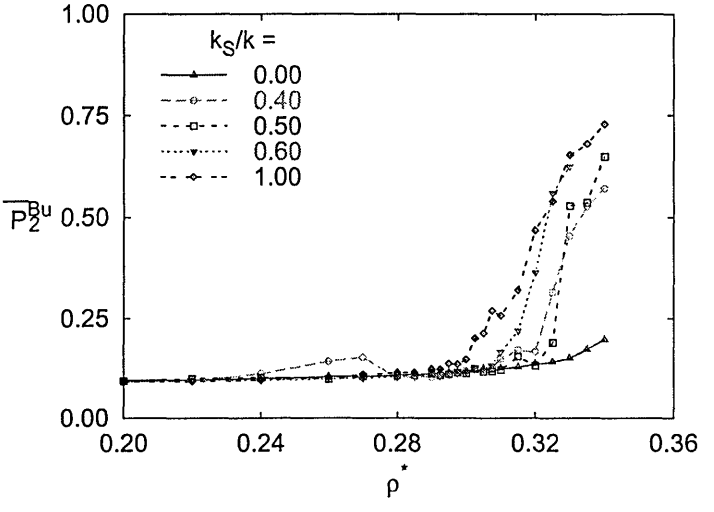

(b) bulk region

Figure 4.22 : Evolution of $\overline{P}_2$ in the interfacial(a) and bulk(b) regions as obtained from simulations at constant k_s/k and increasing densities.

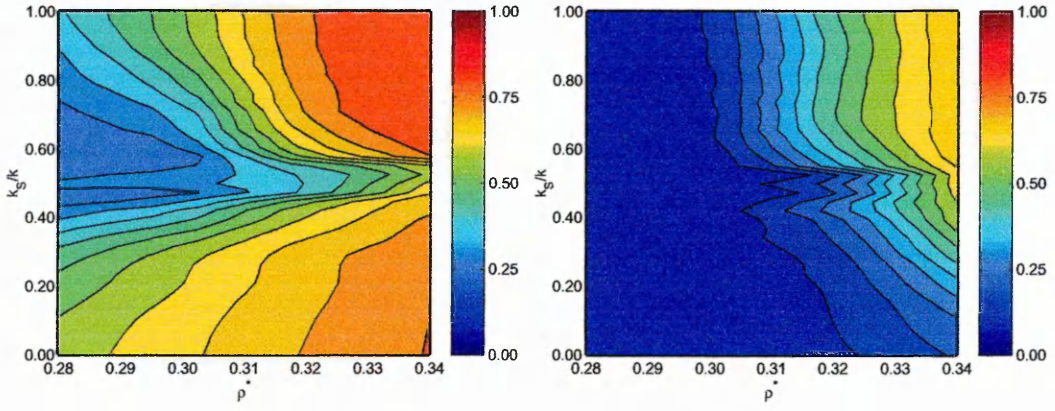

(a) Series with increasing needle length

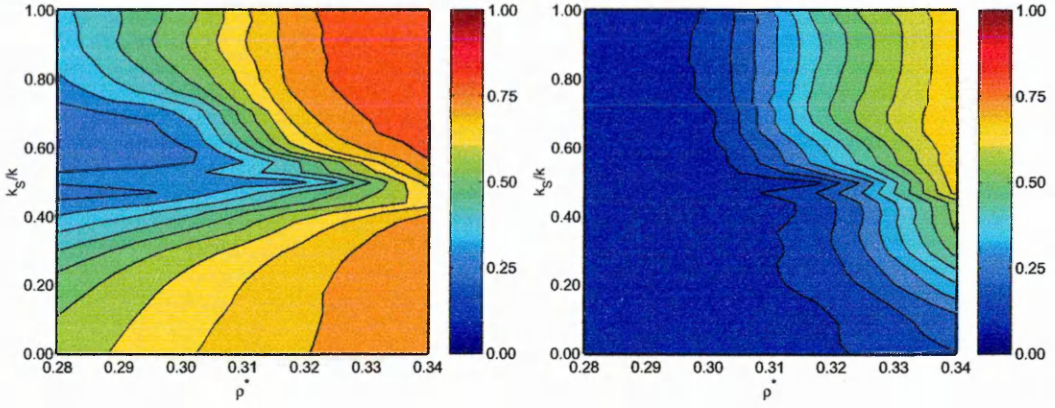

(b) Series with decreasing needle length

Figure 4.23 : Order phase diagrams for $k = 3$ in the interfacial (left) and bulk (right) regions of the slab obtained from series with increasing and decreasing density.

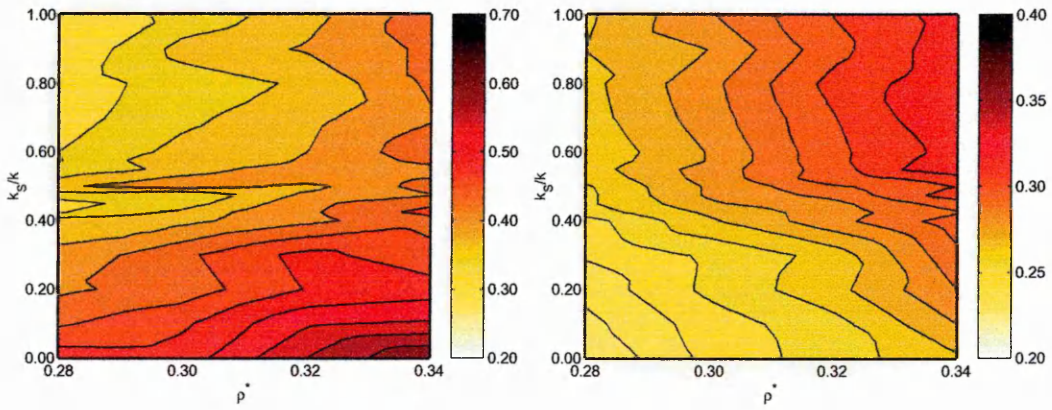

(a) Series with increasing needle length

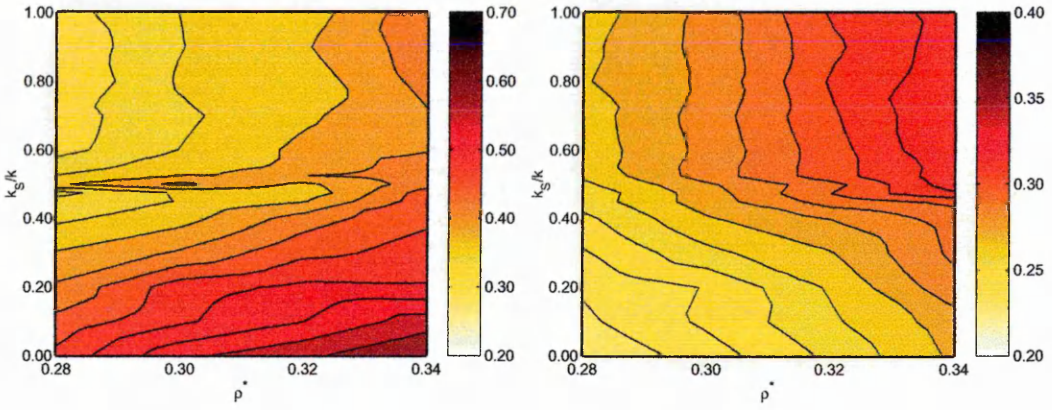

(b) Series with decreasing needle length

Figure 4.24 : average local density $\overline{\rho_\ell^*}$ for $k = 3$ in the interfacial (left) and bulk (right) regions of the slab obtained from series with increasing and decreasing density.

fect of confinement on these systems is to shift the isotropic-nematic transition to lower number densities in the interfacial region and to higher number densities in the bulk region.

Close observation of Figures 4.23 and 4.24 shows, however, that the anchoring conditions have a strong influence on the surface induced shifts in the local density and order parameter values. In particular and in the region corresponding to competing anchoring *i.e.* $k_S \sim 0.5$, $\overline{\rho_\ell^*}$ shows a sudden decrease in value which is accompanied by a region of low orientational order. However, this effect seems to be much stronger on $\overline{P}_2$ than is suggested by the behaviour of $\overline{\rho_\ell^*}$. This is because, in addition to the reduced average local density, the double peaked nature of the z-profiles indicates the particles to have competing preferred orientations, which reduces the value of the order parameter. This leads to a higher shift in the number density of the I-N transition of competing anchoring cases than would be expected purely from local density effects.

The results observed here are consistent with those obtained by Zhou *et al.* [178]. The shifts in $\overline{\rho_\ell^*}$ and $\overline{P}_2$ with number density confirms that for non-competing anchoring conditions, the principal effect of confinement is to enhance order in the systems and shift the location of the I-N transition towards lower number densities. Calculating the observables independently in the interfacial and bulk regions shows that both regions exhibit a qualitatively but not quantitatively similar behaviour; this was not, however, observed in [178], where all observables were averaged over the full samples, so that different shifts in the bulk and surface I-N transition densities were not monitored. Finally, we have shown that the behaviour of the film is dependent on the type of anchoring applied; this issue was not addressed in [178] where only the case of strong planar anchoring was considered.

Conclusion

In this Chapter, the study of surface induced structural changes on a confined system of hard Gaussian overlap particles has been addressed. The choice of the hard needle wall potential for surface interaction allowed the observation of two stable surface arrangements, namely planar and homeotropic according to k_S, the length of the needle embedded in the particles. The mechanism responsible for the change in surface arrangement as a function of k_S is the varying amount of molecular volume that can be absorbed into the surface.

A systematic study of the behaviour of the system as a function of number density and needle length has been performed. From this, an anchoring transition between the two arrangements has been identified and located through the computation of anchoring phase diagrams. Also, differences between the diagrams obtained from series of simulations performed with, respectively increasing and decreasing needle lengths have been used to identify bistability regions, where both homeotropic and planar arrangement remain stable on timescale of a simulation run length.

It has been shown that generally, the effect of confinement is to shift the isotropic-nematic transition to lower number densities close to the surfaces and to higher number densities in the bulk region. In addition, it has been shown that the amount by which this transition is shifted varies with the nature of anchoring conditions adopted.

Chapter 5

More on confined geometries

Introduction

Simulations of confined systems of hard Gaussian overlap particles interacting with the substrates through the hard needle wall potential have shown that, despite the simplicity of the model, a range of surface induced behaviour can be observed. Using this simple setup a thorough and systematic study of the surface induced structural changes has been performed and an anchoring transition has been identified. In this Chapter, the focus is brought to bear on the study of alternative confined system configurations.

First, more realistic surface potentials are studied and their anchoring phase diagrams computed so as to investigate their suitability for the modeling of anchoring transitions. Two such potentials are of interest, namely the rod-sphere potential and the rod-surface potential. For each of these, the the surface induced arrangements are studied and the possibility of bistable regions is explored.

The second part of this Chapter contains a study of hybrid anchored systems performed using the hard needle wall potential; following this, the possibility of simulating easy switching between the hybrid aligned nematic and vertical states of the cell is investigated.

5.1 Realistic surface potentials : the RSP.

5.1.1 The rod-sphere potential.

The rod-sphere surface potential (RSP) describes the interaction between a Gaussian ellipsoid and a sphere located in the surface plane and with the same x and y coordinates as the ellipsoid. Again, the particles (HGO) do not interact directly with the substrate, rather another HGO ellipsoid is inserted in each particle (*e.g.* Figure 5.1). This inner ellipsoid interacts with the surface through $\mathcal{V}^{RSP}$ as :

$$\mathcal{V}^{RSP} = \begin{cases} 0 & \text{if} \quad |z_i - z_0| \geq \sigma_w^{RSP} \\ \infty & \text{if} \quad |z_i - z_0| < \sigma_w^{RSP} \end{cases} \tag{5.1}$$

where σ_w^{RSP} is the contact distance for the interaction between a hard Gaussian overlap particle with length $\sigma_{\parallel}$ and breadth $\sigma_{\perp}$ and a sphere of diameter σ_j. The contact distance for such an interaction is given by Equation (4) of [92] :

$$\sigma_w^{RSP} = \sqrt{\frac{\sigma_{\perp}^2 + \sigma_j^2}{1 - \chi(\mathbf{u_i} \cdot \mathbf{r_{ij}})^2}} \tag{5.2}$$

For implementation into a simulation code, Equation 5.2 is best written in terms of θ and σ_0 ; recalling that the unit of distance $\sigma_0 = \sigma_{\perp}\sqrt{2}$ and for convenience, imposing $\sigma_0 = \sigma_j\sqrt{2}$. Also to enable comparison with the hard needle wall potential, the sphere is taken to be tangent with the substrate so as to keep it out of the simulation box. This leads to the final expression for σ_w^{RSP} as used in the simulations :

$$\sigma_w^{RSP} = \sigma_0 \left(\frac{1}{\sqrt{1 - \chi_S \cos^2\theta}} - \frac{1}{2} \right) \tag{5.3}$$

with :

$$\chi_S = \frac{k_S^2 - 1}{k_S^2 + 1} \tag{5.4}$$

k_S being the length to breadth ratio of the inner ellipsoid. A graphical representation of this contact distance as a function of k_S and θ is shown on Figure 5.2.

The rod-sphere model has already been used as the contact distance for a soft surface potential in studies of confined Gay-Berne particles in single component

Figure 5.1 : Representation of the geometry used for the interaction between the inner HGO particle and the sphere representing the substrate in the RSP surface potential.

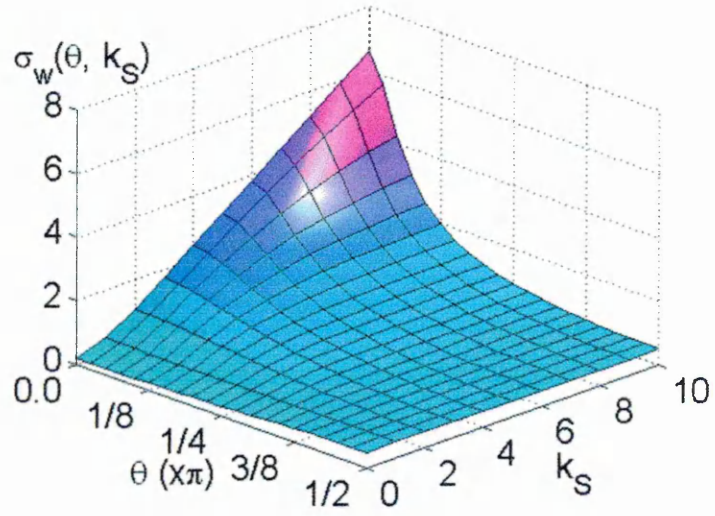

Figure 5.2 : Representation of $\sigma_w^{RSP}(k_S, \cos\theta)$ for the RSP surface potential.

systems [131, 132, 179], binary mixtures [133] and switching situations [180]. In all of these, full particles (*i.e.* $k_S = k$) were used and tilted layers were observed in the interfacial regions. In [132, 179] the tilt was explained to be a consequence of the competition between packing constraints and the form of the surface potential. In other words, the attractive part of the potential was thought to be responsible for the tilt, the authors noticing that increasing the particle-surface coupling α (see equation (9) of [132]) induced a tighter distribution of the particle orientations about the optimal tilt angle. It is interesting to note however, that using the same surface potential, but a molecular elongation $k = 2$ instead of 3, Wall and Cleaver [181] found that the surface anchoring changed from tilted to planar.

Another case of surface tilted arrangement was obtained in the study by Lange and Schmid [165, 166, 167] where Gay-Berne particles were confined between two structureless walls. There, the surface potential used was similar to the RSP, but a different σ_w function was used so as to describe the interaction between a surface and an ellipsoid of revolution; also, they used the common $12-6$ Gay-Berne potential rather the $9-3$ version of [132]. The particles simulated were found to exhibit planar anchoring, but tilted phases were obtained by inclusion of polymer chains grafted on to the surface. The tilt in that case resulted from competition between the planar orientation favoured by the solvent particles and the homeotropic alignment preferred by the polymer chains (since it reduced their bond energy). Again, in that study, tilting behaviour could be explained in terms of the attractive parts of the potential since an anchoring transition between planar and tilted arrangements was obtained by varying the number of grafted polymer chains.

Ascribing the tilt to the attractive part of the potential in [132] was also consistent with the many theoretical treatments of confined hard particle systems [182, 141] : none of these predict tilted surface alignment, planar and homeotropic alignments being the only arrangement predicted.

It is interesting to note, however, that when using a surface made of fixed atoms

and a similar surface potential to that used in [132], Palermo *et al.* [137] did not find any tilt arrangements, rather the natural planar arrangement was adopted at the substrates. This discrepancy would suggest that the interaction described by the rod-surface potential where the particles and substrate sphere have always the same x and y coordinate might be responsible for the tilting behaviour. However, this argument can not be proved just by comparing the results from these existing studies as they employed different forms of the Gay-Berne type surface interaction potential, a 9-3 type in [132] as opposed to 12-6 in [137].

The case of short k_S, that is the case of particles absorbing the substrates, has not been considered in these studies. This case can, however, be readily understood. If the amount of volume absorbed is great enough to induce a significant reduction in the free energy, then a homeotropic arrangement should be more stable, as borne out by the simulation studies of Allen [128].

5.1.2 Simulation results using the RSP.

Further investigations of the surface induced structural changes obtained using the RSP surface potential were performed using Monte Carlo computer simulations in the canonical ensemble. Systems of $N = 1000$ hard Gaussian overlap particles with elongation $k = 3$ confined in an infinitely wide slab geometry of fixed height $L_z = 4k\sigma_0$ were considered, the walls being situated at $z_0 = \pm\frac{L_z}{2}$ and symmetric anchoring conditions applied. Sequence of simulations were performed at constant number density ρ^* and decreasing k_S for several values of ρ^* and the surface induced structural changes were studied using the observable profiles ($\rho^*_\ell(z)$, $Q_{zz}(z)$ and $P_2(z)$) introduced in the previous Chapter. From these profiles, the anchoring and order phase diagrams were computed in the interfacial and bulk regions. These diagrams are shown on Figures 5.3 and 5.4 and were computed using a similar method to that given in the previous Chapter. The difference here was that definition of the boundary between the interfacial and bulk regions was changed such that the interfacial region was taken to extend from the surface to

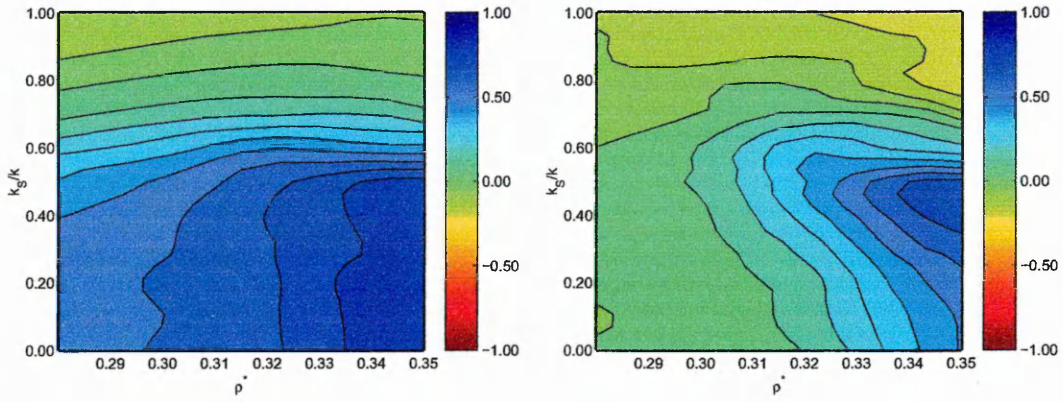

(a) Interfacial region.

(b) Bulk region.

Figure 5.3 : Anchoring phase diagrams obtained from series of simulations of $N = 1000$ *confined HGO particles with* $k = 3$ *at constant density and decreasing* k_S *and using the RSP surface potential.*

the second maximum of ρ_ℓ^* regardless of the surface arrangement obtained for this model. The reason for this definition change lies in the similarity between density profiles obtained for this model at different values of k_S: the primary peaks in $\rho_\ell^*(z)$ were always situated at $|z - z_i| > 0.0$ (see *e.g.* Figures 5.6 and 5.7). Further details regarding these profiles are given later in this Section.

Observation of the order and anchoring phase diagrams reveals that the $\overline{P}_2$ diagrams are qualitatively similar to those obtained with the HNW models, whereas there are some qualitative differences in the $\overline{Q}_{zz}$ diagrams.

In the case of short k_S, the $\overline{Q}_{zz}$ behaviour for the RSP model is not unlike that of the HNW model and confirms the predictions made at the end of the last Section. Throughout the density range considered here and for short k_S, the system adopts an homeotropic arrangement where order increases with increased density. This is further confirmed by configuration snapshots (*e.g.* Figure 5.5(a) for the state point $\rho^* = 0.35$, $k_S/k = 0.0$).

In the case of long k_S (*i.e.* $k_S/k > 0.6$), however, there is a qualitative difference between the diagrams shown in Figure 5.3 and their equivalent for the HNW

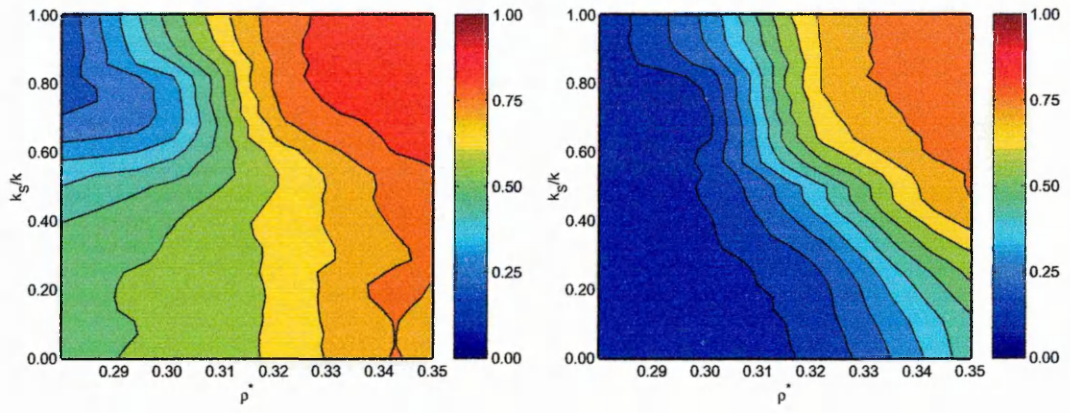

(a) Interfacial region.

(b) Bulk region.

Figure 5.4 : Order phase diagrams obtained from series of simulations of $N = 1000$ *confined HGO particles with* $k = 3$ *at constant density and decreasing* k_S *and using the RSP surface potential.*

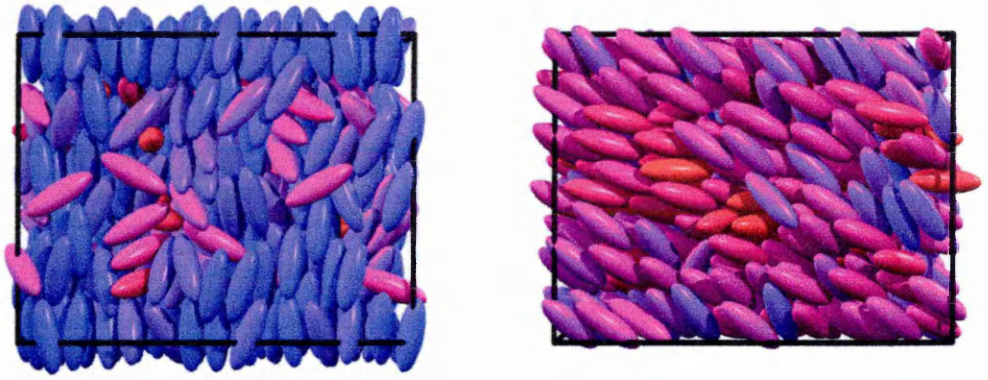

(a) $k_S^{'} = 0.0$

(b) $k_S^{'} = 1.0$

Figure 5.5 : Typical configuration snapshots showing the surface induced homeotropic (a) and tilted (b) surface induced arrangements for confined systems of $N = 1000$ *HGO particles using* $\mathcal{V}^{RSP}$ *for surface interactions and* $\rho^* = 0.35$.

model. Here, throughout the density range considered, the value of $\overline{Q}_{zz}$ does not reach that expected for planar ordering, remaining, instead, low at about 0.2. Although such values can be understood in the low density regime, where $\overline{P}_2$ is compatible with an isotropic phase, this behaviour is rather more surprising in the case of high densities where the corresponding $\overline{P}_2$ diagram shows nematic order. In these latter regions, the low values of $\overline{Q}_{zz}$ are, however, compatible with a tilted arrangement. Observation of typical snapshots for these high densities (*e.g.* Figure 5.5(b)) confirms the presence of a tilt, showing a phase where the average surface alignment is of about $\pi/4$ radians.

Further details of the surface induced structural changes obtained using the RSP potential can be obtained from appropriate z-profiles. These are shown for two states points corresponding to homeotropic and tilted arrangements in Figures 5.6 and 5.7 respectively. These profiles, share some of the features of the equivalent profiles obtained with the HNW potential. The case $k'_S = 0.0$ corresponds to a homeotropic arrangement. This is characterized by positive values of $Q_{zz}(z)$ and peak separations in the oscillations of $\rho^*_\ell(z)$ of about σ_ℓ. The quality of in-plane ordering is similar to that observed with the previous surface potential.
For $k'_S = 1.0$, however, the situation is very different, and there is little similarity between the profiles at $k'_S = 1$ for the RSP and HNW potentials. The layering shown in Figure 5.7 is not as well defined and only two peaks can be clearly observed in $\rho^*_\ell(z)$. Moreover, the peak separation is much larger than σ_0. Finally, $Q_{zz}(z)$ fails to display the negative values associated with planar ordering, even at high density or which the corresponding $P_2(z)$ profile indicates an ordered phase. Those features correspond to a tilted arrangement.

5.1.3 Origin of the tilt

Here, the origins of this tilting behaviour are revisited by studying the form of the RSP as a function of k_S. In Appendix A, it is shown that for a particle with

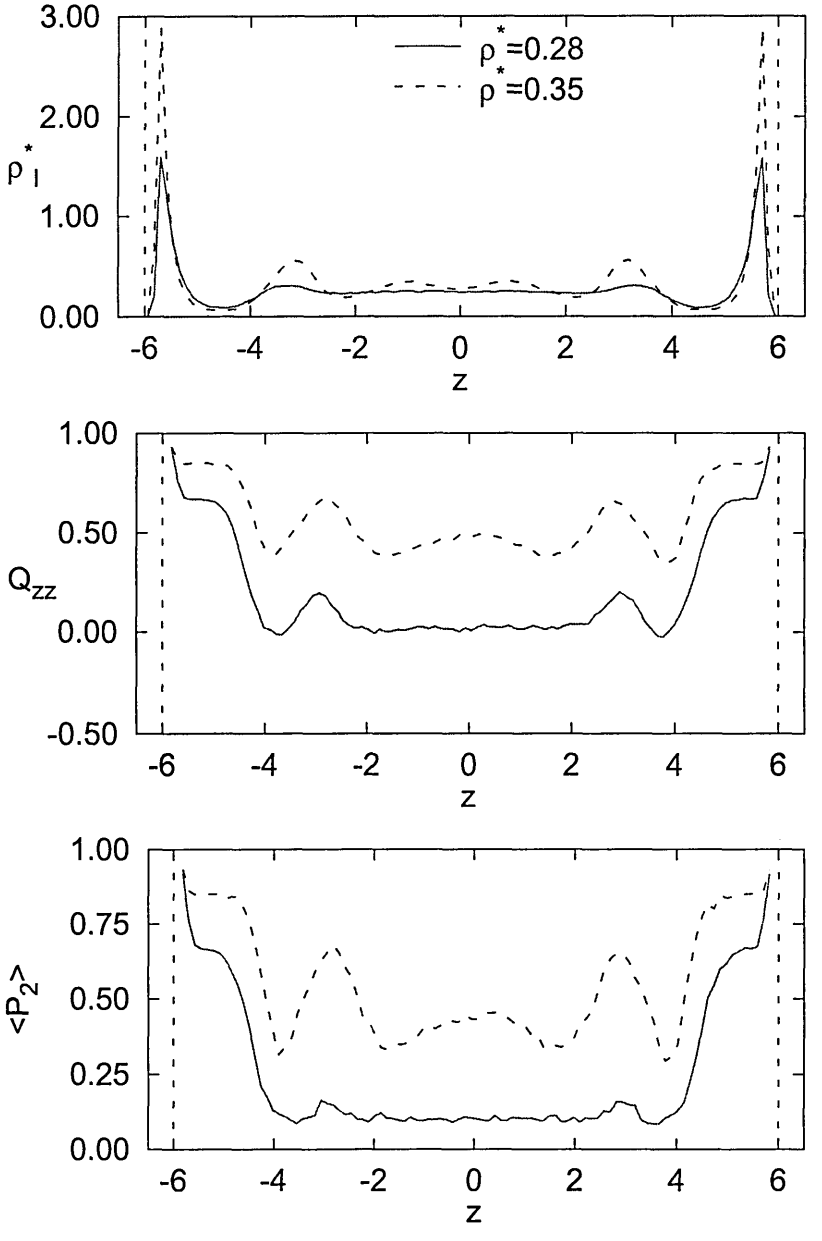

Figure 5.6 : Typical z-profiles for confined systems of HGO particles with $k = 3.0$ and $k'_S = 0.0$ using the RSP potential.

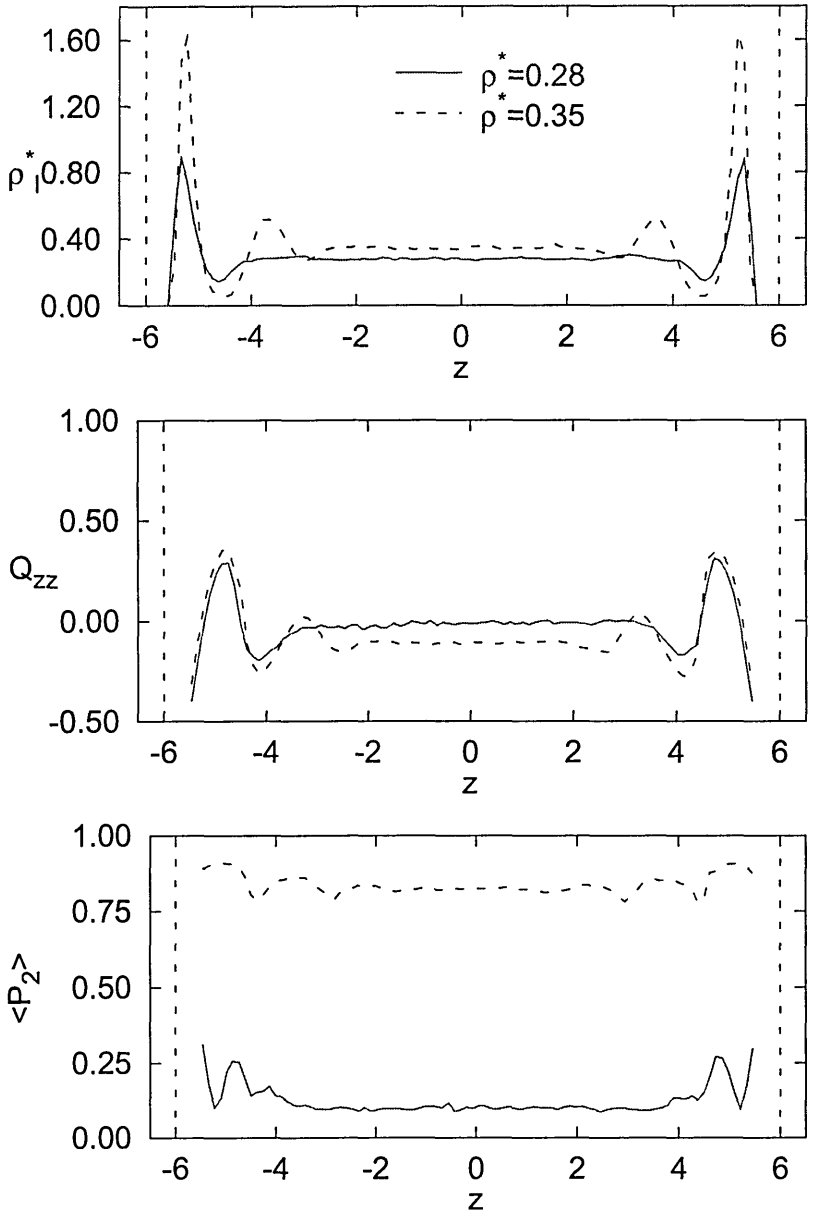

Figure 5.7 : Typical z-profiles for confined systems of HGO particles with $k = 3.0$ and $k_S' = 1.0$ using the RSP potential.

elongation k whose inner ellipsoid is in contact with the substrate surface, the volume $Ve(k_S, \theta)$ absorbed into the surface is given by :

$$Ve = \frac{1}{3}\pi \left(\frac{1}{2} - \sqrt{\frac{\sigma_w^{RSP}}{k^2 \cos^2\theta + \sin^2\theta}} \right)^2 \left(1 + \sqrt{\frac{\sigma_w^{RSP}}{k^2 \cos^2\theta + \sin^2\theta}} \right) \tag{5.5}$$

A graphical representation of this absorbed volume is given in Figure 5.8 for a particle of elongation $k = 3$. The preferred surface induced arrangements can be associated with the maxima in $Ve(k_S, \theta)$. For short k_S, $Ve(k_S, \theta)$ is maximal at $\theta = 0$ and, therefore, the most stable arrangement is homeotropic. In the limit of $k_S = k$, however $Ve(k_S, \theta)$ is maximal for intermediate θ, which suggests that a tilted arrangement may be most stable.

More insight into this result can be found in the expression of the surface potential (Equation 5.3). In the case $k_S = k$, σ_w^{HNW} represents the distance from the substrate to the particle's centre of mass when one of its needle's ends is in contact with the surface plane. σ_w^{RSP}, in contrast, indicates whether or not the HGO particle overlaps a sphere embedded within the substrate.
The difference between the two shape parameter (Figure 5.9) shows that there are some tilt angle for which σ_w^{RSP} is smaller than σ_w^{HNW}, that is the particle ends are able to overlap the surface plane. This region of reduced σ_w^{RSP} coincides with the maximum in $Ve(k_s, \theta)$ and, therefore, can be associated with the tilt behaviour.

The optimum tilt angle θ_{tilt} for which the absorbed volume of a single particle is maximal can be calculated for different values of k. By considering the absorbed volume given by Equation 5.5 and setting $k_S = k$, an expression for $Ve(k, \theta)$ (Figure 5.10) can be obtained. θ_{tilt}, the angle which maximizes $Ve(k, \theta)$, is the angle that solves :

$$\frac{d}{d\theta} Ve(k, \theta) = 0 \tag{5.6}$$

where $\frac{d}{d\theta} Ve(k, \theta)$ is given by :

$$\frac{d}{d\theta} Ve(k, \theta) = k\pi \left(\frac{A_0 (B_0 + C_0)}{D_0} - \frac{A_0 F_0 (B_0 + C_0)}{I_0} \right). \tag{5.7}$$

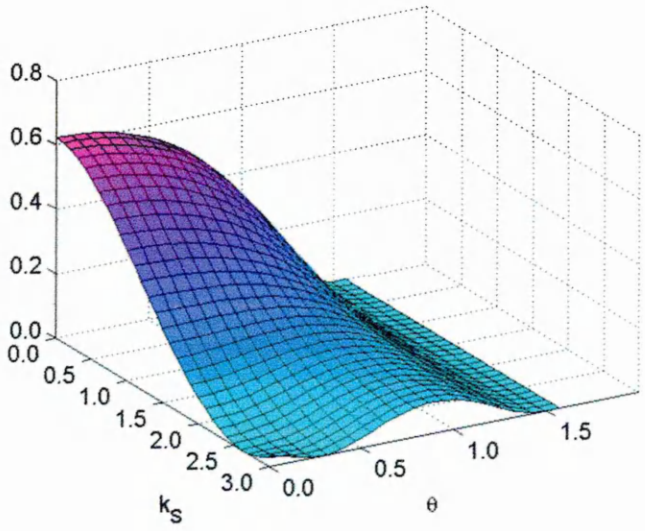

Figure 5.8 : Representation of $Ve(kS, \theta)$ *for the RSP potential and* $k = 3$.

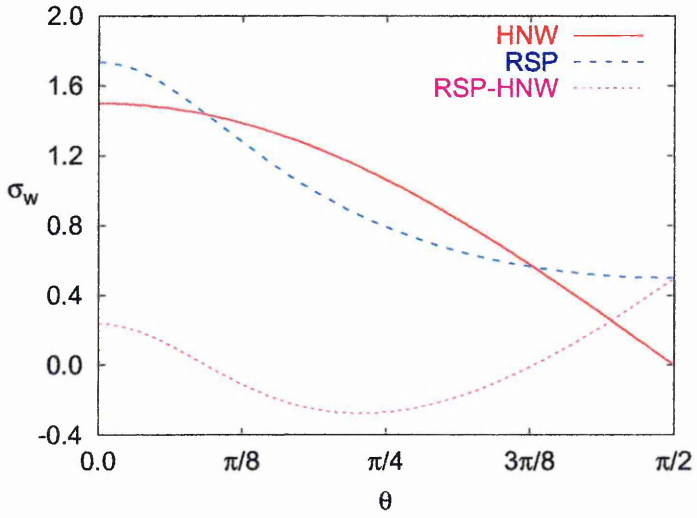

Figure 5.9 : Comparison between σ_w^{HNW} *(solid line) and* σ_w^{RSP} *(dashed line). The dotted line represents the difference between the two* ($\sigma_w^{RSP} - \sigma_w^{HNW}$.)

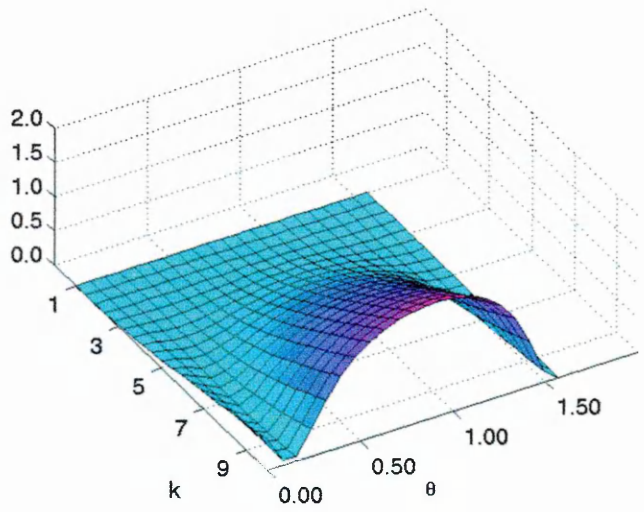

Figure 5.10 : Representation of $Ve(k,\theta)$ for the RSP potential and $k_S = k$.

Here :

$$\begin{aligned}
A_0 &= \left(\frac{1}{2} - \sqrt{\frac{A^2}{B}}\right)^2 \\
B_0 &= -\frac{A^2\left(2\cos\theta\sin\theta - 2k^2\cos\theta\sin\theta\right)}{B^2} \\
C_0 &= -\frac{2A(k^2-1)\cos\theta\sin\theta}{(k^2+1)BC^{\frac{3}{2}}} \\
D_0 &= 6\sqrt{\frac{A^2}{B}} \\
F_0 &= 1 + \sqrt{\frac{A^2}{B}} \\
I_0 &= 3\sqrt{\frac{A^2}{B}}
\end{aligned}$$

and :

$$\begin{aligned}
A &= \frac{1}{\sqrt{C}} - \frac{1}{2} \\
B &= k^2\cos\theta + \sin^2\theta \\
C &= 1 - \frac{(k^2-1)\cos^2\theta}{1+k^2}.
\end{aligned}$$

Equation 5.6 has been solved numerically by computation of the contour of $\frac{d}{d\theta}Ve(k,\theta)$ at level 0, as shown on Figure 5.11. This shows that θ_{tilt} is fairly constant at about

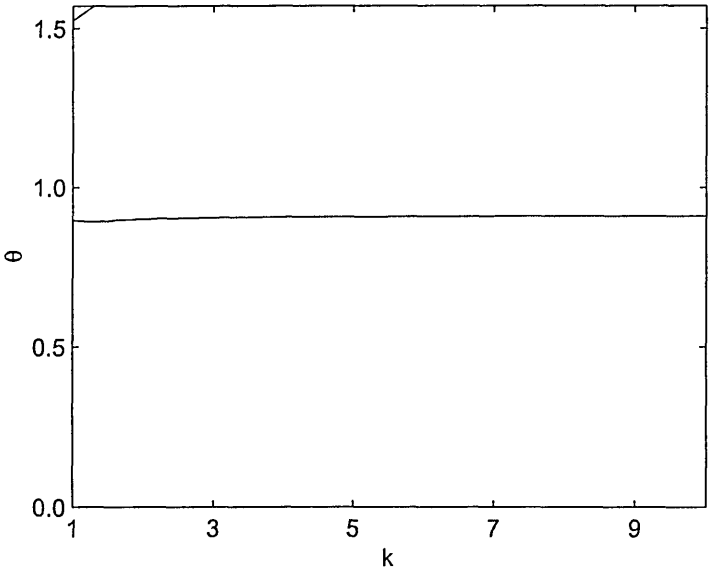

Figure 5.11 : Representation of $\theta_{tilt}(k)$ using the RSP potential and $k_S = k$.

0.9 radians, that is about 50 degrees. As a result, the above treatment suggest that configurations with a tilt angle of about 50 degrees are expected to be favoured from simulations of full HGO particles confined with the RSP potential. However, as many body effects have not been considered here, the existence of such a tilt in a bulk system is not assumed by this result.

That said, the simulations presented in Section 5.1.2 clearly show that such a tilt does develop when using the RSP as a surface potential. Although, the tilt angle was not directly available from observation of the profiles, it can be estimated by use of the definition of $Q_{\alpha\beta}$. At the state point $\rho^* = 0.35$ and $k_S/k = 1.0$ and at the z location where $\rho_\ell^*(z)$ is maximal, $Q_{zz} = 0.209$, this latter value corresponds to the the simulation average. This value of Q_{zz} corresponds to an average tilt angle $\theta = 0.812$ radians, that is 46.6°. This value is consistent with the angle observable on the configuration snapshots.

The difference between the observed and predicted tilt angles (of 9.7%) can be understood from the packing constraints. The packing improves with lower tilt angles which can, in turn, increase system's total absorbed volume. However the

absorbed volume of each particle decreases as the difference between its optimal and actual tilt angles increases. This creates a competition between the amount of absorbed volume that can be obtained with a higher packing fraction but lower average tilt angle and that obtained with an average tilt angle closer to the optimal single particle angle but lower packing fraction.

The simulations and the theoretical treatment described in this Section have shown that a tilted phase can be both predicted and obtained with a purely steric model. As a result, it appears that the tilted phases obtained in [131, 132, 179, 133] arise due to the geometrical characteristics of the rod-sphere potential, rather than competition between packing density and attractive particle-particle and particle-wall interactions. This explanation is consistent with the change from tilted to planar surface alignment observed by Wall and Cleaver [132, 181] when they reduced the molecular elongation from $k = 3$ to $k = 2$. In the latter case, the molecules were too short to significantly absorb at the surface and therefore adopt the planar state. Observation of Figure 5.10 at $k = 2$ confirms this, as for this elongation, the absorbed volume is virtually independent of molecular orientation and, therefore, does not form a tilted arrangement.
In the light of this explanation, it seems reasonable to assume that a planar surface arrangement would have been obtained if the simulations of [132, 179, 133] had been performed using a lattice of fixed spheres to represent the surface, as was done in [137].

5.2 Realistic surface potentials : the RSUP.

5.2.1 The rod-surface potential.

The rod-surface potential (RSUP) represents an alternative interaction between a Gaussian ellipsoid and a plane and is given by :

$$\mathcal{V}^{RSUP} = \begin{cases} 0 & \text{if} \quad |z_i - z_0| \geq \sigma_w^{RSUP} \\ \infty & \text{if} \quad |z_i - z_0| < \sigma_w^{RSUP} \end{cases} \tag{5.8}$$

This time, the contact distance for this is obtained by integration of the rod-sphere potential (without the $\frac{\sigma_0}{2}$ shift) over the x-y plane leading to [180] :

$$\sigma_w^{RSUP} = \sigma_0 \sqrt{\frac{1 - \chi_S \sin^2\theta}{1 - \chi_S}} \tag{5.9}$$

with the same definition for χ_S as with the RSP potential. This potential can be thought of as being equivalent to the RSP but with the important difference that each particle effectively interacts with an infinity of spheres as opposed to just one. Again a shift is introduced so as to remove the virtual spheres from the simulation box. The contact distance used in the simulation is therefore given by :

$$\sigma_w^{RSUP} = \sigma_0 \left(\sqrt{\frac{1 - \chi_S \sin^2\theta}{1 - \chi_S}} - \frac{1}{2} \right). \tag{5.10}$$

A representation of $\sigma_w^{RSUP}(k_S, \theta)$ is given in Figure 5.13 for $k = 3$. Again, the expression for the absorbed volume into the surface can be used to predict the surface behaviour of this model. In the case of the RSUP potential, this volume reads :

$$V_e^{RSUP} = \frac{1}{3}\pi \left(\frac{1}{2} - \sqrt{\frac{\sigma_w^{RSUP}}{k^2 \cos^2\theta + \sin^2\theta}} \right)^2 \left(1 + \sqrt{\frac{\sigma_w^{RSUP}}{k^2 \cos^2\theta + \sin^2\theta}} \right) \tag{5.11}$$

A graphical representation of this volume is shown on Figure 5.14. In the limit $k_S = 0$, $Ve^{RSUP}(k_S, \theta)$ has its maximum at $\theta = 0$ thus indicating an homeotropic arrangement.

In the limit $k_S = k$, V_e^{RSUP} is close to zero for all θ and has a small maximum

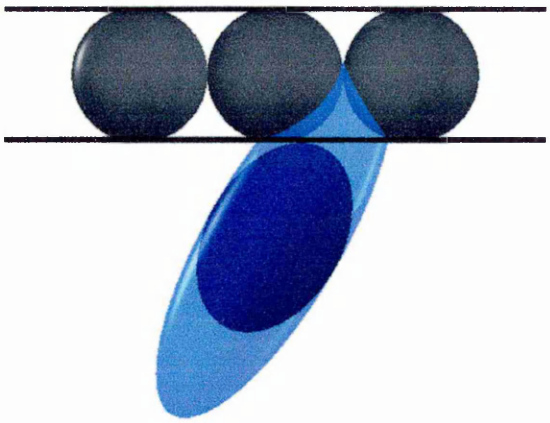

Figure 5.12 : Representation of the geometry used for the interaction between the inner HGO particle and the surface in the RSUP potential. The three spheres represent the substrate which is really made of an infinity of such spheres located between the horizontal lines which effectively mark the substrate location.

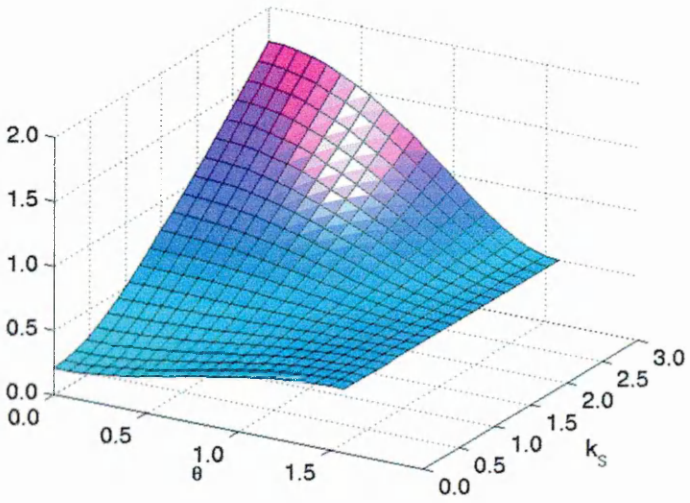

Figure 5.13 : Representation of $\sigma^{RSUP}(k_S, \theta)$ for $k = 3$ using the RSUP potential.

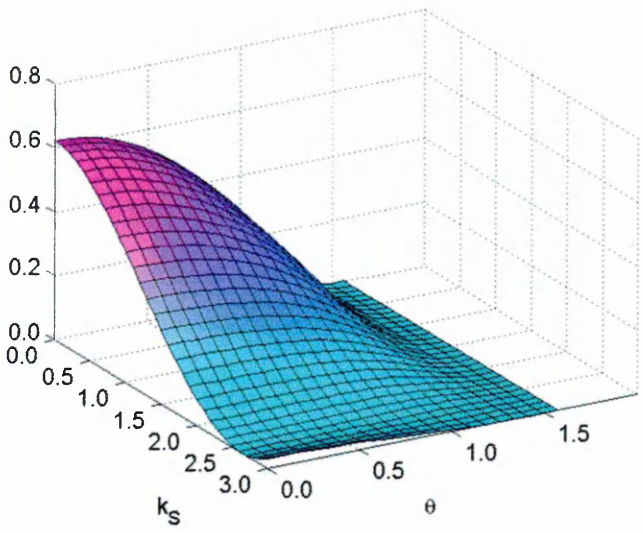

Figure 5.14 : Representation of $Ve(k_s, \theta)$ for the RSUP potential and $k = 3$.

at $\theta = 0$. However, by design, σ_w^{RSUP} forbids any particle adsorption into the substrate if $k_S = k$; this is even further illustrated by the value of $\sigma_w^{RSUP}(k_S = k, \theta = 0)$ which is equal to the contact distance between a HGO particle with $\theta = 0$ and a sphere. As a result, this small maximum in V_e^{RSUP} can be explained to be a result of the approximation of using ellipsoidal shaped particles in Appendix A when deriving the expression for V_e^{RSUP} and, therefore, $V_e^{RSUP}(k_S = k), \theta$ should, in fact, be zero for all values of θ. A consequence of this, the $\theta = 0$ peak in Figure 5.11 does not represent a stable surface arrangement of the RSUP model in the case $k_S = k$, as this is not absorption driven. Rather, it can be safely assumed that the stable arrangement for this system is planar, in common with the findings of previous theoretical and simulation work on rod-shaped objects absorbed at planar surfaces [182, 141, 138, 140].

The mechanism expected to drive an anchoring transition with the RSUP potential is slightly different from that seen with the HNW potential. With the latter, the surface rearrangement is mainly driven by the molecular volume that can be absorbed into the surface, and the transition from homeotropic to planar arrangements occurs when the volume absorbed by the latter is greater than with the former arrangement. In the case of the RSUP potential, however, there is no

absorption in the case of the planar arrangement. However, this is the base state of any rod-shaped object in contact with a surface. Thus, as k_S is decreased from $k_S = k$ to $k_S = 0$, the volume that can be absorbed in a homeotropic arrangement gradually increases. In this case, therefore, an anchoring transition from planar to homeotropic arrangement is expected when the volume that can be absorbed by an homeotropic surface induces a total free energy lower than in that of the planar base state.

5.2.2 Simulation results obtained using the rod-surface potential.

The surface induced structural changes obtained from the rod-surface potential have been studied using Monte Carlo simulations in the canonical ensemble on systems of $N = 1000$ HGO particles with elongation $k = 3$. The simulation slab was the same as that used previously, with the walls situated on the top and bottom of the cell with constant height $L_z = 4k\sigma_0$ and symmetric anchoring conditions. Two series of simulations at each chosen density were performed with,respectively, increasing and decreasing k_S. Typical z-profiles for this model are shown on Figures 5.15 and 5.16 respectively for $k_S = 0.0$ and $k_S = k$.

In the limit of $k_S = 0$, the surface induced structural changes for this model are very similar to their counterparts with the RSP model (Figures 5.6 and 5.7); the two sets of profiles are virtually indistinguishable. The surface arrangement is homeotropic which explains the very strong similarities between the two sets; with $\theta \sim 0$, both models induce the same geometry between the particles and the substrate.

In the limit $k_S = k$, the surface induced effects for $\mathcal{V}^{RSP}$ and $\mathcal{V}^{RSUP}$ are very different. The short peak separation in $\rho_\ell^*(z)$ and the negative values in $Q_{zz}(z)$, coupled with the high values of $P_2(z)$, indicate an induced planar surface arrangement very much in agreement with the predictions made earlier. This is further confirmed by the similarity of the planar arrangement profile features for

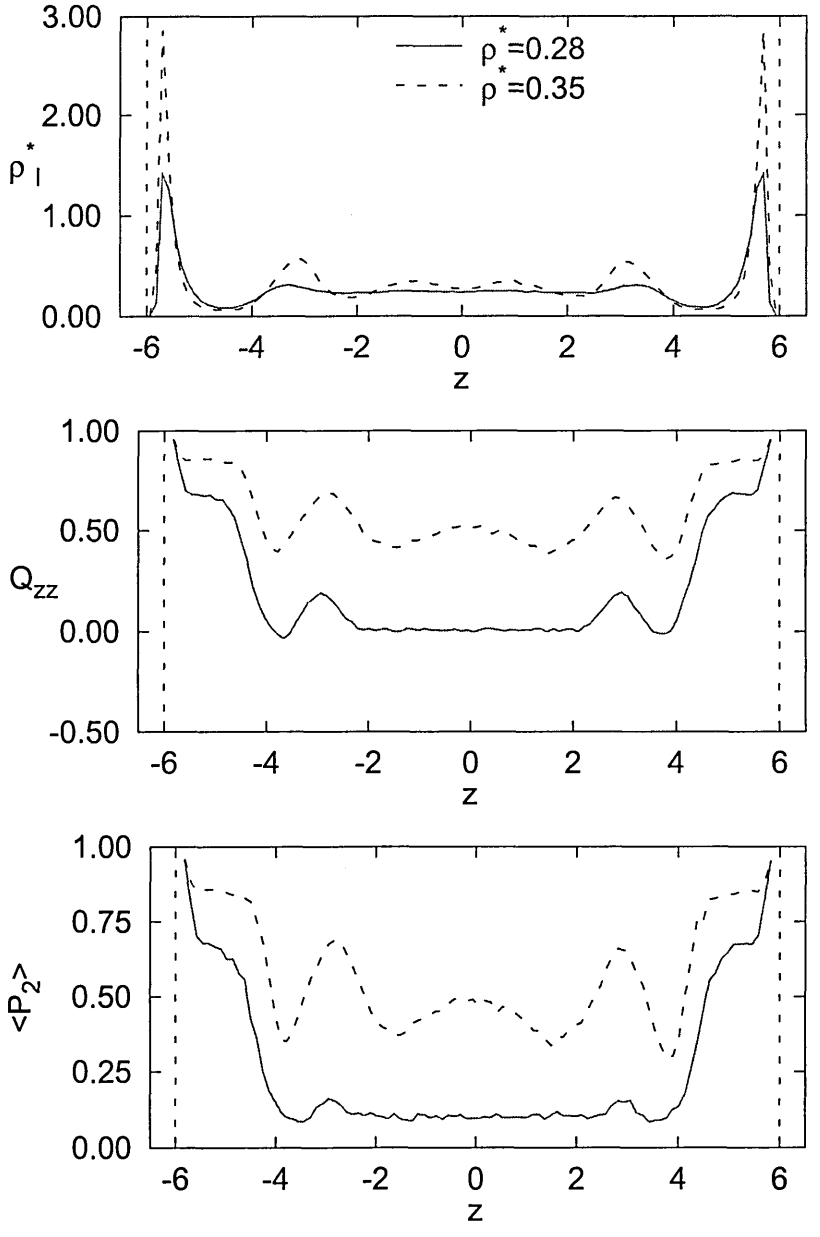

Figure 5.15 : Typical z-profiles for confined systems of $N = 1000$ HGO particles with $k = 3.0$ and $k'_S = 0.0$ using the RSUP potential.

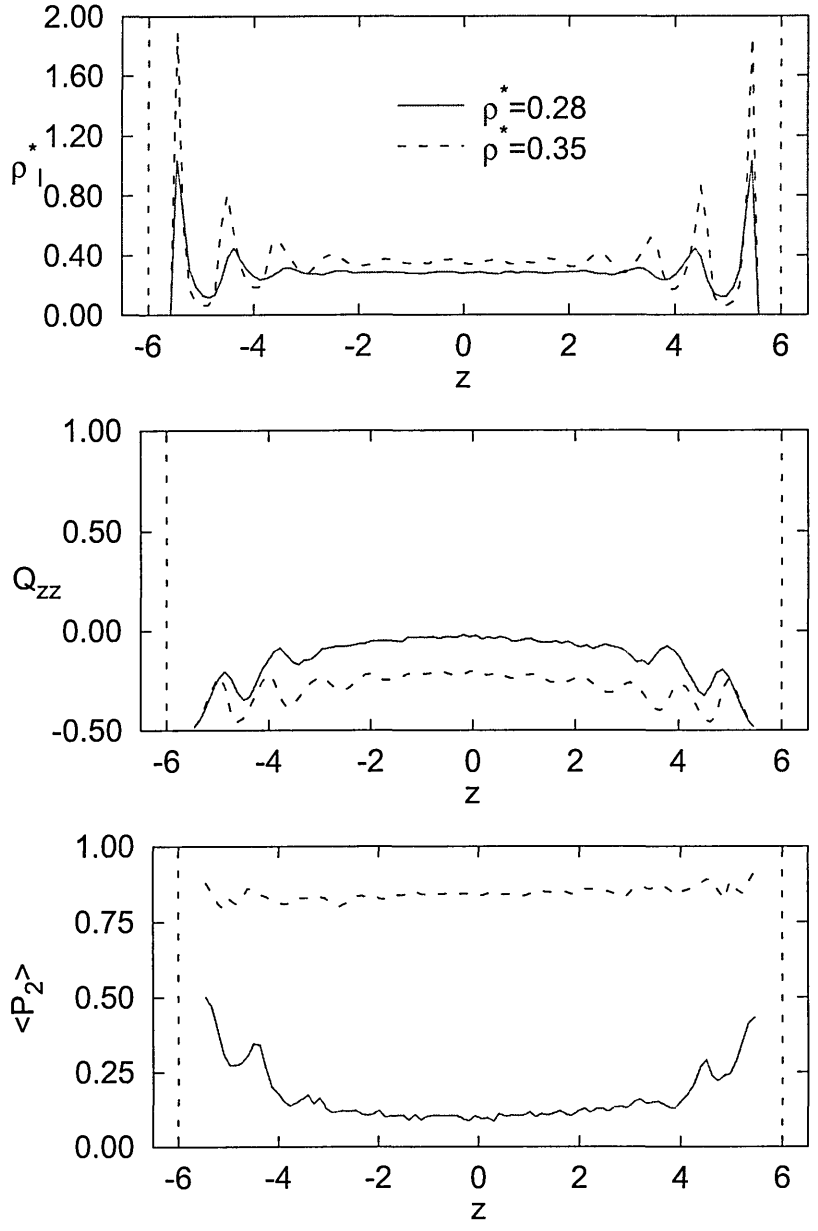

Figure 5.16 : Typical z-profiles for confined systems of $N = 1000$ HGO particles with $k = 3.0$ and $k'_S = 1.0$ using the RSUP potential.

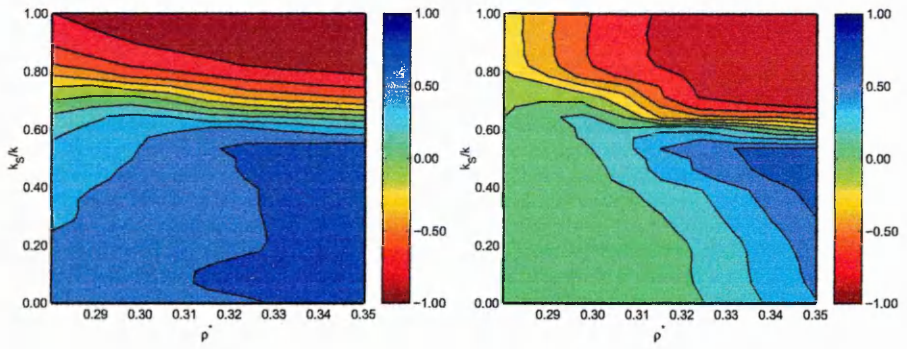

(a) Simulations with decreasing k_S

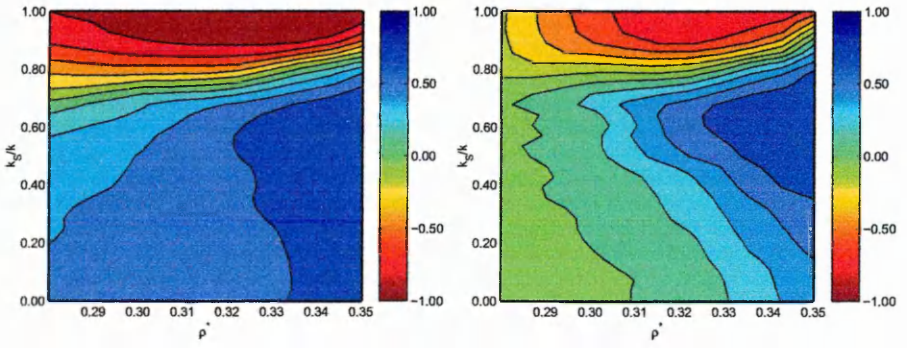

(b) Simulations with increasing k_S

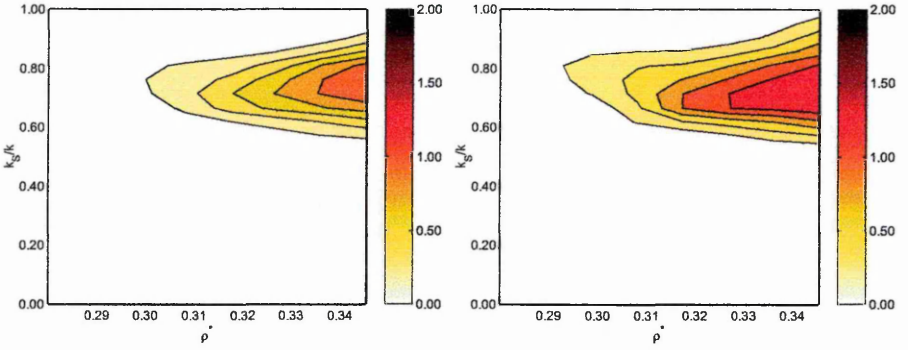

(c) Bistability diagrams

Figure 5.17 : Anchoring phase diagrams obtained from series of simulations of $N = 1000$ *confined HGO particles with* $k = 3$ *at constant density and decreasing* k_S *using the RSUP surface potential. Diagrams on the l.h.s are relative to the interfacial region and those on the r.h.s are relative to the bulk region.*

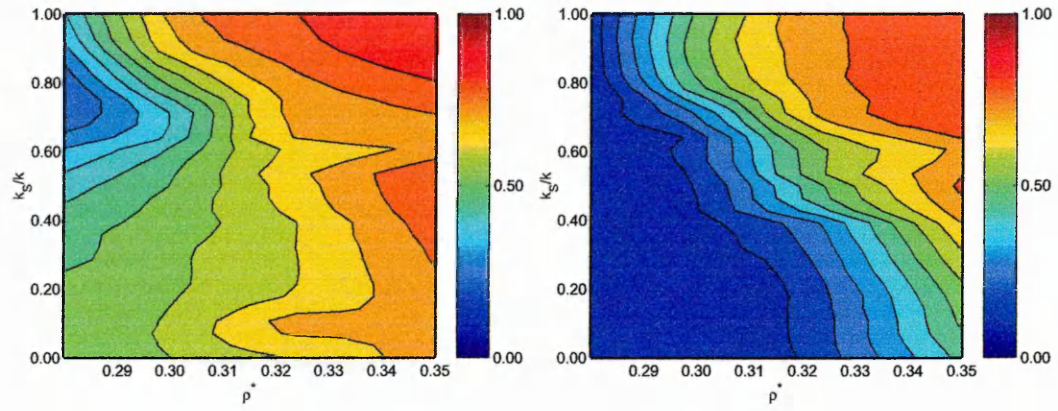

(a) Simulations with decreasing k_S

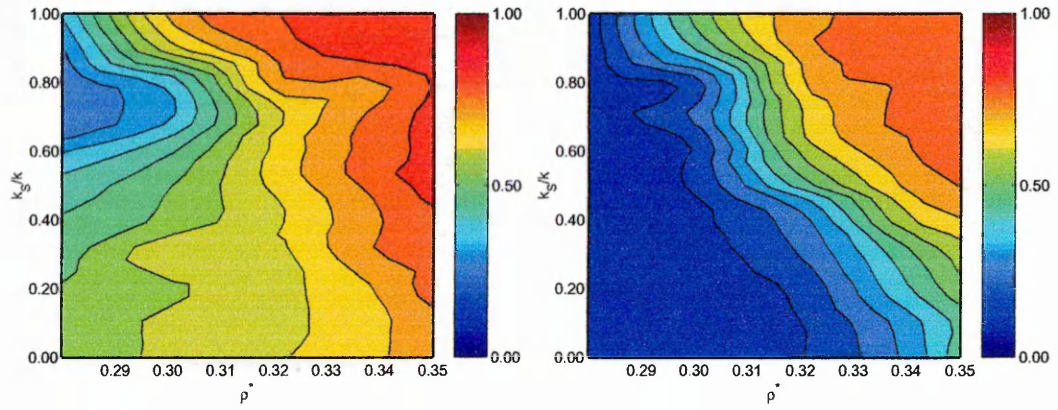

(b) Simulations with increasing k_S

Figure 5.18 : Order phase diagrams obtained from series of simulations of $N = 1000$ confined HGO particles with $k = 3$ at constant density and decreasing k_S using the RSUP surface potential. Diagrams on the l.h.s are relative to the interfacial region and those on the r.h.s are relative to the bulk region. The bistability is negligible.

the HNW and RSUP models. The main difference between the two arises because with the RSUP model, planar particles are not allowed to absorb at the surface. This leads to the regions of zero $\rho_\ell^*(z)$ with a width of $0.5\sigma_0$ close to each substrate.

The full surface induced behaviour of this system has been computed as a function of k_S and θ using the anchoring and order phase diagrams shown in Figures 5.17 and 5.18. The convention adopted to distinguish the interfacial from the bulk region was the same as that used with the RSP model. The anchoring phase diagrams are given in Figure 5.17(a) and (b) for, respectively, decreasing and increasing k_S. From those a strong difference between the two sets can be observed. The corresponding bistability phase diagrams (Figure 5.17c) reports a very wide and strong bistability behaviour for this surface potential. The region of bistability is much greater here than that obtained using the HNW potential, extending over a wider range of density and k_S. Also for a given state point, this potential induces larger bistability values. This makes the RSUP model a very good candidate for the modeling of switching between the two arrangements on a bistable surface.

The improved bistability of the RSUP model when compared with the HNW model lies in the difference between the mechanisms driving the surface-induced anchoring. For the HNW, the competition between the planar and homeotropic alignment is driven by the amount of volume that can be absorbed into the surface for each alignment. This is slightly different from the RSUP case where the planar alignment is the natural state of the system and does not rely on the particles absorbing the surface; homeotropic alignment is introduced as an alternative to this natural states by increasing the possibility of absorption when reducing k_S. As a result the free energy minima corresponding to the two alignments for the two potentials are subtly different. Although free energy data were not determined in this study, the stronger bistability obtained for the RSUP model suggest it has a higher and wider energy barrier between the two locally stable alignment states.

The order phase diagrams for the RSUP model (Fig 5.18) show the same general features as the corresponding diagrams calculated for the HNW model. In the bulk region, the two data sets are very similar. However, the diagrams for the interfacial region present some differences in that the high symmetry around the transition line and the strong disordering of the particles at the transition are diminished somewhat. This can be attributed to the difference in the ρ_ℓ^* profiles for the two potentials, the profiles for the RSUP potential lacking the disorder-related double peak behaviour. As a result, in the case of competing alignment, the local surface order was not reduced due to particles diffusing between the two regions corresponding to the two density peaks.

5.3 Hybrid anchored systems.

In this Section the study of hybrid anchored confined systems is addressed using particles confined in a slab geometry but with different anchoring conditions at each of the two surfaces. This study is performed using Monte Carlo simulations of hard Gaussian overlap particles confined in a slab geometry and interacting with the surfaces through the hard needle wall potential. The aim here is to achieve switching between the Hybrid Aligned Nematic (HAN) and Vertical (V) states using an electrical field as described in [1]. The difference between the switching investigated here and that in Reference [1] is that due the absence of flexoelectricity in the HGO model, two-way switching is attempted by changing the sign of the particles' dielectric anisotropy (as was done in Chapter 4) rather than the sign of the applied field.

5.3.1 Effect of hybrid anchoring.

Here the effects of hybrid anchoring on a confined system are studied ; more specifically the case of different arrangements (*i.e.* planar and homeotropic at two substrates) is of interest.

Cleaver and Teixeira [142] have already studied the structural transition between the arrangements seeded at the surfaces of an hybrid anchored cell of hard Gaussian overlap particles with $k = 5$. They showed that the cell can exhibit either a continuous or discontinuous transition between the homeotropic and planar arrangements according to the values of the surface parameters. This implies that the observation of an HAN state requires an appropriate choice of surface anchoring strengths so as to avoid any director discontinuities. Also, achieving electric-field induced switching requires that the substrate parameters used are compatible with those corresponding to a bistable surface.

Here, the case of hybrid anchored slabs has been investigated using Monte Carlo simulations of systems of $N = 1000$ hard Gaussian overlap particles of elongation $k = 3$ and 5 confined in a slab geometry and interacting with the surfaces using the hard needle wall potential. The anchoring at the top was kept constant at $k'_S = 0.0$ so as to induce strong homeotropic anchoring. The anchoring at the bottom surface was allowed to vary using sequences of simulations with increasing and decreasing k'_S in the range $[0 : 1]$.

Typical profiles for systems with parameterisations at the bottom surface corresponding, respectively, to homeotropic ($k'_{Sb} = 0.2$), competing ($k'_{Sb} = 0.5$) and planar anchoring ($k'_{Sb} = 0.8$) are shown on Figures 5.19 to 5.21. These profiles were obtained from the simulation sequences performed with decreasing k'_{Sb}. Only these results are shown because even in the case of the competing anchoring parameterisation, both series gave very similar results. Also, the profiles or configuration snapshots obtained from simulations with particles of elongation $k = 5$ are not shown as they are very similar to those obtained with $k = 3$.

For all profiles, the top interfacial regions exhibit the features typical of strong homeotropic anchoring as k_{St} was kept constant at 0.0. The bottom surface profiles exhibit features corresponding to the values of the needle lengths used ; they have the same characteristics as were observed in the equivalent cases with symmetric surfaces.

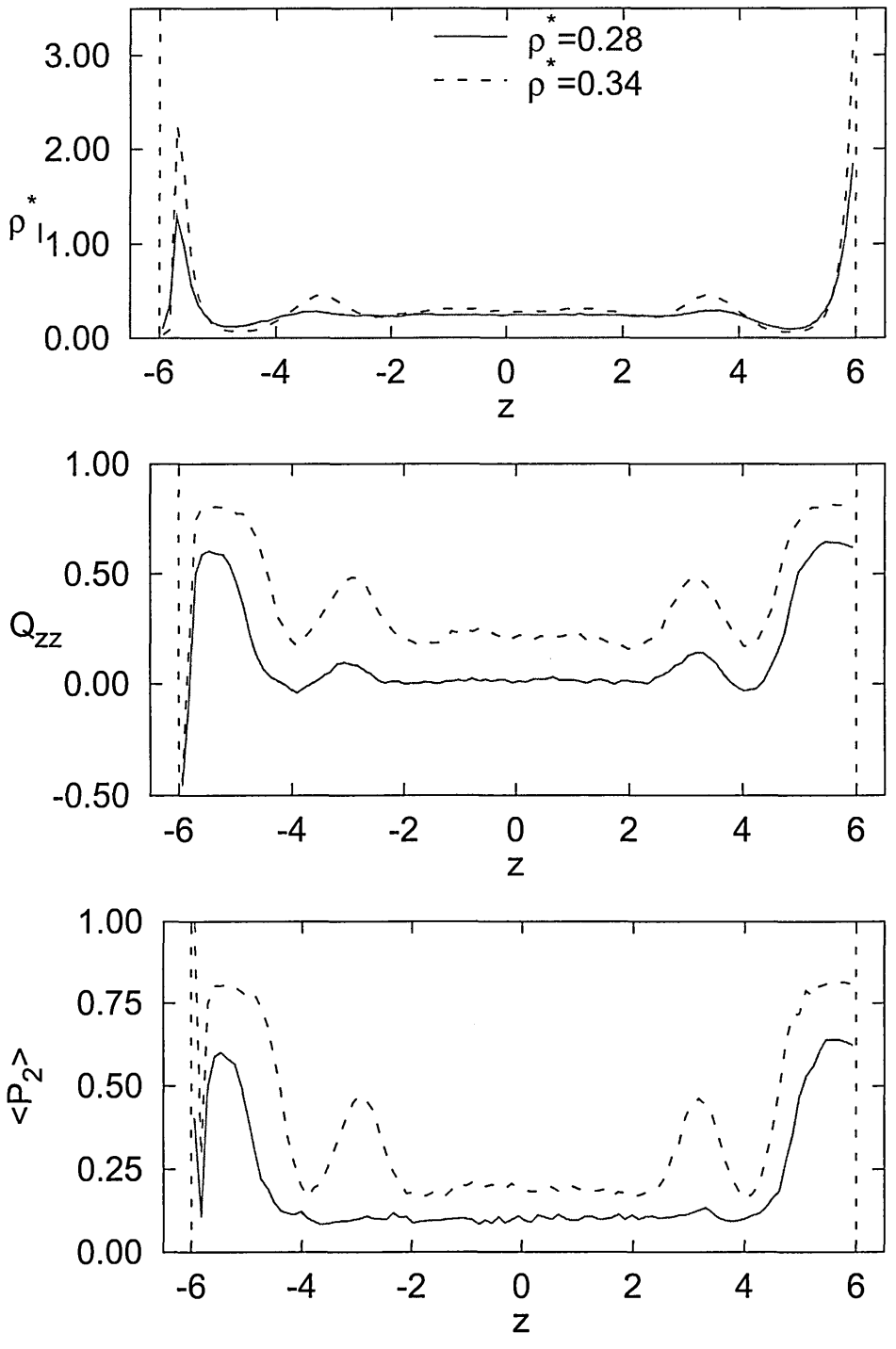

Figure 5.19 : Typical profiles for a hybrid anchored slab of $N = 1000$ HGO particles using the HNW surface potential with an homeotropic top surface ($k'_{St} = 0.0$) and an homeotropic bottom surface ($k'_{St} = 0.2$).

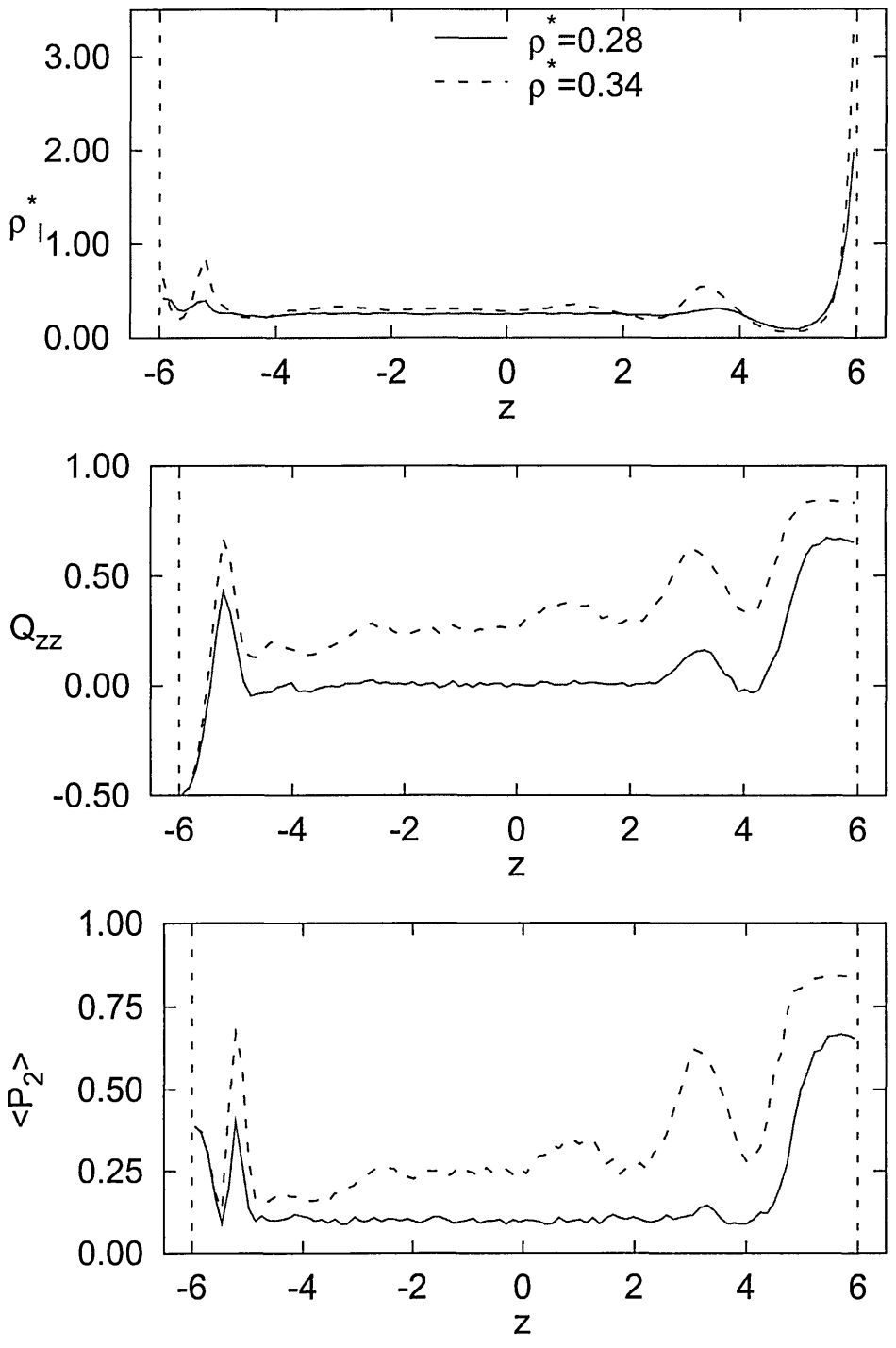

Figure 5.20 : Typical profiles for a hybrid anchored slab of $N = 1000$ HGO particles using the HNW surface potential with an homeotropic top surface ($k'_{St} = 0.0$) and competing anchoring at the bottom surface ($k'_{St} = 0.5$).

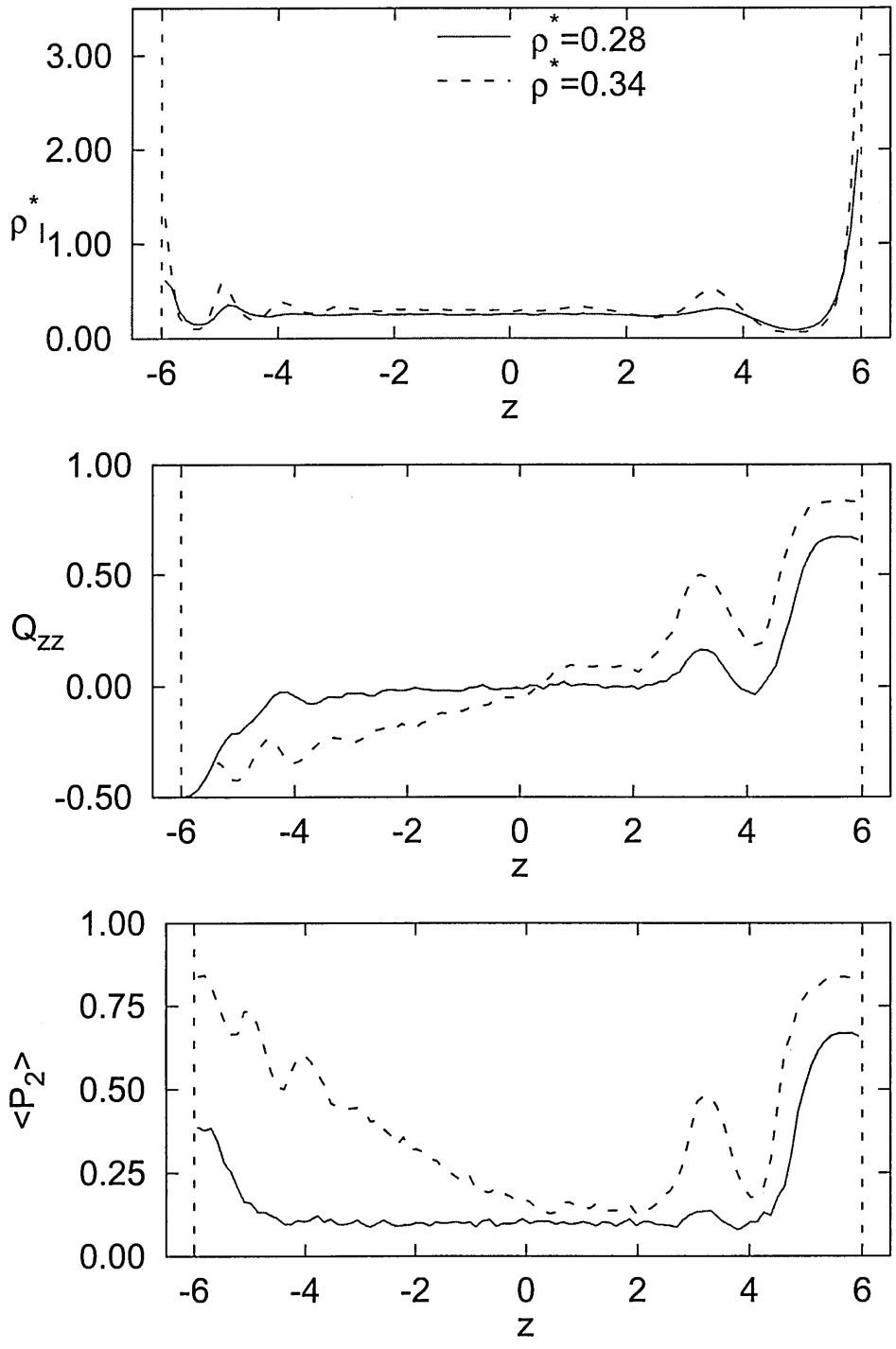

Figure 5.21 : Typical profiles for a hybrid anchored slab of $N = 1000$ HGO particles using the HNW surface potential with an homeotropic top surface ($k'_{St} = 0.0$) and a planar bottom surface ($k'_{St} = 0.8$).

The structural transition between the two surface arrangements, that is the change in molecular orientation from one surface to the other can also be observed on the profiles. At isotropic densities, the surface effects do not extend into the bulk part of the slab and, therefore, this region remains disordered. As a result, both interfacial regions are free of any influence from each other. As the number density is increased to values corresponding to a bulk nematic phase, the surface induced structural changes extend much further into the cell. As a result, the bulk region comes under the competing influences of both surfaces. In all three cases considered here, the profiles seem to indicate a smooth transition between the two surface arrangements, as indicated by the almost linear changes in $\rho_\ell^*(z)$ and $Q_{zz}(z)$ between the surface features.

The structural transition between the surface arrangements can also be observed using configuration snapshots (*e.g.* Figure 5.22). Specifically the case of a slab with planar and homeotropic anchoring is of interest as this corresponds to the geometry where the electric switching is to be performed. For this situation, the snapshots suggest that a slight discontinuity in the planar to homeotropic structural transition can be observed ; the molecular orientation changes rapidly from that corresponding to homeotropic anchoring to that of planar anchoring. This is confirmed by the $< P_2 >$ profile (Figure 5.21) which shows a low value in the bulk part of the cell whereas the snapshots clearly indicate good order throughout the cell. These low values can be understood by the presence of particles with very different orientations in the same slice which in turn lowers the value of $< P_2 >$. This behaviour is not apparent on $Q_{zz}(z)$ as similar values could be obtained from a slice of n particles with $\theta \sim \pi/4$ and a slice of equal number of particles with $\theta \sim 0$ and $\theta \sim \pi/2$.

In the case of a bottom surface with homeotropic or competing anchoring, the profiles and snapshots agree in indicating a continuous structural transition between the two surface induced arrangements. These observation are consistent with

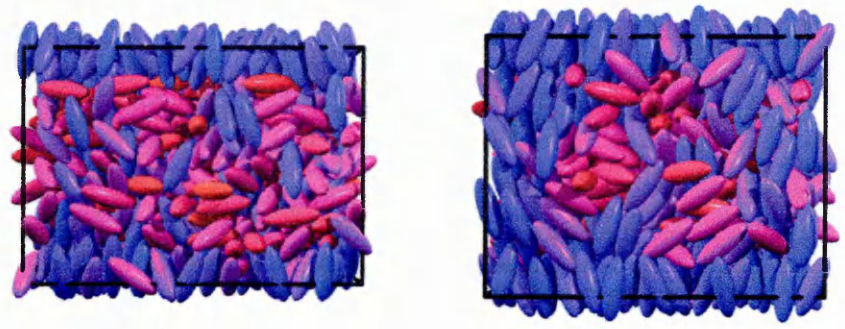

(a) $k'_{Sb} = 0.2$, $\rho^* = 0.28$ (b) $k'_{Sb} = 0.2$, $\rho^* = 0.34$

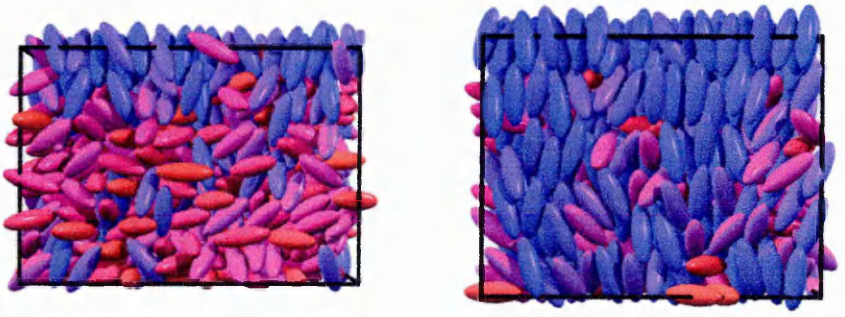

(c) $k'_{Sb} = 0.5$, $\rho^* = 0.28$ (d) $k'_{Sb} = 0.5$, $\rho^* = 0.34$

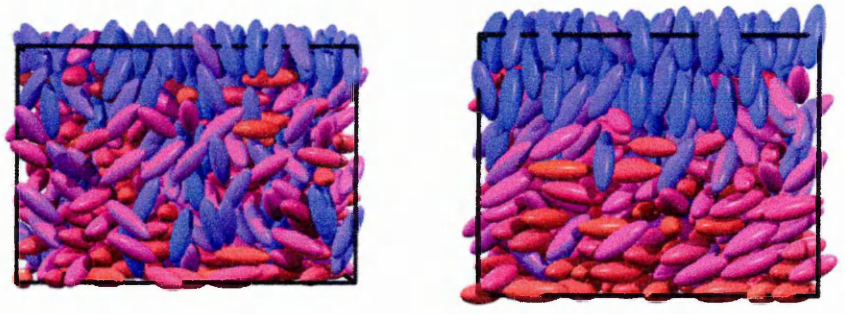

(e) $k'_{Sb} = 0.8$, $\rho^* = 0.28$ (f) $k'_{Sb} = 0.8$, $\rho^* = 0.34$

Figure 5.22 : Configuration snapshots for hybrid anchored slabs with a strong homeotropic anchoring at the top surface ($k'_{St} = 0.0$) and different values for k'_{Sb}. Snapshots for two densities corresponding to isotropic (left) and nematic (right) are shown.

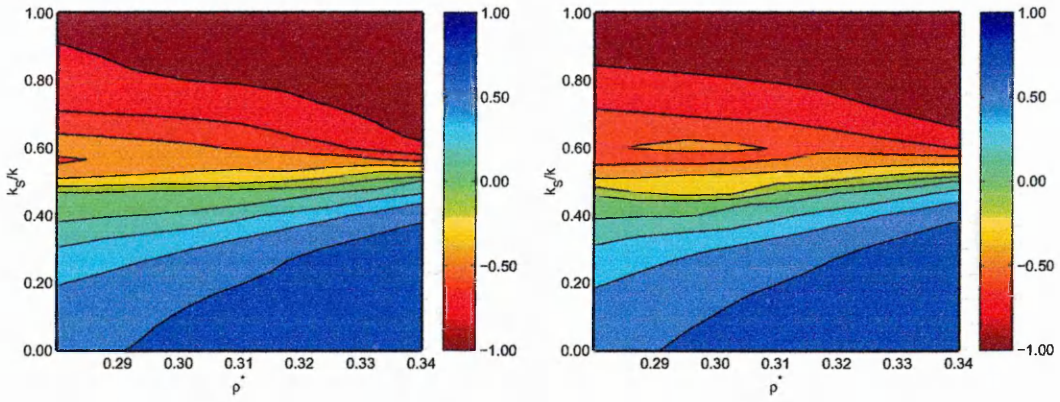

(a) simulations with decreasing k'_{Sb}

(b) simulations with increasing k'_{Sb}

Figure 5.23 : Anchoring phase diagram showing the evolution of $\overline{Q}_{zz}^{Sb}$ of a hybrid anchored slab with $k'_{St} = 0.0$ as a function of number density ρ^* and k'_{Sb}. Systems of $N = 1000$ HGO particles of elongation $k = 3$ and the HNW surface potential have been used.

the simulation of Cleaver and Teixeira [142] who found a discontinuous structural transition between the two surface arrangement provided the anchoring conditions of the two surfaces are made sufficiently different.

The combined effects of density and needle length are shown on the anchoring phase diagrams computed for the bottom surfaces ($\overline{Q}_{zz}^{Sb}$). These were computed using the approach adopted with symmetric systems and are shown in Figure 5.23. The behaviour of $\overline{Q}_{zz}^{Sb}$ for these systems is very similar to that of $\overline{Q}_{zz}^{Su}$ for the symmetric systems and the same remarks apply. However, one striking difference is that, in the case of hybrid systems, the diagrams from series with increasing and decreasing k'_{Sb} are very similar. This means that the hysteresis used to establish bistable regions is not seen in those systems.

This change can be ascribed to the combined effects of the presence of the top surface with strong homeotropic anchoring and the small height of the slab. As a result of these, the elastic forces imposed on the particles at the bottom surface by those on the top surface prevent the former from adopting a planar orientation for

parameterisations corresponding to weak competing anchoring. The consequence of this is that a planar orientation is only observed at the bottom surface if the corresponding anchoring is strong. But this removes the possibility of bistability.

In order to recover the bistable regions, it is necessary to reduce the elastic forces imposed at the bottom surface by the homeotropic anchoring at the top surface. There are two approaches by which to achieve this: to use a weaker homeotropic anchoring at the top surface; or to increase the height of the slab, (and, therefore, the number of particles in the simulation box). In the next section, the second solution is used in an attempt to regain surface bistability.

5.3.2 System size effect.

Here the influence of the height of the slab on the surface bistability in hybrid system is investigated. This has been performed by considering three slabs of hard Gaussian overlap particles with respective height $L_z = 4k\sigma_0$, $L_z = 6k\sigma_0$ and $L_z = 8k\sigma_0$ respectively . In order to keep the width of the slabs big enough so as to avoid interactions between particles and their own images, increase in the slab height was accompanied with an increase in the system sizes, and the height $L_z = 4k\sigma_0$, $L_z = 6k\sigma_0$ and $L_z = 8k\sigma_0$ correspond respectively $N = 1000$, $N = 1250$ and $N = 2000$. Although the cross section surface of the slabs was not equal for the three systems, the short positional correlation of the systems used should imply that the slabs were wide enough so that only the slab height has an effect on the observed planar to homeotropic surface transition.
These systems were studied using Monte Carlo simulations in the canonical ensemble and using the hard needle wall potential for surface interactions. Extreme hybrid anchoring conditions were considered using $k'_{Sb} = 1.0$ and $k'_{St} = 0.0$. Typical profiles at $\rho^* = 0.35$ are shown on Figure 5.24. Here, for comparison purposes, the z coordinates have been renormalized by L_z.

On those profiles, similar interfacial behaviour can be observed for all three sys-

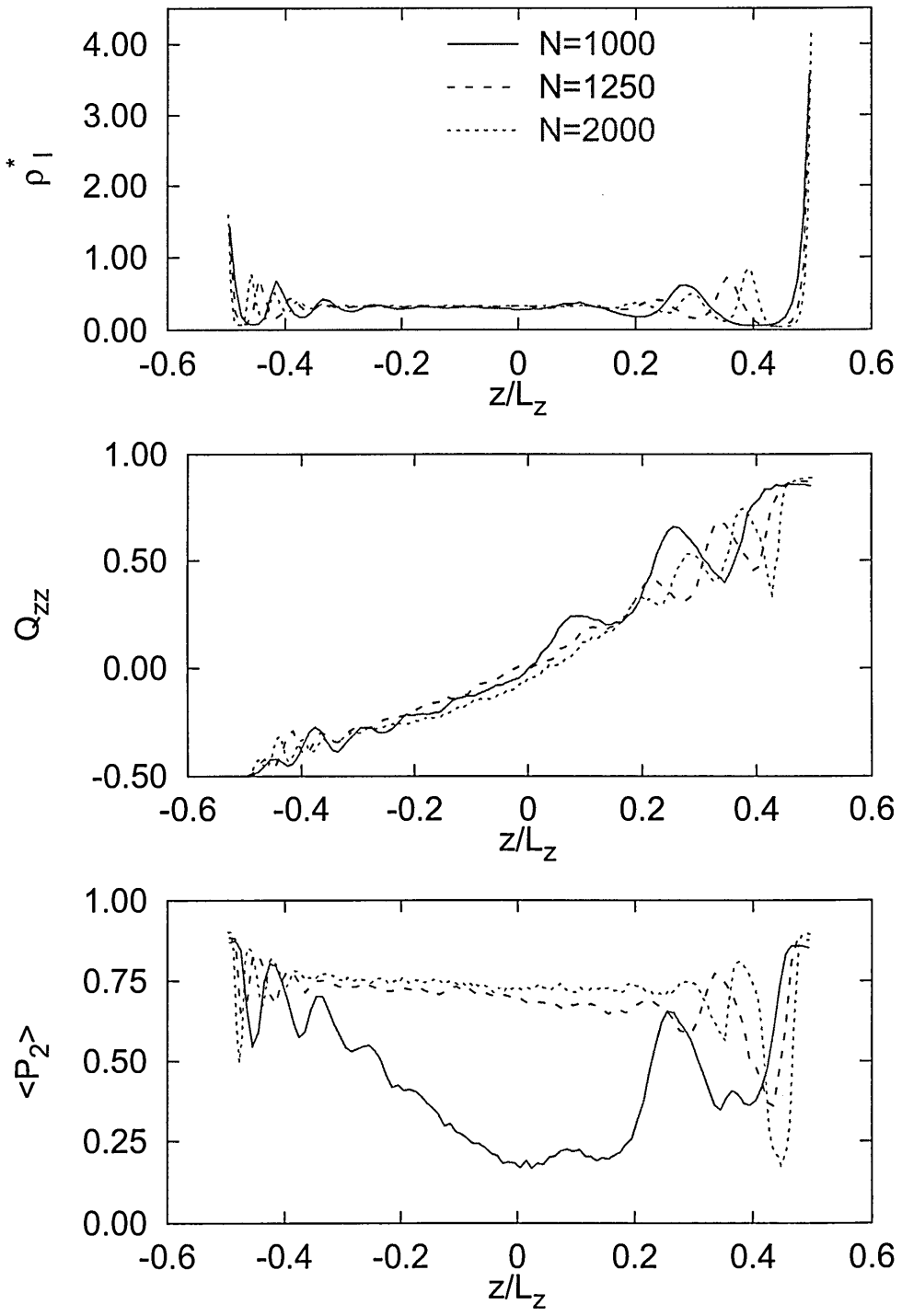

Figure 5.24 : Profiles corresponding to hybrid anchored systems of hard Gaussian overlap particles with $k = 3$ at $\rho^* = 0.35$ and different slab heigh and system sizes. The surface potential is the HNW with parameterisation $k'_{St} = 0.0$ and $k'_{Sb} = 1.0$.

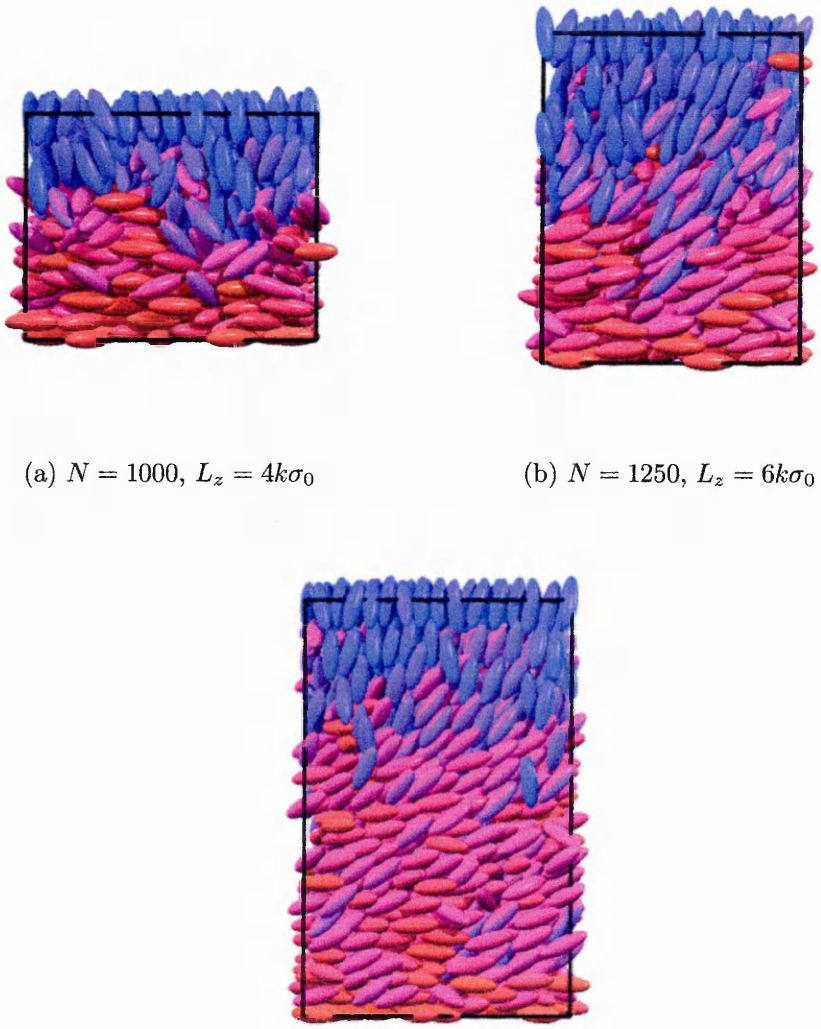

(a) $N = 1000$, $L_z = 4k\sigma_0$

(b) $N = 1250$, $L_z = 6k\sigma_0$

(c) $N = 2000$, $L_z = 8k\sigma_0$

Figure 5.25 : Typical snapshots for hybrid anchored systems of $N = 1000$(a), 1250(b) and 2000(c) hard Gaussian overlap particles with $k = 3$ using the HNW surface potential with $k'_{St} = 0.0$ and $k'_{Sb} = 1.0$.

tems, the profiles displaying features typical of homeotropic anchoring on the top surface and of planar anchoring on the bottom surface.
The $\rho_\ell^*(z/L_z)$ and $Q_{zz}(z/L_z)$ profiles also show similar behaviour for all three systems in the bulk region. All three show a linear increase in Q_{zz} from the bottom to the top surface. The main difference between these is that the regions of linear behaviour extend over larger portions of the cell with increase in L_z, thus indicating bigger 'buffer regions' between the two surfaces.

More important differences can, however, be observed on the $P_2(z/L_z)$ profiles. For the smallest system ($N = 1000$), the $P_2(z/L_z)$ profiles show low values in the bulk regions identified previously. Again, this effect is ascribed to the presence of particles with significantly different orientations in the same analysis slice (Section 5.3.1.) On the other hand, the two bigger systems show very different behaviour, the corresponding $P_2(L_z)$ profiles maintaining high values throughout the cell.
Further insight into this can be obtained from the corresponding configuration snapshots (*e.g.* Figure 5.25). From these, the smallest system clearly shows a discontinuity in the structural transition from planar to homeotropic as can be observed by the rapid change from parallel to perpendicular orientations. The two bigger systems show a different behaviour, however, the transition between the two arrangements being continuous and smooth.
The modest differences between the structures and profiles for the bigger systems with $L_z = 6k\sigma_0$ and $L_z = 8k\sigma_0$ suggest that there is a critical height at which the transition between the two arrangements becomes continuous. The amount of data obtained here only allows to conclude that this critical slab height is in $]4k\sigma_0 : 6k\sigma_0[$.

The results found in this section proved to be fully compatible with the theoretical results of Šarlah and Žummer [144] who found that hybrid anchored films with a thickness of only a few molecular lengths do not show a continuous bent-director

structure. Also, the experimental observation of Vanderbrouck *et al.* [143] confirm the observation made in this Section as they observed that a thin film of 5CB molecules spun cast onto silicon wafer, and thus having planar hybrid anchoring condition at respectively the solid and free surfaces, are stable only if their thickness is greater than 20nm.

5.3.3 HAN to V states switching.

The anchoring phase diagrams presented in Section 5.3.1 have shown no bistability, possibly due to the combination of too strong a homeotropic anchoring at the top surface and the small height used. The smooth structural transitions obtained using larger slab height in Section 5.3.2 suggest, however, that bistable behaviour may be achievable.

As a result switching between the HAN and V states has been attempted. In order to recover the bistability at the bottom surface, a slab of height $L_z = 8k\sigma_0$ and a system size of $N = 2000$ particles have been used and the bottom surface needle length has been set to $k_{Sb}/k = 0.5$ which correspond to a good bistability in an equivalent symmetric anchored system. The first simulations performed used a top surface needle length $k_{St}/k = 0.0$, but that proved to induce too strong an homeotropic anchoring and no bistability at the bottom surface could be observed. By gradually reducing the top surface anchoring strength, the bistability at the bottom surface could be regained using $k'_{St} = 0.4$. Using this latter value of k_{St}, the switching between the HAN and vertical states has been performed using a similar sequence of simulations to that employed in Chapter 4. The evolution of $\overline{Q}_{zz}^{St}$ and $\overline{Q}_{zz}^{Sb}$ as a function of the number of sweeps are shown, respectively, on Figure 5.26(a) and (b). Configuration snapshots corresponding to the last configuration of each phase are shown on Figure 5.27.

The sequence was started using previously equilibrated configuration with a HAN alignment. After $0.5.10^6$ sweeps, an electric field $\mathbf{E} = E\hat{\mathbf{z}}$ with $E = 6.0$ was applied during $0.25.10^6$ sweeps using $\delta\epsilon > 0$ so as to align the particles along $\hat{\mathbf{z}}$.

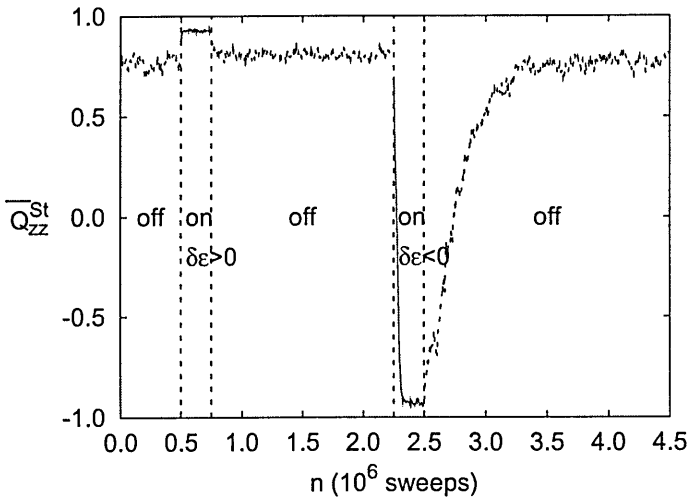

(a) $\overline{Q}_{zz}^{St}(n)$

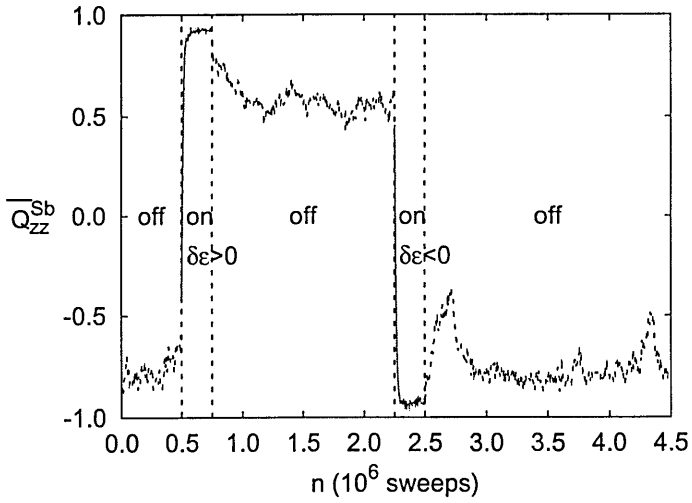

(b) $\overline{Q}_{zz}^{Sb}(n)$

Figure 5.26 : Evolution of $\overline{Q}_{zz}(n)$ as a function of the number of sweeps n for the top(a) and bottom(b) surface regions while switching a hybrid anchored system of $N = 2000$ HGO particles with $k = 3$ between the HAN and V states.

(a) $0.50.10^6$ sweeps (b) $0.75.10^6$ sweeps (c) $2.25.10^6$ sweeps

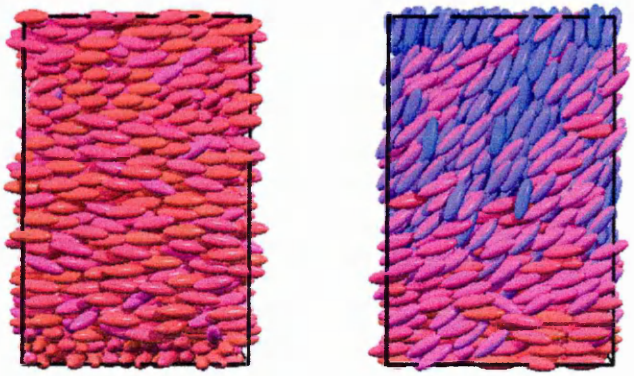

(d) $2.50.10^6$ sweeps (e) $4.50.10^6$ sweeps

Figure 5.27 : Configuration snapshots of a system of $N = 2000$ HGO particles with $k = 3$ at different stages of switching between the HAN and V states.

Upon removal of the field, equilibrium in the vertical state was well established after $1.5.10^6$ sweeps. The field was then reapplied for $0.25.10^6$ sweeps using $\delta\epsilon < 0$ so as to align the particles perpendicular to $\hat{\mathbf{z}}$. Upon removal of the field, equilibrium in the HAN state was achieved after $2.0.10^6$ sweeps.

This sequence shows successful switching between the HAN and vertical states of an hybrid aligned cell corresponding to that considered in [1]. The model used here did not include flexoelectricity and, therefore, only the easy switching namely, HAN to V if $\delta\epsilon > 0$ and V to HAN if $\delta\epsilon < 0$ could be modeled. This is however very encouraging as achievement of the easy switching implies that the reverse ('hard') switching could, in principle, be achieved easily with an appropriate electrical parameterisation of the model.

Conclusion

In this Chapter, two issues have been addressed. In the first part of the Chapter, two more realistic surface potentials have been studied, namely the rod-sphere and the rod-surface potentials. The aim of this work was to find a potential which has a more realistic basis than the hard needle wall potential but which also displays planar and homeotropic surface arrangements. A region of bistability between the two arrangement was also required for future applications relating the modeling of display cells.

The rod-sphere potential was found to be unsuitable as the planar arrangement was replaced by a tilted structure. However, the results obtained using this model proved to be interesting since they showed that a tilted phase can be obtained from purely steric interactions. The rod-surface potential, meanwhile, proved a better candidate for the aim stated above, as it not only recovered the surface behaviour of the HNW potential but actually displayed stronger and wider bistability regions.

In the second part of this Chapter, hybrid anchored systems of HGO particles con-

fined between a homeotropic top surface and a bottom surface with competing anchoring have been studied using the HNW potential for the surface interactions. These simulations showed that the bistability behaviour of the model can be lost if high anchoring strength is used at the top surface or if the slab is too narrow. Using moderate homeotropic anchoring at the top surfaces and systems sizes of $N = 2000$ particles, however, bistability was established and a cell was successfully switched between the HAN and V states if only the easy switching was considered. Achievement of the reverse switching requires the use of flexoelectric particles and a surface potential allowing bistability between planar and homeotropic arrangements for such particles. Those two problems are addressed, respectively, in Chapters 6 and 7.

Chapter 6

Bulk simulations of pear shaped particles

Introduction

The last two Chapters have dealt with surface induced effects in systems of hard Gaussian ellipsoids subject to a range of different surface potentials. For some of these, bistable regions corresponding to different surface arrangements have been found. Here, a new line of work is considered, the focus of which the behaviour of non-centrosymmetric, pear-shaped particles. In the next Chapter, these two threads will be brought together in a study of these pear-shaped particles in confined geometries.

It is recalled that the ultimate aim of this thesis is to model surface induced switching between two arrangements of an hybrid anchored cell following the theoretical treatment of Davidson and Mottram [1]. The system properties required to achieve this are a bistable surface and a stable nematic phase of flexoelectric particles. The former problem has already been addressed; this Chapter deals with the latter. For this, the development of a model for pear-shaped particles is studied as particles of that shape are thought to display flexoelectric behaviour [12].

In this Chapter, two models are studied, the first one hereafter referred to as the HP model is a hard version of the potential used in [2]. Despite having a

rich phase behaviour, we show that this model does not have a stable nematic phase. As a result a second model, which we term the Parametric Hard Gaussian Overlap (PHGO) model, has been developed which does yield the required phase behaviour. The work presented in this Chapter has been submitted for publication to Physical Review E [183].

6.1 The HP model

In 2001, Berardi *et al.* developed the first soft, single site model for non-centrosymmetric anisotropic particles hereafter referred to as the soft pear (SP) model. This model uses a contact distance describing a pear shape embedded within a Gay-Berne like potential. This model was taken as a base for the HP model described here. The HP model defines a steric potential $\mathcal{V}^{\mathrm{HP}}$ between two pear-shaped objects whose contact distance is that of the SP model [2] as :

$$\mathcal{V}^{HP} = \begin{cases} 0 & \text{if} \quad r_{ij} \geq \sigma^{HP}(\hat{\mathbf{u}}_i, \hat{\mathbf{u}}_j, \hat{\mathbf{r}}_{ij}) \\ \infty & \text{if} \quad r_{ij} < \sigma^{HP}(\hat{\mathbf{u}}_i, \hat{\mathbf{u}}_j, \hat{\mathbf{r}}_{ij}) \end{cases} \tag{6.1}$$

where $\sigma^{HP}(\hat{\mathbf{u}}_i, \hat{\mathbf{u}}_j, \hat{\mathbf{r}}_{ij})$ is the contact distance between two particles i and j with orientations $\hat{\mathbf{u}}_i$ and $\hat{\mathbf{u}}_j$ and and $\hat{\mathbf{r}}_{ij} = \frac{\mathbf{r}_{ij}}{r_{ij}}$ where $\mathbf{r}_{ij}$ is the intermolecular separation. With this model, the contact distance is obtained using a numerical method following the approach of Zewdie [106, 107]. The prototype shape of the particles is defined using a set of two Bézier curves (Fig 6.1). The coordinates of the control points of these, $q_{1..6}$, are given in Table 6.1.

Following this a numerical contact distance $\mathcal{L}(\hat{\mathbf{u}}_i, \hat{\mathbf{u}}_j, \hat{\mathbf{r}}_{ij})$ is computed for a given set of $\hat{\mathbf{u}}_i, \hat{\mathbf{u}}_j$. This numerical distance is then fitted to a truncated Stone expansion as :

$$\begin{aligned} \sigma(\hat{\mathbf{u}}_i, \hat{\mathbf{u}}_j, \mathbf{r}_{ij}) &\simeq \mathcal{L}(\hat{\mathbf{u}}_i, \hat{\mathbf{u}}_j, \hat{\mathbf{r}}_{ij}) \\ &= \sum_{L_1, L_2, L_3} \sigma_{L_1,L_2,L_3} S^{*L_1,L_2,L_3}(\hat{\mathbf{u}}_i, \hat{\mathbf{u}}_j, \hat{\mathbf{r}}_{ij}) \end{aligned} \tag{6.2}$$

where S^{L_1,L_2,L_3} is a Stone function [108], and the expansion coefficients σ_{L_1,L_2,L_3}

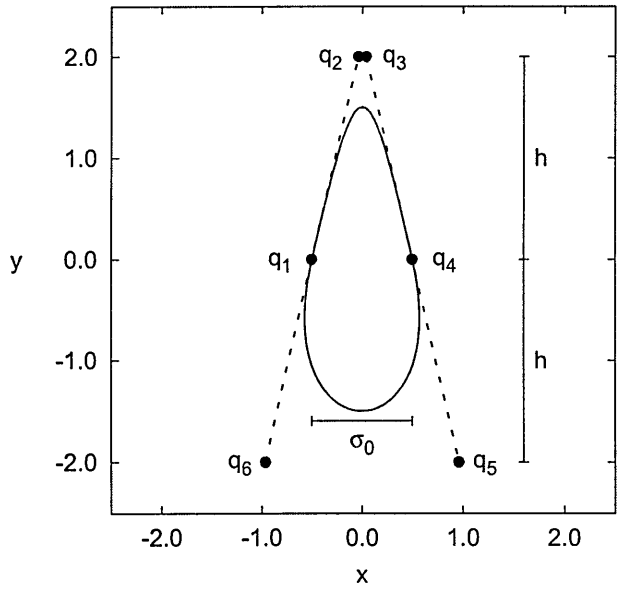

Figure 6.1 : The Bézier curve used for the geometrical definition of the pear shaped of the HP model.

q_i	x	y
q_1	-0.5	0
q_2	$-0.5 + h\tan\alpha$	h
q_3	$0.5 - h\tan\alpha$	h
q_4	0.5	0
q_5	$-0.5 - h\tan\alpha$	$-h$
q_6	$0.5 + h\tan\alpha$	$-h$

Table 6.1 : Coordinates of the Bézier control points for the HP model and $k = 3$.

[000]	1.90456	[011]	0.51113	[101]	0.51113
[022]	2.01467	[202]	2.01467	[033]	−0.11376
[303]	−0.11376	[044]	0.91479	[404]	0.91479
[055]	−0.29937	[505]	−0.29937	[066]	0.41523
[606]	0.41523	[110]	−0.03942	[121]	−0.45400
[211]	−0.45400	[123]	0.59579	[213]	0.59579
[132]	0.17137	[312]	0.17137	[143]	−0.27083
[413]	−0.27083	[220]	−0.56137	[222]	−2.78379
[224]	2.41676	[231]	0.31104	[321]	0.31104
[233]	0.45382	[323]	0.45382	[242]	0.38115
[422]	0.38115	[244]	−1.69388	[424]	−1.69388
[246]	1.40664	[426]	1.40664	[330]	−0.07836
[440]	−0.17713	[442]	−0.52246		

Table 6.2 : The non zero σ_{L_1,L_2,L_3} coefficients for $k = 5$.

are given by :

$$\sigma_{L_1,L_2,L_3} = \frac{\int \mathcal{L}(\hat{\mathbf{u}}_i, \hat{\mathbf{u}}_j, \hat{\mathbf{r}}_{ij}) S^{L_1,L_2,L_3}(\hat{\mathbf{u}}_i, \hat{\mathbf{u}}_j, \hat{\mathbf{r}}_{ij}) d\hat{\mathbf{u}}_i d\hat{\mathbf{u}}_j d\hat{\mathbf{r}}_{ij}}{\int S^{*L_1,L_2,L_3}(\hat{\mathbf{u}}_i, \hat{\mathbf{u}}_j, \hat{\mathbf{r}}_{ij}) S^{L_1,L_2,L_3}(\hat{\mathbf{u}}_i, \hat{\mathbf{u}}_j, \hat{\mathbf{r}}_{ij}) d\hat{\mathbf{u}}_i d\hat{\mathbf{u}}_j d\hat{\mathbf{r}}_{ij}} \tag{6.3}$$

The non-zero coefficients σ_{L_1,L_2,L_3} for particles with elongation $k = 3$ and $\{L_1, L_2, L_3\} \leq 6$ are given in [2] ; the corresponding coefficients for $k = 5$ are given in Table 6.2.

The original study of the SP model revealed stable nematic and smectic phases and, using an appropriate energy parameterisation, the same phases with net polar order were also obtained. A reasonable expectation, therefore, is that the steric version of this model should exhibit at least a stable nematic phase. Such a correlation is found virtually in all soft LC models and their hard-particle equivalent. The best example of this is seen on comparing the Gay-Berne [97, 98] and hard Gaussian overlap phase behaviours [169]. As the former is reduced to its steric equivalent, the smectic phases disappear whereas the nematic-isotropic

phase transition not only persists, but remains at virtually the same density.

As the HP model can not be reduced to the interaction between a particle and a point, the actual shape of the particle and, hence, the accuracy with which this model represents the geometrical Bézier curve is not available. However, for the two elongation considered in this study, some insight into the potential possible behaviour can be obtained by computation of the contact surfaces between two particles. Such surfaces show the location of the contact point between a particle i located at the origin with fixed orientation $\hat{\mathbf{u}}_i$ and a particle j with fixed orientation $\hat{\mathbf{u}}_j$ whose position is uniformly distributed on the unit sphere. Example surfaces, for parallel particles ($\hat{\mathbf{u}}_i = \hat{\mathbf{u}}_j = \hat{\mathbf{z}}$), anti-parallel particles ($\hat{\mathbf{u}}_i = -\hat{\mathbf{u}}_j = \hat{\mathbf{z}}$) and the T-geometry ($\hat{\mathbf{u}}_i = \hat{\mathbf{z}}$, $\hat{\mathbf{u}}_j = \hat{\mathbf{x}}$), are shown on Figure 6.2.

Generally, these show the expected interaction, but it is evident that several non-convex fractures are present; this raises the prospect of possible enhanced stability for some configurations, specifically for those of interlocking side by side anti-parallel particles. The consequence of this would be to unduly stabilize these configurations and as a result prevent particles from 'sliding' along one another. Comparison of these contact surfaces for different elongations reveals different shape and convexity behaviours. Thus rather different phase behaviours are to be expected for systems of particles with different elongations.

Problems related to non convexity of contact surfaces have previously been found by Williamson and Jackson [67] in their study of systems of linear hard sphere chains (LHSC). For that model, the authors noticed that the lack of convexity in the the particle-particle interaction surfaces lead to the formation of glassy phases. For the LHSC model, this problem could be resolved by the inclusion of reptation moves in the Monte Carlo sequence. This, however, is not possible with the single site HP model; the consequence of this is addressed in Section 6.2.

Also the lack of convexity of the contact surfaces for the HP model would suggest that the HP model might display a rather different phase behaviour than that obtained using the SP model. This is because the energy minima of the soft

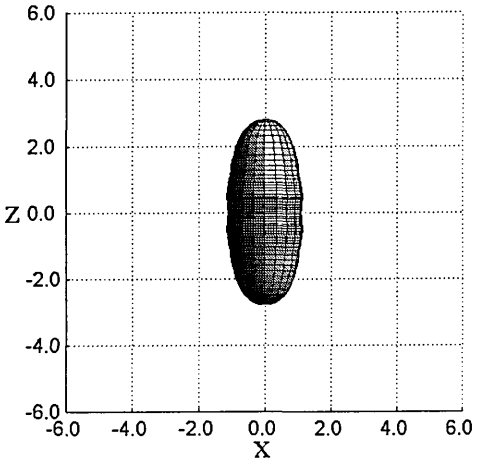

(a) parallel particles

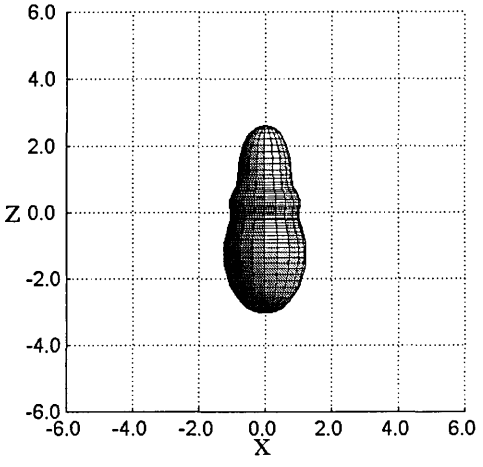

(b) anti-parallel particles

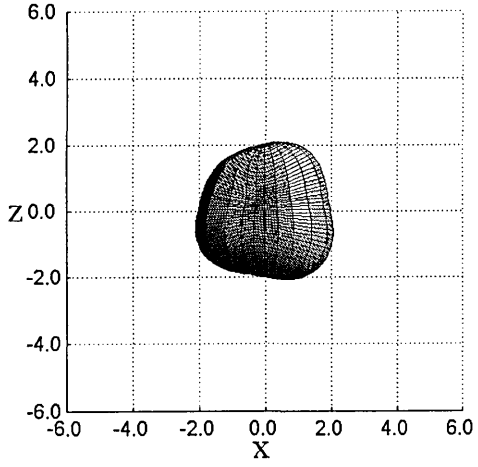

(c) T-geometry, x-z view

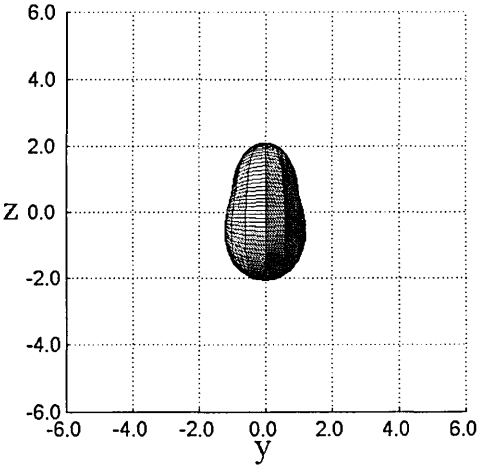

(d) T-geometry, y-z view

Figure 6.2 : Contact surfaces for HP particles with $k = 3$.

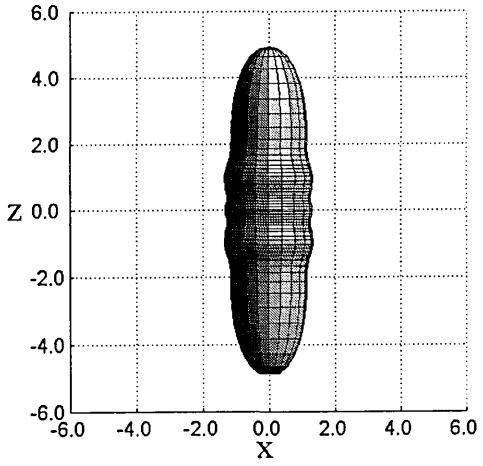

(a) parallel particles

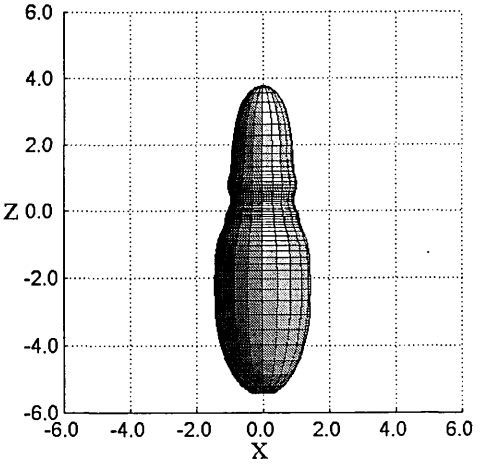

(b) anti-parallel particles

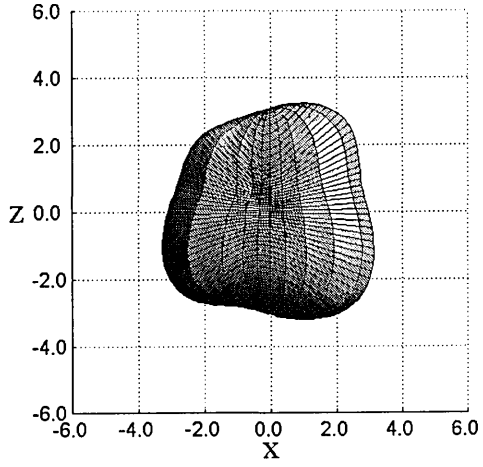

(c) T-geometry, x-z view

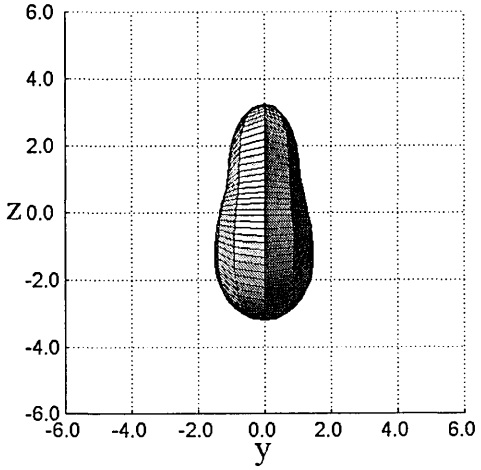

(d) T-geometry, y-z view

Figure 6.3 : Contact surfaces for HP particles with $k = 5$.

tapered model systematically correspond to molecular separations greater than the contact distance and, therefore, the effects of non convexity might not have been accessible to the models considered by the Italian group.

6.2 Simulation results using the HP model.

6.2.1 Particles with $k = 3$.

The phase behaviour of the HP model was computed using Monte Carlo simulations of bulk systems of $N = 1250$ particles in the isothermal-isobaric ensemble. For better sampling of phase space and to ease the formation of possible polar phases, 'flip moves' were included using a probabilistic scheme. These moves involved the inversion of the molecular orientation vector $\hat{\mathbf{u}}_i$ and accounted for 20% of each particle's attempted moves. Compression moves which changed every box length independently were also carried out using a probabilistic scheme, on average once every two MC sweeps (*i.e.* moves per particle). Run lengths were of the order of 1.10^6 sweeps for equilibration and production, but for some of the highest densities up to 5.10^6 sweeps were necessary to achieve equilibration.

The first series of runs used a compression sequence; the pressure range considered was chosen so that it would induce densities of the same order of magnitude as those found for the isotropic-nematic transition of the hard Gaussian overlap model (see Chapter 3.) The pressure and order parameter results obtained are shown in Figure 6.4 under the 'compression' label.
These reveal that during the compression sequence, no spontaneous ordering was observed. Thus, in order to test for the stability of the nematic phase, another series of simulations was performed in a melting sequence of decreasing pressures. The starting configuration for this series was a high density configuration obtained from the compression series, the particles being field aligned along $\hat{\mathbf{z}}$ so as to obtain a nematic phase with an order parameter $P_2 \sim 0.8$. The results for this sequence are shown on Figure 6.4 under the 'melting' label. Surprisingly, these

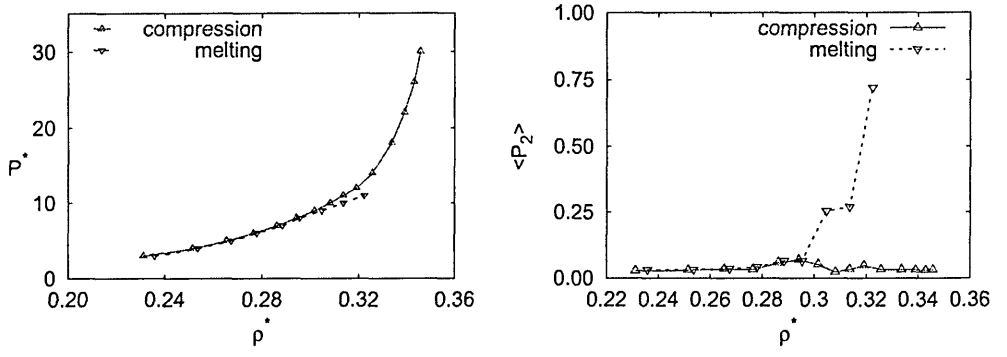

(a) $P(\rho^*)$ (b) $\langle P_2 \rangle(\rho^*)$

Figure 6.4 : Results from constant NPT Monte Carlo simulations in compression and melting sequences of the HP model with $k = 3$.

results suggest a stable nematic phase for densities $\rho^* > 0.3$ and $P^* > 8.0$. This situation seems to be very similar to that found by Williamson and Jackson [67] where a stable nematic phase was present although the model failed to order spontaneously. A further test of the systems behaviour was provided through monitoring the mobility of the molecules (Figure 6.5). This was measured using :

$$\langle \delta r^2(n) \rangle = \langle (\mathbf{r}_n - \mathbf{r}_0)^2 \rangle \tag{6.4}$$

where $\mathbf{r}_n - \mathbf{r}_0$ is the displacement vector moved by a given particle in n consecutive MC sweeps and the angled brackets indicate an average over all particles and the run length. In MC simulations with fixed maximum particle displacement (as was the case here), Brownian diffusion dictates that $\langle \delta r^2(n) \rangle$ should increase linearly with n in a fluid phase. The greater the gradient of $\langle \delta r^2(n) \rangle$, the more fluid the studied phase.

These measurements show that for both the compression and melting series, the diffusion of the particles decreased monotonically with increased density or pressure. If the results are fitted to equations of the form $y = a + bx$, b decreases of about two orders of magnitude between the lowest and highest densities shown. The conclusion from this is that the highest density configurations did not corre-

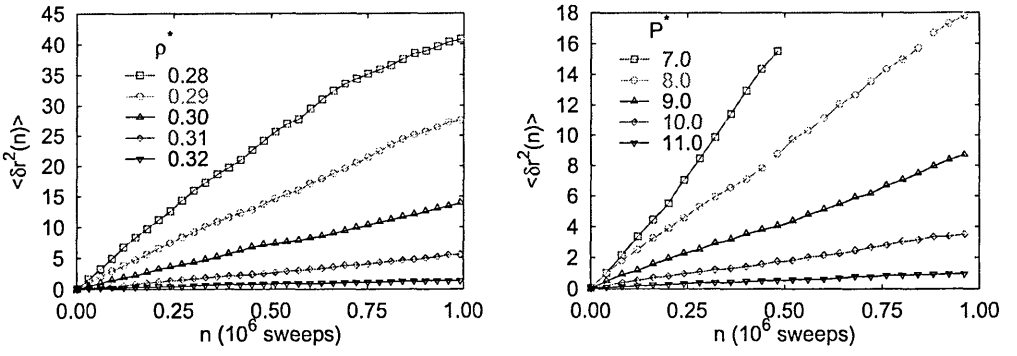

(a) compression sequence

(b) melting sequence

Figure 6.5 : Evolution of $\langle \delta r^2(n) \rangle$ as a function of n the number of Monte Carlo sweeps for the HP model and k=3. The data on the left are for a constant NVT compression sequence with $N = 1000$ and the data on the right for a constant NPT melting sequence with $N = 1250$.

spond to fluid, but to glassy phases which inhibited the ordering of the system. In the melting series, in contrast, the lack of fluidity at the highest densities may have prevented the corresponding systems from disordering into the equilibrium structure. This argument is supported by the order of magnitude of the diffusion which is about half the value obtained from the compression series, thus illustrating the frustrated nature of the ordered phases obtained. The reduction of move acceptance rate from 40% down to 10% between simulations at the lowest and highest density further illustrates this glassiness.

More insight into the phases produced by those two series of simulations can be obtained by studying simulation snapshots (*e.g.* Figure 6.6) and computation of the pair correlation functions. Both the standard $g_{\parallel}(r_{\parallel})$, $g_{\perp}(r_{\perp})$ and $g_{\parallel}^{\mathrm{mol}}(r_{\parallel})$, $g_{\perp}^{\mathrm{mol}}(r_{\perp})$ were computed (see Chapter 3 for a definition). These functions are shown on Figure 6.7.

Little difference can be observed between the two sets of functions; $g_{\parallel}(r_{\parallel})$ and $g_{\parallel}^{\mathrm{mol}}(r_{\parallel})$ indicate that as the density is increased, some short range features ap-

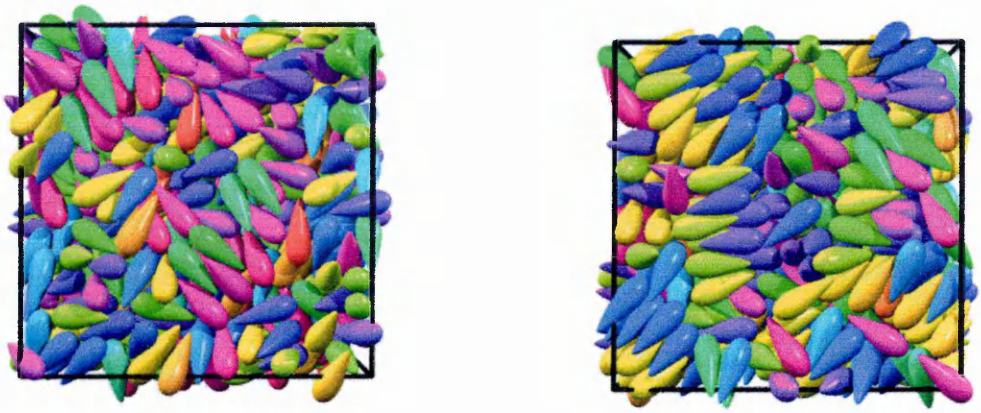

(a) $\rho^* = 0.28$ (b) $\rho^* = 0.32$

Figure 6.6 : Configuration snapshots of the HP model and $k = 3$ *at* $\rho^* = 0.28$ *and* $\rho^* = 0.32$.

pear, corresponding to distances less than the molecular elongation. Comparing this with the configuration snapshots suggests that those short range features reflect the tendency of particles to align anti-parallel with their closest neighbors. $g_\perp(r_\perp)$ and $g_\perp^{\text{mol}}(r_\perp)$ also fail to show signs of ordering, and little variation can be observed throughout the density range considered. However, some signs of the preferred pairwise anti-parallel ordering are visible for the highest density in the form of a peak at $r \sim 0.9$.

The main conclusion to be drawn from these series of simulations is that the HP model with $k = 3$ shows rather surprising phase behaviour. With increased density, the particles exhibit short ranged anti-parallel ordering. The rapid decrease in particle mobility, however leads to the formation of glassy phases and prevents the formation of nematic phases. Instead, at high density the particles form a glassy phase made of small domains with local anti-parallel alignment.

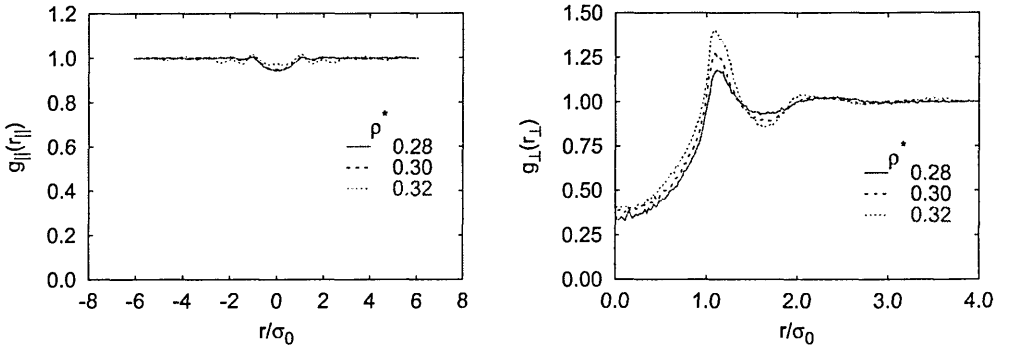

(a) $g_{\|}(r_{\|})$

(b) $g_{\perp}(r_{\perp})$

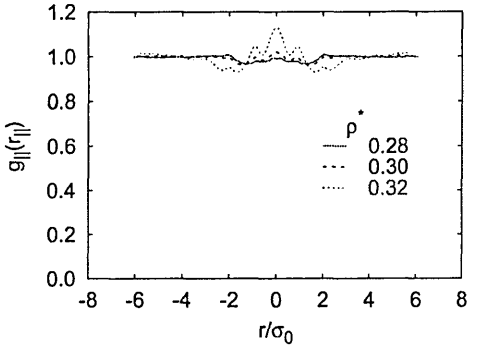

(c) $g_{\|}^{\mathrm{mol}}(r_{\|})$

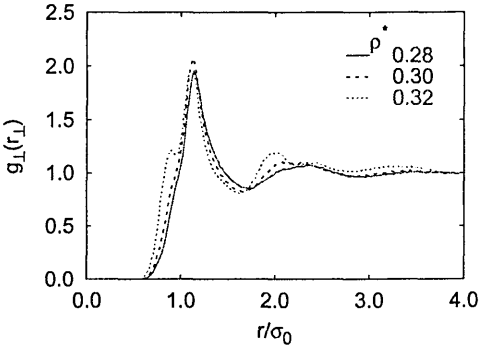

(d) $g_{\perp}^{\mathrm{mol}}(r_{\perp})$

Figure 6.7 : Pair correlation functions for the HP model with $k = 3$ computed with respect to $\hat{\mathbf{n}}$(top) and $\hat{\mathbf{u}}_i$ (bottom).

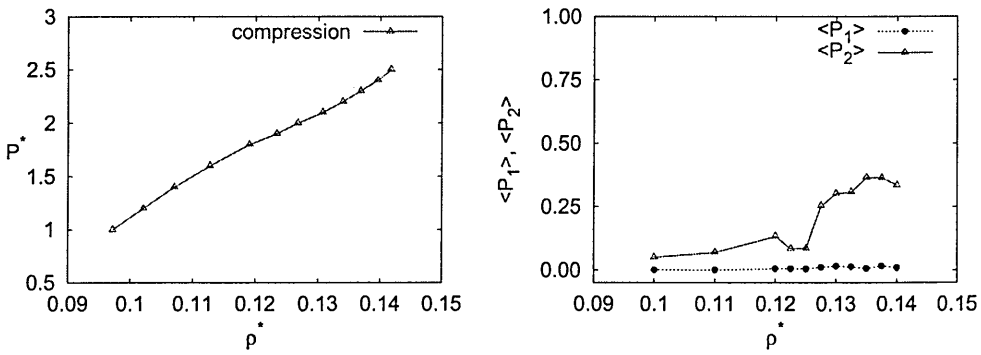

Figure 6.8 : Results from the bulk compression simulation series with the HP model and $k = 5$.

6.2.2 Particles with $k = 5$.

Due to the lack of ordering shown by particles with $k = 3$ and following the idea that increasing the molecular elongation stabilizes the nematic phase, a second study of the HP model was made using particles with $k = 5$. Systems of $N = 1000$ particles were simulated using the Monte Carlo method in both the canonical and isothermal-isobaric ensembles and with inclusion of the 'flip' moves. Similar volume change algorithms and run lengths were used as for runs with $k = 3$. However, only a compression series was performed. The results obtained from this (shown on Figure 6.8) indicate a somewhat different phase behaviour for this longer elongation. $P(\rho^*)$ shows an inflexion point at $\rho^* \sim 0.12$, suggesting a transition to a more ordered phase. This corresponds to a rapid increase in $\langle P_2 \rangle$, having the common 'S' shape of a first order transition, which is consistent with ordering to a nematic phase. However the values of $\langle P_2 \rangle$ are still short of that usually associated with nematic order. For this system, the computation of $\langle \delta r^2(n) \rangle$ (Figure 6.9) shows that all configurations remained fluid throughout the pressure/density range considered.

The nature of the phases formed by this model was investigated by observing configuration snapshots (*e.g.* Figure 6.10) and computing pair correlation functions (Figure 6.11). Again both the standard $g_{\parallel}(r_{\parallel})$, $g_{\perp}(r_{\perp})$ and molecule based

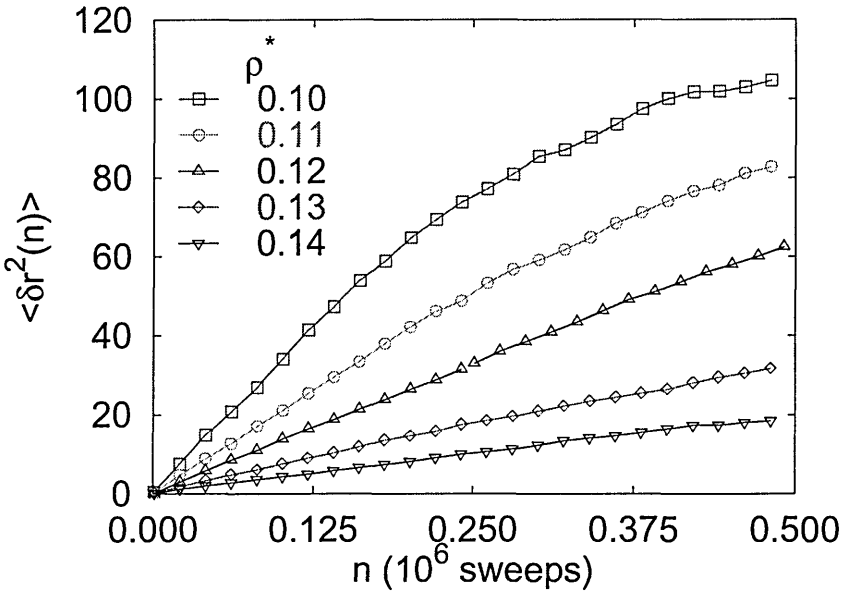

Figure 6.9 : Results for the diffusion of the HP model with $k = 5$ for simulation in the isothermal-isobaric ensemble in a compression series.

$g_{\parallel}^{\mathrm{mol}}(r_{\parallel})$, $g_{\perp}^{\mathrm{mol}}(r_{\perp})$ were computed.

As the density increased, the particles were found to order but also form layers with different orientations. As a result, although the intralayer ordering was very high, this was not reflected by the value of the overall nematic order parameter as the directions of the layers were very different, almost perpendicular in places. This is illustrated by the configuration shown on Figure 6.10(b), obtained from a simulation performed in the canonical ensemble at $\rho^* = 0.14$. A side view of the same configuration (Figure 6.10(c)), would however, suggest phase with a unique alignment direction and smectic-like ordering, with the exception of those particles with different orientations which are sandwiched between the 'layers'. This discrepancy shows the full extent of the non homogenous character of the high density structures obtained here and explains the moderate values of $\langle P_2 \rangle$.

The likelihood of this type of configuration transforming into a smectic phase at higher densities appears low as the particle mobilities at these high densities are rather low. This question has, however, been investigated by performing simulations in the isothermal-isobaric ensemble where the three box lengths were allowed

to vary independently. This approach is known to facilitate the possible formation of smectic phases as the box accommodates the system's natural layer spacing. These simulations however lead to the same structures as were seen in the canonical ensemble. Therefore, this multi-domain layered configuration seems to be the most stable state for this model at high pressures/densities.

A quantitative insight into those phases is provided by the pair correlation functions as shown on Figure 6.11. Again the functions computed with respect to $\hat{\mathbf{n}}$ and $\hat{\mathbf{u}}_i$ show little qualitative differences. As the density is increased, $g_{\parallel}(r_{\parallel})$ and $g_{\parallel}^{\mathrm{mol}}(r_{\parallel})$ display a series of peaks accounting for the domain ordering. The distance between two successive peaks of about $6\sigma_0$ corresponds to the distance between two layers separated by a small number of interstitial particles with perpendicular orientation. The lack of periodicity in these functions reveals that this phase is not smectic, however. The intra-layer, in contrast, is rather close to that of a smectic phase as $g_{\perp}^{\mathrm{mol}}(r_{\perp})$ shows up to four peaks with an average separation $\sim \sigma_0$ accounting for the successive parallel and antiparallel neighbours.

Thus, for the elongation of $k = 5$, the HP model shows a rather surprising phase behaviour which is subtly different from that observed for $k = 3$. For the longer elongation, the model proved to remain fluid over the pressure range considered. With increased pressure, a transition to an ordered phase was observed. At high pressure, the particles formed layered domains with different orientations and high, smectic-like, intra-layer order. The HP model does not, however, fulfill the requirement of having the stable nematic phase needed to simulate the confined flexoelectric particle systems mentioned at the beginning of this Chapter. The modeling of pear-shaped particles which form nematic phases can, however, be achieved using a totally different route to the expression for the contact distance. This new approach is described in the following Sections.

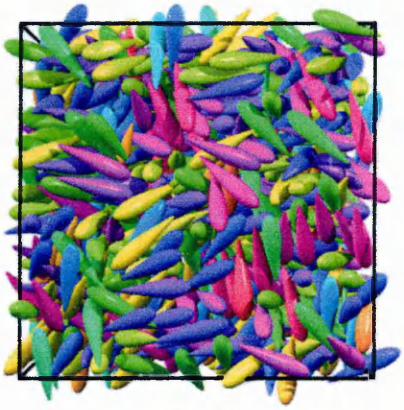

(a) $\rho^* = 0.10$

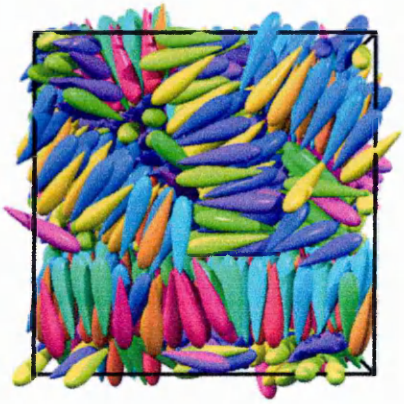

(b) $\rho^* = 0.14$, bottom view

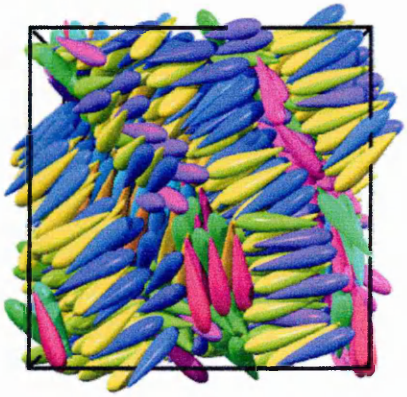

(c) $\rho^* = 0.14$, side view

Figure 6.10 : Configuration snapshots for the HP model with $k = 5$ at $\rho^* = 0.14$. Two views are presented the bottom of the simulation box (left) and a side view looking down along $\hat{\mathbf{y}}$ and $\hat{\mathbf{z}}$ pointing upward.

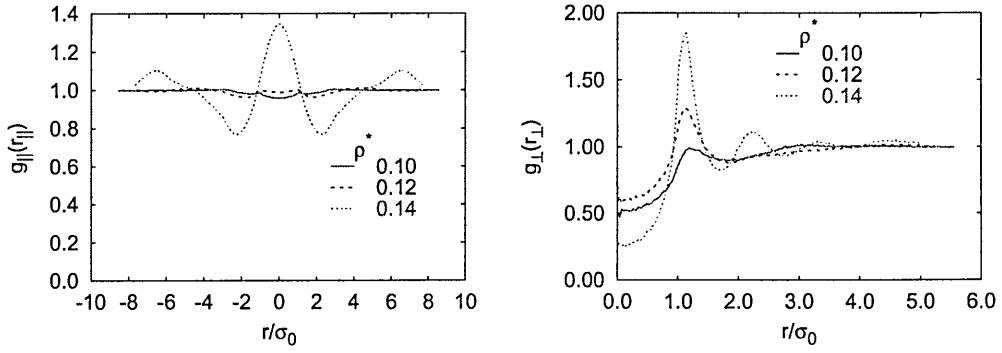

(a) $g_{\parallel}(r_{\parallel})$

(b) $g_{\perp}(r_{\perp})$

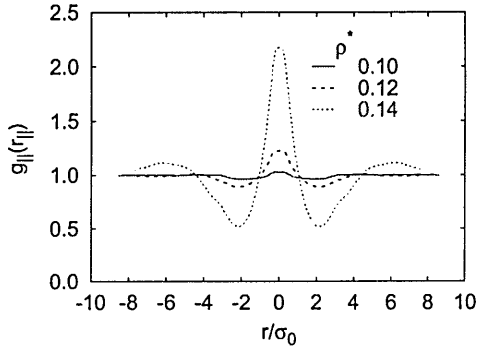

(c) $g_{\parallel}(r_{\parallel})$

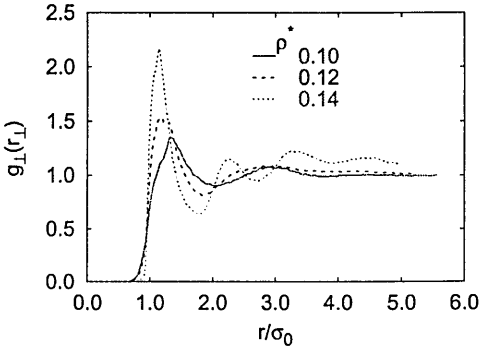

(d) $g_{\perp}(r_{\perp})$

Figure 6.11 : Pair correlation functions for the HP model with $k = 5$ computed with respect to $\hat{\mathbf{n}}$(top) and $\hat{\mathbf{u}}_i$ (bottom).

6.3 The PHGO model.

Here a novel model for non-centrosymmetric particles is described. The route adopted is to extend the generalized Gay-Berne (GGBP) potential [105] to the description of non-centrosymmetric particles thus leading to the so called Parametric Hard Gaussian Overlap (PHGO) model.

6.3.1 Obtaining the contact distance.

The generalized Gay-Berne model describes the interaction between two ellipsoidal particles i, j with arbitrary lengths ℓ_i, ℓ_j and breadth d_i, d_j and orientations $\hat{\mathbf{u}}_i$ and $\hat{\mathbf{u}}_j$ separated by an intermolecular vector $\mathbf{r}_{ij} = r_{ij}\hat{\mathbf{r}}_{ij}$. The contact distance for this model is given by :

$$\sigma(\hat{\mathbf{u}}_i, \hat{\mathbf{u}}_j, \mathbf{r}_{ij}) = \sigma_0 \left[1 - \chi \left\{ \frac{\alpha^2 (\hat{\mathbf{r}}_{ij} \cdot \hat{\mathbf{u}}_i)^2 + \alpha^{-2} (\hat{\mathbf{r}}_{ij} \cdot \hat{\mathbf{u}}_j) - 2\chi (\hat{\mathbf{r}}_{ij} \cdot \hat{\mathbf{u}}_i)(\hat{\mathbf{r}}_{ij} \cdot \hat{\mathbf{u}}_j)(\hat{\mathbf{u}}_i \cdot \hat{\mathbf{u}}_j)}{1 - \chi^2 (\hat{\mathbf{u}}_i \cdot \hat{\mathbf{u}}_j)^2} \right\} \right]^{-\frac{1}{2}} \tag{6.5}$$

with :

$$\begin{aligned} \sigma_0 &= \sqrt{\frac{d_i^2 + d_j^2}{2}} \\ \alpha^2 &= \left[\frac{(\ell_i^2 - d_i^2)(\ell_j^2 + d_i^2)}{(\ell_j^2 - d_j^2)(\ell_i^2 + d_j^2)} \right]^{\frac{1}{2}} \\ \chi &= \left[\frac{(\ell_i^2 - d_i^2)(\ell_j^2 - d_j^2)}{(\ell_j^2 + d_i^2)(\ell_i^2 + d_j^2)} \right]^{\frac{1}{2}}. \end{aligned}$$

If, alternatively, the brackets containing the length and breadth values are grouped as :

$$\begin{aligned} A &= (\ell_i^2 - d_i^2) \quad B = (\ell_j^2 - d_j^2) \\ C &= (\ell_j^2 + d_i^2) \quad D = (\ell_i^2 + d_j^2), \end{aligned}$$

the shape parameter can be rewritten as :

$$\sigma(\hat{\mathbf{u}}_i, \hat{\mathbf{u}}_j, \mathbf{r}_{ij}) =$$
$$\sigma_0 \left[1 - \frac{AC\left(\hat{\mathbf{r}}_{ij} \cdot \hat{\mathbf{u}}_i\right)^2 + BD\left(\hat{\mathbf{r}}_{ij} \cdot \hat{\mathbf{u}}_j\right)^2 - 2AB\left(\hat{\mathbf{r}}_{ij} \cdot \hat{\mathbf{u}}_i\right)\left(\hat{\mathbf{r}}_{ij} \cdot \hat{\mathbf{u}}_j\right)\left(\hat{\mathbf{u}}_i \cdot \hat{\mathbf{u}}_j\right)}{CD - AB\left(\hat{\mathbf{u}}_i \cdot \hat{\mathbf{u}}_j\right)^2} \right]^{-\frac{1}{2}} \tag{6.6}$$

Although the two forms of Equations 6.5 and 6.6 are mathematically equivalent, the second is to be preferred for implementation in a simulation code as it is free of possible division by zero or complex numbers in the limit $\ell = 0$ and $d = 0$.

By design, Equation 6.6 is restricted to the description of particles with fixed ℓ and d. The extension from the *GGB* to the *PHGO* contact distance is to consider particles for which ℓ and d vary parametrically with $(\hat{\mathbf{r}}_{ij} \cdot \hat{\mathbf{u}}_i)$ and $(\hat{\mathbf{r}}_{ij} \cdot \hat{\mathbf{u}}_j)$. As a result the shape of i as 'seen' by j can be tuned to be a function of the relative position and orientation of the particles. This makes it possible to model particles with arbitrary non-centrosymmetric shapes although the approximation made by the model can lead to anomalies if non-convex particle shapes are used.
This method can therefore be applied to the description of particles having the Bézier shape used by the Stone expansion of the HP model as these do satisfy the convexity requirements of the model. When two such particles interact with their sharp ends, ℓ/d needs to be relatively large, whereas the blunt end interaction requires an ℓ/d ratio rather nearer to unity. In order to avoid discontinuities between these two limiting cases, a multitude of parametric forms is possible; here the form of ℓ_i and d_i is limited to simple polynomials of the polar angle $(\hat{\mathbf{r}}_{ij} \cdot \hat{\mathbf{u}}_i)$, that is :

$$d_i(\hat{\mathbf{r}}_{ij} \cdot \hat{\mathbf{u}}_i) = a_{d,0} + \ldots + a_{d,n}(\hat{\mathbf{r}}_{ij} \cdot \hat{\mathbf{u}}_i)^n \tag{6.7}$$

$$\ell_i(\hat{\mathbf{r}}_{ij} \cdot \hat{\mathbf{u}}_i) = a_{\ell,0} + \ldots + a_{\ell,m}(\hat{\mathbf{r}}_{ij} \cdot \hat{\mathbf{u}}_i)^m. \tag{6.8}$$

The main limitation of this model is that the description of concave particles (i.e. dumbells) is not avaliable. The advantages are, however, numerous as the analytical form makes it possible to use the model in both MC and MD codes. Also,

this monosite model does not introduce any discontinuities in the particle-particle contact surfaces. Although the use of polynomials to describe the dependency of ℓ and d over $(\hat{\mathbf{r}}_{ij} \cdot \hat{\mathbf{u}}_i)$ might seem simplistic, this allows a very straightforward implementation in the coefficients A, B, C and D by simply adding higher order terms. Reversibly, the contact distance of the HGO model can be recovered in taking the limit $m = n = 0$.

Finally simulations of multi-component fluids is an easy extension of this model, as a set of $a_{\ell,i}$, $a_{d,i}$ can be assigned to every type of particle. Systems of particles whose shapes vary within a simulation run can also be achieved using this approach.

6.3.2 Parameterizing Bézier pears.

In order to apply the PHGO approach to pear-shaped particles, the coefficients $a_{\ell,i}$ and $a_{d,i}$ need to be computed. This has been performed by numerically fitting the particle-point potential to a geometrical shape. For this, a numerical simplex method [184] has been chosen.

The shape that is considered here is a simple update of the Bézier shape described in Section 6.1, the difference being that the control points q_2 and q_3 are set to be always coincident. This makes the Bézier shape easily scalable with k. This new Bézier shape is shown on Figure 6.12 and the associated control points coordinates as a function of k are given on Table 6.3.

Using the geometrical properties of the Bézier curves, it is possible to extract the coordinates of each point of the pear surface and, hence, the numerical data corresponding to the particle-point contact distance as a function of $(\hat{\mathbf{u}}_i \cdot \hat{\mathbf{r}}_{ij})$. These data are then fitted to the expression for the PHGO contact distance with $\ell_j = d_i = 0$ which in this case reduces to :

$$\sigma(\hat{\mathbf{u}}_i, \mathbf{r}_{ij}) = \frac{d_i(\hat{\mathbf{r}}_{ij} \cdot \hat{\mathbf{u}}_i) l_i(\hat{\mathbf{r}}_{ij} \cdot \hat{\mathbf{u}}_i)}{\left\{ l_i^2(\hat{\mathbf{r}}_{ij} \cdot \hat{\mathbf{u}}_i) + (\hat{\mathbf{u}}_i \cdot \hat{\mathbf{r}}_{ij})^2 \left[d_i^2(\hat{\mathbf{r}}_{ij} \cdot \hat{\mathbf{u}}_i) - l_i^2(\hat{\mathbf{r}}_{ij} \cdot \hat{\mathbf{u}}_i) \right] \right\}^{\frac{1}{2}}} \tag{6.9}$$

The values of the $a_{d,\alpha}$ and $a_{\ell,\alpha}$ coefficients obtained from the fitting procedure are shown on Table 6.4. $n = 10$ and $m = 1$ have been chosen as this was found to be

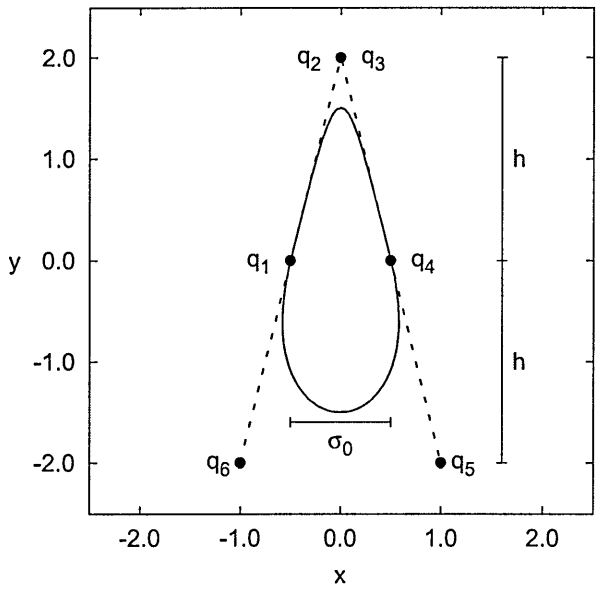

Figure 6.12 : Bézier shape for parameterized with the PHGO model.

q_i	x	y
q_1	$-\frac{1}{2}\sigma_0$	0
q_2	0	$\frac{2}{3}k\sigma_0$
q_3	0	$\frac{2}{3}k\sigma_0$
q_4	$\frac{1}{2}\sigma_0$	0
q_5	σ_0	$-\frac{2}{3}k\sigma_0$
q_6	$-\sigma_0$	$-\frac{2}{3}k\sigma_0$

Table 6.3 : Bézier control points coordinates for the Bézier pear used with the PHGO model.

	$k=3$	$k=4$	$k=5$
$a_{d,0}$	0.501852454	0.501377232	0.497721868
$a_{d,1}$	-0.141145314	-0.129608758	-0.123155821
$a_{d,2}$	-0.060542359	-0.074219217	0.024405876
$a_{d,3}$	0.225813650	0.484166441	0.723627215
$a_{d,4}$	0.832274021	0.923492941	0.389831429
$a_{d,5}$	-1.015039575	-1.987232902	-3.018638148
$a_{d,6}$	-2.504045172	-2.943008017	-1.951629076
$a_{d,7}$	1.375313426	2.808075172	4.413215403
$a_{d,8}$	3.196830129	3.815344782	2.998417509
$a_{d,9}$	-0.699241457	-1.426641750	-2.241573216
$a_{d,10}$	-1.430400139	-1.682476460	-1.416614353
$a_{\ell,0}$	1.498259615	1.995906501	2.493069403
$a_{\ell,1}$	-0.002027616	-0.004518187	-0.008067236

Table 6.4 : Values of the $a_{d,\alpha}$ and $a_{\ell,\alpha}$ for the PHGO pears with $k = 3$, 4 and 5

the best compromise between simulation speed and fit accuracy. The accuracy of the fits can be checked by comparing the contact distances calculated using the coefficients of Table 6.4 and the actual Bézier shape (Figure 6.13). The comparison reveals a very good correspondence between the two sets. The critical region being for $(\hat{\mathbf{r}}_{ij} \cdot \hat{\mathbf{u}}_i) \sim 0$. The level of correspondence between the numerical and analytical result to be achieved in this region dictates the number of coefficients to be used. While using $n = m = 1$ allows a good fit for the head and tail regions of the particles up to $n = 10$ coefficients in $a_{d,\alpha}$ were required to achieve the quality of fits shown on Figure 6.13.

The quality of these fits does not, however, guarantee an appropriate particle-particle interaction and the validity of the latter is assessed by computing the contact surfaces equivalent to those considered for the HP model (*e.g.* Figures 6.2 and 6.3). Again three contact surfaces were computed corresponding to parallel, anti-parallel and T-geometry interactions. The results for $k = 3$ and $k = 5$ are

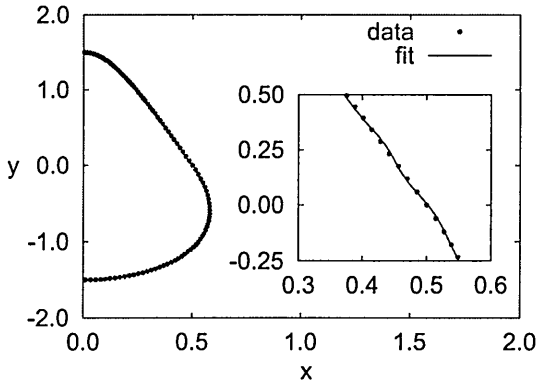

(a) $k = 3$

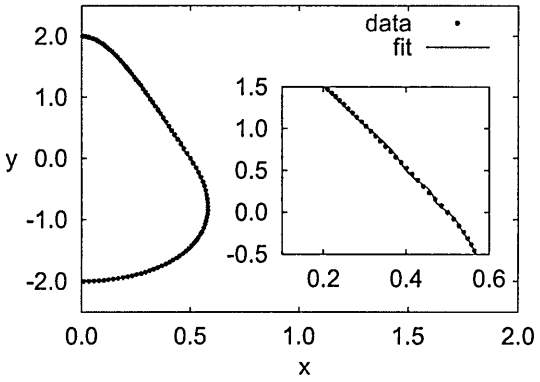

(b) $k = 4$

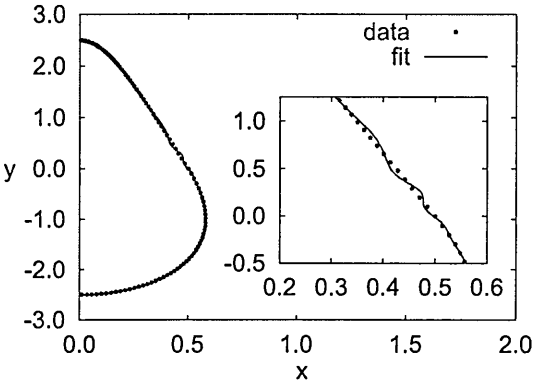

(c) $k = 5$

Figure 6.13 : Comparison between the numerical and geometrical contact distance for the PHGO particle-point potential.

shown on Figures 6.14 and 6.15.

These surfaces show the required shapes, that is approximately ellipsoidal shapes for the parallel interactions and pear shapes for the anti-parallel interactions. Although there is not really a required shape for the T-geometry, the latter do not show any discontinuities that would indicate potential problems. They are also reasonably consistent with those obtained for the corresponding HP contact surfaces.

The difference between the contact surfaces for this model and the HP model are readily understandable. For the PHGO model, ridges in the contact surfaces have disappeared save for small oscillations which are a direct consequence of the degree of truncation of the fits shown on Figure 6.13. However the low amplitude of these oscillation suggests that the PHGO model should be free of the interlocking phenomena shown by the HP model.

6.4 Phase behaviour of the PHGO model.

In order to test the PHGO model applied to the Bézier pear shape, bulk constant NPT MC simulations were performed on systems of $N = 1000$ particles with elongations $k = 3, 4$ and 5. As with the HP model simulations, orientation inversion moves were also included in the MC scheme. These accounted for 20% of the total number of attempted moves. The volume change scheme was performed on average, once two sweeps and allowed each box side to change its length independently. Typical runs comprised of $0.5.10^6$ sweeps for equilibration and production. Close to phase transitions, additional runs were performed on a case by case basis to ensure that equilibration was achieved. All simulations were performed in a compression sequence.

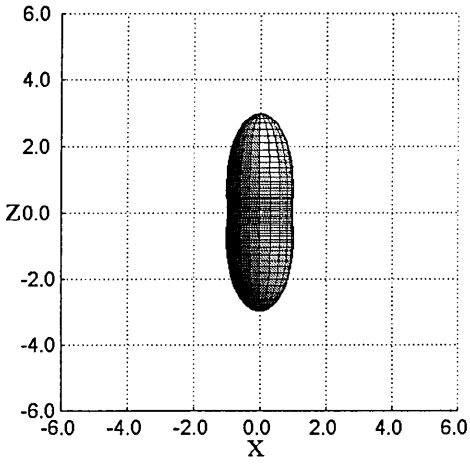

(a) parallel

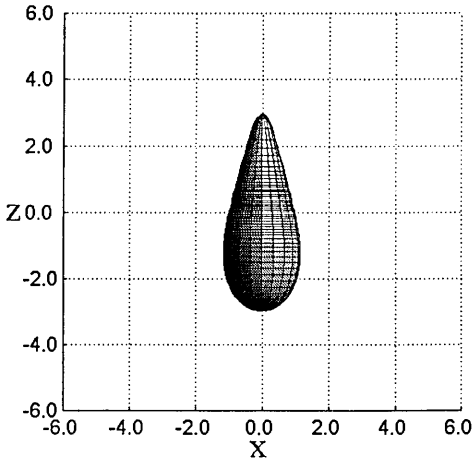

(b) anti-parallel

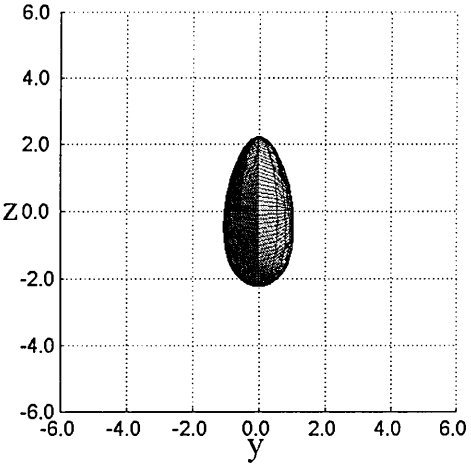

(c) T-geometry, x-z view

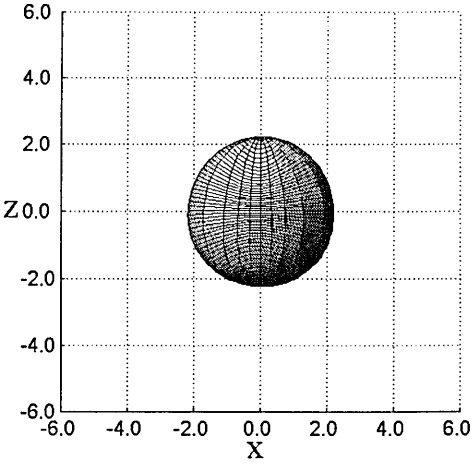

(d) T-geometry, y-z view

Figure 6.14 : Contact surfaces for the PHGO model and $k = 3$.

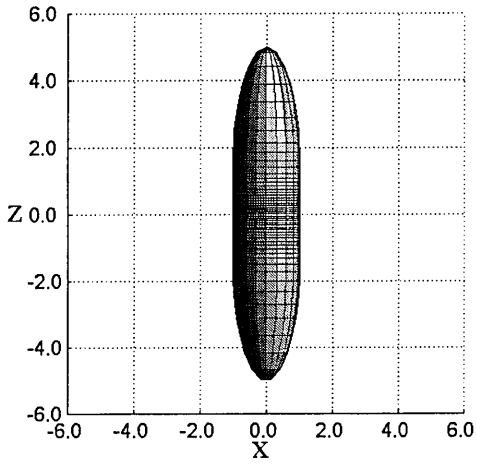

(a) parallel

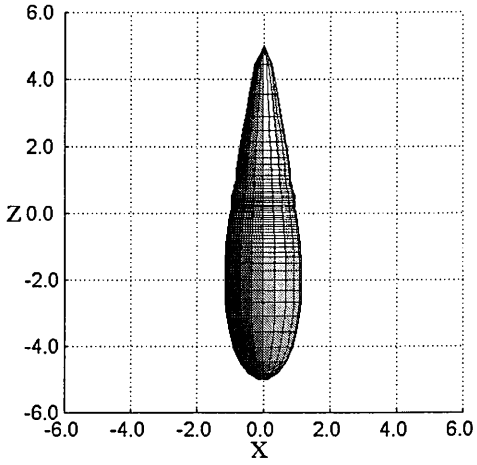

(b) anti-parallel

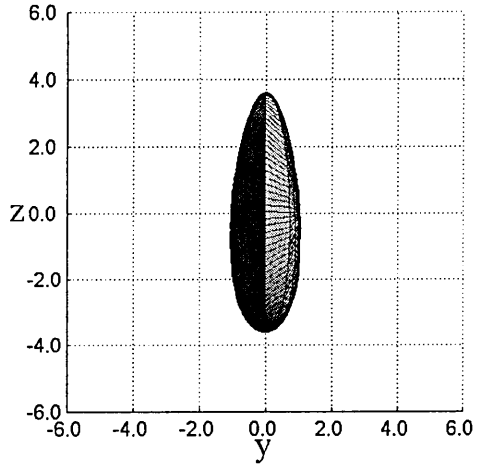

(c) T-geometry, x-z view

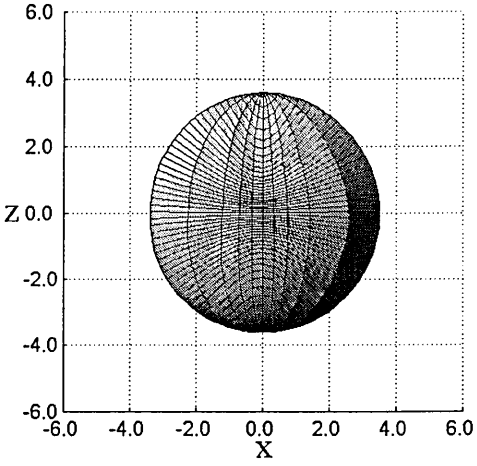

(d) T-geometry, y-z view

Figure 6.15 : Contact surfaces for the PHGO model and $k = 5$.

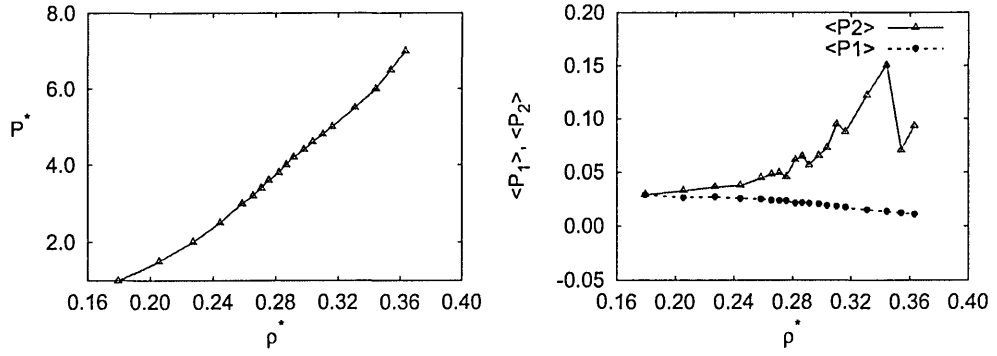

(a) $k = 3$

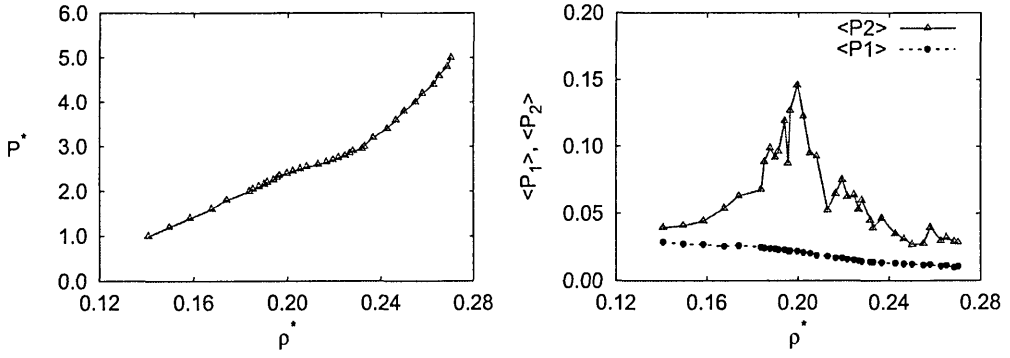

(b) $k = 4$

Figure 6.16 : Phase diagram for the PHGO pears with $k = 3$ and 4.

6.4.1 Particles with $k = 3$ and 4.

The equation of state and order parameter behaviour obtained from simulations with $k = 3$ and 4 are shown in Figure 6.16. The phase behaviour for these two elongations is fairly similar; both $P(\rho^*)$ curves show an inflexion point, respectively at $\rho^* \sim 0.30$ and ~ 0.20, which corresponds to an increase of $P_2(\rho^*)$ to values of the order of 0.15 immediately followed by a rather steep decrease.
The 'plateau' in $P(\rho^*)$ indicates some sort of phase transition to a more ordered phase but, as this is only hardly reported on P_2, this phase change does not corresponds to an isotropic-nematic phase transition. Some more insight into the phase behaviour can be obtained by observation of configuration snapshots (*e.g.* Figure 6.17).
These show that upon increasing the pressure, both systems underwent a phase transition from isotropic to the what we term as a domain ordered BILAYER phase where, the particles form domains in which the local order is very high but where the orientation changes from one domain to the other. Unlike with the HP model, this seems to have been a transition between two genuinely liquid states as the systems maintained high mobility throughout the density ranges considered here (see Figure 6.18). Also, the configuration snapshots suggest continuous orientation changes in moving from one domain to another (*e.g.* Figure 6.17b and d,) unlike the very sharp domain boundaries seen in the HP systems (*e.g.* Figure 6.10b and c.)

More quantitative insight into those domain ordered phases have been obtained through computation of the pair correlation functions. Both $g_{\parallel}(r_{\parallel})$, $g_{\parallel}^{\mathrm{mol}}(r_{\parallel})$ (Figure 6.19(a)) and $g_{\perp}(r_{\perp})$, $g_{\perp}^{\mathrm{mol}}(r_{\perp})$ (Figure 6.19(b)) have been computed for $k = 4$ as the domains are best observed for this elongation.
$g_{\parallel}(r_{\parallel})$ and $g_{\perp}(r_{\perp})$ show some short ranged structure with increasing density but do not give much information about the structures observed on the snapshots because the choice of reference ($\hat{\mathbf{n}}$) for the computation of these curves does not allow one to 'follow' the orientation of the particles in the domains.

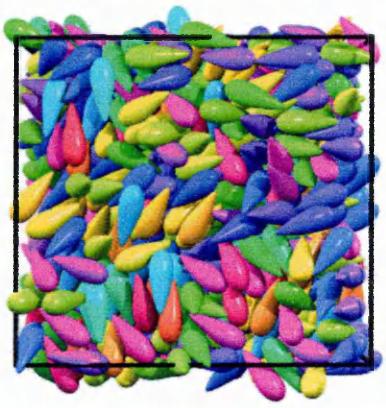

(a) $k = 3$ isotropic

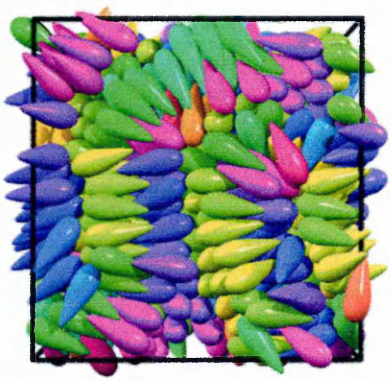

(b) $k = 3$ domain ordered

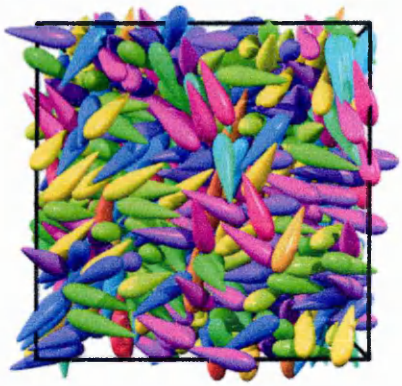

(c) $k = 4$ isotropic

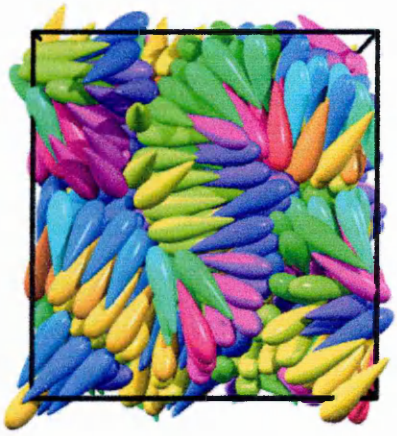

(d) $k = 4$ domain ordered

Figure 6.17 : Configuration snapshots for the pear PHGO model and $k = 3$ and 4.

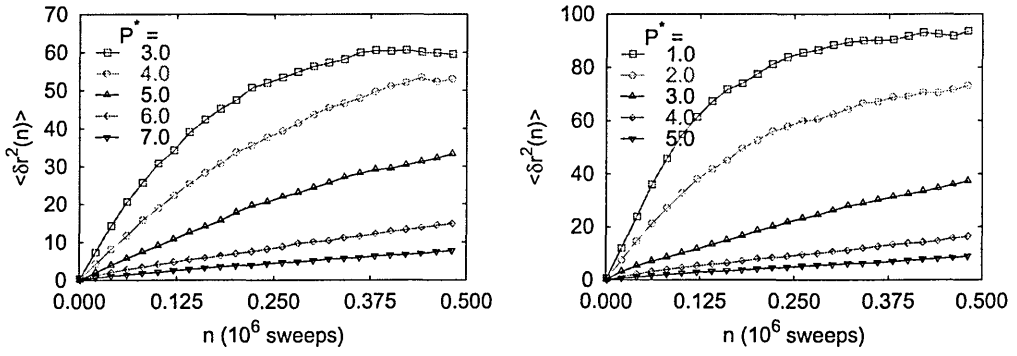

(a) $k = 3$ (b) $k = 4$

Figure 6.18 : Evolution of $\langle \delta r^2(n) \rangle$ for the pear PHGO model and $k = 3$ and 4.

A better reference is the molecular orientation as used when calculating $g_{\parallel}^{\mathrm{mol}}(r_{\parallel})$ and $g_{\perp}^{\mathrm{mol}}(r_{\perp})$ (Figure 6.19(c) and (d)). In this case, the appearance of almost periodic behaviour in $g_{\parallel}^{\mathrm{mol}}(r_{\parallel})$ shows some smectic-like ordering with increased density. $g_{\perp}^{\mathrm{mol}}(r_{\perp})$, however, shows that those domain are fairly short ranged as only three peaks can be observed, the first one accounting for the direct antiparallel neighbors and the subsequent maxima correspond to further shells of parallel and anti-parallel particles.

Thus the PHGO model applied to the Bézier pears with elongation $k = 3$ and 4 has shown some very interesting phase behaviour. Despite the improved contact surfaces, that prevented the formation of glassy phases, still no nematic phases could be observed. Rather, upon increasing the density, the systems underwent a transition from isotropic to a domain ordered phase.

6.4.2 Particles with $k = 5$.

The phase behaviour for particles with $k = 5$ proved to be qualitatively different from the shorter elongations and resembled that of other common LC models, such as the HGO fluid.

$P^*(\rho^*)$ shows a plateau at $P^* \sim 1.2$ which corresponds to an 'S' shaped increase

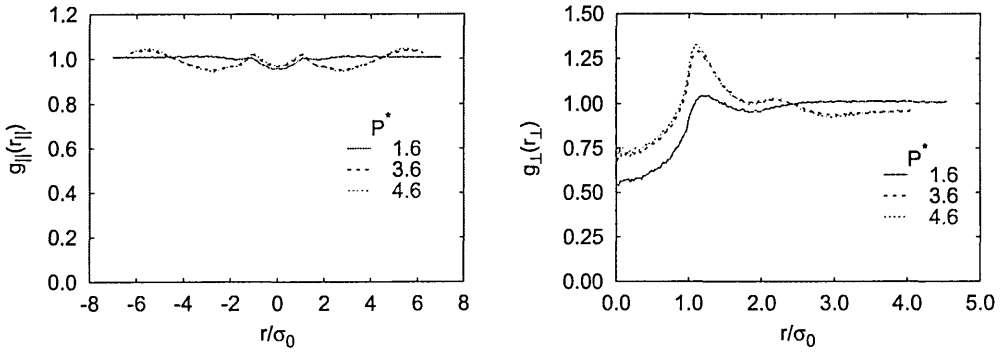

(a) $g_{\parallel}(r_{\parallel})$

(b) $g_{\perp}(r_{\perp})$

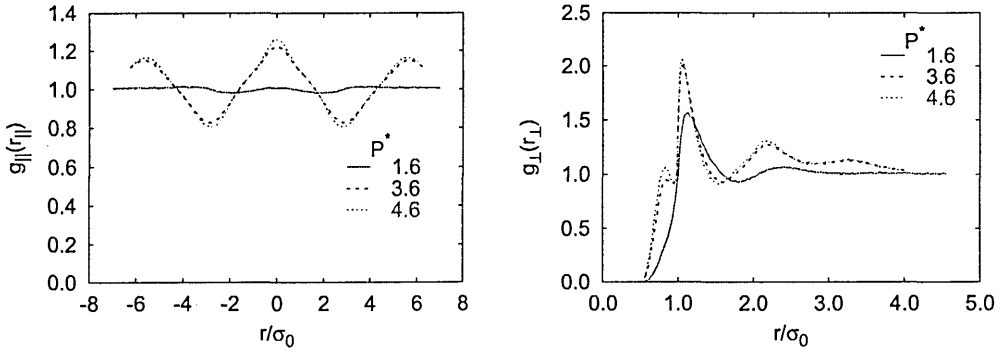

(c) $g_{\parallel}(r_{\parallel})$

(d) $g_{\perp}(r_{\perp})$

Figure 6.19 : Pair correlation functions for the pear PHGO model of $k = 4$ computed with respect to $\hat{\mathbf{n}}$ (top) and to $\hat{\mathbf{u}}_i$ (bottom).

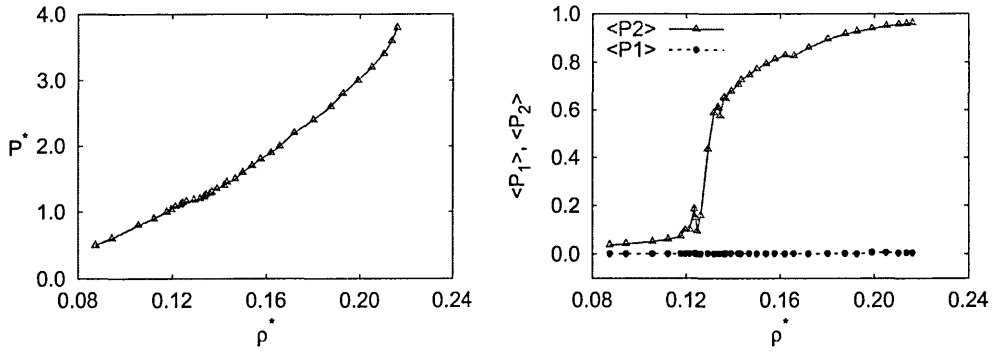

Figure 6.20 : Phase diagram for the PHGO pears with $k = 5$.

in $P_2(\rho^*)$ to values typical of a nematic phase. This phase lacked polar order throughout the density range considered as shown by the low values of $P_1(\rho^*)$. Configuration snapshots illustrating these isotropic and nematic phases are shown on Figure 6.22(a) and (b). Surprisingly a second feature can be observed on the phase diagram in the form of a second inflexion point in $P^*(\rho^*)$ at higher pressure. This corresponds to a second, smaller 'S' shaped increased in $P_2(\rho^*)$ marking a second phase transition, this time to a smectic phase. As the PHGO model is simply a generalization of the Hard Gaussian Overlap model to non-centrosymmetric shapes, this second phase transition was not expected. Observation of the configuration snapshots at the highest densities confirmed the existence of the smectic phase (*e.g.* Figure 6.22(c) .) All the phases found can be shown to be fluid as the gradient in $\langle \delta r^2(n) \rangle$ stayed rather high throughout the density range considered here (Figure 6.21).

In order to gain more insight into the phases found here but also to characterize the smectic phase more precisely, the pair correlation functions have been computed parallel and perpendicular with respect to the nematic director $\hat{\mathbf{n}}$. Only this reference frame has been taken here as, in the absence of domain ordered phases, computation of $g_{\parallel}^{\mathrm{mol}}(r_{\parallel})$ and $g_{\perp}^{\mathrm{mol}}(r_{\perp})$ was not required.

As shown in Figure 6.23, increase in pressure leads to the development of periodic oscillations in $g_{\parallel}(r_{\parallel})$; the amplitudes of these fluctuations were found to grow with increased pressure. In the smectic phase, $g_{\parallel}(r_{\parallel})$ became fully periodic, the

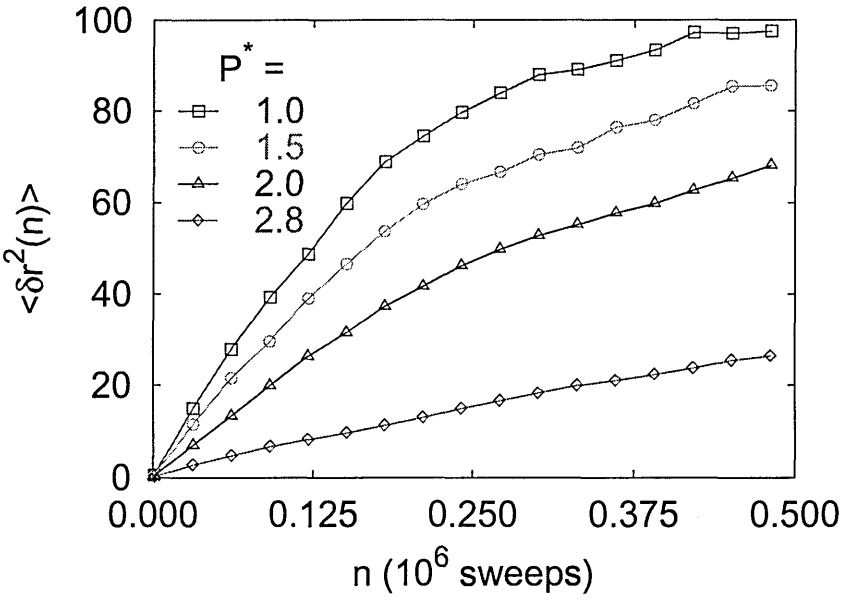

Figure 6.21 : Evolution of $\langle \delta r^2(n) \rangle$ as a function of pressure for the pear PHGO model with $k = 5$.

repeating pattern being composed of one main peak between two smaller ones. At $P^* = 2.8$, the distance between the two main peaks was about $7.389\sigma_0 \approx 1.5k\sigma_0$. This corresponds to the separation of layers with the same polar orientation. The two smaller peaks account for the two spacing of antiparallel layer arrangement. The presence of two peaks (rather than one) can be explained by the difference between the preferred tail-tail and head-head contact distances. The area under these peaks is about half that under the main peaks as each accounts for one type of relative alignment (head-head **or** tail-tail) whereas the main peak account for two types of interaction (head-tail pointing up **and** head-tail pointing down). At the same pressure of $P^* = 2.8$, the peak separation of about σ_0 shows the smectic to be a smectic A phase. Moreover, the interdigitation between the layers as revealed by the configuration snapshots (*e.g.* Figure 6.22(c)) further identifies this smectic phase as a bilayered smectic A_2.

Comparison of $g_{\parallel}(r_{\parallel})$ for different values of P^* in the smectic phase shows an interesting compressibility behaviour and also allows to identify the different peaks

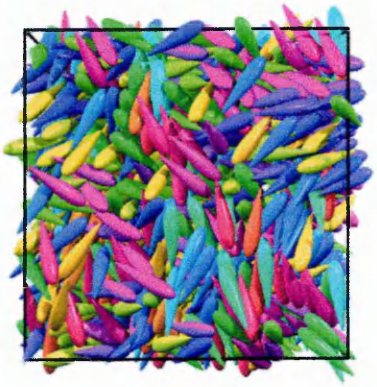

(a) isotropic

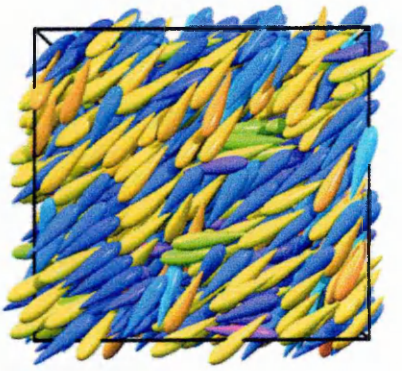

(b) nematic

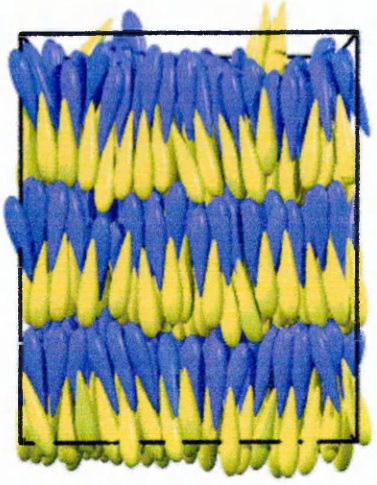

(c) smectic

Figure 6.22 : Configuration snapshots for the PHGO pears with $k = 5$.

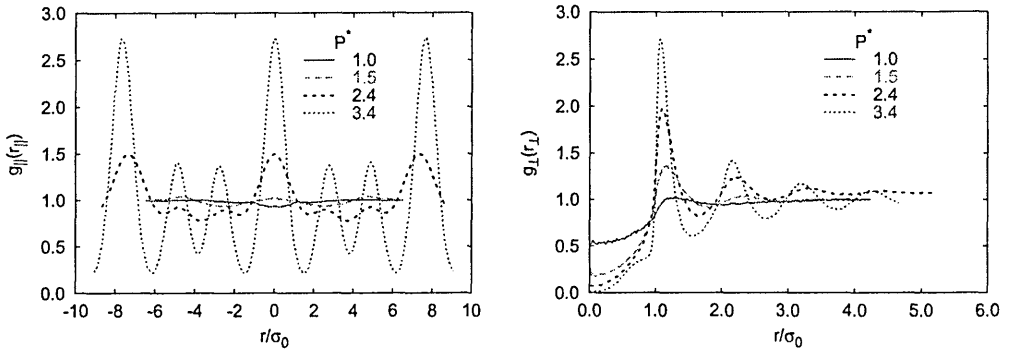

(a) $g_{\parallel}(r_{\parallel})$ (b) $g_{\perp}(r_{\perp})$

Figure 6.23 : Pair correlation functions for the pear PHGO model of $k = 5$ computed with respect to $\hat{\mathbf{n}}$.

with their associated particles interaction geometry. Upon increasing the pressure, the system density rises and the intra-layer separation decreases whereas the bi-layer separation increases (Figure 6.23(a) and (b)). From the measured $g_{\parallel}(r_{\parallel})$ data in the pressure range [2.4 : 3.8], it is found that the distance between the main peaks, which corresponds to the separation of the bilayers, increases from 7.38 to 7.66. The distance from the main peak to the first minor peak, which corresponds to the strongly interdigitating 'tail-tail' configuration increases from 2.49 to 2.76, whereas that to the second minor peak, corresponding to the weakly interdigitating 'head-head' alignment remains effectively constant at 4.85. Thus, the in-plane compression induced by this increase in pressure leads to a 10% increase in the separation within the interdigitated bilayers that comprise the smectic A_2 phase. Figure 6.24 shows the period of $g_{\parallel}(r_{\parallel})$ at $P^* = 2.8$; the distance $C - H_1$ corresponds to the bilayer separation, that is the separation between particles with the same polar orientation ($\triangleleft\triangleleft$ and $\triangleright\triangleright$). The $C - L_1$ distance corresponds to the separation between the strongly interdigitated particles in a tail-tail ($\triangleright\triangleleft$) configuration and the $C - L_2$ distance corresponds to the separation between particles in a head-head ($\triangleleft\triangleright$) configuration.

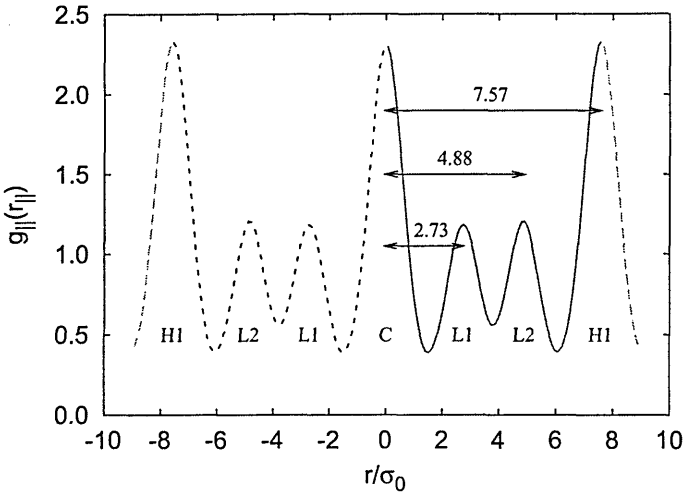

Figure 6.24 : Details of $g_{\parallel}(r_{\parallel})$ for a system of PHGO particles with $k = 5$ and $P^* = 2.8$, which corresponds to a smectic phase.

The results from the simulation of the pear PHGO model with $k = 5$ thus shows an interesting phase behaviour that includes stable nematic and interdigitated smectic A phases. As a result the prerequisite condition for the creation of the model for surface induced switching is fulfilled and pear PHGO particles can be used in confined geometries in an attempt to achieve the main goal of this thesis. Results of the work performed to this end are presented in Chapter 7.

Conclusion

In this Chapter the simulation of non-centrosymmetric, pear-shaped particles has been addressed using two models. The first model used a steric version of the model developed by Berardi *et al.* [2]. The contact distance of this is obtained fitting a numerical contact distance to a truncated Stone expansion. However, this introduced non-convex contact surfaces and, as a result, the model with elongations $k = 3$ and 5 did not display stable nematic phases as they were systematically preceeded by glassy phases. A totally new approach was then taken in the form of the so called parametric hard Gaussian overlap model. For the shorter elongations $k = 3$ and 4, the model did not show any nematic phases; rather at high densities,

the molecules order into interdigitated domains. Upon increasing the elongation to $k = 5$, the model was found to display both nematic and interdigitated smectic A_2 phases. The latter showed some interesting anisotropic compressibility behaviour where compression had the effect of decreasing the intra-layer particle separation while increasing the distances between bilayers. As a result, the PHGO model with an elongation $k = 5$ can be used for the modeling of surface induced switching in hybrid anchored systems of flexoelectric particles; the implementation of this is discussed in the next Chapter.

Chapter 7

Confined pear shaped particles

Introduction

In this Chapter, the knowledge acquired from our earlier studies of confined systems and the development of the pear shaped PHGO model are brought together. The aim here is to construct a model for a liquid crystal display cell in which as proposed by Davidson and Mottram [1], the switching is achieved though a combination of flexoelectric behaviour and surface bistability. This is attempted here using a hybrid anchored slab of confined flexoelectric (pear shaped) particles homeotropically anchored on the top of the cell and with a homeotropic/planar bistable anchoring on the bottom.

This Chapter presents the steps undertaken in order to achieve both the easy and hard switching routes between the hybrid aligned nematic and vertical states of such a display.

7.1 The flexoelectric display

The model proposed by Davidson and Mottram [1] is an idealised representation of an existing display cell, the ZBD device [185], in which the grating morphology of the ZBD device is treated as a planar surface which has homeotropic or planar anchoring states. The geometry considered in [1] is shown in Figure 7.1.

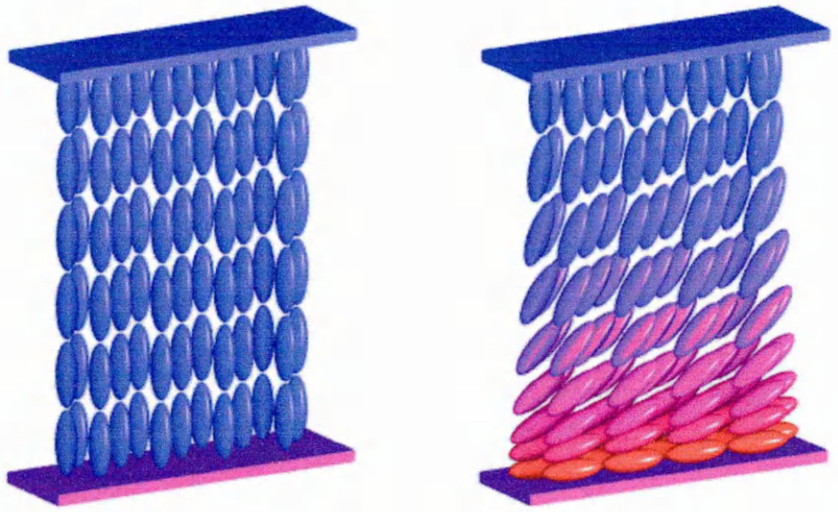

(a) The Vertical state (b) The HAN state

Figure 7.1 : Schematic representation of the two stable states of the display cell considered in [1]. The top surface induces a monostable homeotropic anchoring while the bottom surface is bistable and induces both homeotropic and planar arrangements.

In this, a system of flexoelectric mesogens is confined in a slab geometry; the top surface induces a monostable homeotropic anchoring while the bottom surface is bistable and allows both homeotropic and planar arrangements. In the case of an homeotropic bottom surface anchoring, the cell is in the so called vertical state (Figure 7.1a) and all particles have a vertical orientation; in the case of a bottom planar anchoring, the state is in a so called hybrid aligned nematic (HAN) state (Figure 7.1b) where the particle orientations change continuously from homeotropic on the top surface to planar at the bottom.

Easy switching between these states can be achieved by applying an electric field between the two substrates which will reorient the particles either parallel or perpendicular to the surfaces for respectively a negative or positive molecular dielectric susceptibility. Upon removal of this field, because of the strong homeotropic anchoring at the top surface, particles close to that substrate will recover the

$\delta\epsilon$	easy switching	hard switching
$\delta\epsilon > 0$	HAN to V using $E < 0$	V to HAN using $E > 0$
$\delta\epsilon < 0$	V to HAN using $E > 0$	HAN to V using $E < 0$

Table 7.1 : Electric parameterisation given in [1] required to performed the 'easy' and 'hard' switching between the HAN and vertical states.

homeotropic anchoring whereas particles close to the bottom substrate will keep the field induced orientation because of the bottom surface bistability. As a result both HAN and vertical states can be produced with an appropriate choice of starting configuration and electric field for a given value (and sign) of the molecular dielectric susceptibility.

The difficulty that then arises is that of achieving the reverse switching, the so called hard switching from V to HAN if $\delta\epsilon > 0$ or from HAN to V if $\delta\epsilon < 0$. Davidson and Mottram showed that this 'hard switch' can be made possible by reversing the field orientation and using moderate values of the field strength, if the liquid crystal particles have flexoelectric properties. Upon application of the reverse field, competition is created between the dielectric alignment behaviour and the field-induced splay promoted by the flexoelectricity. For appropriate values of the field, this competition causes the confined liquid crystal to adopt a distorted state which, upon removal of the field, relaxes to the other state thus rendering hard switching possible. Table 7.1 summarizes the parameterisation combinations required to achieve easy and hard switching of the cell.

The treatment used by Davidson and Mottram was, however, based on elastic theory approach. In this Chapter, the aim is to investigate, using molecular simulations, the validity of this and thus get a microscopic picture of the process underlying the switching scheme.

In order to model the display proposed by Davidson and Mottram using molecular simulation methods, a similar slab geometry like that shown on Figure 7.1 is to

be used, that is with an homeotropic top surface and a bistable bottom surface. The flexoelectric molecules are to be represented using the $k = 5$ PHGO model for pear shaped particles developed in Chapter 6.

The competition between the dielectric effect and the field-induced flexoelectric splay is to be achieved through a particle-field interaction made of dielectric and dipolar contributions, as shown in Appendix B. In the case of a negative dielectric susceptibility, for example, the particles need to experience the competitive effects of the dielectric contribution, which tends to align the particles perpendicular to the field, and the dipolar effect which tends to align the particles parallel to it. The latter has the effect of introducing splay distortions due to the preferred packing arrangement of pear shaped particles.

The system electric energy U_e is given by (see Appendix B) :

$$U_e = \sum_{i=1}^{N} \left\{ -\frac{1}{2}\epsilon_0 \delta\epsilon \left(\mathbf{E} \cdot \hat{\mathbf{u}}_i\right)^2 - \mu \left(\mathbf{E} \cdot \hat{\mathbf{u}}_i\right) \right\} \tag{7.1}$$

where ϵ_0 is the unit of energy, $\delta\epsilon$ is the dielectric susceptibility, μ is the dipole moment, $\hat{\mathbf{u}}_i$ is the molecular orientation and $\mathbf{E} = E\hat{\mathbf{E}} = E\hat{\mathbf{z}}$ is the applied electric field.

7.2 Molecular models

To achieve a simulation of the switching in this display cell requires the modeling of pear shaped particles in a confined systems and the presence of bistability between the surface induced homeotropic and planar arrangements.

The modeling of the pear shaped particles is achieved using the PHGO model as described in Chapter 6. Particles with an elongation $k = 5$ are to be used as these particles were found to form a stable nematic phase.

Particle surface interactions are to be based on the approach as developed in Chapters 4 and 5; the particles will not interact directly with the substrate, rather an object embedded into the molecules controls the surface interaction through an

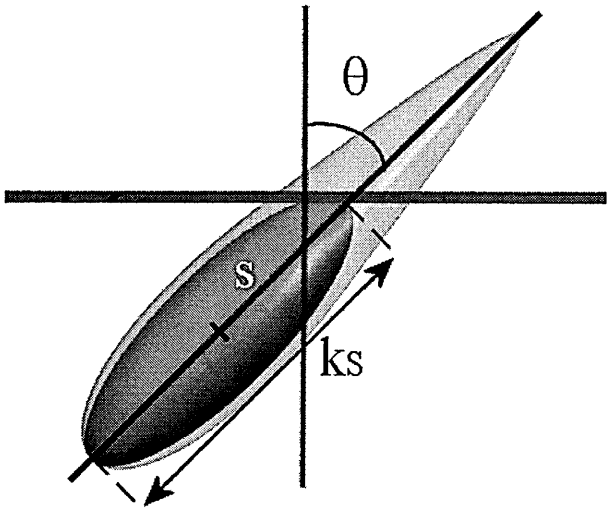

Figure 7.2 : Representation of the configuration used for the surface interaction between a pear shaped particle and the substrate. The interaction is performed by the ellipsoid embedded into the pear ; the former is shifted by an amount s along the molecular orientation.

appropriate steric potential. It has been shown in the preceeding Chapters that in the case of ellipsoidal particles, surface bistability between the homeotropic and planar arrangements can be achieved using either the HNW or the RSUP potentials; since the bistability regions for the latter are wider and stronger, this happens to be the better candidate.

However, $\mathcal{V}^{RSUP}$ represents the interaction between a Gaussian ellipsoid and a surface and its extension to the accurate description of the interaction between a pear having the shape of the Bézier pear of Chapter 6 and a surface is not straightforward.

Therefore, the RSUP potential was chosen to describe the surface interaction here. In order to prevent the inner ellipsoid from overlapping the surface of the pear shaped particle, and to add a more realistic behaviour to the model, the refinement depicted in Figure 7.2 has been made. This involves shifting the position of the inner ellipsoid along the molecular long axis towards the bulky end of the pear so

that the ends of the two objects are coincident. This mimics a situation where the particles can embed their tails but not their heads into a coated substrate. The pear-surface interaction is described by $\mathcal{V}^{PSU}$ as :

$$\mathcal{V}^{PSU} = \begin{cases} 0 & \text{if} \quad |z_{\text{obj}} - z_0| \geq \sigma_w^{PSU} \\ \infty & \text{if} \quad |z_{\text{obj}} - z_0| < \sigma_w^{PSU} \end{cases} \tag{7.2}$$

where z_0 is the position of the substrate and z_{obj} is the height of the inner ellipsoid of elongation k_S :

$$z_{\text{obj}} = z_i - \frac{1}{2}(k - k_S)\cos\theta \tag{7.3}$$

where z_i the position of the particle. σ_w^{PSU} gives the contact distance between the inner ellipsoid and the surface, that is :

$$\sigma_w^{PSU} = \sigma_0 \sqrt{\frac{1 - \chi_S \sin^2\theta}{1 - \chi_S}} \tag{7.4}$$

and χ_S is the shape anisotropy of the inner ellipsoid :

$$\chi_S = \frac{k_S^2 - 1}{k_S^2 + 1}. \tag{7.5}$$

The use of molecular visualisation tools shows that for particles with $k = 5$, the surfaces of the two objects do not overlap provided $k_S \in [2.00 : 3.92]$. As a result, all simulations of this model have been performed with reduced ellipsoid elongation $k_S/k \in [0.4 : 0.8]$ (see Figure 7.3,) the upper limit inducing only a very small overlap tangent to the surface of the pear.

With this model, a homeotropic arrangement is expected in the case of small k_S due to the ability of the tails of the particles to be absorbed by the surface. A planar arrangement is expected in the case of long k_S because, although some volume could be absorbed at the tail of the particle with $\theta = 0$, it was shown in Chapter 5 that the natural tendency of hard rods to adopt planar alignment becomes dominant as k_S/k increases.

The lack of a parametric expression for the Bézier pear shape and, therefore, the lack of an analytical expression for the absorbed volume of a pear into the surface prevented the development of an analytical prediction for the stability of the different surface arrangements. Here, therefore information on the preferred anchoring arrangement can only be obtained using computer simulations.

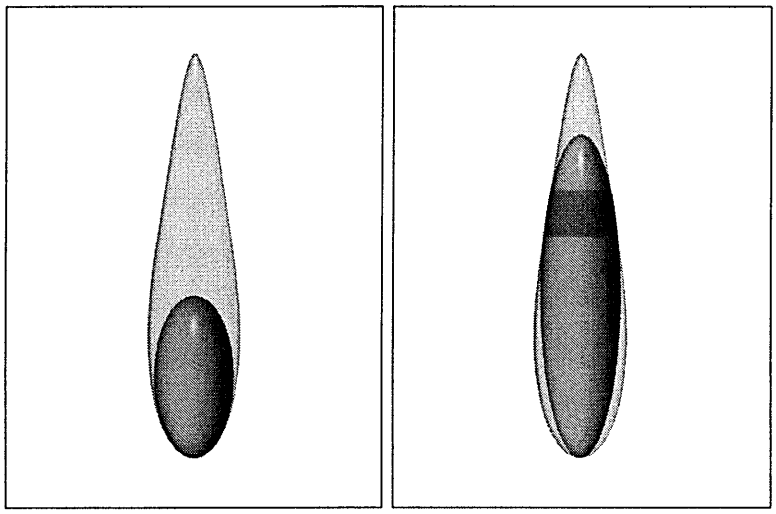

(a) $k'_S = 0.4$ (b) $k'_S = 0.8$

Figure 7.3 : Representation of the configuration of the PSU potential in the limiting cases of $k'_S = 0.4$(a) and $k'_S = 0.8$(b). The black region shows the overlap between the two objects.

7.3 Symmetric systems

Here, the surface arrangements induced by the PSU model are studied using Monte Carlo simulations in the canonical ensemble of systems of $N = 1000$ PHGO particles of elongation $k = 5$ confined in a slab geometry of height $L_z = 4k\sigma_0$ and symmetric anchoring.

Typical z-profiles obtained from those simulations are shown on Figure 7.4 for a density of $\rho^* = 0.15$ which corresponds to a bulk nematic phase and two values for k'_S corresponding to the lower and upper limits of the range available for this parameter.

For $k'_S = 0.4$, the profiles show the features typical of homeotropic anchoring, that is large peak separations in $\rho^*_l(z)$ and $\langle P_2(z)\rangle$, compatible with end to end layering. Also, $Q_{zz}(z)$ displays the typical positive values in regions corresponding to high local density. In the case $k'_S = 0.8$, by contrast, the profiles show the

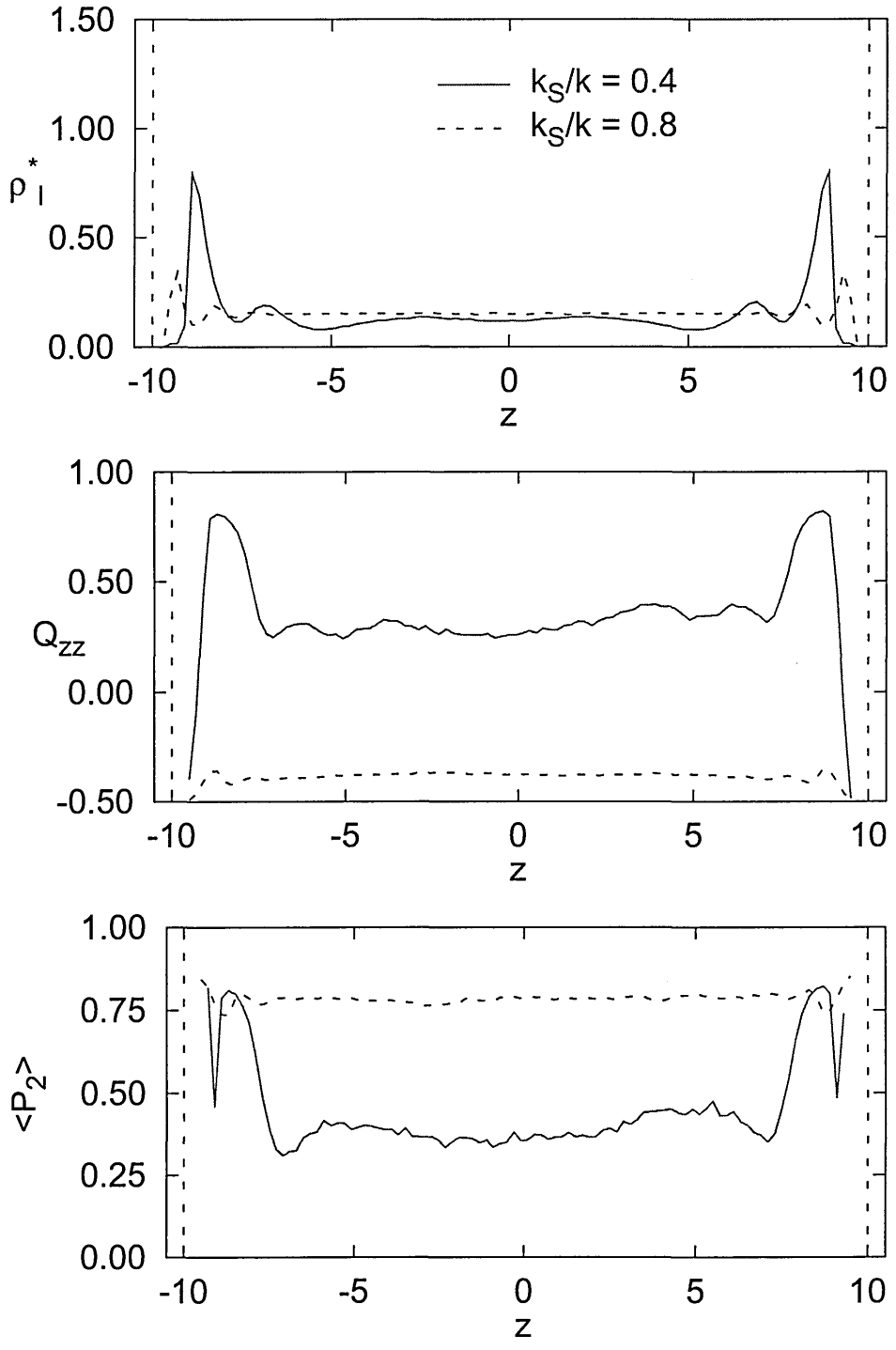

Figure 7.4 : Typical profiles for a confined system of PHGO particles with $k = 5$ *symmetric anchored with* $k'_S = 0.4$ *and* $k'_S = 0.8$ *and* $\rho^* = 0.15$.

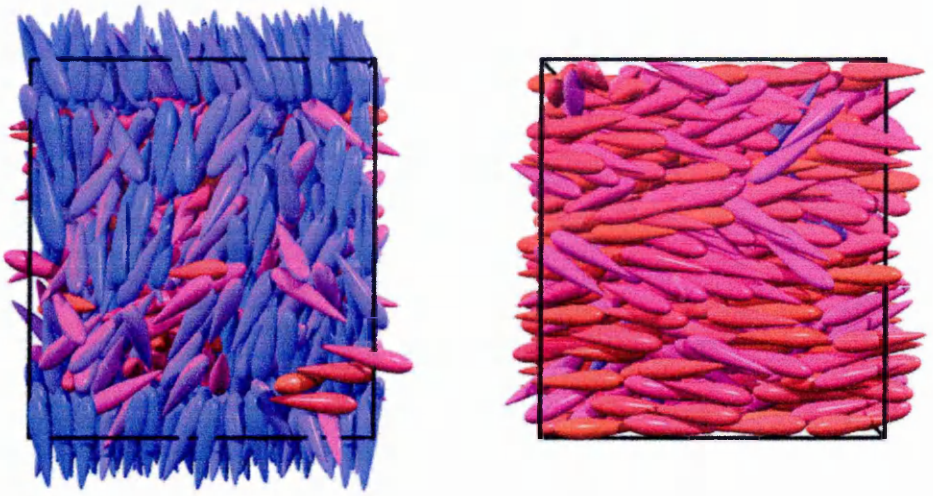

(a) (b)

Figure 7.5 : Typical snapshots for confined systems of $N = 1000$ *PHGO particles with* $k = 5$ *at* $\rho^* = 0.15$ *symmetrically anchored with* $k'_S = 0.4$*(a) and* 0.8*. The particle surface interactions are controlled by* $\mathcal{V}^{PSU}$*.*

characteristics of planar anchoring ; $\rho^*_\ell(z)$ and $\langle P_2(z)\rangle$ have a much shorter peak separation compatible with side by side alignment, and $Q_{zz}(z)$ displays negative values throughout the slab.

Observation of the configuration snapshots (*e.g.* Figure 7.5) confirms the conclusions made from the profiles. This surface behaviour confirms the assertions made in Section 7.2 and confirms the suitability of the PSU potential for the modeling of the HAN and vertical states of the display cell.

The homeotropic to planar anchoring transition has been located using Monte Carlo simulations in the canonical ensemble of symmetric systems at a constant density of $\rho^* = 0.15$ and varying the surface anchoring using series of simulations with increasing and decreasing k'_S in the range $[0.4 : 0.8]$. The location of the anchoring transition and the identification of possible bistable regions have been achieved through the observation of the evolution of $\overline{Q}^{Su}_{zz}(k'_S)$ as shown in Figure 7.6.

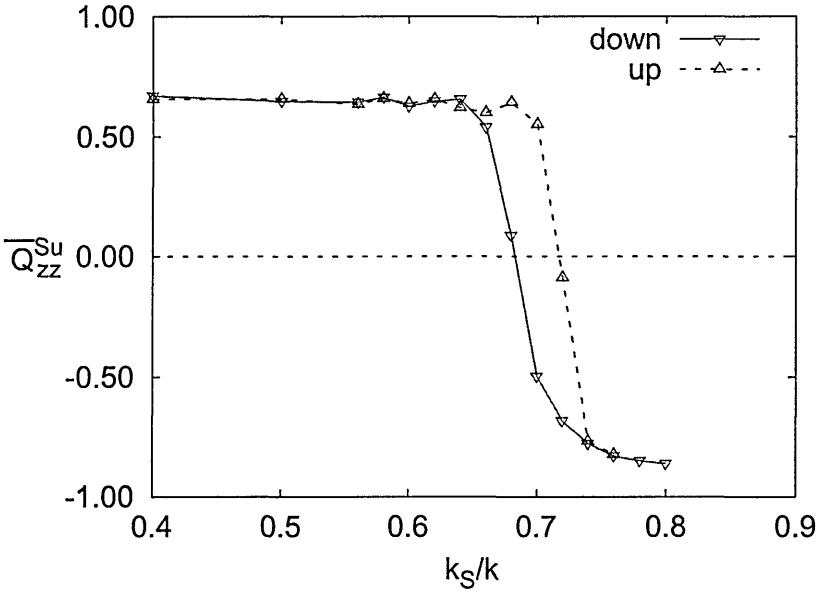

Figure 7.6 : Representation of $\overline{Q}^{Su}_{zz}$ as a function of the reduced inner object molecular elongation k_S/k for a confined system of pear shaped PHGO particles in a symmetric anchored confined geometry. The surface interaction is controlled by $\mathcal{V}^{SU}$.

This shows that the transition between the two surface arrangements takes place in the range $k'_S \in [0.64 : 0.74]$. Also in this region, the differences between the $\overline{Q}^{Su}_{zz}$ data obtained from the two series indicate a region of bistability which is strongest for $k'_S = 0.7$; with a bistability value of 1.09.

This result achieves the requirement of a bistable anchoring transition between the homeotropic and planar surface arrangements for this system. However, as only symmetric anchored systems have been used, the presence of bistability here does not guarantee a similar behaviour in the case of hybrid anchored systems. This question is addressed in the next Section.

7.4 Hybrid systems

The study of hybrid anchored systems of HGO particles presented in Chapter 5 showed that the presence of a top surface with strong homeotropic anchoring

can cause a bottom surface with competing anchoring to lose the bistability of its homeotropic and planar surface arrangements. The bistability behaviour can, however, be recovered by two complementary means. The first of these is to increase the slab height, which has the effect of creating a smoother transition between the homeotropic and planar arrangements. The second solution is to reduce the anchoring strength at the top surface in order to reduce the elastic forces this imposes on the particles anchored at the bottom surface.

Here, therefore, we study the effect of the top surface anchoring parameterisation on the bistability behaviour of the bottom surface in an hybrid anchored system of pear shaped particles interacting with the surfaces through the PSU potential. For this, systems of $N = 1000$ PHGO particles of density $\rho^* = 0.15$ with $k = 5$ confined in an hybrid anchored slab have been studied using Monte Carlo simulations in the canonical ensemble. Series of increasing and decreasing k'_{Sb} in the range $[0.56 : 0.74]$ have been used; this range corresponding to the bistability region of k'_S for symmetric systems. Three values for the top anchoring strength were considered : $k'_{St} = 0.4$, 0.5 and 0.6. The transition between the homeotropic and planar arrangements at the bottom surface was studied through the computation of $\overline{Q}_{zz}^{Sb}$ as a function of k'_{Sb}. A comparison between the $\overline{Q}_{zz}^{Sb}(k'_{Sb})$ data obtained for these hybrid systems and the data obtained from equivalent symmetric systems in Section 7.3 is shown on Figure 7.7. Configuration snapshots from those simulations with $k'_{Sb} = 0.64$ and 0.74 are shown on Figure 7.8. We note that, as in the case of the equivalent HGO systems, the HAN state found for this film thickness suggest discontinuous director profiles.

For the two lower values of k'_{St} (representing stronger homeotropic anchoring), although the two series of simulations lead to hysteresis in the values of $\overline{Q}_{zz}^{Sb}(k'_{Sb})$, no bistability can be observed. None of the state points considered here correspond to a situation where the values of $\overline{Q}_{zz}^{Sb}$ obtained from the two series are both significantly different from zero and of opposite signs.

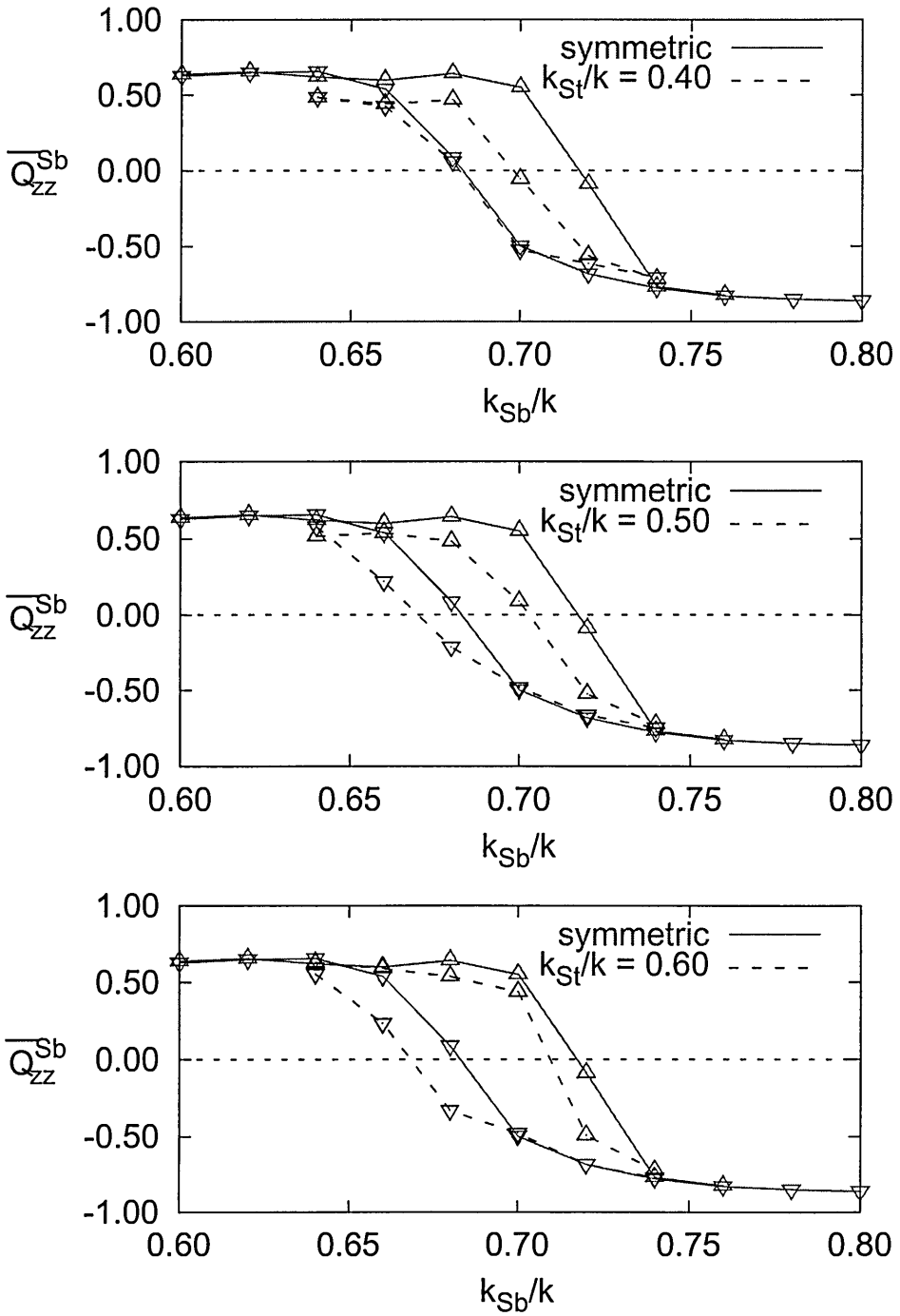

Figure 7.7 : Comparison between $\overline{Q}_{zz}^{Sb}(k'_{Sb})$ (dashed lines) from simulations of hybrid anchored systems of PHGO particles and $\overline{Q}_{zz}^{Su}(k'_S)$ from simulations of symmetric systems described in Section 7.3(solid lines). The arrows indicate whether the simulations have been performed with increasing ($\triangle$) or decreasing ($\triangledown$) values of k'_S

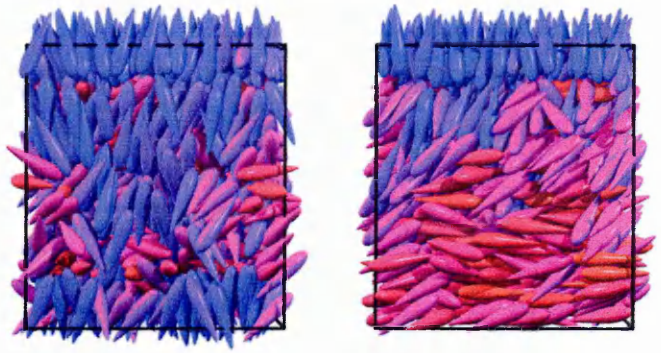

(a) $k'_{St} = 0.4$, $k'_{Sb} = 0.64$ (b) $k'_{St} = 0.4$, $k'_{Sb} = 0.74$

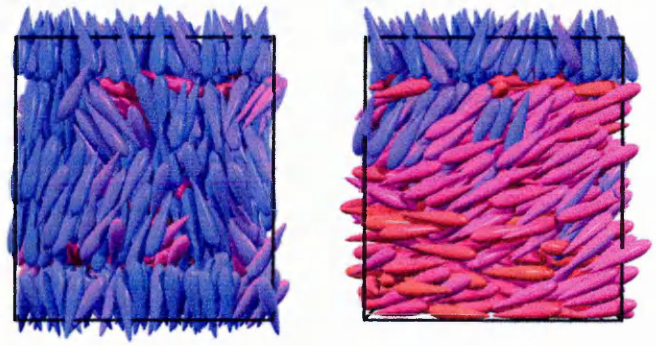

(c) $k'_{St} = 0.5$, $k'_{Sb} = 0.64$ (d) $k'_{St} = 0.5$, $k'_{Sb} = 0.74$

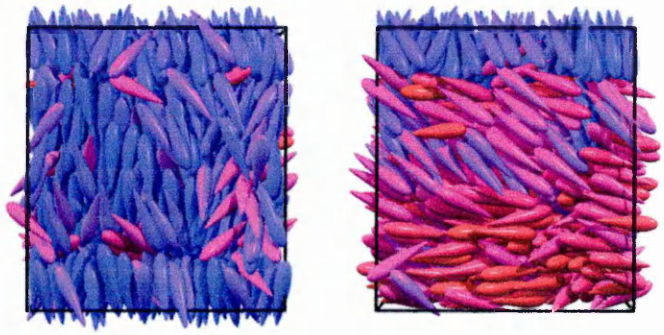

(e) $k'_{St} = 0.6$, $k'_{Sb} = 0.64$ (f) $k'_{St} = 0.6$, $k'_{Sb} = 0.74$

Figure 7.8 : Typical configuration snapshots obtained from simulations of confined systems of $N = 1000$ PHGO particles with $k = 5$ at $\rho^* = 0.15$, hybrid anchoring and different values of k'_{St} and k'_{Sb}.

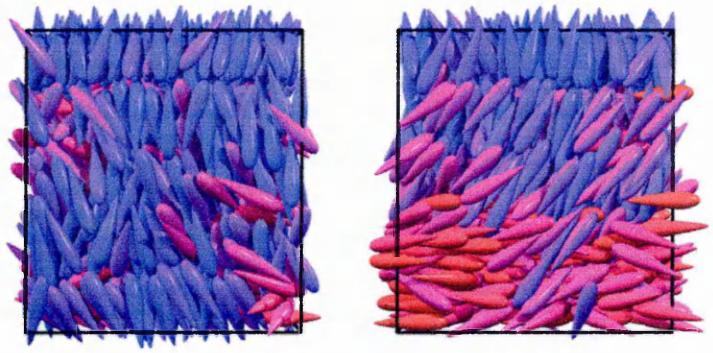

(a) increasing k'_{Sb} (b) decreasing k'_{Sb}

Figure 7.9 : Configuration snapshots showing the HAN and V states of a hybrid anchored slab of $N = 1000$ PHGO particles with $k = 5$ at $\rho^* = 0.15$ with $k'_{St} = 0.6$ and $k'_{Sb} = 0.7$. Those configuration have been obtained from series of simulations with increasing (a) and decreasing (b) values of k'_{Sb}

With $k'_{St} = 0.6$, however, a small bistable region is recovered around $k'_{Sb} = 0.7$; the values of $\overline{Q}_{zz}^{Sb}$ are different and of opposite signs. The bistability value for $k'_{Sb} = 0.7$ is 0.914 which is very close to that obtained with symmetric anchored systems. Configuration snapshots corresponding to the HAN and V states of the cell at this state point are given on Figure 7.9.

These results show that reducing the strength of the anchoring at the top surface allows to recover the bistability region by increasing the hysteresis in $\overline{Q}_{zz}^{Sb}$. The value $k'_{St} = 0.6$ seems to be the highest reasonable that can be used, as according to $\overline{Q}_{zz}^{Su}(k'_S)$, the use of a higher value would not lead to homeotropic anchoring at the top surface.

The results from these simulations are reasonably encouraging for the application of the model to the HAN to V switching since, despite the very narrow bistability region for k'_{Sb}, the difference between the $\overline{Q}_{zz}^{Sb}$ values obtained from the two series with $k'_{St} = 0.6$ appears sufficient for the model to be used in the display modeling.

Also, the snapshots show encouraging HAN and V states which should be further improved by the use of wider systems.

7.5 Flexoelectric switching

Here the possibility of two-way switching between the HAN and vertical states using the flexoelectric properties of the model and the bistable nature of the bottom surface is investigated. This is performed in three steps. First, the stability of the HAN and vertical states are assessed by performing the easy switching between the two states, and considering only the dielectric term in the electric energy (*i.e.* $\mu = 0$). Then, the possibility of hard switching is investigated by including a dipolar term in the electric energy. This requires finding an appropriate combination of values for the electric field magnitude, dielectric anisotropy and the dipole moment. Finally, keeping the same parameterisation as that used to achieve hard switching, the possibility of easy switching is investigated again so as to check that the newly introduced dipolar contribution does not hinder the reverse switching.

In order to use the most favorable conditions for achieving switching and obtaining a smooth structural transition from homeotropic to planar in an HAN cell, all simulations used the Monte Carlo method in the canonical ensemble and used systems of $N = 2000$ particles in a cell of width $8\sigma_0$. Hybrid anchoring with the parameterisation corresponding to the maximum hysteresis obtained in the previous section, that is $k'_{St} = 0.6$ and $k'_{Sb} = 0.7$, was employed.

7.5.1 Easy switching

The aim of the simulations performed here is mainly to test for the stability of the HAN and vertical states found in the previous Section. Therefore, easy switching has been attempted between those two states by considering only the dielectric term in the particle-field interaction (*i.e.* $\delta\epsilon \neq 0, \mu = 0$).

Two series of simulations have been performed using an hybrid anchored slab with

the surface parameterisation given at the beginning of this Section. Starting with an HAN configuration, the first simulation attempted to switch to the vertical state by application and subsequent removal of an electric field and considering the particles to have a positive dielectric anisotropy. Then, taking the particles to have a negative dielectric anisotropy, a second series of simulations was used to switch back to the HAN state starting from the vertical state obtained from the first series.

Each series consisted of a first run of $2.0.10^6$ sweeps, performed to equilibrate the starting configuration with the field off. This was followed by a simulation of $0.5.10^6$ sweeps with the field on, which primed the switching. The resulting system was equilibrated in the new state for another 2.10^6 sweeps with the electric field removed. The electric parameterisation used here was $E = 1.0$, $\delta\epsilon = \pm 1.0$ and $\mu = 0$.

The evolution of $\overline{Q}_{zz}$ at the bottom surface as a function of the number of sweeps is shown on Figure 7.10. The snapshots corresponding to the final configurations from phase of the simulation sequence are shown on Figures 7.11 and 7.12.

These results, along with the corresponding profile data (not shown) confirm both the stability of the HAN and vertical states for this system and the ability of the easy switching mechanism to switch between them.

7.5.2 Hard switching

We now turn to the possibility of achieving hard switching between the HAN and vertical states of the slab, following the theoretical treatment of [1]. Here both the dielectric and dipolar terms in the particle-field interaction are required (*i.e.* $\delta\epsilon \neq 0$ and $\mu \neq 0$). Only the case of particles with a negative dielectric susceptibility is considered. The aim here is to find an appropriate parameterisation which allows for switching from the HAN to the vertical states after application of an electric field along $\hat{\mathbf{z}}$. Reference [1] shows that such switching can be achieved using $E < 0$.

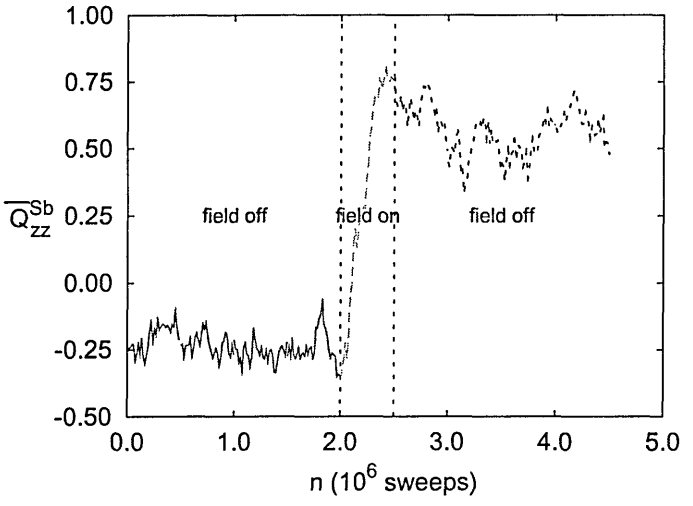

(a)

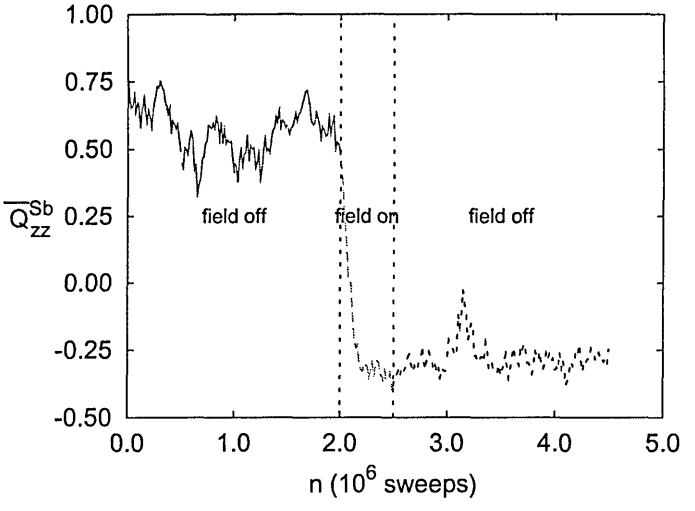

(b)

Figure 7.10 : Evolution of $\overline{Q}_{zz}^{Sb}$ with sweep number in the simulations of the HAN to vertical(a) and vertical to HAN (b) 'easy switching' of the hybrid anchored slab described at the beginning of this Section. Here only dielectric interactions between the particles and the field are considered. The data for the last and first field off series of (a) and (b) respectively have been obtained from the same simulation.

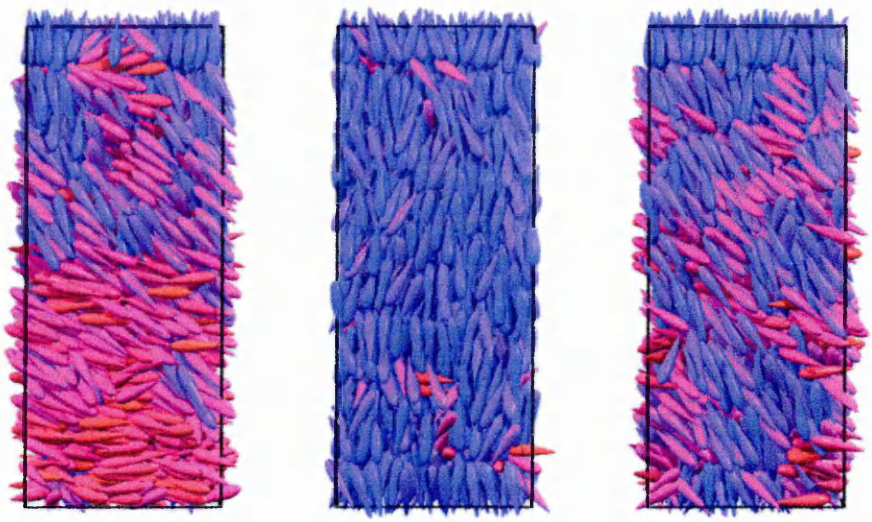

(a) field off (b) field on (c) field off

Figure 7.11 : Configuration snapshots corresponding to three phases (a) to (c) of the HAN to vertical 'easy switching' of the hybrid anchored slab.

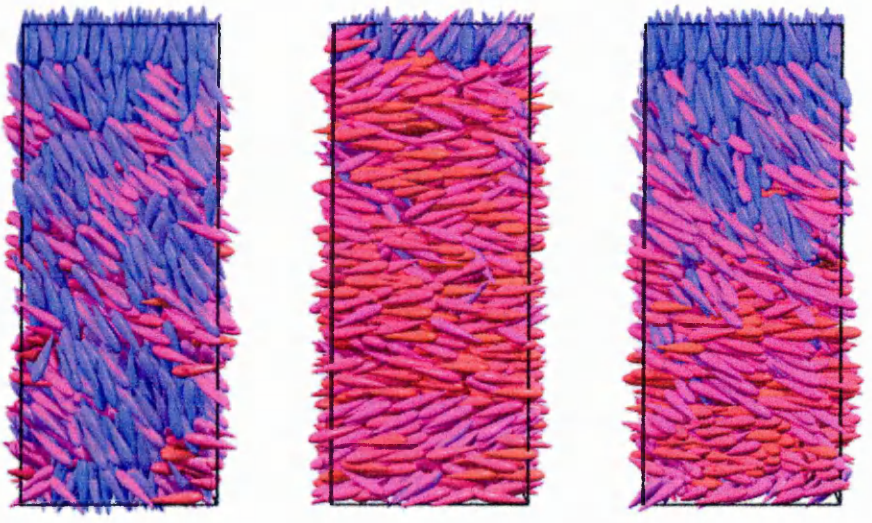

(a) field off (b) field on (c) field off

Figure 7.12 : Configuration snapshots corresponding to three phases (a) to (c) of the vertical to HAN 'easy switching' of the hybrid anchored slab.

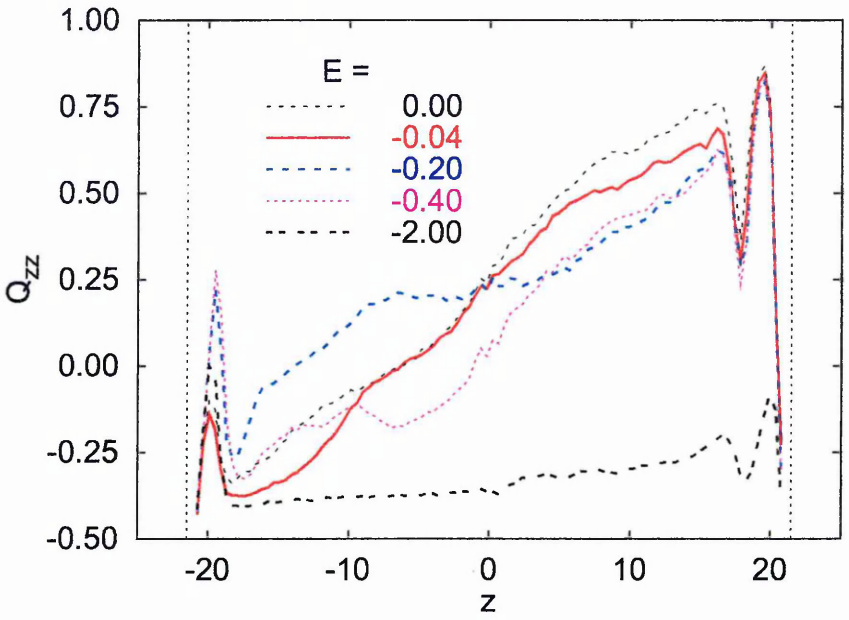

Figure 7.13 : $Q_{zz}(z)$ profiles for an HAN slab subject to an applied electric field along $\hat{\mathbf{z}}$ and different values of E.

Choice of E

The first step is to find an appropriate value for the electric field. This needs to be strong enough to allow the dipolar contribution to distort the director profile and bring the system to an intermediate state that will relax into the vertical state after removal of the field. If the field is too strong, however, the dielectric effect (which scales as E^2) will dominate, causing the HAN state to be stabilised and thus, rendering the switch to the vertical state impossible.

In order to find an appropriate value for E, a slab in a HAN state has been simulated using $\delta\epsilon = -1.0$, $\mu = 1.0$ and different values for the electric field in the range [-0.02:-6.0]. For each value of E, the system was subject to an equilibration run of $0.25.10^6$ sweeps followed by a production run of the same length. Figure 7.13 shows the Q_{zz} profiles obtained from the production runs for a selection of these field strengths.

These results show that, given the chosen parameterisation adopted for $\delta\epsilon$ and μ, values less negative than $E = -0.2$ do not induce any significant distortions near the bistable surface and that, despite the applied electric field, the system

always remains in the HAN state. For fields of strength more negative than -0.4, in contrast, the dielectric contribution dominates and stabilises the HAN state. For the highest absolute values of E, all particles are forced to be parallel to the surfaces, even those subject to the homeotropic anchoring of the top surface. Figure 7.13 however, indicates promising behaviour for $E = -0.2$, for which the dipolar coupling seems to be strong enough to induce a slight distortion of the profile without there being too strong a dielectric effect. This raises the prospect that by increasing the value of μ and keeping all other parameters constant, this distortion can be increased to the extend that switching to the vertical state can be achieved.

Choice of μ

Here, an attempt is made to identify an appropriate value of μ so that, upon application of the electric field with $E = -0.2$, the dipolar effect induces enough of a distortion to cause a HAN configuration system to equilibrate into a vertical state upon removal of the field.

In order to achieve this, simulations of the slab have been carried out taking the HAN configuration as an initial state. For each μ value the simulation sequence performed consisted of two runs (one for equilibration and one for production) with an applied electric field followed by two runs (equilibration and production) where the field was removed. Each run comprised $0.25.10^6$ sweeps and the parameterisation $E = -0.2$ and $\delta\epsilon = -1.0$ was used. The first two runs were used to establish the 'field-on' intermediate state while the last to generated the state to which the system subsequently relaxed. The series of simulations described above was performed with six values of μ in the range $[1.0 : 3.5]$.

The $Q_{zz}(z)$ profiles corresponding to the obtained field 'on' and 'off' configurations are shown on Figure 7.14 and 7.15 along with the profiles corresponding to the HAN and vertical states which are shown for comparison. Configuration snapshots of the field -on and field-off structures for $\mu = 2.5$, 3.0 and 3.5 are shown, respectively, in Figures 7.16, 7.17 and 7.18

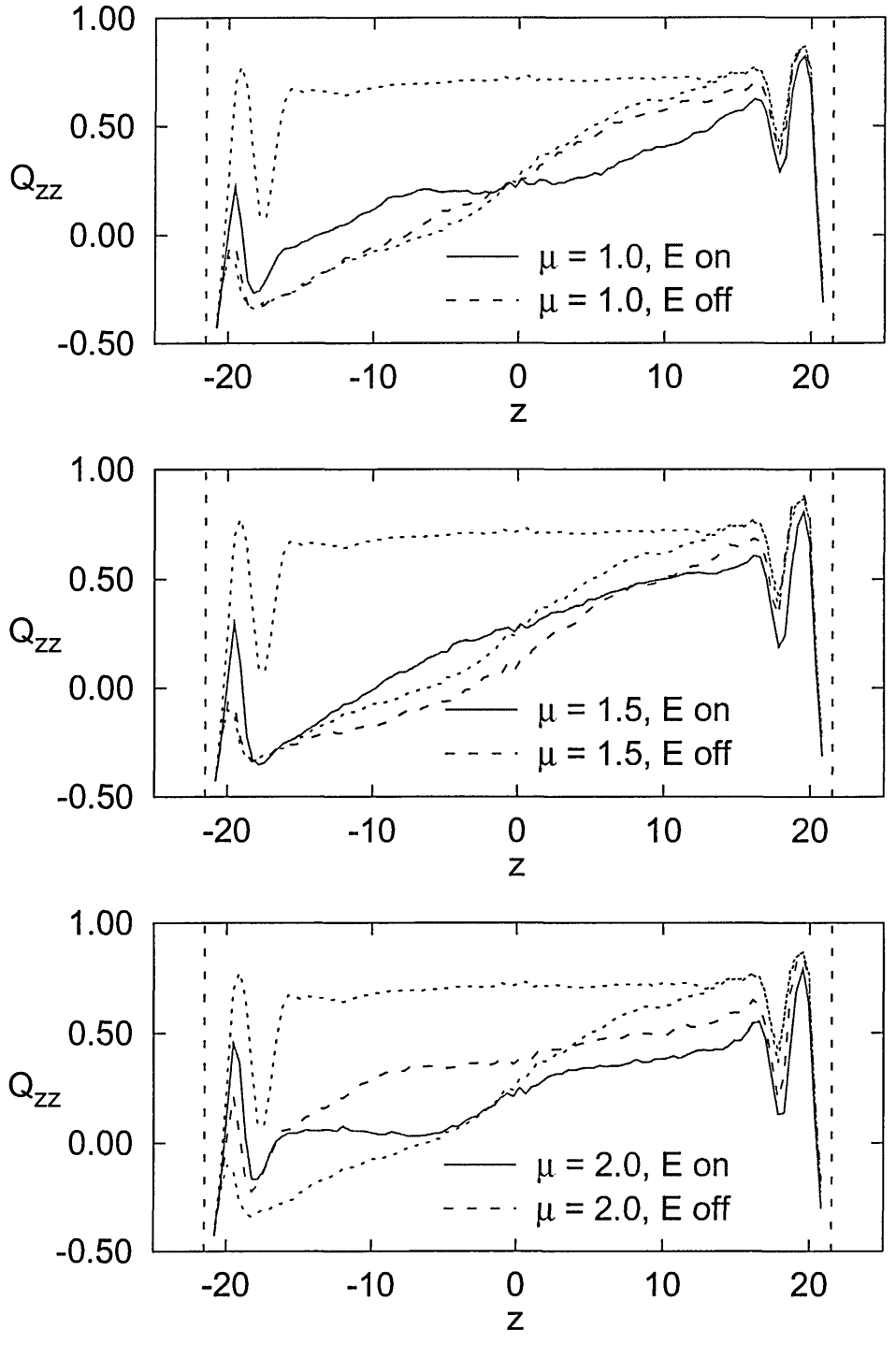

Figure 7.14 : Q_{zz} profiles for an HAN slab subject to an applied electric field with $E = -0.2\hat{\mathbf{z}}$ and $\delta\epsilon = -1.0$ and different values of the dipolar moment $\mu \in [1.0 : 2.0]$.

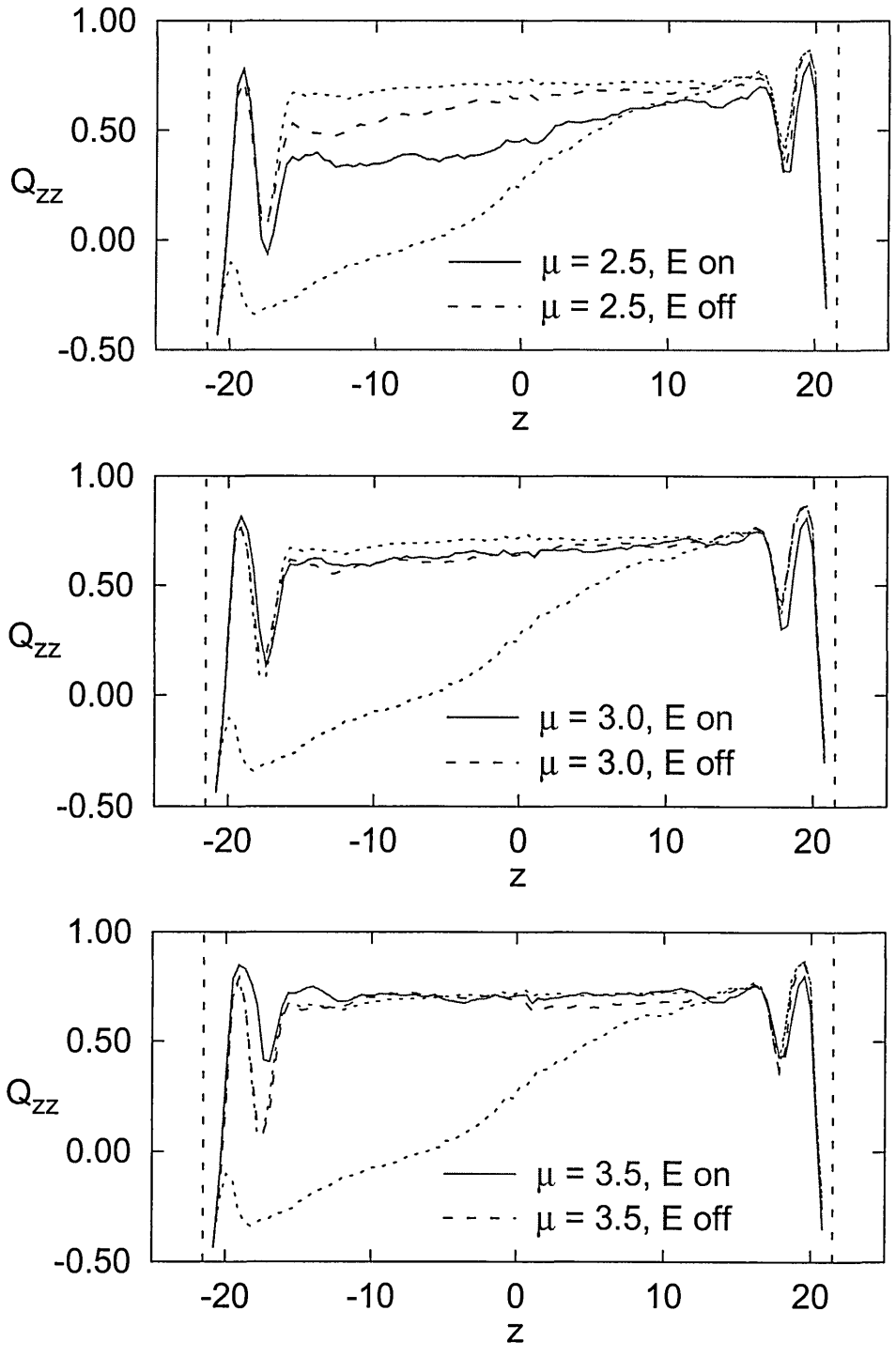

Figure 7.15 : Q_{zz} profiles for a slab in the HAN configuration and subject to an applied electric field with $E = -0.2\hat{\mathbf{z}}$ and $\delta\epsilon = -1.0$ and different values of the dipolar moment $\mu \in [2.5 : 3.5]$.

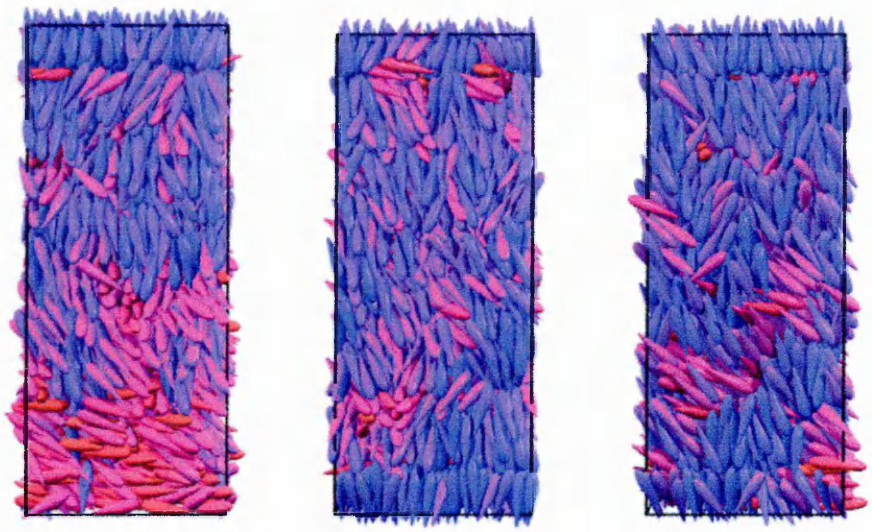

(a) start (b) field on (c) field off

Figure 7.16 : Configuration snapshots corresponding to the hard switching of a slab in an initial HAN state with $E = -0.2\hat{\mathbf{z}}$ *and* $\delta\epsilon = -1.0$ *and* $\mu = 2.5$.

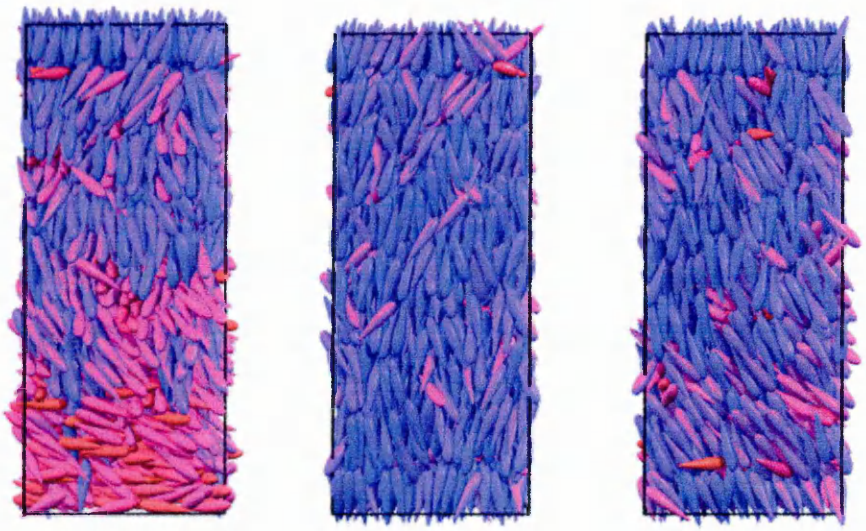

(a) start (b) field on (c) field off

Figure 7.17 : Configuration snapshots corresponding to the hard switching of a slab in an initial HAN state with $E = -0.2\hat{\mathbf{z}}$ *and* $\delta\epsilon = -1.0$ *and* $\mu = 3.0$.

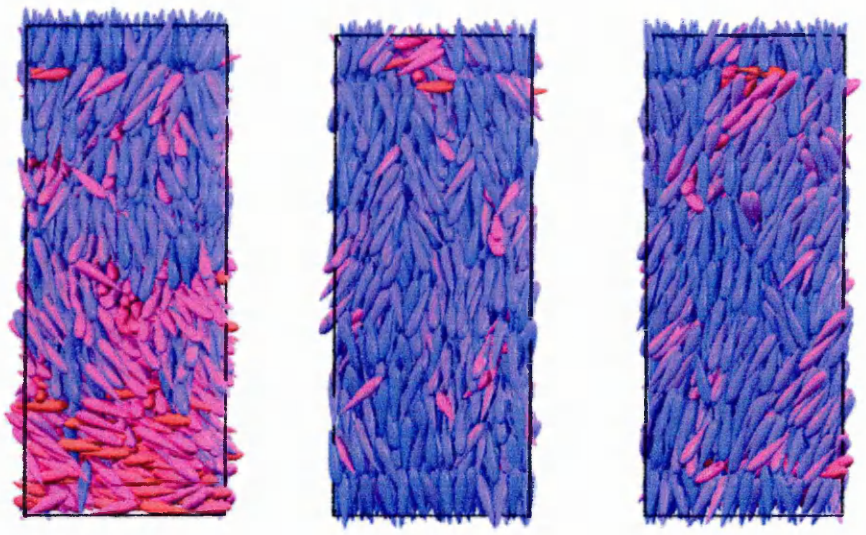

(a) start (b) field on (c) field off

Figure 7.18 : Configuration snapshots corresponding to the hard switching of a slab in an initial HAN state with $E = -0.2\hat{\mathbf{z}}$ *and* $\delta\epsilon = -1.0$ *and* $\mu = 3.5$.

From the $Q_{zz}(z)$ data, it appears that the switching from the HAN state to the vertical state is possible using values of $\mu \geq 2.5$. As μ is increased, so does the distortion induced by the dipolar term in U_e; more specifically, the profile at the bottom surface is changed, so inducing the bulk part of the cell to modify its orientation co-operatively. Upon removal of the field, for μ values at which this distortion is sufficient, the cell equilibrates into the vertical state, thus confirming the results of [1].

7.5.3 Reverse switching

In Sections 7.5.1 and 7.5.2, respectively, it was shown that easy switching between the HAN and vertical states can be achieved using only the dielectric effect and that, using an appropriate parameterisation ($E = -0.2$, $\delta\epsilon = -1.0$ and $\mu \in [2.5 : 3.5]$), hard switching from the HAN to the vertical state can be achieved. However, easy switching from vertical to HAN state is not necessarily possible us-

ing the same parameterisation as that used to achieve hard switching but with $E > 0$ since the dipolar contribution might be too strong to permit the formation of the HAN state.

This issue is addressed here by attempting to perform the easy switching again but this time with both the dielectric and dipolar term included in the particle-field interaction. A similar parameterisation as that used in Section 7.5.2 is applied here, the difference being that the electric field director is taken to be positive. As a result the parameterisation $E = 0.2$, $\delta\epsilon = -1.0$ and $\mu \in [2.5 : 3.5]$ is used. Several values of μ are considered so as to also investigate the effect of increasing μ. These simulations were performed using a similar sequence as that used in 7.5.2, the main difference being that the initial configuration for each series with different μ was the final configuration obtained for the vertical state from the hard switching simulations with the appropriate μ value.
The $Q_{zz}(z)$ profiles corresponding to the 'field-on' and 'field-off' states obtained for each value of μ are shown on Figure 7.19 and the corresponding configuration snapshots for $\mu = 2.5$, 3.0 and 3.5 are shown, respectively, on Figures 7.20, 7.21 and 7.22.

The $Q_{zz}(z)$ data show that, upon application of the field, most of the vertical slab arrangement remains undistorted, expect for a region near the bottom surface which adopts a planar arrangement. Upon removal of the field, this small interfacial distortion proves sufficient to seed this orientation into the bulk part of the cell. Because of the homeotropic top surface influence, the slab then recovers the HAN state. These results also show that the distance from the bottom surface over which the cell's vertical alignment is distorted in the field-on state decreases with increased μ. For the run lengths used here, this has the effect of producing HAN states of reducing quality as μ is increased. This trend suggests that with $\mu > 3.5$, although the hard switching is possible, easy switching might be inhibited by high values of the dipolar coupling term. As a result it can be concluded

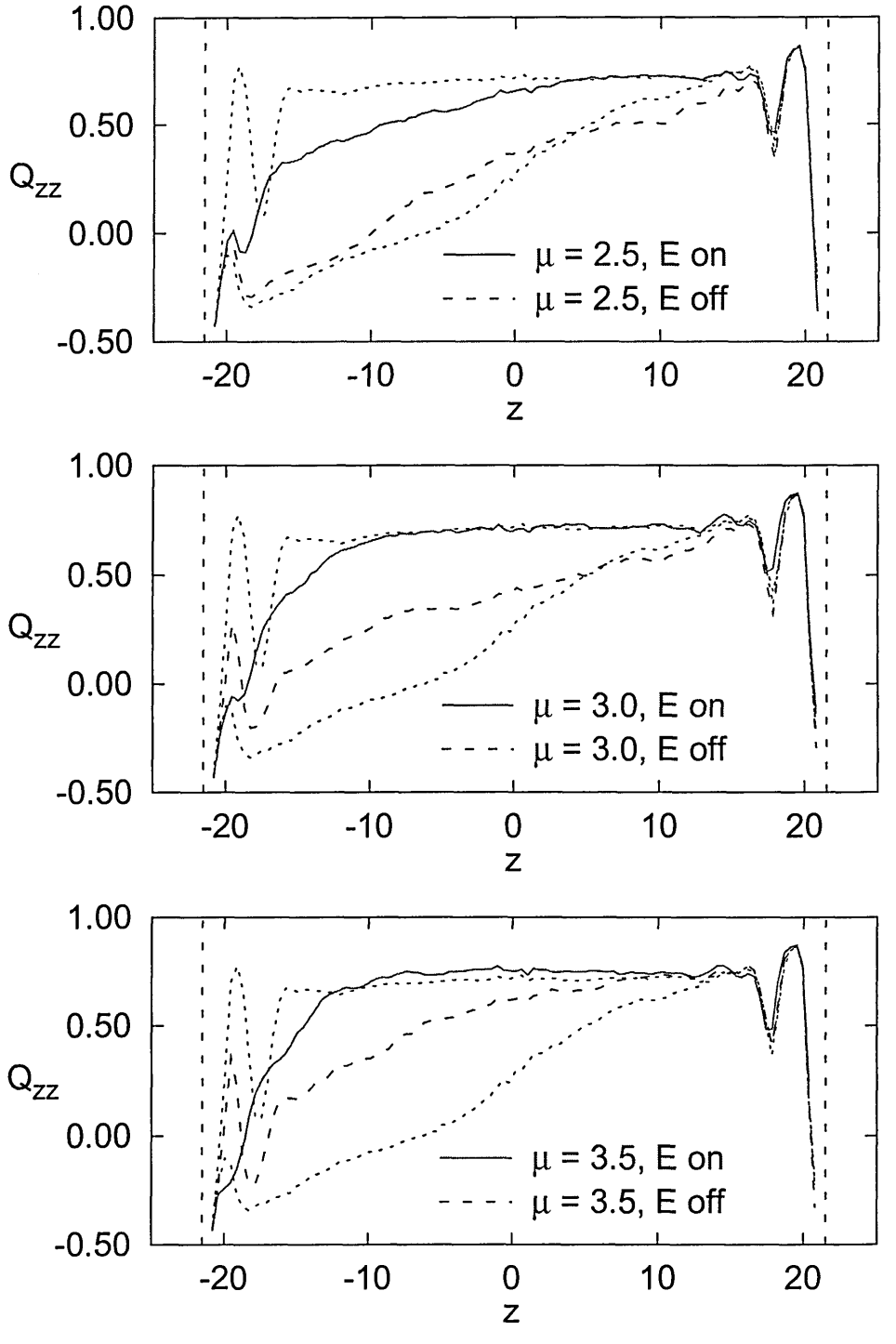

Figure 7.19 : Q_{zz} profiles for a slab in the vertical configuration and subject to an applied electric field with $E = 0.2\hat{\mathbf{z}}$ and $\delta\epsilon = -1.0$ and different values of the dipolar moment $\mu \in [2.5 : 3.5]$.

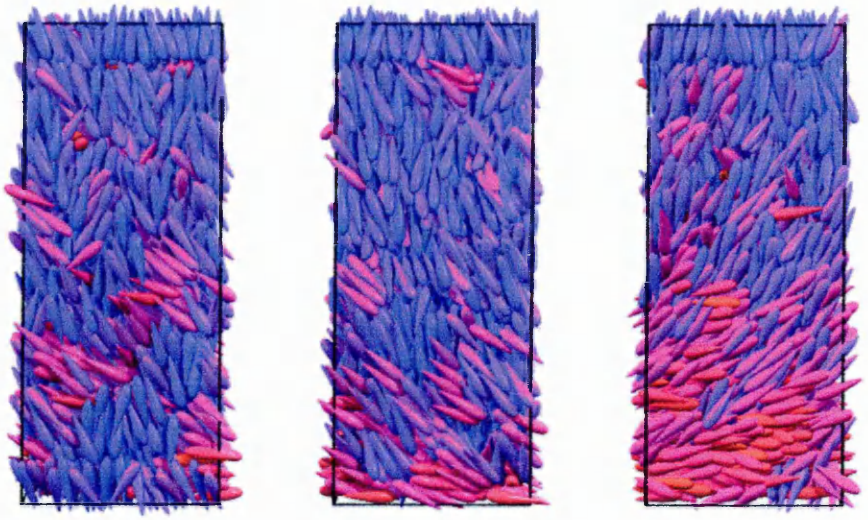

(a) start (b) field on (c) field of

Figure 7.20 : Configuration snapshots corresponding to the hard switching of a slab in an initial vertical state with $E = 0.2\hat{\mathbf{z}}$ *and* $\delta\epsilon = -1.0$ *and* $\mu = 2.5$.

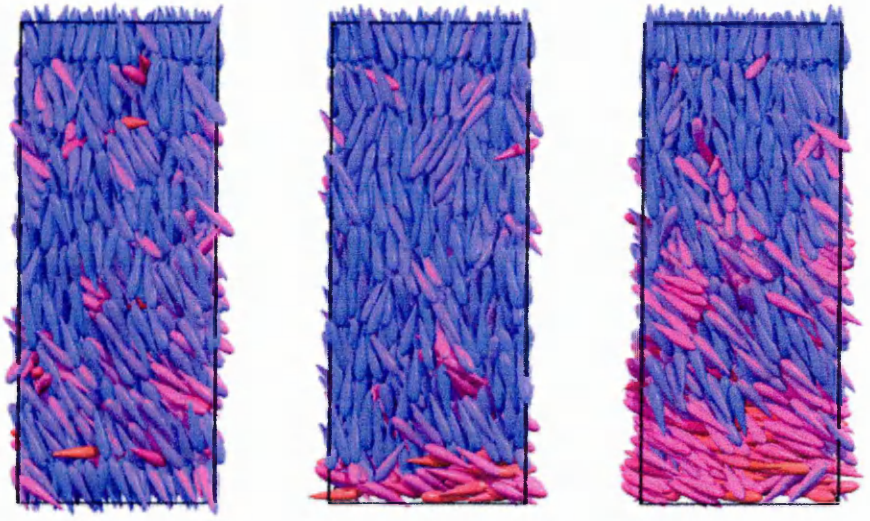

(a) start (b) field on (c) field off

Figure 7.21 : Configuration snapshots corresponding to the hard switching of a slab in an initial vertical state with $E = 0.2\hat{\mathbf{z}}$ *and* $\delta\epsilon = -1.0$ *and* $\mu = 3.0$.

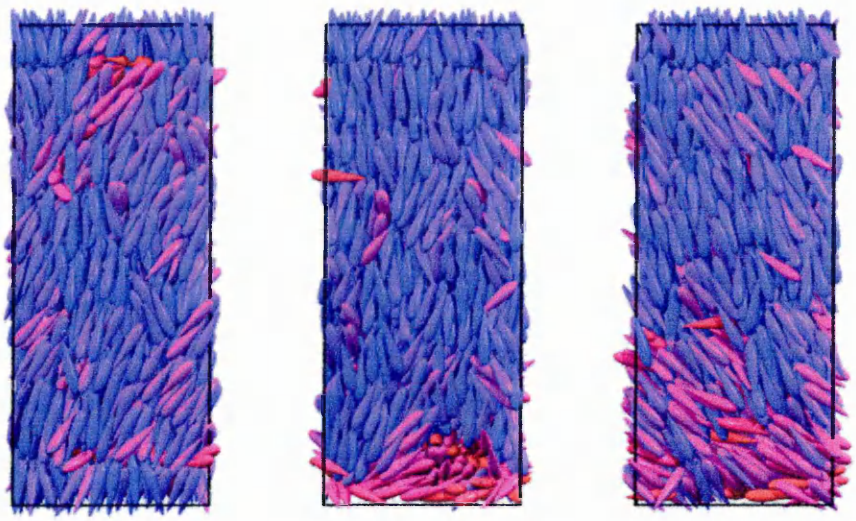

(a) start (b) field on (c) field off

Figure 7.22 : Configuration snapshots corresponding to the hard switching of a slab in an initial vertical state with $E = 0.2\hat{\mathbf{z}}$ *and* $\delta\epsilon = -1.0$ *and* $\mu = 3.5$.

that switching between the HAN and vertical states of the hybrid anchored slab can be achieved if the dipolar term to the electric field is included, but that the parameterisation should be compatible with a window of electric field and dipolar coupling strength and that if $\delta\epsilon =< 0.0$, $E \sim 0.2\delta\epsilon$ and $\mu \sim -2.5\delta\epsilon$.

Conclusion

In this Chapter, two issues have been addressed. First, the surface induced structural changes in confined systems of PHGO pear shaped particles interacting with the surface through the RSUP model have been studied, and bistability regions between the two surfaces arrangements have been found using a surface parameter in the range $k_s \sim 0.7$. Also, it has been shown that this bistability behaviour can be recovered at the bottom surface of an hybrid anchored slab with a top surface homeotropic anchoring provided the latter is not too strong (*i.e.* $k_{St} = 0.6$.) Following this, switching between the HAN and vertical states of such a cell has

been investigated using a particle-field interaction containing both dielectric and dipolar contributions. It has been shown that both easy and hard switching can be performed provided the energy parameterisation is compatible with a window in both the electric field strength and dipolar constant. Both switching direction can be achieved using $E = \pm 0.2\delta\epsilon$ and $\mu = 2.5\delta\epsilon$.

Having achieved the two switching modes presented in [1], with a molecular model, it is apparent that there are several possible mechanisms underlying this switching. The particle-particle and particle-field interactions used have been developed to allow the bulk flexoelectric effects, considered in [1], to play a role in the hard switching. There is also, however, an implicit dipolar symmetry to the particle-substrate interaction used in this work, which may also have played an important role in the simulations presented in Sections 7.5.1 and 7.5.2. Resolving which of these mechanisms is the dominant effect present in both these simulations and the real devices they attempt to model, is beyond the scope of this Thesis; we do, however, comment in the general conclusion Chapter possible steps to be taken to this end.

Conclusions and future work

In this Thesis, the study of confined liquid crystalline systems and the development of a model for tapered pear shaped particles were addressed. These two seemingly very different lines of work have subsequently been united in the study of confined pear shaped particles which lead to towards the final aim of the Thesis: the development of a model for a liquid crystal display cell where switching between the two stable states may be flexoelectricity induced. The development of this latter model required two conditions to be met, the first being a surface potential inducing both planar and homeotropic anchoring and, with appropriate tuning of the model parameter, a bistability region. The second requirement was that of a molecular model for flexoelectric (*i.e.* pear shaped) mesogens displaying a stable nematic phase.

Here, the conclusions that have been drawn from this study are summarized and various avenues for future work are discussed.

Conclusions

The study of confined hard particle liquid crystalline systems has been addressed in Chapters 4 and 5. The Surface induced structural changes in symmetric anchored systems have been studied using three surface interaction models, namely the hard needle wall (HNW), rod-sphere (RSP) and rod-surface (RSUP) potentials. For all three of these models, the surface interaction was not mediated directly by the HGO particles, but by other objects embedded within them. This approach allowed the study to be extended to include consideration of the effect

of varying particle absorption into the surface. Through this, it has been shown that the HNW and RSUP potentials induce planar and homeotropic anchoring for, respectively, long and short elongations of the inner object (k_S) whereas with the RSP potential and long k_S, the planar arrangement was replaced by tilted anchoring. These results have proved to be consistent with a theoretical treatment based on the geometrical characteristics of the surface interaction models. The implications of these results are twofold. The behaviour found for the HNW and RSUP models showed that the anchoring transition between homeotropic and planar arrangements can be controlled by the molecular volume made available to be absorbed into the substrates. Secondly, the tilted phase obtained with the RSP model lead to a revision of the explanation of tilted surface arrangements which had previously always been attributed to attractive forces. The observation of such a structure in this study showed that it can also be obtained with a purely steric potential.

Anchoring and order phase diagrams have been computed for all models. For the HNW and RSUP potentials, using series of simulations at constant densities and either increasing or decreasing k_S, regions of bistability between the planar and homeotropic surface arrangement have been found. Those regions proved to be stronger and wider for the RSUP model. This shows that even in very simple model systems, bistable surface behaviour can be introduced by tuning the competition between two locally stables states. This suggests that similar tuning of real liquid crystal substrate systems may offer a viable route to relatively simple bistable surfaces for low energy device applications.

Hybrid anchored systems with a top homeotropic surface have been studied in Chapter 5 using the HNW as a surface potential in an attempt to create a hybrid anchored slab with a top surface homeotropic anchoring and bistable anchoring at bottom substrate. It has been shown that the bistability behaviour of the model at the bottom surface is lost if the top homeotropic anchoring is made too strong. However, by reducing the latter (*i.e.* reducing k_S), the bistability at the

bottom surface can be recovered. This has been explained in terms of the elastic forces transmitted from the top surface particles onto those at the bottom surface. Reducing the top anchoring strength reduces these forces and, thus, allows bistability to be recovered. The point has also been addressed in Chapter 7. Also, the behaviour of the homeotropic to planar structural transition has been shown to be dependent upon the slab height. For short slabs (*i.e.* small systems), there is a discontinuous structural transition between the two arrangements, whereas this becomes continuous for thicker slabs (*i.e.* bigger systems). These findings are consistent with both experimental and theoretical studies of the effect of thickness on the bent director structure of a hybrid anchored system. Also, this result has shown that the first prerequisite for the modeling of a bistable LCD cell can be met: it is possible to simulate a hybrid anchored slab with a homeotropically anchored top surface and bistable anchoring at the bottom surface using an appropriate parameterisation for the surface model. In addition, provided large enough systems are used, a continuous structural transition from homeotropic to planar alignment can be obtained if the slab is in the HAN configuration.

Chapter 6 has addressed the study of tapered pear-shaped particles. The first model to be used for this was the truncated Stone expansion model; this, however, did not meet the requirement of displaying a stable nematic phase and showed only two phases: an isotropic phase at low density and glassy domain-ordered phase at high density. This behaviour proved to be very surprising as an equivalent soft model used by the Bologna group showed isotropic, nematic and smectic A phases. The lack of ordered fluid phases in the steric model was attributed to concave features in the particles' contact surfaces which had the effect of preventing the particles from sliding along one another. As an alternative, the PHGO model, a generalisation of the HGO model to non-centrosymmetric particles has been developed. This does not show the concave features mentioned above. For the two shortest elongations used, $k = 3$ and 4, the PHGO model only showed isotropic and fluid domain-ordered phases at, respectively, low and high

densities. However, upon increasing the elongation to $k = 5$, the model phase behaviour became much richer, with transitions from isotropic to nematic and then to a bilayered smectic A_2 phase. The study of this latter phase proved to be very interesting, showing anisotropic compressibility behaviour. Thus the PHGO model, with its nematic phase, met the second requirement for the bistable LCD cell model.

In Chapter 7, confined systems of PHGO particles interacting with the substrates through a variant of the RSUP potential have been studied. This surface potential has been shown to exhibit both planar and homeotropic arrangements with a narrow region of bistability around $k_S/k = 0.7$. In the case of hybrid anchored systems of $N = 2000$ particles with a top homeotropic surface, bistability at the bottom surface could be recovered using $k_{St}/k = 0.6$. Due to the large system size used, a continuous structural transition was found in the case of the bent director state.

Using this, a molecular model for the LCD cell was simulated and both hard and easy switching between the HAN and vertical states were attempted using both dielectric and dipolar contributions in the particle-field interactions. Both switching directions could be achieved using a narrow window of electric field strength E and dipole moment μ. A successful parameterisation was $E/\delta\epsilon = \pm 0.2$ and $\mu/\delta\epsilon = 2.5$. However the question as to whether the mechanism underlying this switching behaviour is direct surface effect, indirect flexoelectric behaviour or a combination of the two has not been resolved; this forms, in part, the basis of future work.

Future work

The work performed in this Thesis has lead to the development of a model for a novel bistable LCD cell where two way switching is achieved by the application of a directional electric field pulse. Much of the work that will directly follow

this Thesis concerns the study and improvement of this model. The first task is certainly the implementation of a method for the calculation of the slay flexoelectric coefficient as this would allow a good quantitative measurement of the effects of subsequent alterations to the model. Also, the use of the molecular dynamics method would provide interesting results by giving access to the true dynamics of relaxation properties of the model systems.

The cell model itself should also be improved, for instance by the use of mixtures of ellipsoidal shaped (HGO) and pear shaped particles (PHGO) which would allow independent tuning and/or enhancement of the bulk flexoelectric properties of the cell and the field-direction-dependence of its surface behaviour. This would also make the model a better description of a real liquid crystal cell, since mixtures of several different components are commonly used.

Finally, incorporation of attractive forces into the molecular models should be considered so as to render them more realistic and give access to better control mechanisms for tuning phase and anchoring behaviour. This could include addition of quadrupolar contributions in the particle-particle interaction as it has been shown that quadrupole interactions are predominant in the origins of flexoelectricity in real mesogens.

All of these refinements should lead to the development of, more realistic modeling of both the LCD cell considered in Chapter 7 and the more fundamental behaviour needed to make such cell. The work presented in this Thesis therefore represent a step along the path towards providing more efficient display cells as well as an academic study into the development of models for confined and flexoelectric liquid crystal behaviour.

Appendix A

Absorbed volume of an HGO into a substrate.

A.1 Introduction

The situation considered here is that of an Hard Gaussian Overlap particle close to a substrate and interacting with it via a given particle-surface potential so that the particle is allowed to partially absorb the surface. The problem is to find an expression for V_e the volume absorbed into the surface. Let us consider the setup shown in Fig A.1

The approximation made here is to solve the problem with an ellipsoid of revolution, instead of a Gaussian Overlap since the much simpler expression for the equation of an ellipsoid makes the problem easier.

The idea here is that the problem is easily solved in the case of a unit sphere. This, in turn, can be transformed into the same problem for an ellipsoid of elongation k by scaling the space along one of the axis by a factor k. The volume V_e in that case is equal to:

$$V_e = kV_s \tag{A.1}$$

where V_s is the volume of the sphere absorbed into the substrate.

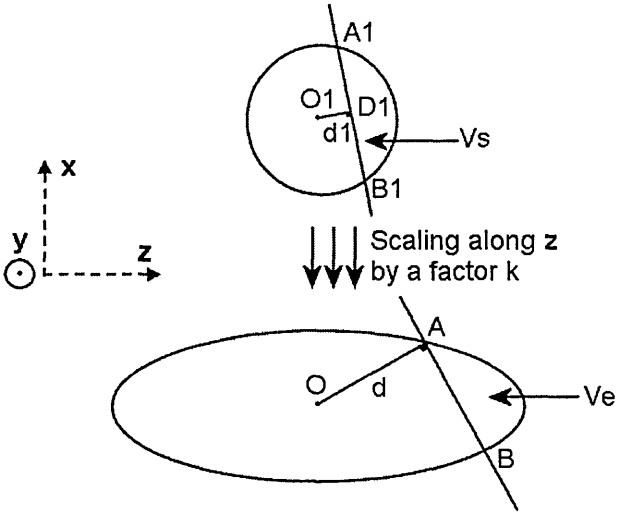

Figure A.1 : Schematic representation of the geometrical configuration considered to calculate the absorbed volume of the ellipsoid into the substrate.

A.2 Case of a sphere.

V_s is given by computing the volume of the sphere of radius a between the z coordinates $z_0 = d_1$ to $z_1 = a$.

The equation of an ellipsoid of semi axis a, b, c along $\hat{\mathbf{x}}, \hat{\mathbf{y}}$ and $\hat{\mathbf{z}}$ is given by :

$$\frac{x^2}{a^2} + \frac{y^2}{b^2} + \frac{z^2}{c^2} = 1 \tag{A.2}$$

V_s is then given by :

$$V_s = \int_{z_0}^{z_1} \int_{y_0}^{y_1} \int_{x_0}^{x_1} dxdydz \tag{A.3}$$

with :

$$\begin{aligned} x_1 &= a\sqrt{1 - \frac{z^2}{c^2} - \frac{y^2}{b^2}} \\ y_1 &= b\sqrt{1 - \frac{z^2}{c^2}} \\ x_0 &= -x_1 \\ y_0 &= -y_1 \end{aligned}$$

Since a sphere is considered here, $a = b = c$ and V_s reads :

$$\begin{aligned} V_s &= \frac{ab\pi}{c^2}\int_{z_0}^{z_1}\left\{c^2 - z^2\right\}dz \\ V_s &= \frac{\pi}{3}(a-d_1)^2(2a+d_1) \end{aligned} \tag{A.4}$$

The distance d_1 can be obtained by considering the triangle OA_1B_1 in the $\hat{\mathbf{x}} - \hat{\mathbf{z}}$ plane. The coordinates of A_1 and B_1 are equal, respectively, to those of A and B rescaled by $\frac{1}{k}$ along z. Hence

$$\begin{aligned} A_1 &= \left(x_A, \frac{z_A}{k}\right) \\ B_1 &= \left(x_B, \frac{z_B}{k}\right) \end{aligned}$$

and therefore

$$A_1B_1 = \sqrt{(x_B - x_A)^2 + \frac{(z_B - z_A)^2}{k^2}} \tag{A.5}$$

since

$$O_1B_1 = a \tag{A.6}$$

$$D_1B_1 = \frac{A_1B_1}{2} \tag{A.7}$$

we get d_1 as :

$$\begin{aligned} d_1 &= \sqrt{O_1B_1^2 - D_1B_1^2} \\ d_1 &= \sqrt{a^2 - \frac{1}{4}\left((x_A - x_B)^2 + \frac{1}{k^2}(z_A - z_B)^2\right)} \end{aligned} \tag{A.8}$$

A.3 Coordinates of A and B

A and B are defined as being the coordinates of the contact points between the ellipse and the plane. Since, these points satisfy both the equation of the ellipse and the plane, they can be found by solving :

$$\begin{cases} \frac{x^2+z^2}{a^2} = 1 & (1) \\ x = \frac{z\cos\theta - d}{\sin\theta} & (2) \end{cases} \tag{A.9}$$

Inserting (2) into (1) gives

$$z^2\left(k^2\cos^2\theta+\sin^2\theta\right)-2zk^2d\cos\theta+d^2k^2-a^2k^2\sin^2\theta. \tag{A.10}$$

the real roots of which are :

$$z_{A,B}=\frac{dk^2\cos\theta\pm\sqrt{k^2\sin^2\theta\left[-d^2+a^2(k^2\cos^2\theta+\sin^2\theta)\right]}}{k^2\cos^2\theta+\sin^2\theta} \tag{A.11}$$

A.4 Expression for d_1

Equation A.8 can now be rewritten using :

$$\begin{aligned}(x_B-x_A)^2 &= \frac{\cos^2\theta}{\sin^2\theta}(z_B-z_A)^2\\ (z_B-z_A)^2 &= 4k^2\sin^2\theta\left[-d^2+a^2\left(k^2\cos^2\theta+\sin^2\theta\right)^2\right]\end{aligned}$$

which after full simplification gives :

$$d_1=\frac{d}{\sqrt{k^2\cos^2\theta+\sin^2\theta}} \tag{A.12}$$

A.5 Expression for V_e

The absorbed volume of the sphere can now be written as :

$$V_s=\frac{\pi}{3}\left(a-\sqrt{\frac{d^2}{k^2\cos^2\theta+\sin^2\theta}}\right)^2\left(2a+\sqrt{\frac{d^2}{k^2\cos^2\theta+\sin^2\theta}}\right) \tag{A.13}$$

which gives the final result for the absorbed volume of the ellipsoid :

$$V_e=\frac{k\pi}{3}\left(a-\sqrt{\frac{d^2}{k^2\cos^2\theta+\sin^2\theta}}\right)^2\left(2a+\sqrt{\frac{d^2}{k^2\cos^2\theta+\sin^2\theta}}\right) \tag{A.14}$$

Appendix B

Particle-field electrostatic interactions

Here, an expression is derived for the interaction between a particle and uniform electric field. Two types of interaction are considered here, namely the dielectric and dipolar interactions. The former describes the interaction between the polarisability of a liquid crystal molecule and an applied electric field, while the latter is the interaction between a permanent dipolar moment and the applied field.

The setup considered is that of a particle i with orientation $\hat{\mathbf{u}}_i = (\cos\phi\sin\theta,$-$\sin\phi\sin\theta, \cos\theta)$ subject to a constant electric field $\mathbf{E}$ as shown in Figure B.1. Although in principle, the particle should be considered to be subject to a constant electric displacement $\mathbf{D}$ rather than a constant field, the approximation of constant $\mathbf{E}$ is made so as to avoid the complication of including the Maxwell relations.

B.1 Dielectric interaction

The field induced polarisation on the dielectric is given by :

$$\mathbf{P} = \epsilon_0 . \boldsymbol{\chi_e} \, . \mathbf{E} \tag{B.1}$$

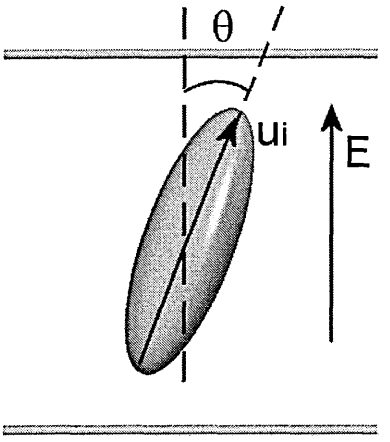

Figure B.1 : Schematic representation of the geometry considered to calculate U_{pf}

where $\mathbf{P}$ is the polarisation induced by the electric field $\mathbf{E}$, ϵ_0 is the dielectric permittivity and $\boldsymbol{\chi_e}$ is the dielectric susceptibility tensor :

$$\boldsymbol{\chi_e} = \begin{pmatrix} \chi_{e\perp} & 0 & 0 \\ 0 & \chi_{e\perp} & 0 \\ 0 & 0 & \chi_{e\parallel} \end{pmatrix}. \tag{B.2}$$

The dielectric energy of the particle is then given by :

$$U_{die} = -\frac{1}{2}\mathbf{D}\cdot\mathbf{E} \tag{B.3}$$

with $\mathbf{D}$ the electric displacement

$$\mathbf{D} = \epsilon_0\mathbf{E} + \mathbf{P}. \tag{B.4}$$

Therefore, the electric energy can be expressed as :

$$U_{die} = -\frac{1}{2}\left(\epsilon_0\mathbf{E} + \mathbf{P}\right)\cdot\mathbf{E} \tag{B.5}$$

and, since $\mathrm{d}\mathbf{E} = 0$, $\mathrm{d}U_{die}$ can be expressed as :

$$\mathrm{d}U_{die} = -\frac{1}{2}\mathbf{E}\mathrm{d}\mathbf{P} \tag{B.6}$$

The expression for $\mathrm{d}\mathbf{P}$ can be obtained by using $\mathbf{E}$ and $\mathbf{P}$ expressed in the molecular frame in term of $\mathbf{E}_{\parallel}$, $\mathbf{P}_{\parallel}$ and $\mathbf{E}_{\perp}$, $\mathbf{P}_{\perp}$ the components of $\mathbf{E}$ and $\mathbf{P}$ respectively

parallel and perpendicular to $\hat{\mathbf{u}}_i$. Thus :

$$\mathbf{E} = \mathbf{E}_{\parallel} + \mathbf{E}_{\perp} \tag{B.7}$$

$$\mathbf{E}_{\parallel} = (\mathbf{E} \cdot \hat{\mathbf{u}}_i)\,\hat{\mathbf{u}}_i \tag{B.8}$$

$$\mathbf{E}_{\perp} = \mathbf{E} - (\mathbf{E} \cdot \hat{\mathbf{u}}_i)\,\hat{\mathbf{u}}_i \tag{B.9}$$

similarly :

$$\mathbf{P} = \mathbf{P}_{\parallel} + \mathbf{P}_{\perp} \tag{B.10}$$

$$\mathbf{P}_{\parallel} = \epsilon_0 \chi_{e\parallel} \mathbf{E}_{\parallel} \tag{B.11}$$

$$\mathbf{P}_{\perp} = \epsilon_0 \chi_{e\perp} \mathbf{E}_{\perp} \tag{B.12}$$

which leads to :

$$\mathbf{P} = \epsilon_0 \left(\chi_{e\parallel} \mathbf{E}_{\parallel} + \chi_{e\perp} \mathbf{E}_{\perp}\right) \tag{B.13}$$

$$\mathbf{P} = \epsilon_0 \left[\chi_{e\parallel} (\mathbf{E} \cdot \hat{\mathbf{u}}_i)\,\hat{\mathbf{u}}_i + \chi_{e\perp} (\mathbf{E} - (\mathbf{E} \cdot \hat{\mathbf{u}}_i)\,\hat{\mathbf{u}}_i)\right] \tag{B.14}$$

and with :

$$\delta\epsilon = \chi_{e\parallel} - \chi_{e\perp} \tag{B.15}$$

$$\mathbf{P} = \epsilon_0 \left(\chi_{e\perp} \mathbf{E} + \delta\epsilon\, (\mathbf{E} \cdot \hat{\mathbf{u}}_i)\,\hat{\mathbf{u}}_i\right) \tag{B.16}$$

and therefore :

$$\mathrm{d}\mathbf{P} = \epsilon_0 \delta\epsilon \left[(\mathbf{E} \cdot \mathrm{d}\hat{\mathbf{u}}_i)\,\hat{\mathbf{u}}_i + (\mathbf{E} \cdot \hat{\mathbf{u}}_i)\,\mathrm{d}\hat{\mathbf{u}}_i\right] \tag{B.17}$$

Equation B.6 then becomes :

$$\mathrm{d}U_{die} = -\frac{1}{2}\epsilon_0 \delta\epsilon \mathbf{E} \cdot \left[(\mathbf{E} \cdot \mathrm{d}\hat{\mathbf{u}}_i)\,\hat{\mathbf{u}}_i + (\mathbf{E} \cdot \hat{\mathbf{u}}_i)\,\mathrm{d}\hat{\mathbf{u}}_i\right] \tag{B.18}$$

$$\mathrm{d}U_{die} = -\epsilon_0 \delta\epsilon\, (\mathbf{E} \cdot \mathrm{d}\hat{\mathbf{u}}_i)\,(\mathbf{E} \cdot \hat{\mathbf{u}}_i) \tag{B.19}$$

Taking the electric field to be $\mathbf{E} = E\hat{\mathbf{E}} = E\hat{\mathbf{z}}$, an expression for $\mathrm{d}U_e$ in terms of θ can be obtained as :

$$\mathrm{d}U_{die} = -\epsilon_0 \delta\epsilon\, (-E \sin\theta \mathrm{d}\theta)\,(E \cos\theta) \tag{B.20}$$

$$\mathrm{d}U_{die} = \epsilon_0 \delta\epsilon E^2 \sin\theta \cos\theta \mathrm{d}\theta \tag{B.21}$$

Thus for every θ_0 the electric energy corresponding to the dielectric interaction is given by :

$$U_{die} = \epsilon_0 \delta\epsilon E^2 \int_0^{\theta_0} \sin\theta \cos\theta \mathrm{d}\theta \tag{B.22}$$

$$U_{die} = \epsilon_0 \delta\epsilon E^2 \left(-\frac{1}{2} \cos^2\theta \right) \tag{B.23}$$

$$\boxed{U_{die} = -\tfrac{1}{2}\epsilon_0 \delta\epsilon \left(\mathbf{E} \cdot \hat{\mathbf{u}}_i\right)^2} \tag{B.24}$$

B.2 Dipolar interaction

The case of the dipolar interaction is much simpler than the previous one. The field interacts with a dipolar moment with energy:

$$U_{dip} = -\left(\boldsymbol{\mu} \cdot \mathbf{E}\right) \tag{B.25}$$

For $\boldsymbol{\mu}$, the dipolar moment, given by :

$$\boldsymbol{\mu} = \mu \hat{\mathbf{u}}_i, \tag{B.26}$$

the energy corresponding to the dipolar interaction is given by :

$$\boxed{U_{dip} = -\mu \left(E \cdot \hat{\mathbf{u}}_i\right)} \tag{B.27}$$

B.3 Particle-field interaction

The energy $U_{pf,i}$ of the particle-field interaction on one particle i is the sum of the dielectric and dipolar contribution and hence :

$$U_{pf,i} = U_{die} + U_{dip} \tag{B.28}$$

$$U_{pf,i} = -\frac{1}{2}\epsilon_0 \delta\epsilon \left(\mathbf{E} \cdot \hat{\mathbf{u}}_i\right)^2 - \mu \left(E \cdot \hat{\mathbf{u}}_i\right). \tag{B.29}$$

As a result, the total energy per particle corresponding to the particle-field interaction is simply :

$$\boxed{U_{pf} = \tfrac{1}{N} \textstyle\sum_{i=1}^{N} -\tfrac{1}{2}\epsilon_0 \delta\epsilon \left(\mathbf{E} \cdot \hat{\mathbf{u}}_i\right)^2 - \mu \left(E \cdot \hat{\mathbf{u}}_i\right)} \tag{B.30}$$

Bibliography

[1] A.J Davidson and N.J. Mottram. Flexoelectric switching in a bistable nematic device. *Physical Review E*, 65:051710, 2002.

[2] R. Berardi, M. Ricci and C. Zannoni. Ferroelectric nematic and smectic liquid crystals from tapered molecules. *ChemPhysChem*, 7:443, 2001.

[3] J.S. Rigden. *Macmillian encyclopedia of physics.* Macmillian, 1996.

[4] A. Guinier . *The Structure of Matter.* Edward Arnold Ltd, 1984.

[5] F. Reinitzer. Beitrage zur kenntniss des cholesterins. *Monatshefte fur Chemie*, 9:421–441, 1888.

[6] O. Lehmann. . *Zeitshrift fur Physical Chemie*, 4:462, 1889.

[7] S. Chandrasekhar. *Liquid Crystals.* Cambridge University Press, 1992.

[8] P.J. Collings. *Nature's delicate phase of Matter.* IOP publishing, 1990.

[9] P.J. Collings and M. Hird. *Introduction to Liquid crystals, Chemistry and Physics.* Taylor and Francis, 1997.

[10] I. W. Hamley. *Introduction to Soft Matter.* Wiley, 2000.

[11] G.R. Luckhurst and G.W. Gray. *The molecular physics of liquid crystals.* Academic press, 1979.

[12] R.B. Meyer. Piezoelectric effects in liquid crystals. *Physical Review Letters*, 22:918, 1969.

[13] P.G. de Gennes. *The Physics of Liquid Crystals, 2nd ed.* Clarendon press, 1993.

[14] A. Derzhanski and A.G. Petrov. A possible relationship between the dielectric permeability and the piezoelectric properties of nematic liquid crystals. *Physics Letters*, 34A:427, 1971.

[15] W. Helfrich. The strengh of piezoelectricity in liquid crystals. *Zeitshrift fur Naturforschung*, 26A:833, 1971.

[16] W. Helfrich. Inherent bounds to the elasticity and flexoelectricity of liquid crystals. *Mol. Cryst.*, 26:1, 1974.

[17] J. Prost and J.P. Marcerou. On the microscopic interpretation of flexoelectricity. *Le Journal de Physique*, 38:315, 1977.

[18] J.P. Marcerou and J. Prost. Flexolectricity in isotropic phases. *Physics Letters*, 66A:218, 1978.

[19] J. Prost and P.S. Pershan. Flexoelectricity in nematic and smectic-A liquid crystals. *Journal of Applied Physics*, 47:2298, 1976.

[20] J.P. Marcerou and J. Prost. Relaxational behavior of flexoelectricity. *Annales de Physique*, V.3:269, 1978.

[21] A. Mazzulla, F. Ciuchi and J.R. Sambles. Optical determination of flexoelectric coefficients and surface polarization in a hybrid aligned nematic cell. *Physical Review E*, 64:021708, 2000.

[22] S.A. Jewell and J.R. Sambles. Fully leaky guided mode study of the flexoelectric effect and surface polarization in hybrid aligned nematic cells. *Journal of Applied Physics*, 92:19, 2002.

[23] J.P. Mearcerou and J. Prost. The different aspects of flexoelectricity in nematics. *Molecular Crystals Liquid Crystals*, 58:259, 1980.

[24] I. Dozov, P. Martinot-Lagarde and G. Durant. Conformational flexoelectricity in nematic liquid crystals. *Le Journal de Physique Lettres*, 44:L817, 1983.

[25] J.P. Straley. Theory of piezoelectricity in nematic liquid crystals and of the cholesteric ordering. *Physical Review A*, A14:1835, 1976.

[26] M.A. Osipov. Molecular theory of flexoelectric effect in nematic liquid crystals. *Soviet Physics JETP*, 58:6, 1983.

[27] M.A. Osipov. The order parameter dependence of the flexoelectric coefficients in nematic liquid crystals. *Le Journal de Physique Lettres*, 45:L823, 1984.

[28] Y. Singh and U.P. Singh. Density-functional theory of the flexoelectric effect in nematic liquids. *Physical Review A*, 39:8, 1989.

[29] A. Ferrarini. Shape model for the molecular interpretation of the flexoelectric effect. *Physical Review E*, 64:021710, 2001.

[30] J. Stelzer, R. Berardi and C. Zannoni. Flexoelectric effects in liquid crystals formed by pear-shaped molecules. a computer simulation study. *Chemical Physics Letters*, 299:9–16, 1999.

[31] J.L. Billeter and R.A. Pelcovits. Molecular shape and flexoelectricity. *Liquid Crystals*, 27:1151–1160, 2000.

[32] C. Denniston and J.M. Yeomans. Flexoelectric surface switching of bistable nematic devices. *Physical Review E*, 87:275505–1, 2001.

[33] J.P. Hansen and I.R. Mc Donald. *Theory of simple liquids.* Academic press, 1986.

[34] J.A. Barker and D. Henderson. What is liquid ? understanding the states of matter. *Reviews of modern physics*, 48:587, 1976.

[35] L. Onsager. The effects of shape on the interaction of colloidal particles. *Annals New York academy of sciences*, 51:627, 1949.

[36] P. Padilla and E. Velasco. The isotropic-nematic transition for the hard gaussian overlap fluid : testing the decoupling approximation. *Journal of Chemical Physics*, 106:10299, 1997.

[37] J. Vieillard-Baron. Phase transitions of the classical hard-ellipse system. *Journal of Chemical Physics*, 56:4729, 1972.

[38] D. Frenkel, B.M. Mulder and J.P. Mc Tague. Phase diagram of a system of hard ellipsoids. *Physical Review Letters*, 52:287, 1981.

[39] D. Frenkel and B.M. Mulder. The hard ellipsoid of revolution fluid I. Monte Carlo simulations. *Molecular Physics*, 55:1171, 1985.

[40] C. Vega. Virial coefficients and equation of state of hard ellipsoids. *Molecular Physics*, 92:651, 1997.

[41] E. Velasco and P. Padilla. Nematic virial coefficients of very long hard molecules and Onsager theory. *Molecular Physics*, 94:335, 1998.

[42] B.M. Mulder and D. Frenkel. The hard ellipsoid of revolution fluid II. the y-expansion equation of state. *Molecular Physics*, 55:1193, 1985.

[43] B. Tjipto-Margo and G.T. Evans. The Onsager theory of the isotropic-nematic liquid crystals transition - incorporation of the higher virial coefficients. *Journal of Chemical Physics*, 93:4254, 1990.

[44] J.D. Parsons. Nematic ordering in a system of rods. *Physical Review A*, 19:1225, 1979.

[45] D.C. Williamson. The isotropic-nematic phase transition : The Onsager theory revisited. *Physica A*, 220:139, 1995.

[46] A. Stroobants and N.W. Lekkerkerker. Liquid crystal phase transitions in a solution of rodlike and disklike particles. *Journal of Physical Chemistry*, 88:3669, 1984.

[47] P.J. Camp and M.P. Allen. Hard ellipsoid rod-plate mixtures : Onsager theory and computer simulations. *Physica A*, 229:410, 1996.

[48] G. Cinacchi and F. Schmid. Density functional for anisotropic fluids. *Journal of Physics : Condensed Matter*, 14:12223, 2002.

[49] W. Maier and A. Saupe. . *Zeitshrift fur Naturforschung*, 13a:564, 1958.

[50] W. Maier and A. Saupe. . *Zeitshrift fur Naturforschung*, 14a:882, 1959.

[51] W. Maier and A. Saupe. . *Zeitshrift fur Naturforschung*, 15a:287, 1960.

[52] R.L. Humphrries, P.G. James and G.R. Luckhurst. Molecular field treatement of nematic liquid crystal. *Journal of the Chemical Society-Faraday Transactions II*, 68:1031, 1971.

[53] I.A. Shanks. The physics and display applications of liquid crystals. *Contemporary Physics*, 23:65, 1982.

[54] T. Geelhaar. Liquid crystals for display applications. *Liquid Crystals*, 24:91, 1998.

[55] R. Eidenschink. New developments in liquid crystal materials. *Molecular Crystals Liquid Crystals*, 123:57, 1985.

[56] R. Eidenschink. Liquid Crystals - new compounds, new applications. *Angew. Chem. Ind. Ed. Engl. Adv. Matter.*, 28:1424, 1989.

[57] M. Kreuzer, T. Tschudi and R. Eidenschink. Erasable optical storage in bistable liquid crystal cells. *Molecular Crystals Liquid Crystals*, 223:219, 1992.

[58] M. Giocondo, I. Lelidis, I. Dozov and G. Durand. Write and erase mechanism of surface controlled bistable nematic pixel. *The European Physical Journal Applied Physics*, 5:227, 1999.

[59] J-H Kim, M. Yoneya and H. Yokoyama. Tristable nematic liquid-crystal device using micropatterened surface alignment. *Nature*, 420:159, 2002.

[60] R. Eidenschink. Liquid crystals in variable friction devices. *Angew. Chem. Ind. Ed. Engl. Adv. Matter.*, 27:1579, 1988.

[61] R. Eidenschink. Eine neue anwendung flussiger kristalle in der Tribologie. *Liquid Crystals*, 5:1517, 1989.

[62] R. Eidenschink. Unusual lift by shearing mesogenic fluids. *Molecular Crystals Liquid Crystals*, 330:327, 1999.

[63] J.W. Goodby. Liquid crystals and life. *Liquid Crystals*, 24:25, 1998.

[64] J.M. Hammersley and D.C. Handscomb. *Monte Carlo methods.* Wiley, 1964.

[65] N. Metropolis, A.W. Rosenbluth, M.N. Rosenbluth, A.H. Teller and E. Teller. Equation of state calculations by fast computing machines. *Journal of Chemical Physics*, 21:1087, 1953.

[66] M.P. Allen and D.J. Tildesley. *Computer simulation of liquids.* Oxford Science Publications, Oxford University Press, Walton Street, Oxford OX2 6DP, 1989.

[67] D.C. Williamson, G. Jackson. Liquid crystalline phase behaviour in systems of hard-sphere chains. *Journal of Chemical Physics*, 108:10294, 1998.

[68] W.W. Wood. Monte Carlo calculations for Hard Disks in the isothermal-isobaric ensemble. *Journal of Chemical Physics*, 48:415, 1968.

[69] J.A. Barker and R.O. Watts. Structure of water: a Monte Carlo calculation. *Chemical Physics Letters*, 3:144, 1969.

[70] B.J. Alder, T.E. Wainwright. Studies in Molecular dynamics, I. General Method. *Journal of Chemical Physics*, 31:459–466, 1959.

[71] L. Verlet. Computer experiments on classical fluids. I. Thermodynamical properties of Lennard-Jones molecules. *Physical Review*, 159:98–103, 1967.

[72] W.C. Swope and H.C. Andersen, . A molecular dynamics method for calculating the solubility of gases in liquids and the hydrophobic hydratation of inert gas atoms in aqueous solution. *Journal of Physical Chemistry*, 88:6548–56, 1984.

[73] W.C Swope et al. A computer simulation method for the calculation of equilibium constants for the formation of physical clusters of molecules: application to small water clusters. *Journal of Chemical Physics*, 76:637–649, 1982.

[74] B.J. Alder, T.E. Wainwright. Studies in Molecular dynamics, II. Behavior of a small number of elastic spheres. *Journal of Chemical Physics*, 33:1439–1451, 1960.

[75] J.W. Perram, M.S. Wertheim, J.L. Lebowitz and G.O. Williams. Monte Carlo simulation of hard spheroids. *Chemical Physics Letters*, 105:277, 1984.

[76] J.W. Perram and M.S. Wertheim. Statistical mechanics of hard ellipsoids. I. Overlap algorithm and the contact function. *Journal of Computational Physics*, 58:409, 1985.

[77] G.J. Zarragoicoecha, G.J. Levesque and J.J. Weis. Monte Carlo study of dipolar ellipsoids. II. Search for an isotropic-nematic phase transition. *Molecular Physics*, 75:989, 1992.

[78] M.P. Allen and C.P. Mason. Stability of the nematic phase for the hard ellipsoid fluid. *Molecular Physics*, 86:467, 1986.

[79] P.J. Camp, C.P. Mason and M.P. Allen. The isotropic-nematic phase transition in uniaxial hard ellipsoid fluids : coexistence data and the approach to the Onsager limit. *Journal of Chemical Physics*, 105:2837, 1996.

[80] M.P. Allen. Computer simulation of a biaxial liquid crystal. *Liquid Crystals*, 8:499, 1990.

[81] P.J. Camp and M.P. Allen. Phase diagram of the hard biaxial ellipsoid fluid. *Journal of Chemical Physics*, 106:6681, 1997.

[82] J.A.N. Zazadzinski and R.B. Meyer. Molecular imaging of tobacco virus lyotropic nematic phases. *Physical Review Letters*, 56:636, 1986.

[83] Z. Dogic and S. Fraden. Smectic phase in a colloidal suspension of semiflexible virus particles. *Physical Review Letters*, 78:2417, 1997.

[84] J.A.C. Veerman and D. Frenkel. Phase behavior of disklike hard-core mesogens. *Physical Review A*, 45:5632, 1992.

[85] M.A. Bates and D. Frenkel. Infinitely thin disks exhibit a first order nematic-columnar phase transition. *Physical Review E*, 57:4824, 1998.

[86] J. Vieillard-Baron. The equation of state of a system of hard spherocylinders. *Molecular Physics*, 28:809, 1974.

[87] D. Frenkel. Computer simulation of hard-core models for liquid crystals. *Molecular Physics*, 60:1, 1987.

[88] D. Frenkel. Onsager's spherocylinder revisited. *Journal of Physical Chemistry*, 91:4912, 1987.

[89] J.A.C Veerman and D. Frenkel. Phase diagram of a system of hard spherocylinders by computer simulation. *Physical Review A*, 41:3237, 1996.

[90] S.C. McGrother, D.C. Williamson and G. Jackson. A re-examination of the phase diagram of hard spherocylinders. *Journal of Chemical Physics*, 104:6755, 1996.

[91] P. Bolhuis and D. Frenkel. Tracing the phase boundaries of hard spherocylinders. *Journal of Chemical Physics*, 106:666, 197.

[92] B.J. Berne and P. Pechukas. Gaussian model potentials for molecular interactions. *Journal of Chemical Physics*, 56:4213–4216, 1972.

[93] J.G. Gay and B.J. Berne. Modification of the overlap potential to mimic a linear site-site potential. *Journal of Chemical Physics*, 74:3316, 1981.

[94] D.J. Adam, G.R. Luckhurst and R.W. Phippen. Computer simulation studies of anisotropic systems. XVII The Gay-Berne model nematogen. *Molecular Physics*, 61:1575, 1987.

[95] G.R. Luckhurst, R.A. Stephens and R.W. Phippen. Computer simulation studies of anisotropic systems. XIX Mesophases formed by the Gay-Berne model mesogen. *Liquid Crystals*, 8:451, 1990.

[96] M.J. Chalam, K.E. Gubbins, E. de Miguel and L.F. Rull. A molecular simulation of a liquid crystal model : bulk and confined fluid. *Molecular Simulation*, 7:357, 1991.

[97] E. de Miguel, L.F. Rull, M.J. Chalam and K.E. Gubbins. Location of the isotropic-nematic transition in the Gay-Berne model. *Molecular Physics*, 72:593, 1991.

[98] E. de Miguel, L.F. Rull, M.J. Chalam and K.E. Gubbins. Liquid crystal phase diagram of the Gay-Berne fluid. *Molecular Physics*, 74:405, 1991.

[99] R. Berardi, A.P.J. Emerson and C. Zannoni. Monte Carlo investigations of a Gay-Berne liquid crystal. *Journal of the Chemical Society-Faraday Transactions*, 89:4069, 1993.

[100] M.P. Allen, M.A. Warren, M.R. Wilson, A. Sauron and W. Smith. Molecular dynamics calculation of elastic constants in gay-berne nematic liquid crystals. *Journal of Chemical Physics*, 105:2850, 1996.

[101] G.R. Luckhurst and P.S.J. Simmonds. Computer simulation studies of anisotropic systems. XXI. Parametrization of the Gay-Berne potential for model mesogens. *Molecular Physics*, 80:233, 1993.

[102] M.A. Bates and G.R. Luckhurst. Computer simulation studies of anisotropic systems. XXX. The phase behavior and structure of a Gay-Berne mesogen. *Journal of Chemical Physics*, 110:7087, 1999.

[103] E. de Miguel, E. Martín del Rio, J.T. Brown and M.P. Allen. Effects of the attractive interactions on the phase behavior of the Gay-Berne liquid crystal model. *Journal of Chemical Physics*, 105:1, 1996.

[104] J.T. Brown, M.P. Allen, E. Martín del Rio and E. de Miguel. Effects of elongation on the phase behavior of the Gay-Berne fluid. *Physical Review E*, 57:6685, 1998.

[105] D.J. Cleaver, C.M. Care, M.P. Allen and M. Neal. Extension and generalization of the Gay-Berne potential. *Physical Review E*, 54:559–567, 1996.

[106] H. Zewdie. Computer simulations of diskotic liquid crystals. *Physical Review E*, 57:1793, 1998.

[107] H. Zewdie. Computer simulation studies of liquid crystals : a new Corner potential for cylindrically symmetric particles. *Journal of Chemical Physics*, 108:2117, 1998.

[108] A.J. Stone. The description of bimolecular potentials, forces and torques : The S and V function expansions. *Molecular Physics*, 36:241, 1978.

[109] R. Berardi and C. Zannoni. Do thermotropic biaxial nematics exist ? A Monte Carlo study of biaxial Gay-Berne particles. *Journal of Chemical Physics*, 113:5971, 2000.

[110] C. Zannoni. Molecular design and computer simulations of novel mesophases. *Journal of Materials Chemistry*, 11:2637, 2002.

[111] R. Berardi, C. Fava and C. Zannoni. A Gay-Berne potential for dissimilar biaxial particles. *Chemical Physics Letters*, 297:8, 1998.

[112] M. Houssa, L.F. Rull and S.C. Mc Grother. Effect of dipolar interactions on the phase behavior of the Gay-Berne liquid crystal model. *Journal of Chemical Physics*, 109:9529, 1998.

[113] M. Houssa, S.C. Mc Grother and L.F. Rull. Computer simulations of dipolar liquid crystal phases. *Computer Physics Communications*, 122:259, 1999.

[114] R. Berardi, S. Orlandi and C. Zannoni. Molecular dipoles and tilted smectic formation. A Monte Carlo simulation study. *Physical Review E*, 67:041708, 2003.

[115] I.M. Withers. Effects of longitudinal quadrupoles on the phase behaviour of the Gay-Berne fluid. 2002.

[116] D. Wei and G.N. Patey. Orientational order in simple dipolar liquids : computer simulation of a ferroelectric nematic phase. *Physical Review Letters*, 68:2043, 1992.

[117] D. Wei and G.N. Patey. Ferroelectric liquid-crystal and solid phases formed by strongly interacting dipolar soft spheres. *Physical Review A*, 46:7783, 1992.

[118] M.P. Neal, A.J. Parker and C.M. Care. A molecular dynamics study of a steric multipole model of liquid crystal molecular geometry. *Molecular Physics*, 91:603, 1997.

[119] B. Jerome J. O'Brien, Y. Ouchi, C. Stanners and Y.R. Shen. Bulk reorientation driven by orientational transition in a liquid crystal monolayer. *Physical Review Letters*, 71:758, 1993.

[120] X. Zhuang, L. Marucci and Y.R. Shen. Surface-monolayer-induced bulk alignment of liquid crystals. *Physical Review Letters*, 73:1513, 1994.

[121] E. Martín del Rio, M.M Telo da Gama and E. de Miguel. Surface-induced alignment at model nematic interfaces. *Physical Review E*, 52:5028, 1995.

[122] P.I.C Teixeira. Structure of a nematic liquid crystal between aligning walls. *Physical Review E*, 55:2876, 1997.

[123] M.A. Osipov and S. Hess. Density functional approach to the theory of interfacial properties of nematic liquid crystals. *Journal of Chemical Physics*, 99:4181, 1993.

[124] B. Tjipto-Margo and D.E. Sullivan. Molecular interactions and interface properties of nematic liquid crystals. *Journal of Chemical Physics*, 88:6620, 1988.

[125] B. Jérome. Surface effects and anchoring in liquid crystals. *Physics reports*, 54:391–451, 1991.

[126] M. Schoen. On the uniqueness of stratification-induced structural tranformations in confined films. *Ber. Bunsenges. Phys. Chem.*, 100:1355, 1996.

[127] M. Schoen. The impact of discrete wall structure on stratification-induced structural phase transitions in confined films. *Journal of Chemical Physics*, 105:2910–2918, 1996.

[128] M.P. Allen. Molecular simulation and theory of liquid crystal surface anchoring. *Molecular Physics*, 96:1391, 1999.

[129] M.M. Telo da Gama, P. Tarazona, M.P. Allen and R. Evans. The effect of confinement on the isotropic-nematic transition. *Molecular Physics*, 71:801, 1990.

[130] D.J. Cleaver and M.P. Allen. Computer simulation of liquid crystal films. *Molecular Physics*, 80:253, 1993.

[131] Z. Zhang, A. Chakrabarti, O.G. Mouristen and M.J. Zuckermann. Substrate-induced bulk alignment of liquid crystals. *Physical Review E*, 53:2461, 1996.

[132] G.D. Wall and D.J. Cleaver. Computer simulation studies of confined liquid-crystal films. *Physical Review E*, 56:4306–4316, 1997.

[133] R. Latham and D.J. Cleaver. Substrate-induced demixing in a confined liquid crystal film. *Chemical Physics Letters*, 330:7–14, 2000.

[134] T. Gruhn and M. Schoen. Microscopic structure of molecularly thin confined liquid-crystal films. *Physical Review E*, 55:2861, 1997.

[135] T. Gruhn and M. Schoen. Grand canonical Monte Carlo simulations of confined 'nematic' Gay-Berne films. *Thin Solid Films*, 330:46, 1998.

[136] T. Gruhn and M. Schoen. A grand canonical ensemble Monte Carlo study of confined planar and homeotropically anchored Gay-Berne films. *Molecular Physics*, 93:681, 1998.

[137] V. Palermo, F. Biscarini and C. Zannoni. Abrupt orientational changes for liquid crystals adsorbed on a graphite surface. *Physical Review E*, 57:R2519, 1998.

[138] R. van Roij, M. Dijkstra and R. Evans. Orientational wetting and capillary nematization of hard-rod fluids. *Europhysics Letters*, 49:350, 2000.

[139] R. van Roij, M. Dijkstra and R. Evans. Interfaces, wetting and capillary nematization of a hard-rod fluid: Theory for the Zwanzig model. *Journal of Chemical Physics*, 117:7689, 2000.

[140] M. Dijkstra, R. van Roij and R. Evans. Wetting and capillary nematization of a hard-rod fluids : a simulation study. *Physical Review E*, 63:051703–1, 2001.

[141] A. Chrzanowska, P.I.C. Teixeira, H. Ehrentraut and D.J. Cleaver. Ordering of hard particles between hard walls. *Journal of Physics : Condensed Matter*, 13:1–13, 2001.

[142] D.J. Cleaver and P.I.C Teixeira. Discontinuous structural transition in a thin hybrid liquid crystal film. *Chemical Physics Letters*, 338:1–6, 2001.

[143] F. Vandenbrouck, M.P. Valignat and A.M. Cazabat. Thin nematic films: metastability and spinodal dewetting. *Physical Review Letters*, 82:2693, 1999.

[144] A. Šarlah and S. Žummer. Equilibrium structures and pretransitional fluctuations in a very thin hybrid nematic film. *Physical Review E*, 60:1821, 1999.

[145] D.J. Cleaver and D.J. Tildesley. Computer modelling of the structure of 4-n-octyl-4'-cyanobiphenyl adsorbed on graphite. *Molecular Physics*, 81:781, 1994.

[146] M. Yoneya and Y. Iwakabe. Molecular dynamics simulations of liquid crystal molecules adsorbed on graphite. *Liquid Crystals*, 18:45, 1995.

[147] D.J. Cleaver, M.J. Callaway, T. Forester, W. Smith and D.J. Tildesley. Computer modelling of the 4-n-alkyl-4'-cyanobiphenyls adsorbed on graphite: energy minimizations and molecular dynamics of periodic systems. *Molecular Physics*, 86:613, 1995.

[148] D.R. Binger and S. Hanna. Computer simulation of interactions between liquid crystal molecules and polymer surfaces. I. Alignment of nematic and smectic A phases. *Liquid Crystals*, 26:1205, 1999.

[149] D.R. Binger and S. Hanna. Computer simulation of interactions between liquid crystal molecules and polymer surfaces. II. Alignment od smectic C forming mesogens. *Liquid Crystals*, 27:89, 2000.

[150] D.R. Binger and S. Hanna. Computer simulation of interactions between liquid crystal molecules and polymer surfaces. III. use of pseudopotentials to represent the surface. *Liquid Crystals*, 28:1215, 2001.

[151] J.S. Patel and H. Yokoyama. Continuous anchoring transition in liquid crystals. *Nature*, 362:525, 1993.

[152] P. Jagemalm and L. Komitov. Temperature induced anchoring transition in nematic liquid crystals with two-fold degenerate alignment. *Liquid Crystals*, 23:1, 1997.

[153] Y-M Zhu, Z-H. Lu, X.B Jia, Q.H. Wei, D. Xiao, Y. Wei, Z.H. Wu, Z.L. Hu and M.G. Xie. Anchoring transition of liquid crystals on crown ether monolayers. *Physical Review Letters*, 72:2573, 1994.

[154] Y-M. Zhu and Y. Wei. Conformation change-driven anchoring transition of liquid crystals on crown ether liquid crystals Langmuir-Blodgett films. *Journal of Chemical Physics*, 101:10023, 1994.

[155] G. Barbero and V. Popa-Nita. Model for the planar-homeotropic anchoring transition induced by trans-cis isomerisation. *Physical Review E*, 61:6696, 2000.

[156] B. Alkhairalla *et al.* Anchoring and orientational wetting of nematic liquid crystals on self-assembled monolayer substrates : an evanescent wave ellipsometric study. *Physical Review E*, 59:3033, 1999.

[157] B. Alkhairalla *et al.* Anchoring and orientational wetting of nematic liquid crystals on semi-fluorinated self-assembled monolayer surfaces. *Europhysics Letters*, 59:410, 2002.

[158] D.N. Stonescu, P. Martinot-Lagarde and I. Dozov. Anchoring transition dominated by surface memory effect. *Molecular Crystals Liquid Crystals*, 329:339, 1999.

[159] T.J. Sluckin. Anchoring transitions at liquid crystal surfaces. *Physica A*, 213:105, 1995.

[160] P.I.C. Teixeira and T.J. Sluckin. Microscopic theory of anchoring transitions at the surfaces of pure liquid crystals and their mixtures. I. The Fowler approximation. *Journal of Chemical Physics*, 97:1498, 1992.

[161] P.I.C. Teixeira and T.J. Sluckin. Microscopic theory of anchoring transitions at the surfaces of pure liquid crystals and their mixtures. II. The effect of surface adsoption. *Journal of Chemical Physics*, 97:1510, 1992.

[162] P.I.C Teixeira, T.J. Sluckin and D.E. Sullivan. Landau-de gennes theory of anchoring transition at a nematic liquid crystal-substrate interface. *Liquid Crystals*, 14:1243, 1993.

[163] T. Zheng Qian and P. Sheng. Liquid-crystal phase transitions induced by microtextured substrates. *Physical Review Letters*, 77:4564, 1996.

[164] T. Zheng Qian and P. Sheng. Orientational states and phase transitions induced by microtextured substrates. *Physical Review E*, 55:7111, 1997.

[165] H. Lange and F. Schmid. Surface anchoring on layers of grafted liquid-crystalline chain molecules : a computer simulation. *Journal of Chemical Physics*, 111:362, 2002.

[166] H. Lange and F. Schmid. An anchoring transition at surfaces with grafted liquid-crystalline chain molecules. *European Physical Journal E*, 7:175, 2002.

[167] H. Lange and F. Schmid. Surface anchoring on liquid crystalline polymer brushes. *Computer physics communications*, 147:276, 2002.

[168] M. Rigby. Hard gaussian overlap fluids. *Molecular Physics*, 68:687, 1989.

[169] E. de Miguel, E. Martín del Río. The isotropic-nematic transition in hard gaussian overlap fluids. *Journal of Chemical Physics*, 115:9072–9082, 2001.

[170] V.R. Bhethanabotla and W. Steele. A comparison of hard-body models for axially-symmetric molecules. *Molecular Physics*, 60:249, 1987.

[171] M. Rigby. Virial expansion for hard nonspherical molecules. *Journal of Chemical Physics*, 53:1021, 1970.

[172] T. Boublík and M. Díaz penã. The equation of state of hard gaussian-overlap fluids. *Molecular Physics*, 70:1115, 1990.

[173] M.J. Maeso and J.R. Solana. An accurate equation of state for hard gaussian overlap fluids from a generalized carnahan-starling method. *Molecular Physics*, 79:449, 1993.

[174] E. de Miguel, E. Martín del Río. Equation of state for hard gaussian overlap fluids. *Journal of Chemical Physics*, 118:1852, 2003.

[175] R. Eppenga and D. Frenkel. Monte carlo study of the isotropic and nematic phases of infinitely thin hard platelets. *Molecular Physics*, 52:1303, 1984.

[176] C. Zannoni. Liquid crystal observables : static and dynamic properties. In P. Pasini and C. Zannoni, editor, *Advances in the computer simulations of liquid crystals*, chapter 2, page 17. Kluwer Academic, 2000.

[177] E. de Miguel. System size effects at the isotropic-nematic transition from computer simulations. *Physical Review E*, 47:3334, 1992.

[178] X. Zhou, H. Chen and M. Iwamoto. Orientational orders of small anisotropic molecules confined in slit pores. 2003.

[179] P.I.C Teixeira, A. Chrzanowska, G.D. Wall and D.J. Cleaver. Density functional theory of a Gay-Berne film between aligning walls. *Molecular Physics*, 99:889, 2001.

[180] R.E. Webster. *Computer simulation of confined liquid crystal dynamics.* PhD thesis, Sheffield Hallam University, November 2001.

[181] G.D. Wall and D.J. Cleaver. Computer simulations of adsorbed liquid crystal films. *Molecular Physics*, 101:1105, 2003.

[182] R. Holyst and A. Poniewierski. Director orientation at the nematic-phase isotropic-phase interface for the model of hard spherocylinders. *Physical Review A*, 35:1391, 1988.

[183] F. Barmes, M. Ricci, C. Zannoni and D.J. Cleaver . Computer simulations of pear shaped particles. *Physical Review E*, in the press, 2003.

[184] W.H. Press et al. *Numerical recipes in C, the art of scientific computing.* Cambridge University Press, 1990.

[185] G.P. Bryan-Brown, C.V. Brown, I.C. Sage and V.C. Hui. Voltage-dependent anchoring of a nematic liquid crystal on a grating surface. *Nature*, 392:365, 1998.